

ISSN en trámite

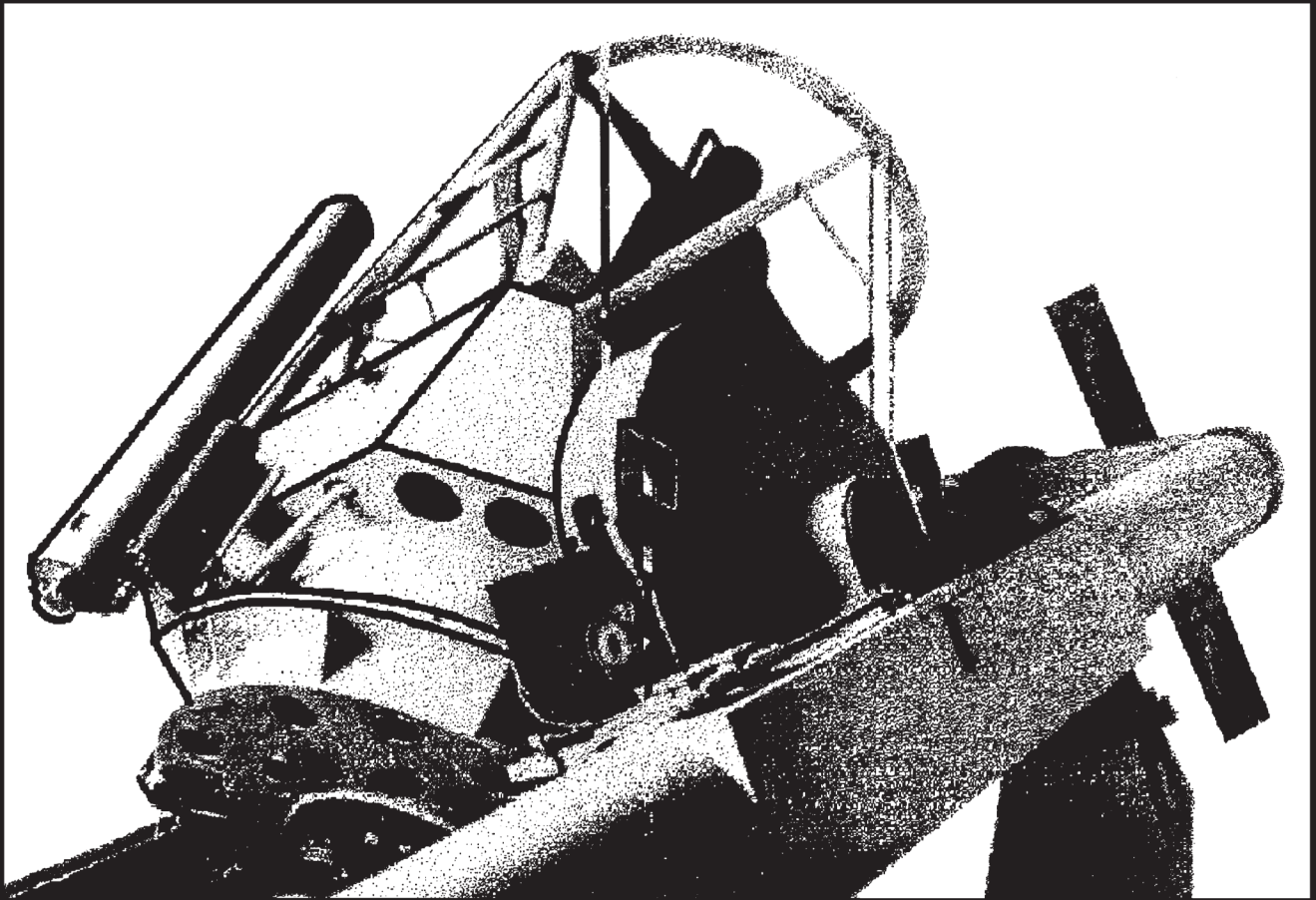
volumen 56, número 2, octubre 2020



instituto de astronomía

unam

# revista mexicana de astronomía y astrofísica



revista mexicana de astronomía y astrofísica

volumen 56  
número 2  
octubre 2020

Instituto de Astronomía  
Universidad Nacional Autónoma de México

# revista mexicana de astronomía y astrofísica

*Editores fundadores*

Eugenio E. Mendoza V., Paris Pişmiş y Silvia Torres-Peimbert

*Revista Mexicana de Astronomía y Astrofísica*

*Editora:* Christine Allen

*Revista Mexicana de Astronomía y Astrofísica. Serie de Conferencias*

*Editora:* Silvia Torres-Peimbert

*Editores asociados*

William Henney

*Comité editorial*

Horacio A. Dottori (Universidade Federal Rio Grande do Sul, Brasil)

Guido Garay (Universidad de Chile, Santiago, Chile)

Gloria Koenigsberger (Universidad Nacional Autónoma de México)

Hugo Levato (Complejo Astronómico El Leoncito, Argentina)

Luis F. Rodríguez (Universidad Nacional Autónoma de México)

José-María Torrelles (Institut d'Estudis Espacials de Catalunya, Barcelona, España)

Alan M. Watson (Universidad Nacional Autónoma de México)

*Asistentes editoriales*

Héctor Miguel Cejudo Camacho

Tulio Lugo Córdova

*Asesoría en cómputo*

Alfredo Díaz Azuara, Carmelo Guzmán Cerón, Liliana Hernández Cervantes

y Francisco Ruíz Sala

D.R. © 2020, Universidad Nacional Autónoma de México

Av. Universidad 3000

Col. Universidad Nacional Autónoma de México, C. U.

Alcaldía Coyoacán

04510 Ciudad de México

ISSN en trámite

URL de DOI: <https://doi.org/10.22201/ia.01851101p.2020.56.02>

[rmaa@astro.unam.mx](mailto:rmaa@astro.unam.mx)

<http://www.astroscu.unam.mx/RMxAA/>

La *RMxAA* aparece indexada en Current Contents, Science Citation Index, Astronomy and Astrophysics Abstracts, Physics Briefs, Publicaciones Científicas en América Latina, Astronomy and Astrophysics Monthly Index, PERIODICA, RedALyC, Latindex y SciELO.

---

*Revista Mexicana de Astronomía y Astrofísica*, volumen 56, número 2, octubre 2020, es una publicación semestral, editada y distribuida por el Instituto de Astronomía, UNAM, Circuito Exterior, Ciudad Universitaria, 04510, Alcaldía Coyoacán, Ciudad de México, Teléfono: 5556223906, Correo Electrónico: [rmaa@astro.unam.mx](mailto:rmaa@astro.unam.mx), ISSN en trámite. Editora responsable: Christine Patricia Allen Armiño. Distribución: Bienes y Servicios del Instituto de Astronomía, UNAM. Impresa por Grupo Edición, S.A. de C.V., Xochicalco 619, Colonia Letrán Valle, 03650, Alcaldía Benito Juárez, Ciudad de México. Fecha de impresión: 27 de septiembre de 2020. Número de ejemplares impresos: 500 en papel Couché de 100 gramos los interiores y en cartulina Couché de 250 gramos los forros. Precio de la publicación: gratuito.

$\gamma$ DOR: A PULSATING COMPONENT OF KIC 8043961 IN A STELLAR TRIPLE SYSTEM	<i>C. Kamil, H. A. Dal, O. Özdarcan, &amp; E. Yoldaş</i>	179
A SEARCH FOR PULSATION IN TWENTY-ONE WHITE DWARFS	<i>E. Paunzen, G. Handler, J. Janík, Z. Zemanová, M. Rode-Paunzen, M. S. O'Brien, T. K. Watson, &amp; M. Drózdź</i>	193
THE INFLUENCE OF THE MASS DISTRIBUTION OF STELLAR OBJECTS ON THEIR GRAVITATIONAL FIELDS	<i>V. A. Stephanovich, W. Godłowski, M. Biernacka, &amp; B. Mrzygłód</i>	201
INFRARED TRANSITIONS OF DIATOMIC MOLECULES AND THE TELLURIC LINES	<i>D. Lozano-Gómez, A. García-Varela, &amp; B. Sabogal</i>	217
FIRST PHOTOMETRIC INVESTIGATION OF TWO ECLIPSING BINARY SYSTEMS CRTS J213033.6+213159 AND 1SWASP J212454.61+203030.8	<i>M. Martignoni, C. Barani, F. Acerbi, &amp; R. Michel</i>	225
THE ADF AND THE $t^2$ FORMALISM IN H II REGIONS BASED ON THE UPPER MASS LIMIT OF THE IMF FOR THE MW	<i>L. Carigi, A. Peimbert, M. Peimbert, &amp; G. Delgado-Inglada</i>	235
AN ASTROMETRIC AND PHOTOMETRIC STUDY OF THE INTERMEDIATE-AGE OPEN CLUSTER NGC 2158 AND ITS ECLIPSING BINARY [NBN2015]78	<i>A. E. Abdelaziz, Y. H. M. Hendy, A. Shokry, S. M. Saad, F. Y. Kamal, &amp; K. A. Edris</i>	245
PHOTOMETRIC STUDY OF THREE SHORT PERIOD VARIABLE STARS	<i>J. H. Peña, S. B. Juárez, A. A. Soni, H. Huepa, A. Rentería, &amp; A. L. Zuñiga</i>	259
DYNAMICS AROUND AN ASTEROID MODELED AS A MASS TRIPOLE	<i>L. B. T. dos Santos, L. Marchi, P. A. Sousa-Silva, D. M. Sanchez, S. Aljbaae, &amp; A. F. B. A. Prado</i>	269
ANALYSIS OF A SHORT PERIODIC PULSATOR: SX PHOENICIS STAR XX CYG	<i>Mohamed Abdel-Sabour, Ahmed Shokry, &amp; Ahmed Ibrahim</i>	287
THIRTEEN YEARS OF WEATHER STATISTICS AT SAN PEDRO MARTIR OBSERVATORY	<i>I. Plauchu-Frayn, E. Colorado, M. G. Richer, &amp; C. Herrera-Vázquez</i>	295
FOUR NEW $\gamma$ DORADUS VARIABLES IN ECLIPSING BINARIES: REVISED PULSATION PERIOD RELATIONS	<i>O. Özdarcan &amp; Ö. Çakırlı</i>	321
AUTHOR INDEX		331

## $\gamma$ DOR: A PULSATING COMPONENT OF KIC 8043961 IN A STELLAR TRIPLE SYSTEM

C. Kamil, H. A. Dal, O. Özdarcan, and E. Yıldas

Department of Astronomy and Space Sciences, University of Ege, İzmir, Turkey.

Received February 5 2018; accepted April 20 2020

### ABSTRACT

We present new findings about KIC 8043961. We find the effective temperatures of the components as  $6900 \pm 200$  K for the primary, and  $6598 \pm 200$  K for the secondary, while the logarithm of the surface gravities are found to be  $4.06 \text{ cm s}^{-2}$  and  $3.77 \text{ cm s}^{-2}$ , respectively. Combination of the light curve with the spectroscopic orbit model results leads to a mass ratio of  $1.09 \pm 0.07$  with an orbital inclination of  $73.71 \pm 0.14$  and a semi-major axis of  $8.05 \pm 0.22 R_{\odot}$ . Masses of the primary and secondary components are calculated as  $1.379 \pm 0.109 M_{\odot}$  and  $1.513 \pm 0.181 M_{\odot}$ , while the radii are found to be  $1.806 \pm 0.084 R_{\odot}$  and  $2.611 \pm 0.059 R_{\odot}$ . In addition, we obtain a considerable light contribution ( $\approx 0.54\%$ ) of a third body. We compute a possible mass for the third body as  $0.778 \pm 0.002 M_{\odot}$ . We find that the primary component exhibits  $\gamma$  Dor type pulsations with 137 frequencies.

### RESUMEN

Presentamos nuevos hallazgos sobre KIC 8043961. Encontramos que la temperatura efectiva es de  $6900 \pm 200$  K para la primaria, y de  $6598 \pm 200$  K para la secundaria, mientras que los logaritmos de las gravedades superficiales son, respectivamente,  $4.06 \text{ cm s}^{-2}$  y  $3.77 \text{ cm s}^{-2}$ . Combinamos la curva de luz con un modelado espectroscópico de la órbita y obtenemos un cociente de masas de  $1.09 \pm 0.07$ , una inclinación orbital de  $73.71 \pm 0.14$  y un semieje mayor de  $8.05 \pm 0.22 R_{\odot}$ . Calculamos las masas de la primaria y de la secundaria, y obtenemos  $1.379 \pm 0.109 M_{\odot}$  y  $1.513 \pm 0.181 M_{\odot}$ . Los radios son, respectivamente,  $1.806 \pm 0.084 R_{\odot}$  y  $2.611 \pm 0.059 R_{\odot}$ . Además encontramos una contribución apreciable de un tercer cuerpo, ( $\approx 0.54\%$ ). Calculamos la masa posible del tercer cuerpo y obtenemos  $0.778 \pm 0.002 M_{\odot}$ . Encontramos que la primaria muestra pulsaciones tipo  $\gamma$  Dor con 137 frecuencias.

*Key Words:* techniques: photometric — methods: data analysis — stars: binaries: eclipsing — stars: individual:  $\gamma$  Dor, KIC 8043961

### 1. INTRODUCTION

Astronomers have been trying to find a better way to understand stellar evolution in detail. Like the Kepler Mission, the space missions have been giving a new perspective on this point, as expected. For instance, the Kepler Mission first aimed to detect exo-planets (Borucki et al. 2010; Koch et al. 2010; Caldwell et al. 2010). For this aim, scientists counted on its highest quality and sensitivity ever obtained in the photometry (Jenkins et al. 2010a,b). Indeed, the high quality data accumulated by the Kepler Satellite revealed the presence of numerous variable targets, such as new eclipsing binaries, apart from

discovering thousands of exo-planets (Slawson et al. 2011; Matijević et al. 2012). Many of the newly discovered eclipsing binaries possess chromospherically active components (Balona 2015), while lots of them have pulsating components with several frequencies (Kamil and Dal 2017; Özdarcan and Dal 2017).

Stellar pulsation is an important phenomenon to understand stellar evolution. On this point, the very high precision photometry of the Kepler Satellite provides a remarkable chance to astronomers. Before the space missions, the photometric observations revealed the presence of several types of pulsating stars, such as  $\gamma$  Doradus,  $\delta$  Scuti type pulsat-

TABLE 1  
LITERATURE PARAMETERS FOR THE TARGET

$T$ (K)	$\log(g)$ ( $\text{cms}^{-2}$ )	$R$ ( $R_{\odot}$ )	$M$ ( $M_{\odot}$ )	[Fe/H]	Ref
6565	-	-	-	0.270	Ammons et al. (2006)
6348-6666	3.620	-	-	-0.380	Pinsonneault et al. (2012)
6657	3.621	3.177	1.532	-0.375	Huber et al. (2014)
6626-6935	4.100	-	-	-0.130	Frasca et al. (2016)
6649	3.619	3.177	1.532	-0.380	Mathur et al. (2017)

ing, and also solar-like oscillating stars on the main sequence of the Hertzsprung-Russell (hereafter HR) diagram. Although there are several types of pulsating stars out of the main sequence, these samples are located close to the main sequence, sometimes side by side. In addition, the physical processes behind the pulsating nature of these stars are easily demonstrated by astroseismology, depending on the analysis of the pulsation frequencies. This is why the pulsating stars play a key role to understand stellar evolution (Cunha et al. 2007; Aerts et al. 2010).

Recent studies in the literature demonstrated that some stars can pulsate in both pressure ( $p$ ) and gravity ( $g$ ) modes. These stars are generally classified as  $\gamma$  Dor /  $\delta$  Scuti hybrid pulsators. It is well known that  $p$ -modes, which are observed in the  $\delta$  Scuti type variables, are generally sensitive to the outer layers of the star, while  $g$ -modes, which are observed in the  $\gamma$  Doradus type stars, are sensitive to the stellar interior (Aerts et al. 2010). After analyzing data obtained by the Kepler Satellite, the number of hybrid pulsators has remarkably increased (Grigahcène et al. 2010; Uytterhoeven et al. 2011; Tkachenko et al. 2013; Balona 2014).

One of such systems worth examining is KIC 8043961 (Kirk et al. 2016), on which nature there are several debates. Although there are several studies on KIC 8043961, they are generally grouped into two areas, such as temperature and triplicity. Ammons et al. (2006) computed the target  $E(B-V)$  as  $0^m.023$  for its estimated distance of 76 pc. According to Pickles and Depagne (2010), KIC 8043961 is a main sequence source of spectral type F6, while Watson et al. (2006) listed the target as a variable star with a period of 1.559231 d. They also gave the stellar distance as 589.757 pc depending on  $A_v = 0^m.358$ . Frasca et al. (2016) indicated that the target was a main sequence source with a spectral type of F0-F2. Some physical parameters given in the literature are listed in Table 1 and, as seen from the table, the physical nature of system is not absolutely determined. The most important study about KIC 8043961 is that of Conroy et al. (2014), where they

posited a third body in an almost circular orbit with period of 478 day, depending on the eclipse time variation, and an amplitude of 184 s. Recently, Borkovits et al. (2016) also found a variation with a period of 478.6 d from the eclipse times. Taking the total mass as  $\approx 2M_{\odot}$  for the eclipsing binary, they estimated a minimum mass of  $0.61 M_{\odot}$  for the third body, with  $e = 0.247$  and  $\omega = 13$  degree.

In this study, we try to reveal the nature of KIC 8043961, separately analyzing each variation detected in its light curve together with spectroscopic observations. In the next section, we summarize the observations and data reductions. Then, we determine the radial velocity variation from the available spectroscopic observations in § 3.1; we estimate the temperatures of the components from the same observations in § 3.2. To determine the size of the third body, we examine the  $O - C$  variation in § 3.3, and we model the light curve of the eclipsing binary in § 3.4. In § 3.5 we further analyse the out-of-eclipse variations. We summarize and discuss our findings in the last section.

## 2. OBSERVATIONS AND DATA REDUCTIONS

### 2.1. Spectral Observation

We carried out spectroscopic observations of the system with the 1.5-m Russian - Turkish telescope and the Turkish Faint Object Spectrograph Camera (TFOSC<sup>1</sup>) at Tubitak National Observatory. Using the échelle mode of TFOSC, we achieve an actual resolution of  $R = \lambda / \Delta\lambda \approx 3000$  around  $5500\text{Å}$ . The whole spectrum covers a wavelength interval between  $3900 - 9100\text{Å}$  in 11 échelle orders. All spectra were recorded with a back illuminated  $2048 \times 2048$  pixels CCD camera, which has a pixel size of  $15 \times 15 \mu\text{m}^2$ .

We recorded eight optical spectra of KIC8043961 between the 2014 and 2017 observing seasons. In addition, we obtained optical spectra of  $\iota$  Psc (HD 222368, F7V,  $v_r = 5.656 \text{ kms}^{-1}$ ) and  $o$  Aql (F8V,  $v_r = 1.40 \text{ kms}^{-1}$ ) with the same instrumental

<sup>1</sup><http://www.tug.tubitak.gov.tr/rtt150.tfosc.php>

set-up. The spectra of these two stars were used as templates for radial velocity determinations and preliminary spectral type estimations. Typical signal-to-noise ratios (SNR) of observed spectra are between 140 and 190 for a single observation with an hour of exposure time.

We reduced and extracted the observed spectra by following standard steps for reducing and extracting échelle spectra. In the first step, bias correction was applied to all images, and a normalized flat-field image was obtained via bias-corrected halogen lamp frames. Then, all science and Fe-Ar calibration frames were divided by the normalized flat-field frame; scattered light correction was applied to all bias and flat-field corrected images. At that point, reduced science and Fe-Ar images were obtained. Next, spectra were extracted from the reduced images. In the following steps, wavelength calibration was applied to the reduced and extracted science frames via Fe-Ar images, and finally wavelength calibrated science images were normalized to the continuum by using cubic spline functions. The whole procedure was applied under IRAF<sup>2</sup> environment.

## 2.2. Photometric Data

In the light curve and  $O-C$  analyses, we mainly use long cadence (29.4 minutes of exposure time, hereafter LC) Kepler photometry, which is available in the Kepler eclipsing binary catalogue<sup>3</sup> as detrended and normalized fluxes (Slawson et al. 2011; Prša et al. 2011). We also use the short cadence (hereafter SC) data from the same database in the same format, in order to investigate possible high frequency variations. The data were collected over a broad wavelength interval between 4100Å and 9100Å, which suffers from lack of color information, but provides very high precision. The LC data cover  $\approx 4$  years of time base without any considerable time gap. The reported light contamination is 0.3% in the MAST database, practically meaning no light contribution of any light sources from the background. Available SC and LC photometry is shown in Figure 1. In the figure, we computed the phase-folded light curve with respect to the light elements in equation (1) given by Slawson et al. (2011).

<sup>2</sup>The Image Reduction and Analysis Facility is hosted by the National Optical Astronomy Observatories in Tucson, Arizona at iraf.noao.edu.

<sup>3</sup><http://keplerebs.villanova.edu/>

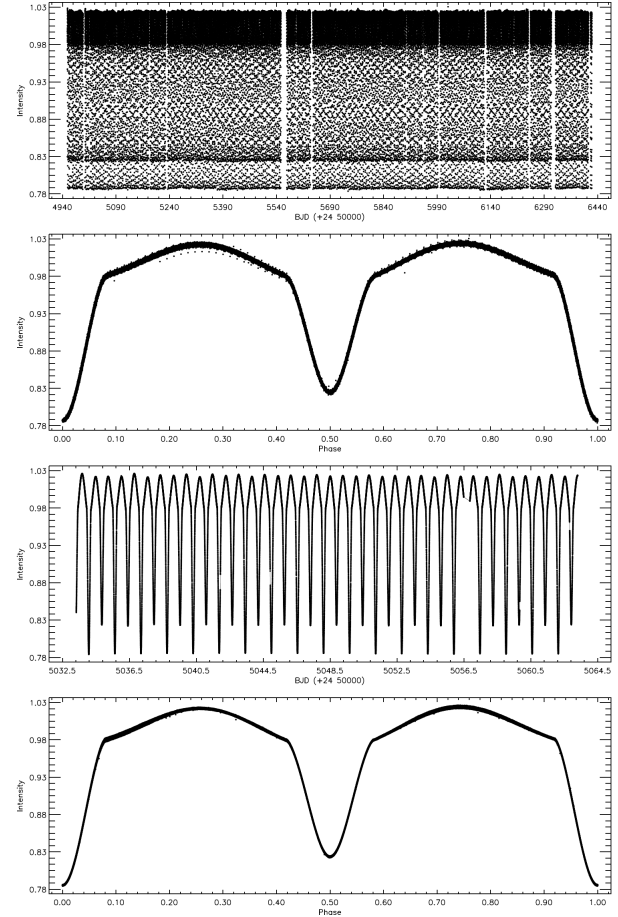


Fig. 1. KIC 8043961 light curve derived with the data taken from the Kepler Database. In the upper two panels, the light variation is plotted versus time and phase depending on available LC Data; it is plotted for the SC data in the bottom two panels.

## 3. ANALYSES AND MODELS

### 3.1. Radial Velocities and Spectroscopic Orbit

We start our analysis with the measurement of the radial velocities of each component, in order to determine the spectroscopic orbit of the system. For this purpose, we cross-correlate each observed spectrum of KIC 8043961 with spectra of  $\iota$  Psc and  $o$  Aql. The cross correlation was applied according to the method proposed by Tonry and Davis (1979). The practical application of the method was done with the FXCOR task under IRAF environment. Among the two template stars,  $\iota$  Psc provided a slightly better cross-correlation and was adopted as the radial velocity template. Cross-correlation was performed for the wavelength range between 4900 - 5400Å, ignoring strongly blended spectral lines. In Figure 2,

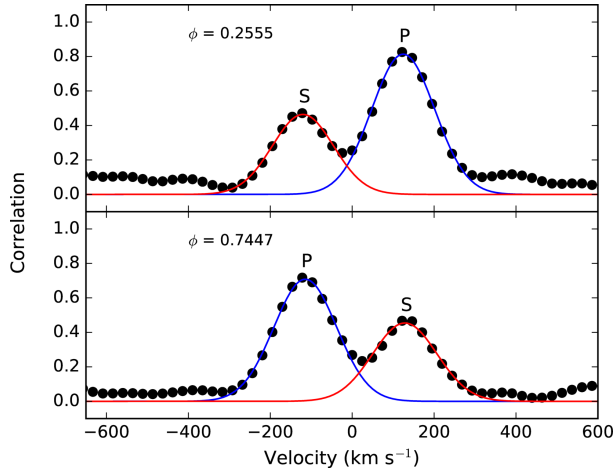


Fig. 2. Cross-correlation functions of KIC 8043961 obtained at orbital quadratures. The letter  $\phi$  shows the orbital phase in each panel. P and S denote the primary and secondary component, respectively. The color figure can be viewed online.

we show the cross-correlation functions of spectra obtained at orbital quadratures, where both components are clearly resolved.

We tabulate the measured radial velocities in Table 2, together with brief observational information. In the table, orbital phases are calculated via ephemeris time and period given by Borkovits et al. (2016). These light elements are adopted for phasing the radial velocities and light curve.

Before attempting an orbital solution, we inspected the orbital eccentricity via phased folded Kepler photometry. Primary and secondary eclipses are located precisely at 0.0 and 0.5 phases, respectively, indicating a non-eccentric orbit. Therefore, we model the spectroscopic orbit assuming a circular orbit. The orbital solution was achieved by applying the Levenberg-Marquardt algorithm (Levenberg 1944), and Markov Chain Monte Carlo simulations via EMCEE software developed under a Python environment (Foreman-Mackey et al. 2013). We tabulate the final spectroscopic orbit parameters and their uncertainties in Table 3, and we plot the phase-folded radial velocities, theoretical models and residuals from the best-fitting models in Figure 3. We notice that the less massive, smaller and hotter component is eclipsed at the primary minimum, hence we interpret the numerical values in Table 3 according to this finding.

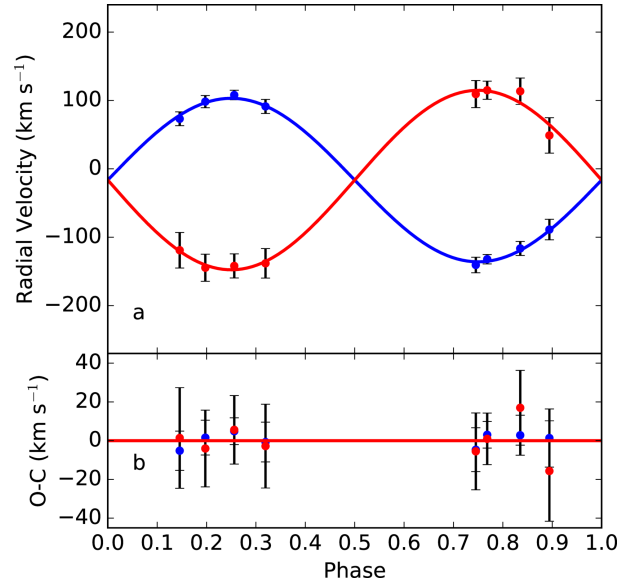


Fig. 3. (a) Measured radial velocities of the primary and the secondary component (blue and red filled circles, respectively), and corresponding model orbit (blue and red curve). (b) Residuals from the model. The color figure can be viewed online.

### 3.2. Spectral Type

In order to estimate atmospheric properties of the components reliably, we use the TFOSC spectrum of KIC 8043961 obtained at HJD 2456842.3645, corresponding to  $\approx 0.75$  orbital phase, where we can clearly resolve spectral lines of both components. The SNR of that spectrum is around 170, based on photon statistics. Before searching for the best atmospheric parameters, we fixed the micro-turbulence velocity of each component at  $2 \text{ km s}^{-1}$ , and the logarithm of the surface gravity  $\log(g)$  of the primary and secondary components at 4.04 and 3.77, respectively. These  $\log(g)$  values are calculated from combination of spectroscopic orbit parameters and light curve modeling results (see next section). Then we adjusted effective temperatures and metallicities of the components via the spectral synthesis method in a wavelength interval 4750 - 5750 Å. In practice, we used the latest version of the Python framework *iSpec* (Blanco-Cuaresma et al. 2014). Synthetic spectra were calculated for temperatures between 6250 - 7250 K with steps of 50 K, and for metallicities between solar (0.0) and  $-1.0$  with steps of 0.25. Among the different radiative transfer code options provided by *iSpec*, we adopted SPECTRUM<sup>4</sup> code

<sup>4</sup><http://www.appstate.edu/~grayro/spectrum/spectrum.html>

TABLE 2  
SPECTROSCOPIC OBSERVATIONS AND RADIAL VELOCITIES

HJD (24 00000+)	Orbital Phase	Exposure time (s)	Primary		Secondary	
			$V_r$ km s <sup>-1</sup>	$\sigma$ km s <sup>-1</sup>	$V_r$ km s <sup>-1</sup>	$\sigma$ km s <sup>-1</sup>
56842.3645	0.7447	3000	-140.6	11.3	109.3	19.8
56842.4005	0.7678	3000	-132.1	6.9	115.0	13.3
56846.3781	0.3188	3000	91.3	10.3	-138.1	21.6
56888.2869	0.1970	3000	98.3	9.0	-144.6	19.8
56891.4965	0.2555	3000	108.0	6.9	-141.9	17.7
57592.4858	0.8344	1200	-116.4	10.3	113.5	19.3
57616.3579	0.1448	3600	73.2	10.1	-119.0	26.0
57854.5254	0.8934	2700	-88.7	15.0	48.9	25.9

TABLE 3  
SPECTROSCOPIC ORBITAL ELEMENTS OF  
KIC 8043961\*

Parameter	Value
$P_{\text{orb}}$ (days)	1.5592121 (fixed)
$T_0$ (HJD2454+)	954.555903 (fixed)
$\gamma$ (km s <sup>-1</sup> )	-15.4 ± 3
$K_1$ (km s <sup>-1</sup> )	131 ± 7
$K_2$ (km s <sup>-1</sup> )	120 ± 3
$e$	0 (fixed)
$\omega$	...
$a \sin i$ ( $R_{\odot}$ )	7.7 ± 0.2
$M \sin^3 i$ ( $M_{\odot}$ )	2.56 ± 0.18
Mass ratio ( $q = M_2/M_1$ )	1.09 ± 0.07
rms1 (km s <sup>-1</sup> )	3.4
rms2 (km s <sup>-1</sup> )	8.9

\*  $M_1$  and  $M_2$ , masses of the primary and secondary component,  $M$  the total mass of the system.

(Gray and Corbally 1994) along with ATLAS9 model atmospheres (Castelli and Kurucz 2004) and a line list obtained from the third version of the Vienna atomic line database (VALD3) (Ryabchikova et al. 2015).

All calculated synthetic spectra were convolved with a Gaussian line spread function to match their resolution to the TFOSC spectra. After we obtained the instrumentally broadened synthetic spectra, we started to calculate the composite spectrum of the system. At that point, we selected a trial synthetic spectrum for the primary component. Next, we selected a synthetic spectrum for the secondary component, with a proper temperature as indicated by the preliminary light curve modelling. Then, we applied a proper radial velocity shift to each selected

synthetic spectrum to match its spectral lines to the lines of the corresponding component in the observed spectrum. Finally, we calculated the composite spectrum of the system via synthetic spectra mentioned above, and the radius ratio,  $R_1/R_2 = r_1/r_2 = 0.69$ , where  $r$  means fractional radius, found from the light curve analysis. We repeated this process for every possible synthetic spectra configuration and searched the best matched composite spectrum of the system, i.e. the best-fitting synthetic spectrum for each component. We checked the reliability of the parameters suggested by the best matched synthetic spectra, with the best-fitting light curve model parameters. Confirming the light curve and spectroscopic modelling results iteratively, we find the self-consistent effective temperature of the primary and the secondary component as 6900 K and 6600 K. The temperatures and the surface gravities suggest F3V and F5 III-IV spectral types for the hot and cool components, respectively (Gray 2005). The resulting overall metallicity of the system is found to be  $[M/H] = 0.25$ . Estimated uncertainties are 200K in temperature and -0.25 in metallicity, which are predicted by considering the temperature and metallicity steps in the model atmospheres, the SNR of observed spectra and the instrumental resolution of TFOSC spectra.

Furthermore, we observe a perceivable effect of rotational broadening in our spectra. Full width at half-maximum (FWHM) of the instrumental profile of TFOSC spectra is  $\approx 1.8\text{\AA}$  around 5500  $\text{\AA}$ , meaning that any projected rotational velocities ( $v \sin i$ ) above  $\approx 50 \text{ km s}^{-1}$  could be observed. From the combined spectroscopic orbit and light curve modelling, we estimate  $v \sin i$  values of the primary and the secondary component as  $81 \text{ km s}^{-1}$  and  $54 \text{ km s}^{-1}$ , respectively, assuming synchronous rotation. Since numerical fitting attempts of  $v \sin i$  velocities did not

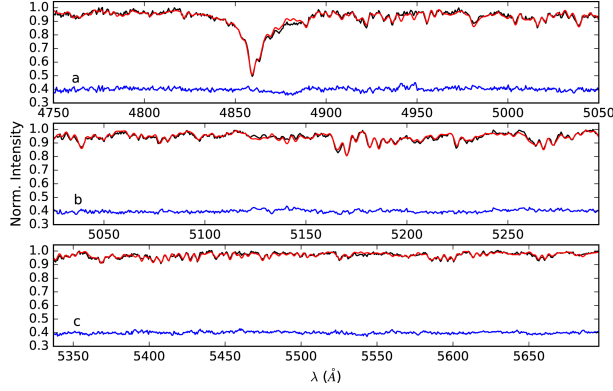


Fig. 4. Observed spectrum (black line), best-fitting composite synthetic spectrum (red line) and residuals (blue line). Residuals are shifted upwards by 0.4 for a better view. The color figure can be viewed online.

TABLE 4

TIMES OF MINIMA AND  $O - C$  RESIDUALS\*

MJD (Obs)	E	Type	O-C (II) (day)
54953.77420	-0.5	II	-0.00141
54954.55380	0.0	I	-0.00142
54955.33380	0.5	II	-0.00103
54956.11340	1.0	I	-0.00103
54956.89260	1.5	II	-0.00144
54957.67220	2.0	I	-0.00145
54958.45190	2.5	II	-0.00135
54959.23150	3.0	I	-0.00136
54960.01120	3.5	II	-0.00127
54960.79080	4.0	I	-0.00127

\*Obtained from the Kepler SC and LC data.

yield stable and reliable results, we only applied rotational broadening to the corresponding synthetic spectrum of the components, by using the estimated velocities above, and then calculated the composite spectrum of the system. In Figure 4, we plot observed spectrum, best fitting composite synthetic spectrum and residuals.

### 3.3. Orbital Period Variation

In order to study the orbital period variation of KIC 8043961, we determine mid-times of primary and secondary eclipses, where we obtain 1688 minima times in total, of which 844 are the primary minima and 844 the secondary times of minimum. For each minimum, we only consider the orbital cycle that includes the corresponding minimum, and

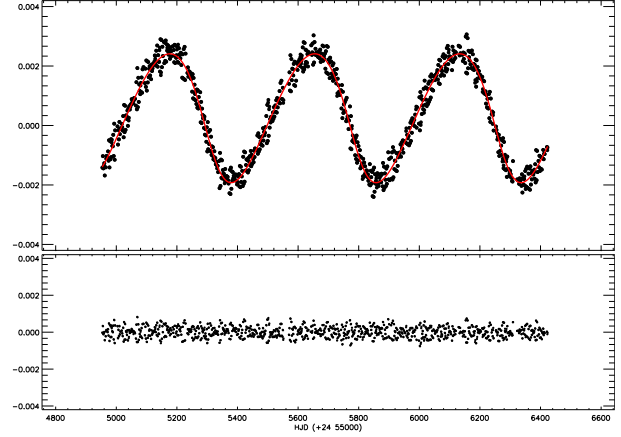


Fig. 5. The  $O - C$  variations of KIC 8043961. In the figure, the ( $O - C$ ) II variation, derived after the linear correction, is shown in the upper panel, together with the best-fitting orbit (smooth red curve), while the residuals are shown in the bottom panel. The color figure can be viewed online.

then run the differential correction program of the Wilson-Devinney code by only adjusting ephemeris time and keeping all other parameters fixed. This process is fairly straightforward for primary eclipses, while we need to change the role of the components during the iterations, in order to compute secondary eclipses. Ten computed minima times are listed in Table 4, while the rest of them are available upon request. For each observed eclipse time, we compute expected eclipse times by using the following light elements (equation 1) to obtain  $O - C$  values:

$$JD (Hel.) = 24\,54954.555903 + 1^d.5592121 \times E. \quad (1)$$

Inspecting the  $O - C$  values, we notice a clear sinusoidal variation, which is presumably due to the light travel time effect (hereafter LTTE) caused by an unseen third body in the system. Taking the light elements given in equation (1) as initial values, we modelled the sinusoidal variation together with the linear trend. Corrected ephemeris time and period are given by equation (2):

$$JD (Hel.) = 24\,54954.555221(1) + 1^d.5592129(1) \times E + \Delta t, \quad (2)$$

where  $\Delta t$  is term for the LTTE of the third body. Using the corrected ephemeris time and the period, we calculate ( $O - C$ )<sub>II</sub> residuals. Applying the LTTE equation given by Irwin (1959) to the ( $O - C$ )<sub>II</sub> residuals, we calculate the orbit of the third body. In Figure 5, we show ( $O - C$ )<sub>II</sub> residuals together with

TABLE 5

THIRD BODY PARAMETERS OF KIC 8043961\*

$T_0$	$55311.00 \pm 1.57$
$P$ (day)	$478.339 \pm 0.489$
$a \sin i$ (AU)	$0.387 \pm 0.002$
$w$ (deg)	$204 \pm 1.11$
$e$	$0.266 \pm 0.008$
$n$	$0.01314 \pm 0.00001$
$f(m)$	$0.0337 \pm 0.0035$
$M_3 (M_\odot)$	4.909 (for $i = 15$ (deg))
$M_3 (M_\odot)$	1.161 (for $i = 45$ (deg))
$M_3 (M_\odot)$	0.799 (for $i = 75$ (deg))
$M_3 (M_\odot)$	0.767 (for $i = 90$ (deg))

\*Derived from O-C analysis.

the best-fitting third body orbit. Calculated third body parameters are listed in Table 5.

Assuming that the orbital inclination of the presumed third body is the same as the inclination of the eclipsing binary, and using the calculated total mass of the eclipsing binary ( $2.892 M_\odot$ ) for the absolute parameters of the components, we estimated the mass of the third body as listed in Table 5 for different  $i$  values.

### 3.4. Light Curve Analysis

To determine the physical conditions of the components, we model the average SC light curve by using 2015 version of the Wilson - Devinney Code (Wilson and Devinney 1971; Wilson and Van Hamme 2014). The shape of the light curve clearly indicates a detached configuration. In the analysis, we fix the two critical parameters, mass ratio and effective temperature of the primary component ( $T_1$ ) to 1.09 and 6900 K, respectively, which are found from the spectroscopic orbit modelling and the spectral type estimation. Considering the spectral type corresponding to this temperature, the albedos ( $A_1$  and  $A_2$ ) and the gravity-darkening coefficients ( $g_1$  and  $g_2$ ) of the components are adopted for the stars with convective envelopes (Lucy 1967; Rucinski 1969). The nonlinear limb-darkening coefficients ( $x_1$  and  $x_2$ ) of the components are taken from Van Hamme (1993). In the analyses, the temperature of the secondary component ( $T_2$ ), the dimensionless potentials of the components ( $\Omega_1$  and  $\Omega_2$ ), the fractional luminosity of the primary component ( $L_1$ ), the inclination of the system ( $i$ ), the mass ratio of the system ( $q$ ), the semi-major axis ( $a$ ) and the third light are adopted

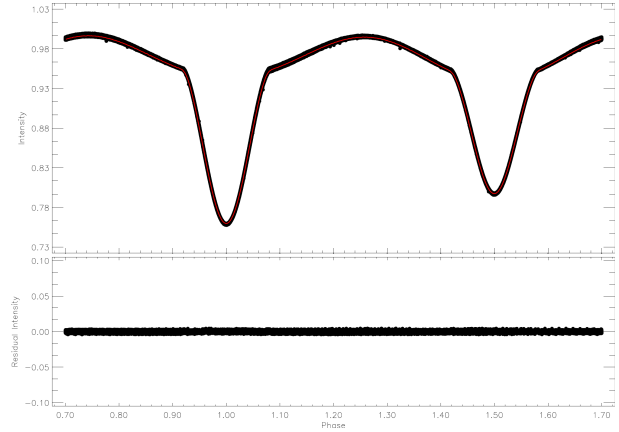


Fig. 6. Phase-folded LC light curve (filled circles) taken from the Kepler Database, and the best-fitting model (smooth red curve). The color figure can be viewed on-line.

as adjustable parameters. Although the synthetic curve derived by these parameters covers the entire observed light curve, a stable sinusoidal variation is still seen at out-of-eclipses. Considering the temperatures of the components, we modelled this variation by a stellar cool spot on the secondary component. We list the best-fitting model results in Table 6, and show the averaged phase-folded light curve together with the model in Figure 6.

The combination of results obtained from both the spectroscopic orbit and light curve modelling yields the physical parameters of the system listed in Table 7. These parameters show that the smaller, hotter and less massive primary component is still on the main sequence, while the larger, cooler and more massive secondary component appears to have evolved off the main sequence. We show the position of the components on the  $\log(T_{\text{eff}})$ - $\log(L/L_\odot)$  plane in Figure 7. In the bottom panel of the figure, the evolutionary status of the components is shown in the same plane with isochrones for  $[M/H] = -0.25$  (Bressan et al. 2012). The average age of the system is about  $2.2 \pm 0.3$  Gyr.

### 3.5. The Variation at Out-Of-Eclipses

Inspecting the residuals from the light curve modelling, we find a clear signal of a sinusoidal variation at out-of-eclipses. Considering the place of the primary component of KIC 8043961 in the HR diagram, the source of the variation is possibly a  $\gamma$  Doradus type pulsation. We analyse the residual data to search for possible pulsation frequencies, using the PERIOD04 software (Lenz and Breger 2005) that is based on the

TABLE 6  
LIGHT CURVE MODELLING RESULTS FOR  
KIC 8043961\*

Parameter	Value
$q$	$1.09 \pm 0.07$
$i$ ( $^\circ$ )	$73.71 \pm 0.02$
$T_1$ (K)	6900 (fixed)
$T_2$ (K)	$6598 \pm 200$
$\Omega_1$	$5.581 \pm 0.003$
$\Omega_2$	$4.432 \pm 0.002$
$L_1/L_T$	$0.3450 \pm 0.0005$
$L_2/L_T$	0.6008
$L_3/L_T$	$0.0542 \pm 0.0012$
$g_1, g_2$	0.32 (fixed), $0.457 \pm 0.007$
$A_1, A_2$	0.50 (fixed), $0.451 \pm 0.003$
$x_1, x_2$	0.654, 0.663 (fixed)
$y_1, y_2$	0.283, 0.274 (fixed)
$\langle r_1 \rangle$	$0.2261 \pm 0.0001$
$\langle r_2 \rangle$	$0.3286 \pm 0.0002$
Phase Shift	$-0.000208 \pm 0.000009$
$Co - Lat_{SpotI}$ (rad)	$1.519 \pm 0.118$
$Long_{SpotI}$ (rad)	$1.808 \pm 0.021$
$R_{SpotI}$ (rad)	$0.183 \pm 0.004$
$T_{ISpotI}$	0.98 (fixed)

\*Internal uncertainty of  $T_2$  is found as a few Kelvin, which is unrealistic, therefore it is assumed to be the same as the uncertainty of  $T_1$ .

TABLE 7  
PHYSICAL PARAMETERS OF KIC 8043961

Parameter	Primary	Secondary
Mass ( $M_\odot$ )	$1.379 \pm 0.109$	$1.513 \pm 0.181$
Separation ( $R_\odot$ )	$8.06 \pm 0.27$	
Radius ( $R_\odot$ )	$1.806 \pm 0.084$	$2.611 \pm 0.059$
$\log L$ ( $L_\odot$ )	$0.833 \pm 0.004$	$1.075 \pm 0.002$
$\log g$ ( $\text{cms}^{-2}$ )	$4.06 \pm 0.01$	$3.78 \pm 0.03$
$M_{bol}$ (mag)	$2.70 \pm 0.15$	$2.10 \pm 0.16$

discrete Fourier transform (hereafter DFT) method (Scargle 1982). As seen in Figure 8, we found 137 frequencies which exceed the  $3\sigma$  level. We tabulate these frequencies in Table 8, and plot the resulting model obtained from these frequencies together with the residual light curve in Figure 9.

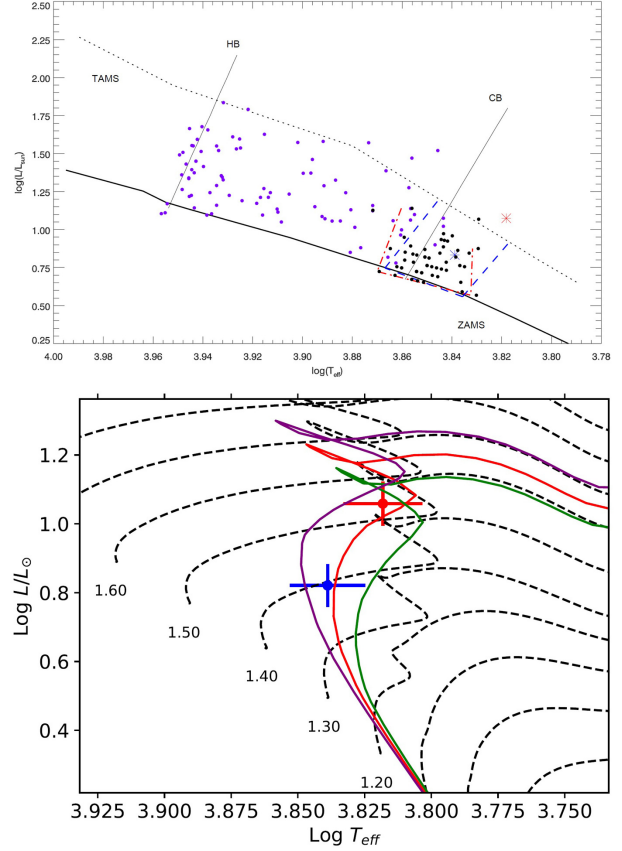


Fig. 7. Upper panel. Positions of the primary (blue asterisk) and the secondary (red asterisk) components of KIC 8043961 on the  $\log(T_{eff})$ - $\log(L/L_\odot)$  plane. The primary appears to be located among the  $\gamma$  Doradus type stars; the ZAMS and TAMS were taken from Girardi et al. (2000). The small filled black circles represent  $\gamma$  Doradus type stars listed in Henry et al. (2005). The dash-dotted lines (red) represent the borders of the area, in which  $\gamma$  Doradus stars appear. The blue dashed lines indicate the theoretical cool and hot boundaries of the  $\gamma$  Doradus instability strip, given by Warner et al. (2003). In addition, we plot the hot (HB) and cool borders (CB) computed from Rolland et al. (2002) of the  $\delta$  Scuti stars for comparison. The small filled purple circles represent detached and semi-detached binaries taken from Soydogan et al. (2006). Bottom panel. Individual components in the same plane with three different isochrones (Bressan et al. 2012). The filled circle shows the less massive, smaller but hotter component, while the red filled circle shows the more massive, larger but cooler component. The green, red and purple isochrones are for  $\log age$  of 9.40, 9.35 and 9.30, respectively. The color figure can be viewed online.

#### 4. RESULTS AND DISCUSSION

Spectroscopic analysis and light curve modelling of KIC 8043961 reveal that the system is a slightly

TABLE 8  
 FREQUENCY LIST OF  $\gamma$  DOR PULSATION FOUND IN THE ANALYSIS\*

Frequency	Frequency	Amplitude	Phase	Noise	SNR
F1	0.916416	0.000975	0.976502	0.000015	69.954572
F2	0.942190	0.000792	0.568788	0.000012	67.223506
F3	0.956949	0.000353	0.562851	0.000011	31.818026
F4	0.993697	0.000308	0.028697	0.000010	30.623664
F5	0.949851	0.000273	0.393345	0.000010	28.959837
F6	0.923608	0.000243	0.363458	0.000010	26.495071
F7	1.873358	0.000231	0.189382	0.000005	50.902279
F8	0.974498	0.000216	0.338794	0.000009	25.021613
F9	0.887055	0.000210	0.765381	0.000008	25.319987
F10	0.275072	0.000177	0.791680	0.000010	16.599333
F11	0.300848	0.000144	0.306613	0.000009	15.496189
F12	0.668357	0.000113	0.388377	0.000007	16.524546
F13	0.366276	0.000130	0.127347	0.000008	15.950863
F14	0.376595	0.000111	0.761279	0.000008	13.586635
F15	0.984063	0.000092	0.535489	0.000008	12.104475
F16	1.858608	0.000087	0.763904	0.000004	21.211509
F17	0.868183	0.000091	0.198983	0.000007	11.746275
F18	1.047241	0.000076	0.320245	0.000007	10.264264
F19	0.761510	0.000070	0.821559	0.000007	10.089111
F20	0.881004	0.000068	0.608747	0.000007	10.238665
F21	0.931190	0.000072	0.225136	0.000007	10.314234
F22	0.822440	0.000072	0.054409	0.000007	10.020085
F23	0.838783	0.000065	0.057601	0.000007	10.032803
F24	1.755210	0.000077	0.656801	0.000004	15.728606
F25	0.813057	0.000071	0.114027	0.000007	9.982051
F26	0.111354	0.000066	0.958094	0.000010	6.260455
F27	0.340336	0.000079	0.796978	0.000008	9.859690
F28	1.232040	0.000081	0.621758	0.000007	9.553888
F29	1.571022	0.000063	0.671356	0.000005	13.521431
F30	0.264255	0.000068	0.477712	0.000009	6.833383
F31	0.965094	0.000059	0.188122	0.000007	8.480951
F32	0.899936	0.000063	0.045391	0.000007	8.709595
F33	0.315615	0.000067	0.768945	0.000008	6.948675
F34	0.237268	0.000058	0.947569	0.000009	5.865668
F35	0.404073	0.000055	0.148505	0.000007	8.085690
F36	0.348656	0.000050	0.010840	0.000007	7.620083
F37	0.836521	0.000051	0.294970	0.000006	8.112678
F38	0.943443	0.000049	0.595186	0.000006	7.689664
F39	1.557797	0.000058	0.084863	0.000004	13.069212
F40	1.900344	0.000049	0.169896	0.000004	13.102947
F41	1.624016	0.000048	0.644379	0.000004	11.457698
F42	0.352339	0.000053	0.656969	0.000007	7.038268
F43	1.778928	0.000043	0.665775	0.000004	11.216445
F44	0.050852	0.000050	0.030521	0.000011	4.903525
F45	0.606112	0.000048	0.492856	0.000006	8.230251
F46	1.636105	0.000045	0.454696	0.000004	11.144403
F47	0.045897	0.000046	0.610881	0.000011	4.116043
F48	0.332966	0.000054	0.719763	0.000007	7.587804
F49	0.969087	0.000040	0.442950	0.000006	6.680742
F50	0.033530	0.000040	0.260326	0.000011	3.946902

\*The frequency number is listed in the first column, the found frequency in the second column. The amplitude of the signal, its phase and the SNR value of the signal are listed in the following columns.

TABLE 8. CONTINUED

Frequency	Frequency	Amplitude	Phase	Noise	SNR
F51	0.041740	0.000047	0.429774	0.000011	4.078355
F52	0.062306	0.000037	0.493489	0.000010	4.169141
F53	0.923070	0.000043	0.116737	0.000006	7.247459
F54	3.848074	0.000041	0.054995	0.000002	26.143136
F55	0.875308	0.000042	0.639336	0.000006	6.855955
F56	0.899008	0.000044	0.795619	0.000006	7.304526
F57	0.035574	0.000044	0.888834	0.000011	3.755091
F58	0.893106	0.000039	0.673879	0.000006	6.583598
F59	0.071598	0.000043	0.565349	0.000010	3.878613
F60	1.217177	0.000035	0.448149	0.000006	6.225868
F61	1.113841	0.000039	0.919774	0.000006	6.361630
F62	0.084857	0.000036	0.273882	0.000010	3.841943
F63	0.862411	0.000036	0.413632	0.000006	6.209853
F64	0.308531	0.000042	0.978470	0.000007	5.737678
F65	0.039757	0.000037	0.482542	0.000010	3.592632
F66	0.086183	0.000044	0.204570	0.000010	3.904434
F67	0.028510	0.000036	0.522162	0.000010	3.593336
F68	0.037625	0.000033	0.879902	0.000010	3.707129
F69	0.066868	0.000036	0.694784	0.000010	3.749136
F70	0.833279	0.000034	0.689229	0.000006	6.115674
F71	1.935889	0.000034	0.797306	0.000003	10.342439
F72	0.046928	0.000033	0.926278	0.000010	3.641927
F73	0.752865	0.000032	0.937067	0.000006	5.713433
F74	0.282383	0.000036	0.613151	0.000007	4.667376
F75	0.072970	0.000028	0.029980	0.000009	3.490809
F76	0.810075	0.000034	0.929619	0.000006	5.908784
F77	1.040132	0.000031	0.368693	0.000006	5.415959
F78	1.583709	0.000039	0.872553	0.000004	9.394488
F79	0.118384	0.000038	0.211363	0.000009	3.530131
F80	0.122063	0.000033	0.274277	0.000009	3.576727
F81	0.044769	0.000031	0.735394	0.000010	3.384484
F82	0.805382	0.000030	0.060741	0.000006	5.294651
F83	0.780749	0.000031	0.365751	0.000006	5.371773
F84	1.020802	0.000027	0.375184	0.000006	5.185010
F85	0.846646	0.000030	0.693919	0.000006	5.545416
F86	0.043761	0.000034	0.107477	0.000009	3.412263
F87	0.034585	0.000039	0.200139	0.000010	3.459900
F88	0.245707	0.000031	0.792545	0.000007	4.078792
F89	0.067848	0.000035	0.019685	0.000009	3.554611
F90	0.359000	0.000035	0.418093	0.000006	6.172003
F91	0.088419	0.000031	0.117918	0.000009	3.347851
F92	0.049519	0.000031	0.486309	0.000009	3.294346
F93	0.063776	0.000033	0.104108	0.000009	3.338091
F94	2.562753	0.000026	0.981644	0.000003	8.832871
F95	1.050964	0.000028	0.679146	0.000006	5.069696
F96	0.120176	0.000027	0.035077	0.000008	3.521058
F97	1.832863	0.000027	0.560490	0.000003	8.258790
F98	0.054958	0.000026	0.032402	0.000009	3.240881
F99	0.818258	0.000029	0.418968	0.000005	5.095555
F100	0.032542	0.000031	0.505786	0.000009	3.299345
F101	0.061774	0.000029	0.393201	0.000009	3.545683
F102	2.304441	0.000028	0.820278	0.000003	9.129813
F103	1.916937	0.000027	0.628618	0.000003	8.333952
F104	1.017917	0.000028	0.195242	0.000006	4.844850

TABLE 8. CONTINUED

Frequency	Frequency	Amplitude	Phase	Noise	SNR
F105	0.122733	0.000029	0.432214	0.000008	3.368645
F106	0.950408	0.000028	0.602112	0.000005	5.224705
F107	0.821818	0.000027	0.269326	0.000005	4.904104
F108	0.841843	0.000026	0.694110	0.000005	4.802736
F109	0.829256	0.000026	0.364050	0.000005	4.815170
F110	1.924095	0.000026	0.710283	0.000003	8.248569
F111	1.803526	0.000026	0.101545	0.000003	7.742789
F112	0.110544	0.000026	0.860448	0.000008	3.174831
F113	0.121371	0.000028	0.336842	0.000008	3.299731
F114	0.667256	0.000026	0.971549	0.000005	5.183159
F115	1.085479	0.000025	0.856127	0.000005	4.717625
F116	0.078042	0.000026	0.774947	0.000008	3.147375
F117	0.139951	0.000025	0.056737	0.000008	3.302504
F118	0.879551	0.000025	0.330724	0.000005	4.705819
F119	0.325674	0.000030	0.500824	0.000006	4.975161
F120	0.289150	0.000028	0.489091	0.000006	4.504696
F121	0.097427	0.000026	0.330393	0.000008	3.024391
F122	0.183915	0.000024	0.516818	0.000007	3.389604
F123	0.679402	0.000023	0.754883	0.000005	4.665421
F124	0.785210	0.000024	0.650818	0.000005	4.493476
F125	0.349622	0.000024	0.885464	0.000005	4.458943
F126	0.976807	0.000023	0.012797	0.000005	4.546269
F127	0.826710	0.000023	0.947968	0.000005	4.591718
F128	0.135705	0.000023	0.926925	0.000007	3.195712
F129	0.073810	0.000025	0.799563	0.000008	3.098061
F130	0.096326	0.000025	0.795353	0.000008	3.195557
F131	0.065866	0.000026	0.081159	0.000008	3.400311
F132	2.568079	0.000022	0.918795	0.000003	7.820700
F133	0.124682	0.000023	0.168908	0.000007	3.082160
F134	0.850509	0.000022	0.945916	0.000005	4.448453
F135	1.598305	0.000027	0.093608	0.000004	7.420767
F136	1.288222	0.000022	0.231931	0.000004	4.861027
F137	0.027343	0.000023	0.735913	0.000008	2.869449

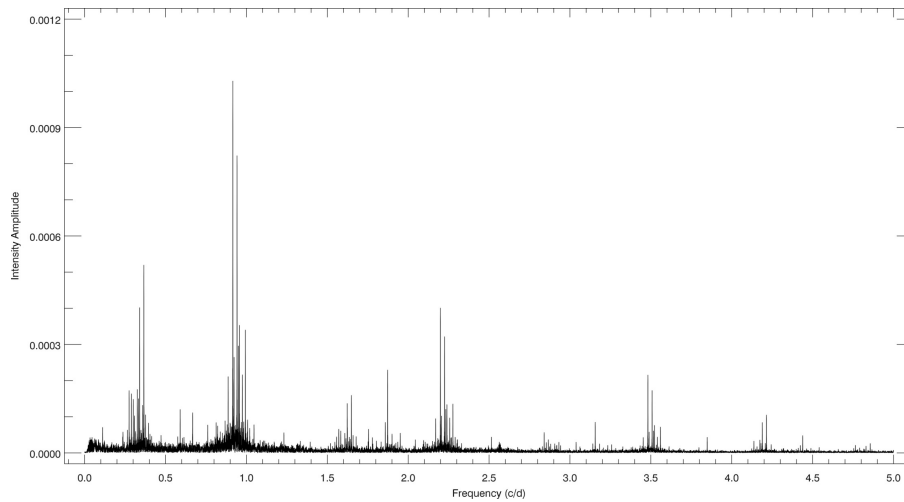


Fig. 8. KIC 8043961's Fourier amplitude spectrum derived from the DFT.

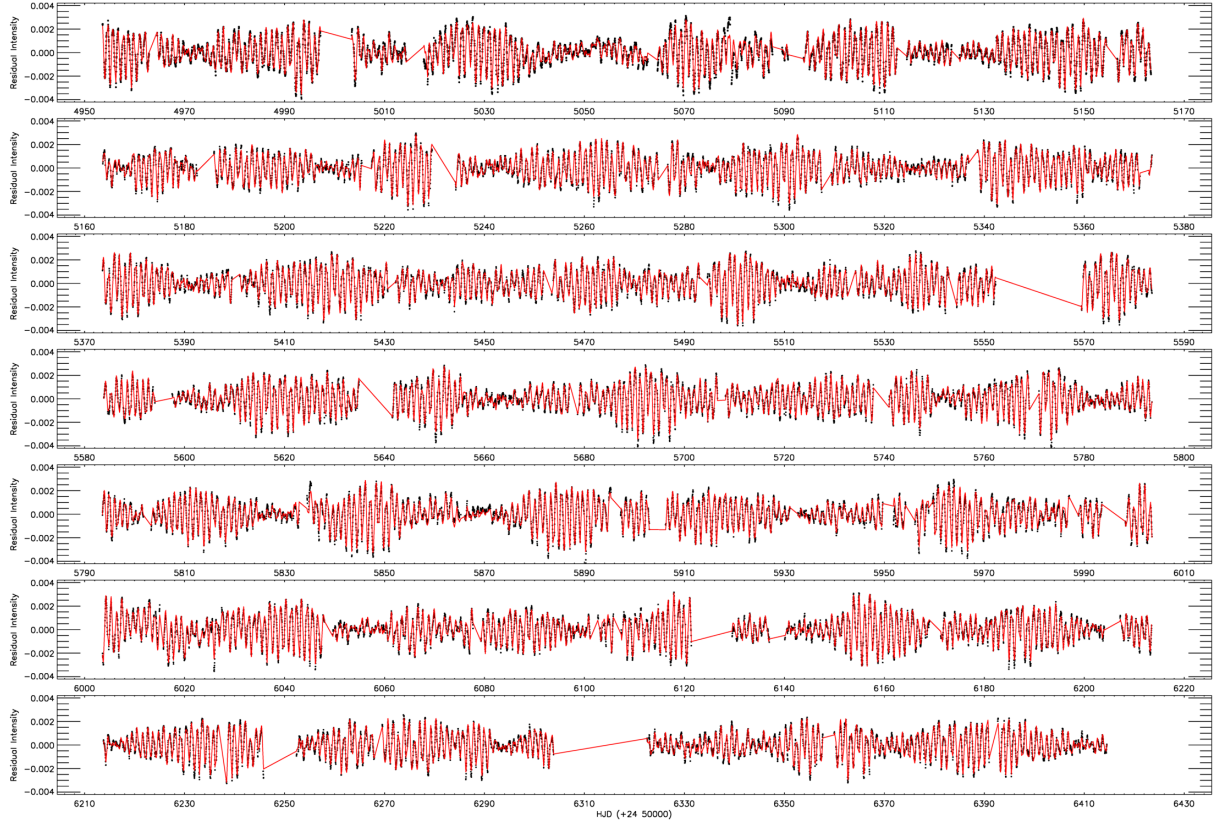


Fig. 9. The variation at out-of-eclipses and the synthetic model derived by the frequencies obtained from the DFT. The filled circles represent the observations, while the red line represents the model. The color figure can be viewed online.

metal-poor and detached eclipsing binary with a tertiary component. The eclipsing binary is composed of F3V and F5 III-IV stars, where the primary component is less massive and hotter than the evolved F5 III-IV secondary component. The average age of the system is found as 2.2 Gyr, based on PARSEC stellar evolutionary tracks and isochrones. Binary star evolution models must be considered for a more accurate age determination. The positions of the components on the  $\log(T_{eff})$ - $\log(L/L_{\odot})$  plane suggest that the primary is a  $\gamma$  Doradus type pulsator candidate. Inspecting the Fourier amplitude spectrum of the observed light variation at out-of-eclipses, we find 137 frequencies above the  $3\sigma$  level. Most of the frequencies also confirm that one of the components is a  $\gamma$  Doradus type star.

Although Borkovits et al. (2016) computed the orbit of the tertiary component via eclipse time variation analysis, we re-compute eclipse times during the light curve modelling, and model the orbit of the third body via these eclipse times. We find very similar orbital parameters, except for the longitude of the periastron, which differs by 180 degrees from

the value found by Borkovits et al. (2016). The difference is likely due to the different reference plane of the orbit; we adopt the definitions of Irwin (1959) but Borkovits et al. (2016) shift the reference plane of the orbit to the focal point of the ellipse.

Using the computed total mass of the eclipsing binary and assuming that the inclination of the third body orbit is the same as the inclination of the eclipsing binary, we find the mass of the third body to be about  $0.778 M_{\odot}$ . However, we estimated the mass of the third body as listed in Table 5 for different inclination values. The mass of the third body was found to range from  $4.909 M_{\odot}$  for  $i = 15$  deg to  $0.767 M_{\odot}$  for  $i = 90$  deg. Considering the estimated masses of the primary and secondary components listed in Table 7 and also the value of  $L_3/L_T$  in Table 5, the acceptable mass should range from  $0.799 M_{\odot}$  for  $i = 75$  deg to  $0.767 M_{\odot}$  for  $i = 90$  deg. Assuming that the tertiary component is a main sequence star, this mass corresponds to the effective temperature of 4990 K (Tokunaga 2000).

We thank the referee for useful comments that have contributed to the improvement of the paper. We also wish to thank the Turkish Scientific and Technical Research Council (TÜBİTAK) for supporting this work through Grant No. 116F349 and for partial support in using the RTT-150 (Russian-Turkish 1.5-m telescope in Antalya) with Project Number 14BR1150-667.

## REFERENCES

- Aerts, C., Christensen-Dalsgaard, J., & Kurtz, D. W. 2010, *Asteroseismology*, ed. W. B. Burton and V. Trimble (New York, NY: Springer), 49
- Ammons, S. M., Robinson, S. E., Strader, J., et al. 2006, *ApJ*, 638, 1004
- Balona, L. A. 2014, *MNRAS*, 437, 1476
- \_\_\_\_\_. 2015, *MNRAS*, 447, 2714
- Blanco-Cuaresma, S., Soubiran, C., Heiter, U., & Jofré, P. 2014, *A&A*, 569A, 111
- Borkovits, T., Hajdu, T., Sztakovics, J., et al. 2016, *MNRAS*, 455, 4136
- Borucki, W. J., Koch, D., Basri, G., et al. 2010, *Sci*, 327, 977
- Bressan, A., Marigo, P., Girardi, L., et al. 2012, *MNRAS*, 427, 127
- Caldwell, D. A., Kolodziejczak, J. J., & Van Cleve, J. E. 2010, *ApJL*, 713, 92
- Castelli, F. & Kurucz, R. L. 2004, *New Grids of ATLAS9 Model Atmospheres*, (eprint arXiv:astro-ph/0405087), Available as Poster A20 on the CD-ROM which is part of the Proceedings of the IAU Symp. No 210; IAU Symp. No 210, IAUS 210, *Modelling of Stellar Atmospheres*, eds. N. Piskunov et al. 2003, poster A20
- Conroy, K. E., Prša, A., Stassun, K. G., et al. 2014, *AJ*, 147, 45
- Cunha, M. S., Aerts, C., Christensen-Dalsgaard, J., et al. 2007, *A&ARev.*, 14, 217
- Foreman-Mackey, D., Hogg, D. W., Lang, D., & Goodman, J. 2013, *PASP*, 125, 306
- Frasca, A., Molenda-Żakowicz, J., De Cat, P., et al. 2016, *A&A*, 594, 39
- Girardi, L., Bressan, A., Bertelli, G., & Chiosi, C. 2000, *A&AS*, 141, 371
- Gray, D. F. 2005, *The Observation and Analysis of Stellar Photospheres*, 3rd ed., (Cambridge, MA: CUP)
- Gray, R. O. & Corbally, C. J. 1994, *AJ*, 107, 742
- Grigahcène, A., Antoci, V., Balona, L., et al. 2010, *ApJ*, 713, 192
- Henry, G. W., Fekel, F. C., & Henry, S. M. 2005, *AJ*, 129, 2815
- Huber, D., Silva Aguirre, V., Matthews, J. M., et al. 2014, *ApJS*, 211, 2
- Irwin, J. B. 1959, *AJ*, 64, 149
- Jenkins, J. M., Caldwell, D. A., Chandrasekaran, H., et al. 2010a, *ApJ*, 713, 87
- Jenkins, J. M., Chandrasekaran, H., McCauliff, S. D., et al. 2010b, *SPIE*, 7740, 77400
- Kamil, C. & Dal, H. A. 2017, *PASA*, 34, 29
- Kirk, B., Conroy, K., Prša, A., et al. 2016, *AJ*, 151, 68
- Koch, D. G., Borucki, W. J., Basri, G., et al. 2010, *ApJ*, 713, 79
- Lenz, P. & Breger, M. 2005, *CoAst*, 146, 53
- Levenberg, K. 1944, *QApMa*, 164
- Lucy, L. B. 1967, *ZA*, 65, 89
- Mathur, S., Huber, D., Batalha, N. M., et al. 2017, *ApJS*, 229, 30
- Matijević, G., Prša, A., Orosz, J. A., et al. 2012, *AJ*, 143, 123
- Özdarcan, O. & Dal, H. A. 2017, *PASA*, 34, 17
- Pickles, A. & Depagne, É. 2010, *PASP*, 122, 1437
- Pinsonneault, M. H., An, D., Molenda-Żakowicz, J., et al. 2012, *ApJS*, 199, 30
- Prša, A., Batalha, N., Slawson, R. W., et al. 2011, *AJ*, 141, 83
- Rolland, A., Costa, V., Rodríguez, E., et al. 2002, *CoAst*, 142, 57
- Ruciński, S. M. 1969, *A&A*, 19, 245
- Ryabchikova, T., Piskunov, N., Kurucz, R. L., et al. 2015, *PhysS*, 90, 4005
- Scargle, J. D. 1982, *ApJ*, 263, 835
- Slawson, R., Prša, A., Welsh, W. F., et al. 2011, *AJ*, 142, 160
- Soydugan, E., Soydugan, F., Demircan, O., & İbanoğlu, C. 2006, *MNRAS*, 370, 2013
- Tkachenko, A., Aerts, C., Yakushechkin, A., et al. 2013, *A&A*, 556, 52
- Tokunaga, A. T. 2000, in *Allen's Astrophysical Quantities*, ed. A. N. Cox (4th ed.; New York, NY: Springer) 143
- Tonry, J. & Davis, M. 1979, *AJ*, 84, 1511
- Uytterhoeven, K., Moya, A., Grigahcène, A., et al. 2011, *A&A*, 534, A125
- Van Hamme, W. 1993, *AJ*, 106, 2096
- Warner, P. B., Kaye, A. B., & Guzik, J. A. 2003, *ApJ*, 593, 1049
- Watson, C. L., Henden, A. A., & Price, A. 2006, *SASS*, 25, 47
- Wilson, R. E. & Devinney, E. J. 1971, *ApJ*, 166, 605
- Wilson, R. E. & Van Hamme, W. 2014, *ApJ*, 780, 151

H. A. Dal, C. Kamil, O. Özdarcan, and E. Yoldaş: Department of Astronomy and Space Sciences, University of Ege, Bornova, 35100 İzmir, Turkey (ali.dal@ege.edu.tr).

## A SEARCH FOR PULSATION IN TWENTY-ONE WHITE DWARFS

E. Paunzen<sup>1</sup>, G. Handler<sup>2</sup>, J. Janík<sup>1</sup>, Z. Zemanová<sup>3</sup>, M. Rode-Paunzen<sup>4</sup>, M. S. O’Brien<sup>5</sup>, T. K. Watson<sup>6</sup>, and M. Drózd<sup>7</sup>

*Received February 5 2020; accepted April 24 2020*

### ABSTRACT

Well-defined astrophysical constraints of white dwarfs (WDs), such as on the presence or absence of pulsational variability, are very much needed to refine and develop current models. Because these stars are rather faint and variability periods are mostly below one hour, only a very limited amount of space-based data is currently available for these objects. We present about 68 hours of high-quality ground-based photometric time-series data for twenty-one WDs acquired at five different observatories. No new pulsators were detected but the derived upper limits of variability, which are typically on the order of only a few mmags, provide important input for pulsation models.

### RESUMEN

Es muy necesario contar con cotas astrofísicas bien definidas para los parámetros de las enanas blancas (WD) con el objeto de mejorar los modelos actuales. Dado que estas estrellas son débiles y tienen períodos de variabilidad de menos de una hora, actualmente sólo contamos con datos muy limitados basados en observaciones espaciales. Presentamos 68 horas de datos fotométricos de alta calidad obtenidos en cinco observatorios terrestres para 21 enanas blancas. No se encontraron pulsadores nuevos, pero los límites superiores para la variabilidad que determinamos, del orden de unas cuantas mmags, son importantes para la construcción de modelos de pulsación.

*Key Words:* stars: variables: general — white dwarfs

### 1. INTRODUCTION

White dwarfs (WDs) are the last stage of evolution for most stars. Probing their internal structures provides us with important insights on the complex evolutionary paths that led up to this stage. Furthermore, evolution is still ongoing in the WD stage, where it is primarily dominated by cooling (e.g. Salaris et al. 2013). WD interiors are characterized by stratified layers of different masses which mix and settle at certain temperatures. Therefore, as a WD cools down, its surface composition changes (e.g. Tremblay et al. 2013). Consequently, in the different phases (or temperature ranges) of WD evolution, one encounters WDs with H-dominated atmospheres (DAs) and non-DAs (He-atmosphere DOs and DBs).

On its evolutionary path, a WD crosses several instability strips, which are determined by atmospheric composition and total mass. The resulting pulsational vari-

ability opens up possibilities to probe the internal structure; for instance, Romero et al. (2014) demonstrated that nonradial gravity mode (g-mode) pulsations allow the study of the stellar interior via the technique of asteroseismology.

Asteroseismology of WDs gained momentum with the work of Winget et al. (1994), who derived precise stellar parameters for the DBV GD 358 from more than 180 significant peaks in its frequency spectrum. The corresponding group of variable stars was later designated V777 Her objects, which pulsate in g-modes with periods between 100 and 1200 s (Beauchamp et al. 1999). Their cooler cousins, the ZZ Ceti stars, consist of pulsating H-rich DAV WDs and exhibit variability with periods between 70 and 2000 s (Romero et al. 2019). During the last two decades, ground-based and satellite observations of WDs have significantly widened our knowledge in this field of study (Kepler et al. 2005; Hermes et al. 2014) by discovering and analysing many pulsating WDs.

However, several important questions about the pulsational behaviour of WDs remain: What exactly defines the borders of the instability strip? Do all WDs situated inside the instability strip pulsate? If not, what are the important astrophysical parameters?

<sup>1</sup>Department of Theoretical Physics and Astrophysics, Masaryk University, Czech Republic.

<sup>2</sup>Nicolaus Copernicus Astronomical Center, Poland.

<sup>3</sup>High school, Uherské Hradiště, Czech Republic.

<sup>4</sup>Nicolaus Copernicus Astronomical Center, Poland.

<sup>5</sup>Space Telescope Science Institute, Baltimore, USA.

<sup>6</sup>Information Technology, Southwestern University, USA.

<sup>7</sup>Mt. Suhora Observatory, Poland.

TABLE 1  
TARGET STARS AND THEIR ASTROPHYSICAL  
PARAMETERS FROM THE LITERATURE

WD	$T_{\text{eff}}$ [K]	$\log g$ [dex]	$\log \text{H/He}$	$\log \tau$	Ref
0002+729	14 410	8.27	-5.95	8.52	4
0017+136	18 130	8.08	-4.63	8.07	4
0038+555	8 860	8.00		8.96	2
0231+570	13 790	8.03		8.43	2
0449+252	11 520	8.00		8.62	2
0454+620	10 960	8.88		9.30	2
0713+399	65 000	7.50			5
0835+340	22 230	8.25	< -4.63	7.90	4
0921+091	19 470	8.01	-4.72	7.90	4
0949+094	18 694	8.09	-4.52		3
1052+273	23 930	8.41		7.96	2
1107+265	15 130	8.11	-5.77	8.35	4
1149-133	20 370	8.30	-3.77	8.08	4
1326-037	19 950	8.03	< -4.81	7.87	4
1540+680	22 240	7.96	< -4.43	7.58	4
1612-111	23 430	7.96	< -4.75	7.46	4
1727+560	12 500	8.00	-3.70		1
2147+280	12 940	8.86	-5.74	9.08	4
2234+064	23 770	8.07	< -4.72	7.56	4
2246+120	26 840	7.92	< -4.30	7.13	4
2250+746	16 560	8.15	< -6.18	8.26	4

1. Wegner & Koester (1985), 2. Limoges et al. (2015), 3. Koester & Kepler (2015), 4. Rolland et al. (2018), 5. Werner et al. (2018)

In this paper, we present high-quality ground-based time-series of twenty-one WDs, including one hot He-rich DO, with  $V$  magnitudes between 13.7 and 16.7 mag. These objects are too faint for most current automatic ground-based surveys and at the limit of observability even for satellite-based missions such as *Kepler* (Doyle et al. 2017). Among the first published results from the TESS mission was an investigation of the known pulsating DBV WD 0158-160 (Bell et al. 2019). With a main period of about 640 s and an amplitude of about 22 mmag, this object is quite typical among pulsating WDs. Generally, TESS data are of limited use in this field of study because of the employed observing cadences (2 and 30 min), the faintness of most WDs, and the expected amplitudes.

## 2. TARGET SELECTION, OBSERVATIONS AND REDUCTION

We selected interesting WDs situated within or close to the heuristically established instability strip (Althaus

et al. 2010). Several He-rich and He-weak objects were included to cover different atmospheric characteristics. In addition, our sample covers a wide range of ages. The astrophysical parameters of our target stars from the literature are listed in Table 1.

Photometric observations were performed at the following four sites using the described telescopes and instruments:

- Hvar Observatory, University of Zagreb, 1.0m, Austrian-Croatian Telescope (ACT), Apogee Alta U47 CCD camera, integration time 15 s for all targets, no filter,
- Institute of Astronomy of the University of Vienna, 0.8m, “vienna little telescope” (vlt), SBIG STL-6303E CCD camera, integration time 20 to 30 s, no filter,
- McDonald Observatory (McD), 2.1m, Argos, integration time 10 to 25 s for all targets, BG40 filter,
- Mt. Suhora Observatory (MSO), Poland, 0.6m, Zeiss telescope, Apogee Alta U47 CCD, integration time 30 s for all targets, no filter,
- South African Astronomical Observatory (SAAO), 0.75m, high-speed CCD photometer, integration time 5 to 10 s, no filter.

Data reduction and differential photometry were performed using three different program packages:

- Image Reduction and Analysis Facility (IRAF, Stetson 1987),
- Munipack (Chrastina & Hroch 2008),
- Multiple object and multiple frame CCD photometry (MOMF, Kjeldsen & Frandsen 1992).

For IRAF and Munipack, classical aperture photometry was applied; the MOMF package combines this with point spread function photometry. None of our target fields were very crowded, but the resulting noise level from each program package was tested. Time-series analysis of the differential light curves was conducted applying a standard Fourier technique and the Phase-Dispersion Method. All computations were done within the programme package Peranso (Paunzen & Vanmunster 2016). To account for different seeing conditions, several apertures were used and tested. For each data set, we chose the aperture which yielded the smallest scatter in the differential light curves. For all objects, several comparison stars were available, which were checked individually to exclude variable objects.

TABLE 2  
OBSERVATION LOG AND RESULTS FROM THE TIME-SERIES ANALYSIS

WD	Other	$V$ [mag]	HJD(start) [2450000+]	$\Delta t$ [min]	$N$	Site	UL [mmag]	Freq [mHz]	Amp [mmag]
0002+729	GD 408	14.3	8806.221126	296.6	517	MSO	1.2		
0017+136	Feige 4	15.4	5418.541842	71.0	246	ACT	4.3		
0038+555	EGGR 245	14.1	8807.286154	108.8	206	MSO	3.0		
0231+570	GD 283	13.7	8823.262619	305.6	557	MSO	0.8		
0449+252	PM J04523+2519	14.9	8806.437791	189.3	335	MSO	1.7		
			8824.394303	176.1	312	MSO	1.8		
0454+620	PM J04586+6209	14.5	8823.500997	304.6	551	MSO	1.0		
0713+399	HS 0713+3958	16.2	2262.816274	27.0	99	McD	3.4		
			2263.795979	99.5	198	McD	1.9		
			2266.794590	99.5	198	McD	2.4		
			2267.801534	89.5	180	McD	2.3		
			2268.811951	69.5	140	McD	2.1		
0835+340	CSO 197	16.0	4560.591748	57.0	323	McD	3.6		
0921+091	PG 0921+092	16.2	4555.278322	107.7	228	vlt	6.6		
			4557.278634	89.7	190	vlt	7.2		
			4563.582199	55.5	310	McD	1.7		
0949+094	PG 0949+094	16.0	4205.309769	163.3	300	vlt	3.6		
			4206.336458	124.8	224	vlt	4.4		
			4562.600301	56.2	286	McD	1.8		
1052+273	GD 125	14.2	8824.524161	251.9	425	MSO	1.4		
1107+265	GD 128	15.9	4202.345671	108.2	194	vlt	3.7		
			4203.310475	161.0	307	vlt	3.4		
1149–133	HE 1149–1320	16.1	3792.577824	97.2	356	SAAO	4.6		
1326–037	PG 1326–037	15.7	3794.604931	63.4	529	SAAO	5.7		
			3795.595417	74.7	428	SAAO	1.3		
1540+680	PG 1540+681	16.2	5419.310115	94.4	249	ACT	3.5		
1612–111	GD 198	15.5	3790.591169	75.2	423	SAAO	2.8		
1727+560	G 227–5	16.1	5417.399217	84.5	269	ACT	1.9		
2147+280	EGGR 583	14.7	8824.189224	209.3	369	MSO	3.1		
2234+064	PG 2234+064	16.0	5418.463723	104.7	369	ACT	2.9		
2246+120	V393 Peg	16.7	5417.477938	198.6	699	ACT		3.05	15.8
2250+746	GD 554	16.7	5421.460083	88.0	318	ACT	2.6		

First, the upper limits of variability of the WDs were compared, which yielded the same overall noise level of  $\pm 0.2$  mmag for all three methods. No trend of the noise level with frequency was detected. Furthermore, we checked the multiperiodic solution for WD 2246+120. Here, usage of the MOMF package resulted in a slightly better detection probability than provided by the other two packages.

The observation log and results from the time-series analysis are shown in Table 2. In total, we analysed 10 335 frames spanning 4 103 minutes of observations. All images and data are available on request from the first author.

### 3. RESULTS

No new pulsating WDs were identified among our sample of twenty-one WDs; however, we have derived upper limits of variability that are also important input parameters for the test and development of pulsation models.

The results of the time-series analysis are shown in Figures 1 and 2. Defining the upper limit of variability is not straightforward and has often been discussed in the literature (Reegen et al. 2008). In general, the statistical significance of the noise in the Fourier spectrum is underestimated. We here employ a conservative approach and define the upper limit of variability as the upper envelope of the peaks in an amplitude spectrum (Figures 1

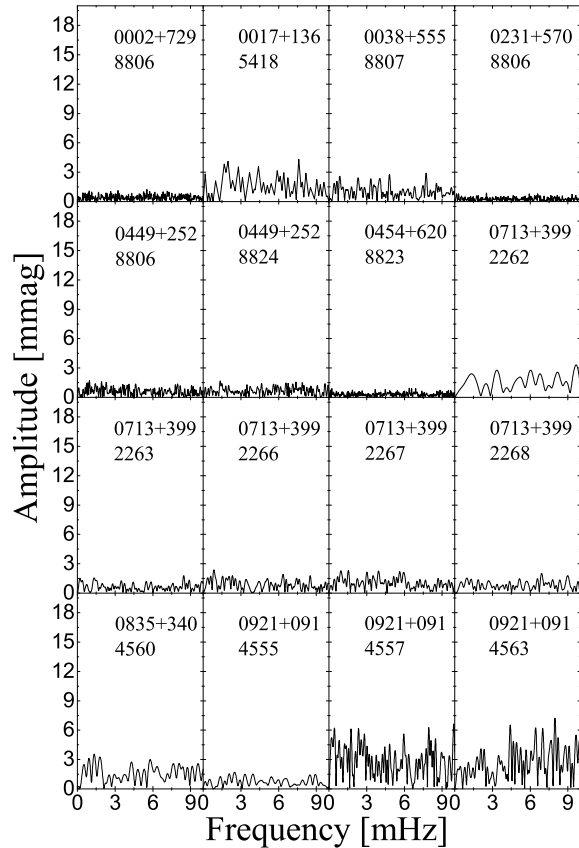


Fig. 1. Fourier spectra of our target stars. Each panel lists the WD number and the JD 2450000+ of the observing night.

and 2). None of the detected amplitudes exceed a significance of  $1.3\sigma$  of the noise level in the corresponding spectrum. Typically, we achieved an upper limit for these targets of a few mmag. In the following, information on the individual stars is provided.

*WD 0002+729*: This is a carbon-poor and metal-rich WD that does not show any signs of a surrounding dust disk (Farihi et al. 2009). The origin of its peculiar abundance pattern is still not well understood.

*WD 0017+136*: Limoges et al. (2015) published a parallax-based distance of 33.3 pc from the Sun for this  $0.65 M_{\odot}$  object. They concluded that it is one of the seven DBs known to be closer than 40 pc. However, the spectroscopy-based distance of 75 pc (Bergeron et al. 2011) does not agree with that, which could be caused by (hitherto undetected) binarity. Bailer-Jones et al. (2018) published a distance of 78.9 pc on the basis of Gaia DR2 (Lindgren et al. 2018). In the latter work, WD 0017+136 is not flagged as a binary. Gaia DR3, which is scheduled for 2021, is going to include a list of binaries, which might finally solve this issue.

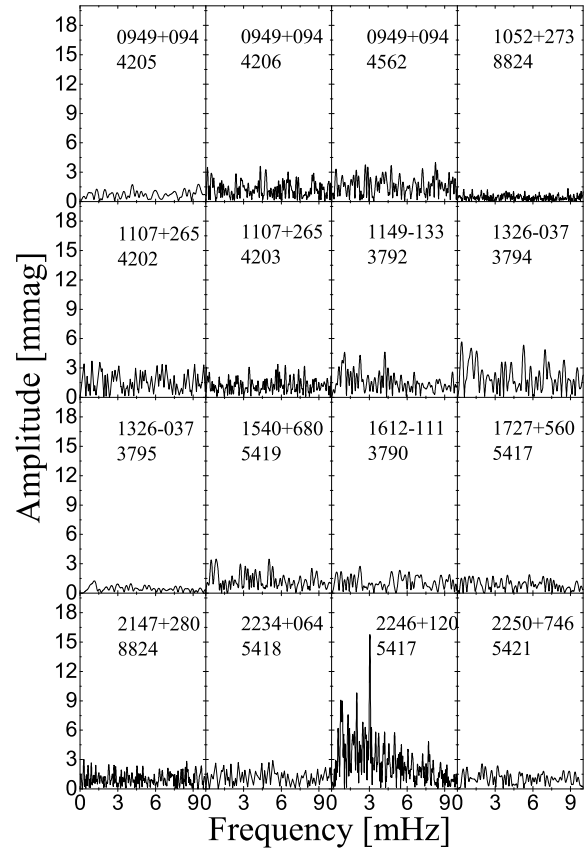


Fig. 2. Fourier spectra of our target stars. Each panel lists the WD number and the JD 2450000+ of the observing night. WD 2246+120 is a known pulsator immediately noticeable from its rich frequency spectrum.

*WD 0038+555*: Marinoni et al. (2016) included this object in their photometric short-term variability monitoring survey, which formed a part of the Gaia spectrophotometric standard star calibration. They derived an upper limit of variability of 2 mmag in Johnson *B* and, within their criteria, accepted WD 0038+555 as a constant star. Our results are in line with this study.

*WD 0231+570*: This is one of the *UBVRI* photoelectric standard stars of Landolt (2013), which were observed within a period of 17 years at the Kitt Peak National and Lowell Observatories. Since no individual errors are given by the authors, an independent check of variability on short timescales is important. We here derive an upper limit of 0.8 mmag for this star.

*WD 0449+252* and *WD 0454+620*: Both stars are included in the paper of Bognár et al. (2018), who searched for new WD pulsators for observations by the TESS space telescope. The authors reported no signs of short-term variability.

*WD 0713+399*: This DO star is remarkable in several respects. Werner et al. (1995) detected unusually strong He II absorption lines that could not be reproduced by a simple DO model atmosphere. They speculated that the star may belong to a new subgroup of hot He-rich WDs. Later, Dreizler & Werner (1996) investigated an up-to-date list of these WDs and concluded that they represent the non-DA cooling sequence from the hot end down to the DB gap. The observed mean mass value of about  $0.6 M_{\odot}$  coincides very well with those of DA and DB WDs.

*WD 0835+340*: Wagner et al. (1986) were the first to classify this star as a DB3, which was later confirmed by several other studies. Furthermore, Girven et al. (2011) did not find any IR-excess for this object, which implies that no low-mass stellar companion or dusty debris disc is present around it.

*WD 0921+091*: This star has a very low total hydrogen mass ( $M_{\text{H}} = 6.753 \times 10^{-14} M_{\odot}$ ) as compared to similar WDs (Voss et al. 2007), which renders it an interesting object for defining constraints on pulsation models. Robinson & Winget (1983) observed WD 0921+091 photometrically using a high-speed two-star photometer. They presented upper limits of variability (semi-amplitude) between 5.6 and 8.0 mmag. Comparing their results to ours, it is interesting to note that the CCD technology delivers results of the same quality as the best classical photoelectric instruments with much smaller telescopes.

*WD 0949+094*: Castanheira et al. (2006) presented 1.25 h (193 data points) of photometric observations of this star. However, they did not discover any significant signals in the observed Fourier spectrum (noise of about 6 mmag). Our limits of variability range between 1.6 and 4.4 mmag (Table 2).

*WD 1052+273*: Several studies unsuccessfully searched for a dust disk and an IR-excess around this rather bright WD (Wilson et al. 2019).

*WD 1107+265*: Several studies of this object are available in the literature (Bergeron et al. 2011). The log H/He value is very low (Table 1). Robinson & Winget (1983) derived upper limits of variability (semi-amplitude) between 4.2 and 5.7 mmag. Our results are compatible with these values.

*WD 1149–133*: Detailed analyses from the UV to the IR region are available in the literature for this He-rich WD (Liebert et al. 1986). The results from our single observing run indicate a rather high upper limit of variability (4.6 mmag). The star should be re-observed.

*WD 1326–037*: This WD is included as constant object in the database of synthetic photometry in the GALEX ultraviolet bands for the stellar sources

observed with the International Ultraviolet Explorer (Beitia-Antero & Gómez de Castro 2016).

*WD 1540+680*: According to Beauchamp et al. (1999), this object is situated just on the red edge of the instability strip.

*WD 1612–111*: The search for a low-luminosity companion to this object yielded a null-result (Farihi et al. 2005).

*WD 1727+560*: The spectrum of this massive DQ WD contains strong emission features of O I and C II (Provencal et al. 2005). Unexpectedly, as compared with carbon, oxygen is overabundant by a factor of about 160 in the chromosphere. In summary, WD 1727+560 is an outstanding object for which we have not detected any signs of variability.

*WD 2147+280*: With an age of more than 1 Gyr, this star is one of the oldest objects in our sample.

*WD 2234+064*: This is one of the rare WDs that show a weak Ca II K-line of interstellar origin (Zuckerman et al. 2010).

*WD 2246+120*: In order to check the reliability of our observational strategy and reduction techniques, we observed this known variable star, which is a pulsating He-atmosphere DB (Handler 2001). It shows variability with periods between 255 and 300 s. The periods and amplitudes derived in the present study are in excellent agreement with the literature values, which lends confidence to our analysis.

*WD 2250+746*: Robinson & Winget (1983) derived upper limits of variability (semi-amplitude) between 3.0 and 7.1 mmag, which is comparable to our results.

We have compared our derived upper limits of variability (column “UL” in Table 2) with the extensive surveys aimed at the detection of pulsating WDs by Mukadam et al. (2004), Mullally et al. (2005) and Castanheira et al. (2010). These authors also used CCD observations with comparable time bases and integration times. The observations by Mukadam et al. (2004) and Mullally et al. (2005) were done with the same equipment we employed at the McDonald Observatory, whereas Castanheira et al. (2010) used the 4.1m SOAR telescope. The limit for non-variability (NOV) was established using a classical Fourier transformation technique defining the highest white-noise peak as the detection threshold. The latter is given in the unit of millimodulation amplitude (mma), which corresponds to a 0.1% change in intensity. Typically, NOV limits between 2 and 8 mma were reached. This is well within the range of our results. Castanheira et al. (2010) re-observed stars with high NOV limits and detected new variables with amplitudes below the NOV limits among them. Therefore, we caution that there might well be some undetected low-amplitude variables among the WDs of our sample.

## 4. CONCLUSIONS

The two primary temperature regimes in which isolated cooling WDs are observed to pulsate are  $T_{\text{eff}} \approx 12\,000\text{ K}$  for the DAVs, and  $T_{\text{eff}} \approx 25\,000\text{ K}$  for the DBVs. Pulsations are driven in a subsurface partial ionization zone of the dominant surface chemical element, have periods between 70 and 2000 s, and are composed of nonradial gravity modes.

Among the hotter WDs, we find the GW Vir objects with  $T_{\text{eff}}$  between 75 000 K and 200 000 K and periods between 300 and 5 000 s. Here, the pulsations are driven by ionized carbon and oxygen.

Pulsating WDs provide an important glimpse into the future of the vast majority of stars and their interiors. With asteroseismic tools, it is possible to trace the stellar structure down to the core.

For modeling efforts, it is not only important to analyse the pulsational characteristics of variable WDs but also apparently non-variable objects in the same region of the Hertzsprung-Russell diagram. The search for (dis)similarities between pulsators and non-pulsators can significantly improve the framework of astrophysical parameters in which pulsation occurs.

In this work, we presented high-quality photometric time-series observations of twenty-one WDs from five different sites. To cover interesting regions of the instability strip, our sample encompassed He-rich and He-weak objects. Although we have not detected any new pulsating WD, the derived upper limits of variability are important input parameters for pulsation models.

The authors are grateful to Elisabeth Guggenberger, Patrick Lenz, Stefan Meingast and Monika Lendl for taking part in the observations and to Stefan Hümmerich for helping with the language editing. GH acknowledges support by the Polish NCN grant UMO-2015/18/A/ST9/00578.

## REFERENCES

- Althaus, L. G., Córscico, A. H., Isern, J., & García-Berro, E. 2010, *A&ARv*, 18, 471
- Bailer-Jones, C. A. L., Rybizki, J., Foesneau, M., Mantelet, G., & Andrae, R. 2018, *AJ*, 156, 58
- Beauchamp, A., Wesemael, F., Bergeron, P., et al. 1999, *ApJ*, 516, 887
- Beitia-Antero, L. & Gómez de Castro, A. I. 2016, *A&A*, 596, A49
- Bell, K. J., Córscico, A. H., Bischoff-Kim, A., et al. 2019, *A&A*, 632, 42
- Bergeron, P., Wesemael, F., Dufour, P., et al. 2011, *ApJ*, 737, 28
- Bognár, Z., Kalup, C., Sódor, Á., Charpinet, S., & Hermes, J. J. 2018, *MNRAS*, 478, 2676
- Castanheira, B. G., Kepler, S. O., Handler, G., & Koester, D. 2006, *A&A*, 450, 331
- Castanheira, B. G., Kepler, S. O., Kleinman, S. J., Nitta, A., & Fraga, L. 2010, *MNRAS*, 405, 2561
- Chrastina, M. & Hroch, F. 2008, *OEJV*, 95, 21
- Doyle, T. F., Howell, S. B., Petit, V., & Lépine, S. 2017, *MNRAS*, 464, 3464
- Dreizler, S. & Werner, K. 1996, *A&A*, 314, 217
- Farihi, J., Becklin, E. E., & Zuckerman, B. 2005, *ApJS*, 161, 394
- Farihi, J., Jura, M., & Zuckerman, B. 2009, *ApJ*, 694, 805
- Girven, J., Gänsicke, B. T., Steeghs, D., & Koester, D. 2011, *MNRAS*, 417, 1210
- Handler, G. 2001, *MNRAS*, 323, 43
- Hermes, J. J., Charpinet, S., Barclay, T., et al. 2014, *ApJ*, 789, 85
- Kepler, S. O., Castanheira, B. G., Saraiva, M. F. O., et al. 2005, *A&A*, 442, 629
- Kjeldsen, H. & Frandsen, S. 1992, *PASP*, 104, 413
- Koester, D. & Kepler, S. O. 2015, *A&A*, 583, 86
- Landolt, A. U. 2013, *AJ*, 146, 131
- Liebert, J., Wesemael, F., Hansen, C. J., et al. 1986, *ApJ*, 309, 241
- Limoges, M. M., Bergeron, P., & Lépine, S. 2015, *ApJS*, 219, 19
- Lindegren, L., Hernández, J., Bombrun, A., et al. 2018, *A&A*, 616, 2
- Marinoni, S., Pancino, E., Altavilla, G., et al. 2016, *MNRAS*, 462, 3616
- Mukadam, A. S., Mullally, F., Nather, R. E., et al. 2004, *ApJ*, 607, 982
- Mullally, F., Thompson, S. E., Castanheira, B. G., et al. 2005, *ApJ*, 625, 966
- Paunzen, E. & Vanmunster, T. 2016, *AN*, 337, 239
- Provencal, J. L., Shipman, H. L., & MacDonald, J. 2005, *ApJ*, 627, 418
- Reegen, P., Gruberbauer, M., Schneider, L., & Weiss, W. W. 2008, *A&A*, 484, 601
- Robinson, E. L. & Winget, D. E. 1983, *PASP*, 95, 386
- Rolland, B., Bergeron, P., & Fontaine, G. 2018, *ApJ*, 857, 56
- Romero, A. D., Amaral, L. A., Klippel, T., et al. 2019, *MNRAS*, 490, 1803
- Romero, A. D., Kepler, S. O., Córscico, A. H., Althaus, L. G., & Fraga, L. 2014, *RMxAC*, 44, 54
- Salaris, M., Althaus, L. G., & García-Berro, E. 2013, *A&A*, 555, 96
- Stetson, P. B. 1987, *PASP*, 99, 191
- Tremblay, P. E., Ludwig, H. G., Steffen, M., & Freytag, B. 2013, *A&A*, 559, 104
- Voss, B., Koester, D., Napiwotzki, R., Christlieb, N., & Reimers, D. 2007, *A&A*, 470, 1079
- Wagner, R. M., Sion, E. M., Liebert, J., Starrfield, S. G., & Zotov, N. 1986, *PASP*, 98, 552
- Wegner, G. & Koester, D. 1985, *ApJ*, 288, 746
- Werner, K., Dreizler, S., Heber, U., et al. 1995, *A&A*, 293, 75
- Werner, K., Rauch, T., & Kruk, J. W. 2018, *A&A*, 609, 107
- Wilson, T. G., Farihi, J., Gänsicke, B. T., & Swan, A. 2019, *MNRAS*, 487, 133
- Winget, D. E., Nather, R. E., Clemens, J. C., et al. 1994, *ApJ*, 430, 839
- Zuckerman, B., Melis, C., Klein, B., Koester, D., & Jura, M. 2010, *ApJ*, 722, 725

Marek Drózdź: Mt. Suhora Observatory, Pedagogical University, Podchorążych 2, 30-084 Kraków, Poland.

Gerald Handler: Nicolaus Copernicus Astronomical Center, Bartycka 18, 00-716 Warsaw, Poland.

Jan Janík and Ernst Paunzen: Department of Theoretical Physics and Astrophysics, Masaryk University, Kotlářská 2, 611 37 Brno, Czech Republic (epaunzen@physics.muni.cz).

Sean O'Brien: Space Telescope Science Institute, 3700 San Martin Drive, Baltimore, MD 21218, USA.

Monika Rode-Paunzen: BAS:IS, Austrian Academy of Sciences Dr. Ignaz Seipel-Platz 2, 1010 Vienna, Austria.

Todd K. Watson: Information Technology, Southwestern University, Georgetown, TX, USA.

Zora Zemanová: High School, Velehradská třída 218, 686 01 Uherské Hradiště, Czech Republic.

## THE INFLUENCE OF THE MASS DISTRIBUTION OF STELLAR OBJECTS ON THEIR GRAVITATIONAL FIELDS

Vladimir Stephanovich<sup>1</sup>, Włodzimierz Godłowski<sup>1</sup>, Monika Biernacka<sup>2</sup>, and Błażej Mrzygłód<sup>1</sup>

*Received February 2 2020; accepted May 5 2020*

### ABSTRACT

We study the influence of the mass randomness of astronomical objects on the distribution function of their gravitational fields. Based on purely theoretical arguments and on a comparison with extensive data collected from observations and numerical simulations, we show that while mass randomness does not alter the non-Gaussian character of the gravitational field distribution, it does change the dependencies of mean angular momenta of galaxies and clusters on their richness. The specific form of such dependencies is determined by the interplay of the character of the mass distributions and different assumptions about cluster morphology. We trace the influence of the mass distribution on the time evolution of the angular momenta of stellar objects in CDM and  $\Lambda$ CDM models. Our theoretical predictions are in very good agreement with the statistical results derived both from observational data and numerical simulations.

### RESUMEN

Estudiamos la influencia de la distribución aleatoria de las masas de objetos astronómicos sobre la función de distribución de sus campos gravitatorios. Basados en argumentos teóricos y en una comparación con numerosos datos observacionales y resultados de simulaciones numéricas mostramos que, si bien la distribución aleatoria de las masas no altera el carácter no Gaussiano de las funciones de distribución del campo gravitatorio, sí cambia la dependencia del momento angular medio de las galaxias y de los cúmulos en función de su riqueza. La forma específica de estas dependencias se determina a partir de la influencia mutua de las distribuciones de masa y de diferentes suposiciones sobre la morfología de los cúmulos. Investigamos la influencia de la distribución de masa sobre la evolución temporal del momento angular de objetos estelares para modelos CDM y  $\Lambda$ CDM. Nuestras predicciones teóricas concuerdan muy bien con los resultados estadísticos obtenidos tanto a partir de datos observados como de simulaciones numéricas.

*Key Words:* Galaxy: formation — Galaxy: general

### 1. INTRODUCTION

As the gravitational fields are highly nonuniform during the formation of galaxies and their clusters, the distribution of the former plays an important role. Moreover, the character of the gravitational field distribution permits to discern the specific scenario of galaxy formation. The classical scenarios of such formation were proposed a long time ago (Peebles 1969; Zeldovich 1970; Sunyaev & Zeldovich 1972; Doroshkevich 1973; Shandarin 1974; Efstathiou & Silk 1983; Dekel 1985) and dealt primarily with the mechanical instability of the so-called Zeldovich pancake model (Zeldovich 1970), based on a large gravitating body (of pancake shape, hence the name), without any randomness in the gravitational fields of the constituents (Zeldovich 1970; Shandarin & Zeldovich 1989; Longair 2008). These classical scenarios have not lost significance since new scenarios are essentially modifications of the classical ones and can be classified according to them. The improved form of the above classical scenarios has been put forward more recently (see Shandarin et al. 2012; Giahi-Saravani & Schäfer 2014 for relevant references). The presence or absence of the random gravitational field

<sup>1</sup>Uniwersytet Opolski, Institute of Physics, Opole, Poland.

<sup>2</sup>Institute of Physics, Jan Kochanowski University, Kielce, Poland.

fluctuations contributes to the studies of the angular momentum acquisition of galaxies during their formation stages. This may in principle permit to specify the most probable (among many other) scenario of the emergence of large stellar objects. This is because the final test of the correctness of a given scenario is the comparison of its predictions with observations. The investigations of the variations of the angular momenta of structures gives us the opportunity to do so. Note that different scenarios make different predictions about galaxy orientations, i.e. the angular momenta alignments in structures (Peebles 1969; Doroshkevich 1973; Shandarin 1974; Efstathiou & Silk 1983; Catelan & Theuns 1996; Li 1998; Lee & Pen 2000, 2001, 2002; Navarro et al. 2004; Trujillo et al. 2006; Zhang et al. 2013). For this reason the analysis of the orientation of the galaxy planes is regarded as a standard test of different scenarios of cosmic structure formation (Romanowsky & Fall 2012; Joachimi et al. 2015; Kiessling et al. 2015).

One of the natural sources of randomness of gravitational fields is the mass distribution of stellar objects. The simplest possible model of the mass distribution dates back to Chandrasekhar (1943), where the *a priori* given distribution function of masses  $\tau(M)$  has been considered. In this paper, all characteristics of the stellar ensemble are expressed through the different average powers of mass. The mass averaging was performed implicitly with the above function  $\tau(M)$ . In principle, such an approach can be generalized to averaging over quadrupole and higher multipole moments of galaxies in the spirit of Stephanovich & Godłowski (2015). Although this effect may change some of the results quantitatively, we speculate that its overall influence will be rather weak. The next step was done by Press & Schechter (1974), who considered the distribution function of stellar object masses within the model of a self-similar gravitational condensation. In this work, within the model of the expanding Universe in a Friedmann cosmology, the stellar ensembles were represented as a “gas” of self-gravitating masses, which could condense into aggregates with larger mass, forming finally very large clumpy objects. This model permits to derive the distribution of masses in the form

$$f(m) = A \left( \frac{m}{m_*} \right)^\alpha e^{-m/m_*}, \quad (1)$$

where  $A$  is a normalization constant, (see below). Note that the explicit expression of the Schechter function (1) has been listed in Schechter (1976), a work devoted to the luminosity distribution of galaxies. Below we will use function (1) for the calculation of the amended (on the mass distribution) distribution function of the gravitational fields and angular momenta. Using this function, we assume that the mass is proportional to the first power of the luminosity:  $m \sim L$ . Below we give arguments why a possible nonlinearity  $m \sim L^\gamma$  ( $\gamma \neq 1$ ) will not change our results qualitatively.

In the present paper, we consider tidal interactions in the ensemble of galaxies and their clusters in a Friedmann-Lemaître-Robertson-Walker Universe with a Newtonian self-gravitating dust fluid ( $p = 0$ ) containing both luminous and dark matter. The commonly accepted model of such a Universe is the spatially flat homogeneous and isotropic  $\Lambda$ CDM model. The clumpy objects like galaxies and their clusters are formed as a result of almost scale-invariant Gaussian fluctuations (Silk 1968; Peebles & Yu 1970; Sunyaew & Zeldovich 1970). This assumption is the base of the so-called hierarchical clustering model (Doroshkevich 1970; Dekel 1985; Peebles 1969). The models with non-Gaussian initial fluctuations have also been considered in Bartolo et al. (2004). The non-Gaussian character of the distribution function was postulated there, rather than calculated. A calculation was presented in Stephanovich & Godłowski (2015, 2017), where the non-Gaussian distributions of gravitational fields and momenta were calculated using the method of Chandrasekhar (1943). Here we generalize this calculation considering the mass distribution (1). Note that the calculations made in Stephanovich & Godłowski (2015, 2017) dealt with the equilibrium situation only. To consider a non-equilibrium situation, it is necessary to use differential equations of Fokker-Planck type with so-called fractional derivatives (Garbaczewski & Stephanovich 2009, 2011). In this case we can begin with an ubiquitous Gaussian distribution and arrive at a non-Gaussian one as a result of a primordial, fast time evolution. After it, the slower evolution, dictated by the  $\Lambda$ CDM scenario, takes place. Note that recently time evolution of intrinsic galaxy alignments has been found by Schmitz et al. (2018).

In the hierarchical clustering approach, the large clumpy structures form as a result of gravitational interactions between smaller objects. In other words, the spin angular momenta of galaxies arise as a result of tidal interactions with their neighbors (Schäfer 2009). Note that, in the present paper, the angular momentum is the result of tidal interactions with the entire environment, which occur via interaction transfer from close to distant galaxies (see below). That is to say, our approach is the generalization of Schäfer & Merkel (2012); Catelan & Theuns (1996, 1996a); Lee & Pen (2002), where the average tidal interaction with the entire environment has been considered. In the present work we perform the theoretical and statistical analysis of the influence of tidal interactions between astronomical objects on the formation of larger (then initial) structures. We also perform the comparison of our model predictions with vast data arrays, derived from observational and numerically simulated data. It turns out that our theoretical results are in good coincidence with

the above observational and numerical data. Our theoretical model includes an additional mass distribution, obeying the Shechter function (1). It turns out that the mass distribution (1) does not change our main result (Stephanovich & Godłowski 2015, 2017) that in stellar systems with multipole (tidal) gravitational interactions, the distribution function of gravitational fields cannot be Gaussian. The crux of the matter here is the long-range character of the Newtonian (and derived multipole) interaction between stellar objects. Such a character implies that distant objects (like galaxies, their clusters and even dark matter haloes) still “feel each other”, which is not the case for a Gaussian distribution. The derived non-Gaussian distribution function allows us to calculate the distribution of virtually any observable (like angular momentum) of the astronomical structures (not only galaxy clusters, but also smooth components like halos, which mass-dominate the total mass of a cluster (see Kravtsov & Borgani 2012) in any Eulerian approach (linear or non-linear).

The relation between the angular momentum of galaxy clusters and their mass has also been investigated observationally. It is not difficult to analyze the distribution of angular momenta for the luminous matter. In the real universe, the luminous galaxies and their structures are surrounded by dark matter halos. These halos are often much more extended and massive than the luminous component of the structures. Unfortunately, direct observation of dark matter halos and their angular momenta is complicated. One should not forget, however, that there are observed correlations between luminous and dark matter (sub)structures. This implies the certain dependence between dark matter halos and luminous matter (real galaxies) orientations (Trujillio et al. 2006; Paz et al. 2008; Pereira et al. 2008; Bett et al. 2010; Paz et al. 2011; Kimm et al. 2011; Varela et al. 2012). Recently, the results of Okabe et al. (2018); Codis et al. (2018) based on Horizon-AGN simulation show a similar dependence. This allows to conclude that the analysis of angular momentum of luminous matter gives also information about the angular momentum of the total structure (i.e. that with dark matter halos). As a result, the analysis of the angular momentum of “real” (luminous) galaxies and their structures, is still important as a test for a possible structure formation scenario. Note that investigations of galaxy orientation in clusters are also very important for the analysis of weak gravitational lensing (see Heavens et al. 2000; Heymans et al. 2004; Kiessling et al. 2015; Stephanovich & Godłowski 2015; Codis et al. 2016 for more details).

As generally galaxy clusters do not rotate (Hwang & Lee 2007; Tovmassian 2015), the angular momentum of a cluster is primarily due to the spins of member galaxies. Unfortunately, usually we do not know the angular momenta of galaxies. So the orientations of galaxies are investigated instead (Oepik 1970; Hawley & Peebles 1975; see Romanowsky & Fall 2012; Pajowska et al. 2019 for recent reviews), since it is assumed that the rotational axes of galaxies are normal to their planes. Such an assumption seems to be quite reasonable at least for spiral galaxies. As a result, a stronger alignment of galaxies in a structure means a larger angular momentum of the latter.

The question is whether there is any relation between the alignment and mass of the structure. The general result of the previous papers is that there is insufficient evidence for galaxy alignment in less massive structures like groups and poor clusters. However, we do observe the alignment of galaxies in rich clusters; see Godłowski (2011); Pajowska et al. (2019) for a review. The first results (Godłowski, Szydlowski, & Flin 2005; Aryal et al. 2007) were qualitative only. Because of that, Godłowski et al. (2010) and Godłowski (2012) investigated quantitatively the orientation of galaxies in a sample of 247 rich Abell clusters, using the improved Hawley & Peebles (1975) method (see Pajowska et al. 2019 for the latest review). In these papers, it was found that the alignment is present in the above sample. Moreover, galaxy orientation increased with richness of the cluster. However, the data were insufficient both to resolve the question about the exact form of this relationship and to confirm the hypothesis that the angular momentum of the structure increases with time. This is the reason why we decided to extend our sample and to compare observational results with those obtained from the simulations.

## 2. THE FORMALISM

Similar to the papers by Stephanovich & Godłowski (2015, 2017) we consider here the quadrupolar (tidal) interaction of the stellar objects

$$\mathcal{H} = -G \sum_{ij} Q_i m_j V(\mathbf{r}_{ij}), \quad V(\mathbf{r}) = \frac{1}{2} \frac{3 \cos^2 \theta - 1}{r^3}, \quad (2)$$

where  $G$  is the gravitational constant,  $Q_i$  and  $m_i$  are, respectively, the quadrupole moment and mass of  $i$ -th object,  $r_{ij} \equiv |\mathbf{r}_{ij}|$ ,  $\mathbf{r}_{ij} = \mathbf{r}_j - \mathbf{r}_i$  is a relative distance between objects, and  $\theta$  is the apex angle. The Hamiltonian function (2) describes the interaction of quadrupoles formed both from luminous and dark matter; see Stephanovich & Godłowski (2017) for details.

To account for the mass distribution (1), we begin with the expression for the characteristic function  $F(\rho)$  of the random gravitational fields distribution (Stephanovich & Godłowski 2015, 2017).

$$F(\rho) = \int_V n(\mathbf{r}) \left[ 1 - \frac{\sin \rho E(\mathbf{r})}{\rho E(\mathbf{r})} \right] d^3 r. \quad (3)$$

In the spirit of the article of Chandrasekhar (1943), we rewrite the expression (3) in the form

$$F(\rho) = \int_{V,m} n(\mathbf{r}, m) \left[ 1 - \frac{\sin \rho E(\mathbf{r}, m)}{\rho E(\mathbf{r}, m)} \right] d^3 r dm, \quad (4)$$

where  $n(\mathbf{r}, m)$  is the number density (concentration, proportional to probability, see below) of stellar objects (galaxies, their clusters, and also dark matter haloes) at the position  $\mathbf{r}$  with a mass  $m$ . As the average density at large scales can be regarded as constant (slowly spatially fluctuating to be specific, see Chandrasekhar 1943; Press & Shechter 1974), the number density  $n$  in equation (4) can be safely considered to be spatially uniform, i.e.  $n = n(m)$ . In this case the expression (4) reads

$$F(\rho) = \int_{V,m} n(m) \left[ 1 - \frac{\sin \rho E(\mathbf{r}, m)}{\rho E(\mathbf{r}, m)} \right] d^3 r dm, \quad (5)$$

where

$$E(\mathbf{r}, m) = E_0 \frac{3 \cos^2 \theta - 1}{r^4}, \quad E_0 = \frac{1}{2} GQ, \quad Q \approx mR^2 \quad (6)$$

is the quadrupolar field (Stephanovich & Godłowski 2015),  $m$  is the mass of a stellar object (like a galaxy or cluster) and  $R$  is its mean radius. We take the function  $n(m) \equiv f(m)$  in the form of the Shechter function (1), where  $m_*$  and  $\alpha$  are adjustable parameters. We obtain the normalization constant  $A$  from the condition (see equation 4 of Press & Shechter 1974)

$$n = \int_0^\infty n(m) dm, \quad (7)$$

where  $n$  is our previous constant concentration (Stephanovich & Godłowski 2015, 2017). Note that there is no problem to take any other dependence  $n(m)$  which will not complicate our consideration. As we mentioned above, here following Shechter (1976), we assume that the luminosity is directly proportional to the first power of the mass  $\tilde{L} \sim m$ . But there is no problem to consider the higher powers in this relation, like  $\tilde{L} \sim m^k$ ,  $k = 4$ . In this case, the argument of the function (1) will be  $m^k$  instead of  $m$ .

The explicit calculation gives

$$n = A \int_0^\infty \left( \frac{m}{m_*} \right)^\alpha e^{-m/m_*} dm = A m_* \Gamma(1 + \alpha), \quad \Rightarrow A = \frac{n}{m_* \Gamma(1 + \alpha)}. \quad (8)$$

Here  $\Gamma(z)$  is Euler  $\Gamma$  - function (Abramowitz & Stegun 1972). Finally we have from (5)

$$F(\rho) = \frac{n}{m_* \Gamma(1 + \alpha)} \int_V \int_0^\infty dm \left( \frac{m}{m_*} \right)^\alpha e^{-m/m_*} \left[ 1 - \frac{\sin \rho E(\mathbf{r}, m)}{\rho E(\mathbf{r}, m)} \right] d^3 r, \quad (9)$$

where  $E(\mathbf{r}, m)$  is given by equation (6). It turns out that equation (8) can be reduced to equations (17) and (18) from Stephanovich & Godłowski (2015) but with a slightly renormalized coefficient before  $\rho^{3/4}$ . This is because, under the assumption that  $n$  does not depend on the coordinates (it depends only on the mass, see equation 1), the coordinates and the mass turn out to be effectively decoupled. To proceed, we perform first the integration over  $d^3 r$  in (8). This integration is exactly the same as that in Stephanovich & Godłowski (2015) (since the mass enters equation (6) through parameter  $E_0$  which is unimportant for coordinate integration) so that we have from (9)

$$F(\rho) = 2\pi \cdot 0.41807255 \rho^{3/4} E_{10}^{3/4} \int_0^\infty m^{3/4} n(m) dm, \quad E_{10} = \frac{1}{2} GR^2. \quad (10)$$

The integral in (10) can be performed as follows

$$\begin{aligned} I &= \int_0^\infty m^{3/4} n(m) dm = \frac{n}{m_* \Gamma(1 + \alpha)} \int_0^\infty m^{3/4} \left( \frac{m}{m_*} \right)^\alpha e^{-m/m_*} dm = \\ &= \frac{n m_*^{7/4}}{m_* \Gamma(1 + \alpha)} \int_0^\infty x^{\alpha+3/4} e^{-x} dx = n m_*^{3/4} \frac{\Gamma(\alpha + \frac{7}{4})}{\Gamma(\alpha + 1)}. \end{aligned} \quad (11)$$

Finally

$$F(\rho) = 2\pi n m_*^{3/4} \frac{\Gamma(\alpha + \frac{7}{4})}{\Gamma(\alpha + 1)} E_{10}^{3/4} \cdot 0.41807255 \cdot \rho^{3/4} \equiv \kappa \rho^{3/4}, \quad (12)$$

where

$$\kappa = 2\pi n \cdot 0.41807255 \cdot E_0^{*3/4} \frac{\Gamma(\alpha + \frac{7}{4})}{\Gamma(\alpha + 1)}, \quad E_0^* \equiv m_* E_{10} = \frac{1}{2} G m_* R^2 \equiv \frac{1}{2} G Q^*. \quad (13)$$

The expressions (12), (13) give the answer for the case when we have a Shechter distribution for the galaxy masses. The difference between the previous case (Stephanovich & Godłowski 2015, 2017) of a single mass is that now the width of the distribution function of random gravitational fields depends on the fitting parameters  $m_*$  and  $\alpha$ . Note that for *any* function  $n(m)$  the result for the characteristic function  $F(\rho)$  will be equation (12) but with a different coefficient  $\kappa$ .

### 3. CALCULATION OF THE MASS DEPENDENCE OF THE MEAN ANGULAR MOMENTUM

To derive the mass dependence of the mean angular momentum, we should first calculate the distribution function of gravitational fields  $f(E)$ , then using a linear relation between angular momentum  $L$  and field  $E$  (here, without loss of generality, we consider the moduli of corresponding vectors, see Stephanovich & Godłowski 2015, 2017 for details), we derive the distribution function  $f(L)$ , from which we obtain the desired dependence.

The expression for the field distribution reads (Stephanovich & Godłowski 2015)

$$f(E) = \frac{1}{(2\pi)^3} \int e^{iE\rho - F(\rho)} d^3\rho \equiv \frac{1}{2\pi^2 E} \int_0^\infty \rho e^{-\kappa\rho^{3/4}} \sin \rho E d\rho, \quad (14)$$

where  $F(\rho)$  is the characteristic function (12). Function  $f(E)$  is normalized as follows

$$4\pi \int_0^\infty E^2 f(E) dE = 1, \quad (15)$$

and coefficient  $\kappa$  is given by the expression (13). The distribution function of angular momenta can be expressed in the usual way from the  $f(E)$ :

$$f(L) = f[E(L)] \left| \frac{dE(L)}{dL} \right|. \quad (16)$$

This gives explicitly (see Stephanovich & Godłowski 2015, 2017)

$$f(\lambda) = \frac{I(\lambda)}{2\pi^2 \lambda^3 \kappa^4 L_0(t)}, \quad (17)$$

where

$$\lambda = L/(L_0(t)\kappa^{4/3}), \text{ and } I(\lambda) = \int_0^\infty x \sin x \exp \left[ - \left( \frac{x}{\lambda} \right)^{3/4} \right] dx. \quad (18)$$

Function  $L_0(t)$  defines the model (CDM or  $\Lambda$ CDM) used by Stephanovich & Godłowski (2017).

#### 3.1. CDM Model

Equation (12) shows that the distribution function of angular momenta for the case of distributed masses is similar to that from Stephanovich & Godłowski (2015) with the only change  $\alpha \rightarrow \kappa$ . This means that the mean dimensionless angular momentum reads (Stephanovich & Godłowski 2015, 2017)

$$\lambda_{max} = 0.602730263. \quad (19)$$

Now we should express the parameter  $\kappa$  through the galaxy mass  $m$  (but not the cluster mass, which still is equal to  $M = mN$ , where  $m$  is the galaxy mass,  $M$  is the cluster mass,  $N$  is the number of galaxies in a cluster, see Stephanovich & Godłowski 2015, 2017). This quantity is now defined as an average mass, with the distribution (1)

$$m = \int_0^\infty m_1 n(m_1) dm_1 \equiv \frac{n m_*^2 \Gamma(\alpha + 2)}{m_* \Gamma(1 + \alpha)} = (\alpha + 1) m_* n. \quad (20)$$

Expression (20) implies that the galaxy mass  $m$  is related to the mass distribution parameter  $m_*$  as

$$m_* = \frac{m}{n(\alpha + 1)}. \quad (21)$$

The next step is to substitute expression (21) in expression (13) for  $\kappa$  and express it in terms of galaxy mass  $m$  instead of  $m_*$ . We have from equation (13)

$$\kappa^{4/3} = \frac{mE_{10} n^{1/3}}{\alpha + 1} \left[ 2\pi \cdot 0.41807255 \cdot \frac{\Gamma(\alpha + \frac{7}{4})}{\Gamma(\alpha + 1)} \right]^{4/3}. \quad (22)$$

In the CDM model, the function  $L_0(t)$  has the form (Stephanovich & Godłowski 2017)

$$L_0(t) = \frac{2I}{3} \frac{t}{t_0^2}, \quad (23)$$

where  $I \approx mR^2$  is the galaxy moment of inertia and  $t_0$  is a time scale. We have from equation (19) in dimensional units

$$\begin{aligned} L_{max} &= \lambda_{max} L_0 \kappa^{4/3} \equiv 0.6027 \frac{2I}{3} \frac{t}{t_0^2} \frac{mE_{10} n^{1/3}}{1 + \alpha} \left[ 2\pi \cdot 0.418 \cdot \frac{\Gamma(\alpha + \frac{7}{4})}{\Gamma(\alpha + 1)} \right]^{4/3} \\ &= 0.7281884 \frac{t}{t_0^2} \frac{m^2 n^{1/3}}{1 + \alpha} \zeta^{4/3} G R^4, \quad \zeta = \frac{\Gamma(\alpha + \frac{7}{4})}{\Gamma(\alpha + 1)}. \end{aligned} \quad (24)$$

The comparison of expression (24) with equation (12) from Stephanovich & Godłowski (2015) shows that their only difference is the power of  $n$ . Namely, while equation (12) involves  $n^{4/3}$ , our expression (24) contains  $n^{1/3}$ . This is the consequence of the star mass distribution according to the Shechter function. We note also that the above mass distribution leaves the power of the galaxy mass  $m$  intact, i.e. both expressions involve  $m^2$ . This means that in the first scenario (see below and equation 13 of Stephanovich & Godłowski 2017) the dependence of  $L_{max}$  on galaxy cluster mass  $M = mN$  will be the same,  $\sim M^{5/3}$ . In the second scenario (equation 15 of Stephanovich & Godłowski 2017) the dependence on  $M$  will be  $M^{1/3}$  instead of  $M^{4/3}$ . We now derive the dependencies on  $M$  within both scenarios of Stephanovich & Godłowski (2017).

### 3.1.1. First Scenario

In this scenario we represent the galaxy volume as  $V = R^3$  (Stephanovich & Godłowski 2017), where  $R$  is the mean radius of a galaxy. In this case we have from (24)

$$\begin{aligned} L_{max} &= \eta m^2 n^{1/3} R^4 = \eta m^2 R^4 \frac{N^{1/3}}{V^{1/3}} \equiv \eta m^2 R^4 \frac{N^{1/3}}{R} = \eta m^2 R^3 N^{1/3} = \\ &= \eta \frac{R^3}{N} M^{5/3} \frac{m^{1/3}}{N^{1/3}} = \eta \frac{1}{n} M^{5/3} \frac{\rho^{1/3}}{n^{1/3}} = \eta M^{5/3} \frac{\rho^{1/3}}{n^{4/3}}, \quad \eta = \frac{t}{t_0^2} \frac{0.728G}{1 + \alpha} \zeta^{4/3}, \\ \rho &= \frac{m}{V}, \quad n = \frac{N}{V}. \end{aligned} \quad (25)$$

The comparison of equation (25) and equation (13) from Stephanovich & Godłowski (2017) shows that the  $M^{5/3}$  is the same, but the galaxy concentration  $n$  now enters with power 4/3 instead of 1/3. One more difference is that now the Shechter exponent  $\alpha$  (see equation 1) enters the answer via parameters  $\eta$  and  $\zeta$ . It should be extracted from the best fit between expression (25) and the data, taken either from observations or from numerical simulations.

### 3.1.2. Second Scenario

In this scenario the galaxy volume is  $V = R_A^3$ , where  $R_A$  is a mean galaxy cluster radius. We have from (24)

$$\begin{aligned} L_{max} &= \eta m^2 n^{1/3} R^4 = \eta m^2 R^4 \frac{N^{1/3}}{R_A} = \eta \frac{R}{R_A} R^3 m^2 N^{1/3} = \\ &= \eta \frac{R}{R_A} R^3 m^2 \frac{M^{1/3}}{m^{1/3}} = \eta \frac{R}{R_A} R^3 m^{5/3} M^{1/3}. \end{aligned} \quad (26)$$

It is seen that contrary to equation (15) of Stephanovich & Godłowski (2017), here we have  $M^{1/3}$ . Also, the Shechter parameter  $\alpha$  enters into the answer.

3.2.  $\Lambda$ CDM Model

Here, similar to Stephanovich & Godłowski (2015), we should isolate the contribution from the time dependent functions  $f_{1,2}(\tau)$  ( $\tau = t/t_0$ ,  $t_0 = 2/(3H_0\sqrt{\Omega_\Lambda})$ ), see equation (46) of Stephanovich & Godłowski (2015);  $i = 1, 2$  numbers the orders (first and second respectively) of perturbation theory. Following Stephanovich & Godłowski (2015), we have for the argument of the distribution function  $H(\lambda, t)$  (equation 44).

$$\lambda(\tau) = \frac{L}{I\kappa^{4/3}} \frac{1}{f_i(\tau)}. \tag{27}$$

Similar to the above CDM model, the maximum of the distribution function  $\lambda_{max} = 0.602730263$  generates the following relation

$$L_{max} = I\kappa^{4/3} \cdot 0.6027 f_i(\tau) \equiv \eta_{\Lambda CDM i}(\tau) m^2 R^4 n^{1/3},$$

$$\eta_{\Lambda CDM i}(\tau) = f_i(\tau) \frac{0.6027 \Psi^{4/3} G}{2(\alpha + 1)}, \quad \Psi = 2\pi \cdot 0.418 \cdot \frac{\Gamma(\alpha + \frac{7}{4})}{\Gamma(\alpha + 1)}. \tag{28}$$

The relation (28) is almost similar both in CDM and  $\Lambda$ CDM models. The only difference is in the functions  $f_i(\tau)$ , where in the CDM model

$$f_1(\tau) = (2/3)\tau, \quad f_2(\tau) = (-4/3)\tau^{1/3}. \tag{29}$$

It is seen that the substitution of functions  $f_{1,2}$  (29) yields immediately the expressions (25) and (26) for the CDM model. In the  $\Lambda$ CDM model the functions  $f_{1,2}(\tau)$  should be taken from the solution of the differential equations (30) and (31) of Stephanovich & Godłowski (2015).

As the expression (28) for  $L_{max}$  is formally equivalent to equations (25) and (26), the dependencies  $L_{max}(M)$  are the same as those defined by equations (25) and (26) except that we should use now  $\eta_{\Lambda CDM i}(\tau)$ .

The representative plots of the function  $H(\lambda, \tau) = 2I(\lambda, \tau)/(\pi\lambda)$  (Stephanovich & Godłowski 2015) and the maximal value  $\lambda_{max}(\tau)$  for the mass-dependent density (1) are reported in Figure 1. The left and middle panels show the results for the first (equation 30 of Stephanovich & Godłowski 2015) and second orders (equation 31) of the perturbation theory. First, it is seen that the distribution of masses does not make a qualitative difference in the shape of the distribution function. That is, the shape of the dashed black curves (those without mass distribution) and the red and blue ones is the same. At the same time, the distribution functions  $H(\lambda, \tau)$  have substantially smaller amplitudes in the case of a mass distribution. This means that the presence of a mass distribution changes the functions  $H(\lambda, \tau)$  quantitatively. The influence of the Shechter exponent  $\alpha$  (Press & Shechter 1974; Shechter 1976) is minimal - the curves  $H(\lambda, \tau)$  as well as  $\lambda_{max}(\tau)$  (right panel) are almost the same for very different values of  $\alpha = 1.25$  and  $0.5$ . This means that while the distribution of masses by itself changes the distribution function quantitatively, the value of the constant  $\alpha$  in that distribution is of minute influence. Our analysis shows that the above tendency persists for any time instant (in Figure 1 we have only two time instants  $\tau = 0.5$  and  $1$ ) and any reasonable  $\alpha > 0$ . The maximal values  $\lambda_{max}$  are almost independent of the presence of a mass distribution. Really, it is seen from the right panel of Figure 1 that the curves for no mass distribution (black dashed lines) and those for it lie very close to each other. This means simply that the physics of the system under consideration is determined by the distribution of random gravitational fields, rather than that of the masses of stellar objects. Maybe the ‘‘complete’’ dependence  $n(\mathbf{r}, m)$  (4) (rather than the present simplified situation  $n(m)$  in each spatial point  $\mathbf{r}$  (5)) will improve the situation. On the other hand, it is acceptable that the robust distribution of gravitational fields is simply not susceptible to small corrections like a mass distribution. The latter, in turn, may mean that the next important step in the physics of galaxies formation is to consider the short-range interaction between galaxies (due to the presence of dark matter, for instance) so that the real average angular momentum (and not the distribution function maximum, considered so far) will appear; see equation (48) of Stephanovich & Godłowski (2015) and equation (28) of Stephanovich & Godłowski (2017).

4. OBSERVATIONAL DATA

The first part of our data is the sample of rich Abell clusters containing at least 100 member galaxies each (Pajowska et al. 2019). The sample contains 247 clusters and was selected on the basis of the PF catalogue (Panko & Flin 2006, see Pajowska et al. 2019 for details). However, in the present paper we decided to restrict ourselves to 187 clusters

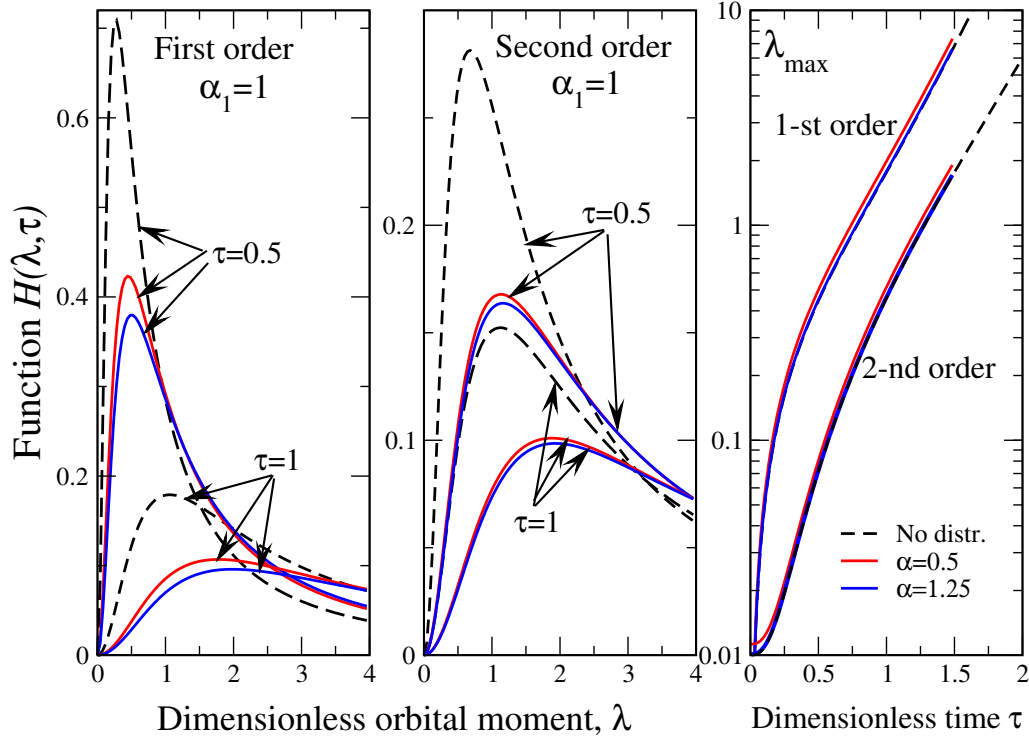


Fig. 1. Time evolution of the distribution function  $H(\lambda, \tau)$  in the  $\Lambda$ CDM model for the case of mass-dependent density (1). Left panel: first order perturbation theory. Middle panel: second order. Right panel: the dependence  $\lambda_{max}(\tau)$  on the first and second orders of perturbation theory. In all panels, dashed lines (marked as “No distr.” in the right panel) correspond to the previous case of mass-independent density  $n$ . We consider two Shechter exponents  $\alpha = 0.5$  (red curves) and  $1.25$  (blue curves), coded by colors and explained in the legend in the right panel. Parameter of  $\Lambda$ CDM model  $\alpha_1 = \left(\frac{1-\Omega_\Lambda}{\Omega_\Lambda}\right)^{1/3} = 1$ . The color figure can be viewed online.

which have explicit redshifts. As our PF cluster sample was not numerous enough to confirm the hypothesis that galaxy alignment decreases with redshift, we decided to enlarge our sample with the DSS base.

From the ACO Catalogue (Abell, Corwin & Olowin 1989) we selected all Abell clusters with galactic latitude  $b > 40^\circ$  and richness class  $\geq 1$ . This gave us 1238 structures of galaxies from which we selected only those with redshifts  $z < 0.2$  (Struble & Rood 1999). Therefore, 377 clusters were left for analysis. From DSS we extracted the area covering  $2\text{Mpc} \times 2\text{Mpc}$  ( $h = 0.75$ ,  $q_0 = 0.5$ ) around each cluster. We applied the FOCAS package (Jarvis & Tyson 1981) to the extracted regions and obtained catalogues of galaxies, considering objects within the magnitude range  $(m_3, m_3 + 3)$ , where  $m_3$  is the magnitude of the third brightest galaxy. The catalogues obtained automatically were visually corrected in order to reduce the possible incorrect star/galaxy classification. FOCAS calculates the catalogue parameters using the moments of pixel distribution in an object. There are three steps from the basic image to the object list in FOCAS: segmentation, area assembly and object evaluation. The various parameters characterizing the individual images in the segmented areas were calculated. In FOCAS, the object location is defined by centroids:

$$\bar{x} = \frac{1}{M_{00}} \sum_A x_i [I(x, y) - I_s], \quad (30)$$

$$\bar{y} = \frac{1}{M_{00}} \sum_A y_i [I(x, y) - I_s], \quad (31)$$

where  $M_{00}$  is the zero moment, which is equal to:

$$M_{00} = \sum_A [I(x, y) - I_s]. \quad (32)$$

The summation over A means that the sum includes all pixels in the object-defining area A.  $I(x, y)$  is the intensity corresponding to the density at the location  $(x, y)$  in the digital plate image.  $I_s$  is the intensity corresponding to the average plate density at the object location. Shape information about the object is obtained from the higher central moments:

$$M_{ij} = \sum A(x - \bar{x})^i (y - \bar{y})^j [I(x, y) - I_s]. \quad (33)$$

The object position angle is calculated using the above central moments:

$$\tan(2\theta) = \frac{2M_{11}}{M_{20} - M_{02}}. \quad (34)$$

The galaxy ellipticity is

$$e = 1 - \frac{\lambda_2}{\lambda_1}, \quad (35)$$

where

$$\begin{aligned} \lambda_1^2 &= \frac{1}{2} \left( (M_{20} + M_{02}) + \sqrt{(M_{20} - M_{02})^2 + 4M_{11}^2} \right), \\ \lambda_2^2 &= \frac{1}{2} \left( (M_{20} + M_{02}) - \sqrt{(M_{20} - M_{02})^2 + 4M_{11}^2} \right). \end{aligned} \quad (36)$$

Each catalogue contains information about the right ascension and declination of each galaxy, its coordinates  $x$  and  $y$  on the photographic plate, instrumental magnitude, object area, galaxy ellipticity and the position angle of the major axis of the galaxy image. The equatorial galaxy coordinates for the epoch 2000 were computed according to the rectangular coordinates of the DSS scans. We calculate the position angle and ellipticity of each galaxy cluster using the method described by Carter & Metcalfe (1980) which is also based on the first five moments of the observed distribution of galaxy coordinates  $x_i, y_i$ .

## 5. STATISTICAL STUDIES

Hawley & Peebles (1975) proposed to analyze the distribution of galaxies angular momenta by that of the observed position angles of the galactic image major axes. The direction of the angular momentum is then believed to be perpendicular to that of the major galaxy axis. This means that in the original version of the method the face-on and nearly face-on galaxies must be excluded from the analysis. This method can also be extended to studies of the spatial orientation of galaxy planes (Flin & Godłowski 1986).

The idea of Hawley & Peebles (1975) is to use the statistical tests to investigate the position angle distribution. A high value of statistics means a greater deviation from an isotropic distribution i.e. a stronger alignment of galaxy angular momenta in the analyzed structures. Since the Hawley & Peebles (1975) paper, this method has become the standard tool for searching galactic alignments. A recent improvement and revision of this method was presented by Pajowska et al. (2019).

In the present paper we follow the analysis from Stephanovich & Godłowski (2017). The entire range of investigated angles is divided into  $n$  bins. As the aim of the method is to detect non-random effects in the galaxy orientation, we first check if the considered distribution deviates from an isotropic one. Following Stephanovich & Godłowski (2017), in the present paper we use  $\chi^2$  and Fourier tests. We also extend our analysis with first auto-correlation and Kolmogorov-Smirnov (K-S) tests (Hawley & Peebles 1975; Flin & Godłowski 1986; Godłowski et al. 2010; Godłowski 2012; see Pajowska et al. 2019 for last review).

The statistic  $\chi^2$  is:

$$\chi^2 = \sum_{k=1}^n \frac{(N_k - N p_k)^2}{N p_k} = \sum_{k=1}^n \frac{(N_k - N_{0,k})^2}{N_{0,k}}, \quad (37)$$

where  $p_k$  are probabilities that the chosen galaxy falls into the  $k$ -th bin,  $N$  is the total number of galaxies in a sample (in a cluster in our case),  $N_k$  is the number of galaxies within the  $k$ -th angular bin and  $N_{0,k} = N p_k$  is the expected number of galaxies in the  $k$ -th bin. Note that the number of degrees of freedom of the  $\chi^2$  test is  $n - 1$ , mean value  $E(\chi^2) = n - 1$  while the variance  $\sigma^2(\chi^2) = 2(n - 1)$ . As in our analysis  $n = 36$ , we obtain the values  $E(\chi^2) = 35$  while  $\sigma^2(\chi^2) = 70$ , i.e.  $\sigma(\chi^2) = 8.367$ .

The first auto-correlation test quantifies the correlations between galaxy numbers in neighboring angle bins. The statistic  $C$  is given by

$$C = \sum_{k=1}^n \frac{(N_k - N_{0,k})(N_{k+1} - N_{0,k+1})}{[N_{0,k}N_{0,k+1}]^{1/2}}, \quad (38)$$

where  $N_{n+1} = N_1$ . When, as in the present paper, we analyze the distribution of the position angles, than all  $N_{k,0} = N p_k$  are equal to each other and  $E(C) = -1$  while  $D(C) \approx n$  (i.e.  $\sigma(C) \approx \sqrt{n} = 6$ ), see Godłowski (2012); Pajowska et al. (2019) for details.

If we assume that the deviation from isotropy is a slowly varying function, we can use the Fourier test:

$$N_k = N_{0,k}(1 + \Delta_{11} \cos 2\theta_k + \Delta_{21} \sin 2\theta_k + \Delta_{12} \cos 4\theta_k + \Delta_{22} \sin 4\theta_k + \dots). \quad (39)$$

In this test, statistically important are the amplitudes

$$\Delta_1 = (\Delta_{11}^2 + \Delta_{21}^2)^{1/2}, \quad (40)$$

(only the first Fourier mode is taken into account) or

$$\Delta = (\Delta_{11}^2 + \Delta_{21}^2 + \Delta_{12}^2 + \Delta_{22}^2)^{1/2}, \quad (41)$$

where the first and second Fourier modes are analyzed together. We investigate the statistics  $\Delta_1/\sigma(\Delta_1) = (\Delta_{11}^2/\sigma^2(\Delta_{11}) + \Delta_{21}^2/\sigma^2(\Delta_{21}))^{1/2}$  and  $\Delta/\sigma(\Delta) = (\Delta_{11}^2/\sigma^2(\Delta_{11}) + \Delta_{21}^2/\sigma^2(\Delta_{21}) + \Delta_{12}^2/\sigma^2(\Delta_{12}) + \Delta_{22}^2/\sigma^2(\Delta_{22}))^{1/2}$  (see Godłowski et al. 2010; Godłowski 2012; Pajowska et al. 2019 for details). Note that the expression  $\frac{\Delta_j^2}{\sigma^2(\Delta_j)}$  means that the elements of  $\Delta^2$  should be divided by their errors rather than the total factor  $\Delta_j^2$  divided by its error. The expectation values of the total factors are  $E\left(\frac{\Delta_1}{\sigma(\Delta_1)}\right) = 1.2247$  and  $E\left(\frac{\Delta}{\sigma(\Delta)}\right) = 1.8708$  while  $\sigma^2(\Delta_1/\sigma(\Delta_1)) = 1/2$ , and  $\sigma^2(\Delta/\sigma(\Delta)) = 1/2$  (i.e. errors of the total factors equal to  $\sqrt{2}$  - see Godłowski 2012; Pajowska et al. 2019 for details).

In the case of the K-S test, the statistic under study is  $\lambda$ :

$$\lambda = \sqrt{N} D_n, \quad (42)$$

which is given by limiting Kolmogorov distribution, where

$$D_n = \sup |F(x) - S(x)|, \quad (43)$$

and  $F(x)$  and  $S(x)$  are the theoretical and observational distributions of the investigated angle, respectively. Wang et al. (2003) analyzing the limiting form of the  $D_n$  function, found that  $\mu(\lambda) = 0.868731$  while  $\sigma^2(\lambda) = 0.067773$  i.e.  $\sigma(\lambda) = 0.260333$  (see also Pajowska et al. 2019 for discussion).

Using the extended Hawley & Peebles (1975) method it is possible to analyze both the alignment dependence on a particular parameter, like richness of a galaxy cluster Godłowski et al. (2010), and to quantitatively answer the question if an alignment is present in a sample (see Pajowska et al. 2019 for last revision). In our previous papers (Godłowski et al. 2010; Stephanovich & Godłowski 2017), using a sample of 247 PF rich Abell clusters, it was shown that the alignment of galaxies in a cluster increases significantly with its richness. Unfortunately, the available data were insufficient for a persuasive conclusion about the correctness of the theoretically predicted dependence of the analyzed statistics on redshift  $z$  (Stephanovich & Godłowski 2015, 2017).

For this reason we performed the investigations of our samples of galaxy clusters checking if there is a significant dependence between the analyzed statistics and both richness and redshift of the clusters. As a first step we analyzed the linear model  $Y = aX + b$ . The  $Y$  are the values of the statistics i.e.  $\chi^2$ ,  $\Delta_1/\sigma(\Delta_1)$ ,  $\Delta/\sigma(\Delta)$ ,  $C$  and  $\lambda$  (see Stephanovich & Godłowski 2017 for details) while  $X$  is the number of analyzed galaxies in each particular cluster or its redshift  $z$  respectively. Our null hypothesis  $H_0$  is that the statistic  $Y$  does not depend on  $X$ . This means that we should analyze the statistic  $t = a/\sigma(a)$ , which is Student's distribution with  $u - 2$  degrees of freedom, where  $u$  is the number of analyzed clusters. In other words, we test the  $H_0$  hypothesis that  $t < 0$  against the  $H_1$  hypothesis that  $t > 0$ , where  $t > 0$  corresponds to the case of dependence on the number of member galaxies in clusters and  $t < 0$  to the case of dependence on redshift  $z$ . In order to reject the  $H_0$  hypothesis, the value of observed statistic  $t$  should be greater than  $t_{cr}$  which could

TABLE 1  
STATISTIC  $T = A/\sigma(A)$  FOR OUR SAMPLE OF ABELL CLUSTERS\*

Test Sample A	$S = f(N)$	$S = f(z)$	Test Sample B	$S = f(N)$	$S = f(z)$
$\chi^2$	1.872	-0.769	$\chi^2$	3.402	-2.342
$\Delta_1/\sigma(\Delta_1)$	1.613	0.611	$\Delta_1/\sigma(\Delta_1)$	2.857	-1.452
$\Delta/\sigma(\Delta)$	1.964	-0.066	$\Delta/\sigma(\Delta)$	3.142	-1.646
$C$	1.352	1.343	$C$	1.825	-1.305
$\lambda$	2.366	0.176	$\lambda$	2.333	-1.953

\*Sample A - 247 rich Abell clusters from PF catalogue (as in Stephanovich & Godłowski 2017). Sample B - full sample of 564 clusters (directly known redshift)

be obtained from the tables. For example, for sample of 247 clusters analyzed in Stephanovich & Godłowski (2017) (our sample A) at the significance level  $\alpha = 0.05$ , the value  $t_{cr} = 1.651$ . For our sample B (564 clusters) at the significance level  $\alpha = 0.05$ , the value  $t_{cr} = 1.648$ .

The results of our analysis are presented in Table 1 and Figures 2, 3. One could discern from the Table 1 that if the analysis of sample A confirms that the alignment increases with cluster richness, then any test confirms the negative deviation of the linear regression parameter from zero in the case of the alignment depending on redshift. However, both the above dependencies can be confirmed from the analysis of the full sample (564 clusters). At first we analyzed the statistic i.e. alignment, which increases significantly with the richness of a cluster, confirming the result obtained in Godłowski et al. (2010); Stephanovich & Godłowski (2017) as well as the theoretical prediction (Stephanovich & Godłowski 2015). The details are also presented in Figures 2(a) - 2(e). Moreover, we could conclude that the alignment decreases with  $z$ , which means that it increases with time as predicted by Stephanovich & Godłowski (2015, 2017); Schmitz et al. (2018) (see Figures 3a - 3e).

However, a closer look at the results shows that situation is not yet clear. This is because in the real data the cluster richness usually decreases also with redshift  $z$ . Quantitatively, in a linear model, the dependence between richness and redshift of a cluster is  $N(z) = az + b$ . In this model, we obtain the value of the  $t$  statistic  $t = -7.066$ . This is the reason why we repeated our analysis as a 3D model  $Y = a_1N + a_2z + b$ . Note that until now, such a 3D analysis has not been performed in galaxy alignment studies, but due to the above reason, we consider it to be necessary here. In this extended analysis, the test statistic  $t$  is given by formulae  $t_1 = a_1/\sigma(a_1)$  and  $t_2 = a_2/\sigma(a_2)$ . From Table 2, we could confirm that the alignment increases significantly with cluster richness. One should note that all our tests show that the statistic is decreasing with  $z$ . However, the values of  $t$  are too small to be statistically significant (significance level  $\alpha = 0.05$ ).

## 6. SIMULATIONS

The Illustris Project (2018) was the simulation base for our present study. The Project uses the AREPO code for the hydrodynamic realizations of a  $(106.5 \text{ Mpc})^3$  cosmological volume (Springel 2010). The simulation assumes a  $\Lambda$ CDM cosmology with  $\Omega_m = 0.2726$ ,  $\Omega_\Lambda = 0.7274$ ,  $\Omega_b = 0.0456$ ,  $\sigma_8 = 0.809$ ,  $n_s = 0.963$ , and  $H_0 = 100 \cdot h \cdot \text{km} \cdot \text{s}^{-1} \text{Mpc}^{-1}$  with  $h = 0.704$ . It contains multiple resolution runs with the highest resolution performed for Illustris - 1. Three different physical configurations have been applied: dark matter only, as well as non-radiative and full galaxy formation. In the first case (dark matter only), the mass was treated as collisionless in the simulations. The non-radiation configuration also adds gas hydrodynamics, but ignores radiative cooling and star formation processes. The full galaxy formation physics contains (in addition to the previously mentioned ones) also processes related to galaxy emergence, through a model described in Vogelsberger et al. (2013). Illustris-1 consists of 136 runs for different redshifts  $z$ , where the initial conditions were generated at  $z = 127$  for snapshot 0 and evolved to  $z = 0$  for snapshot 135.

Illustris successfully follows the coevolution of dark and visible matter. Haloes, subhaloes, and their basic properties have been identified with the FOF and SUBFIND algorithms (Davis et al. 1985; Springel et al. 2001; Dolag et al. 2009), at every one of the 136 stored snapshots. We have added information from the supplementary catalog to the resulting directory of Haloes from Zjupa & Springel (2017). The code was written in such a manner that it can run both as a postprocessing option to increase existing catalogues, or as part of the regular group finding.

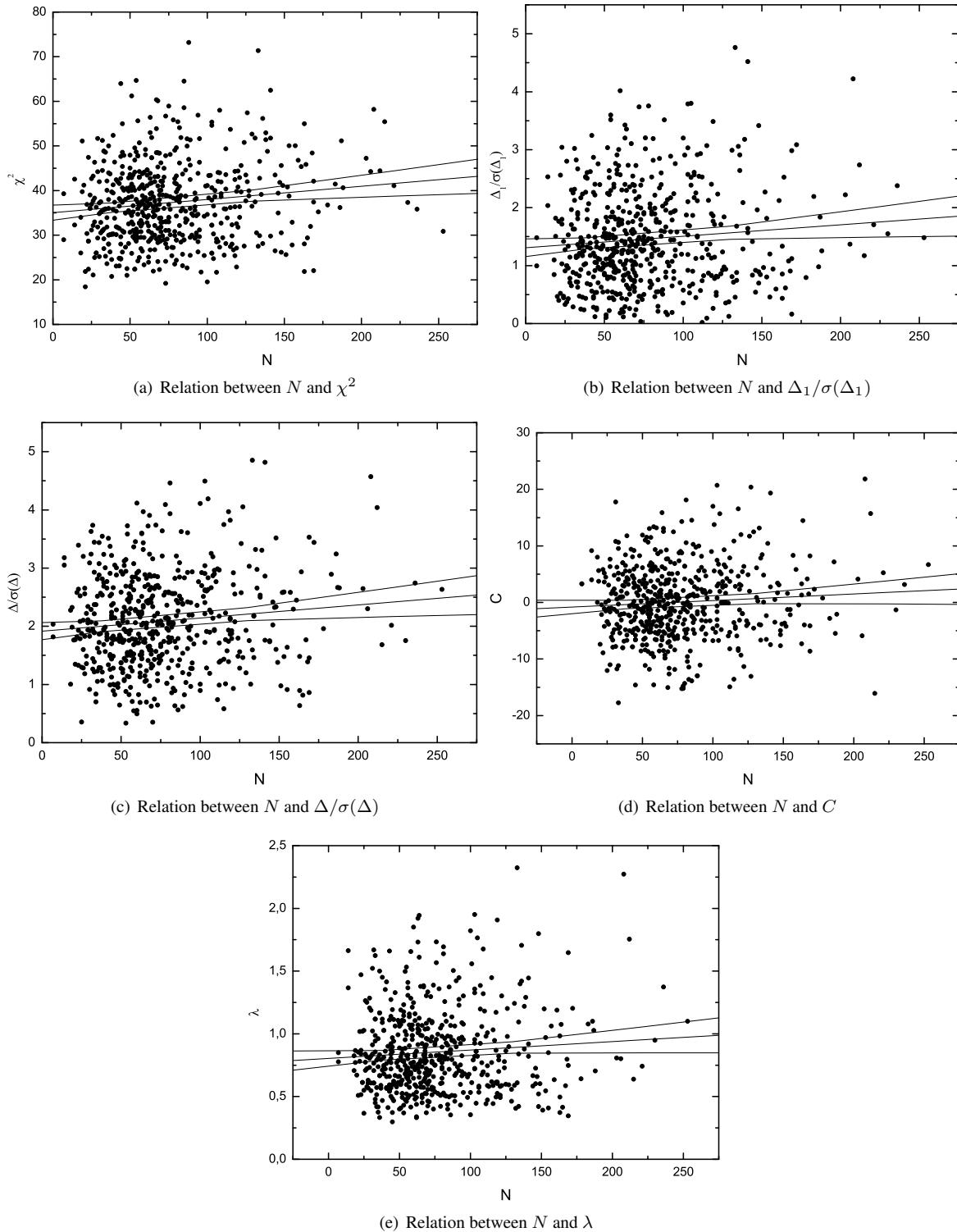


Fig. 2. The dependence of the number  $N$  of galaxies in a cluster on different statistical parameters of the Sample B. The error boundaries, at a confidence level 95%, are presented as well.

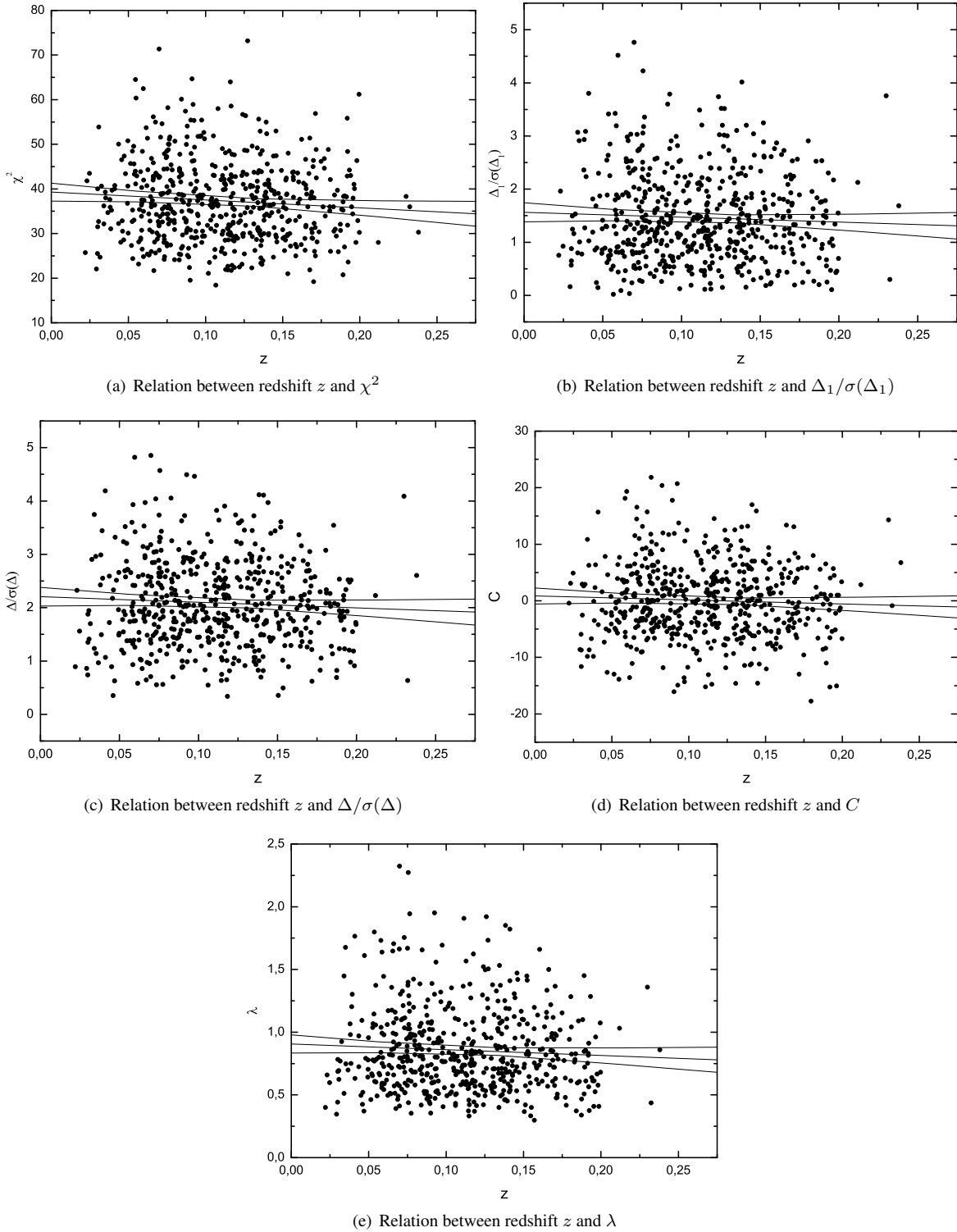


Fig. 3. The dependence of cluster redshift  $z$  on different statistical parameters of the Sample B. The error boundaries at a confidence level 95%, are presented as well.

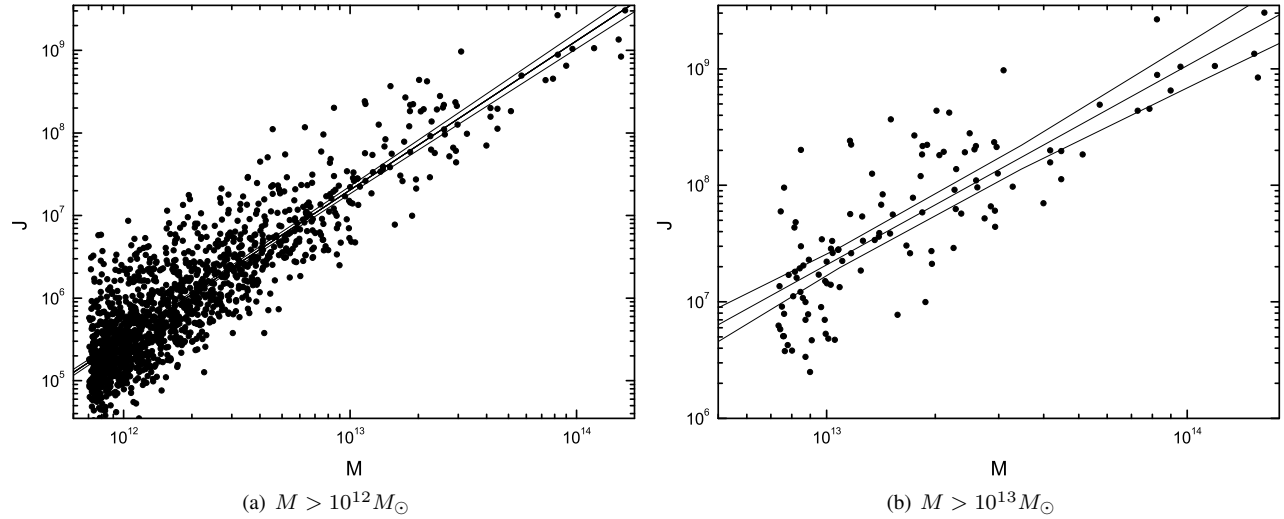


Fig. 4. Relation between angular momentum and mass of a cluster derived from the Illustris simulation for different total masses  $M$ . The error boundaries at a confidence level 95%, are presented as well.

TABLE 2

THE STATISTIC  $T = A/\sigma(A)$  FOR THE 3D ANALYSIS OF OUR SAMPLE\*

Test Sample $B$	$S = f(N)$	$S = f(z)$
$\chi^2$	2.846	-1.434
$\Delta_1/\sigma(\Delta_1)$	2.250	-0.718
$\Delta/\sigma(\Delta)$	2.625	-0.811
$C$	1.538	-0.814
$\lambda$	2.000	-1.302

\*Abell clusters. Sample B - full sample of 564 clusters (directly known redshift).

TABLE 3

RELATION BETWEEN ANGULAR MOMENTUM AND MASS\*

Mass	$a$	$\sigma(a)$	$t = a/\sigma(a)$
$> 10^{12}$	1.807	0.028	66.93
$> 10^{13}$	1.708	0.114	14.94

\*From Illustris simulations.

From Illustris-1 we selected haloes at  $z = 0$ . We obtained 119 haloes with total mass exceeding  $10^{13} M_{\odot}$  and 1435 with total mass larger than  $10^{12} M_{\odot}$ . The angular momentum parameter for the extracted haloes was taken from Zjupa & Springel (2017).

Illustris simulations give direct values of both the mass of the structures and their angular momentum. Present available data from Illustris are evolved to  $z = 0$ , so it is possible to study the dependence of angular momentum as a function of cluster mass, but unfortunately not of redshift. However, as we know directly the cluster angular momentum, it is not necessary to assume a linear relation between angular momentum and mass. Since theoretical modeling predicts usually power law relations (see also Stephanovich & Godłowski 2015 for review) we could study the model  $J = b \cdot M^a$ . The latter relation could easily be rendered as a linear model:  $\ln J = \ln b + a \ln M$ .

The results of the analysis are presented in Table 3 and Figure 4. The analysis of Illustris simulations confirms that the angular momentum of a cluster increases with its mass. In this case, the coefficient  $a = 1.807 \pm 0.028$  (Figure 4a). The analysis of a sample with only the most massive clusters (mass  $M > 10^{13}$  solar mass) left, gives  $a = 1.708 \pm 0.114$  (Figure 4b) which is close to the most popular theoretical prediction  $a = 5/3 \approx 1.667$  (see Godłowski et al. 2010; Stephanovich & Godłowski 2015, 2017 for details).

## 7. OUTLOOK

In the present paper we have shown that the distribution of mass of the stellar objects does not alter substantially the distribution function of their gravitational fields. This shows that the main contribution to the latter distribution function

comes from the long-range Newtonian interaction between astronomical objects, rather than from the distribution of their masses. At the same time, the mass distribution alters the dependence of  $L_{max}$  on the concentration of astronomical objects  $n$  (see equation 25) and on the total cluster mass  $M$  (see equation 26), which is observationally important. To discern which of the dependencies (25) or (26) is realized in practice, additional observational data are needed. As the total interaction potential contains both luminous and dark matter components, one can ask a question about the alignment of sub-dominant galaxies, even though the majority of the angular momenta of galaxy clusters is related to the smooth dark matter halo component. This question becomes important in view of the fact that the mass distribution (1) alters the dependence on total cluster mass  $M$  (26). In the halo model (Schneider & Bridle 2010) where the galaxies are embedded in a dark matter halo, the latter may mediate the intergalactic interaction, adding possible short-range terms to it. That is to say, to “see each other” in a dark matter halo, the galaxies should be closer than in an empty space.

Note that the observational results about a lack of alignment of galaxies for less clumpy (so called poor) clusters, as well as evidence for such an alignment in the clumpy (rich) ones (Godłowski, Szydlowski, & Flin 2005; Aryal et al. 2007; see also Godłowski 2011 for incremental study and relevant references) clearly show that the angular momentum of galaxy groups and clusters increases with their mass (richness). The generalized analysis, based on equation (4), where  $n = n(r, m)$  (i.e. the mass becomes spatially distributed), will improve the overall understanding, which can additionally be tested against observed galaxy shape distributions and alignments. The problem of angular momenta alignment due to their interactions, as well as those with dark matter haloes, has been simulated by Hahn et al. (2007). The main effect there is the presence of a threshold cluster mass (richness) value. The latter is related to the mutual alignment of clusters and dark matter haloes axes. This fact can be analyzed on the base of a more general model (4), which accounts for a spatially inhomogeneous distribution of the number density of stellar objects, as well as for its mass dependence. We postpone the consideration of this interesting question for future publications.

Our formalism permits studying this effect (see Stephanovich & Godłowski 2017) as well as the nonequilibrium time evolution of luminous astronomical objects (with respect to dark matter haloes) within the  $\Lambda$ CDM model. The combination of stochastic dynamical approaches (Garbaczewski & Stephanovich 2009, 2011) along with a deterministic one defined by the  $\Lambda$ CDM model, may permit to answer (at least qualitatively) the question about the initial alignment of galaxies and their clusters) at the time of their formation. The questions about how dark matter haloes influence (mediate) the latter alignment can also be answered within the above dynamical approach.

Our statistical analysis of the Abell cluster sample shows that the alignment of the angular momenta of galaxies and their clusters increases substantially with cluster mass. This result is confirmed also by 3D analysis, consisting in the study of the dependence of galaxy alignment in a cluster both on its richness and redshift. We have also found that the alignment decreases with redshift i.e. increases with time, but 3D studies show that this effect is too faint to be confirmed statistically at the significance level  $\alpha = 0.05$ . A probable reason is that the corresponding relaxation time is too long. So, for future investigations more extensive data containing larger numbers of galaxy clusters (and with higher redshifts) are required. The comparison of our theoretical results with those of the Illustris simulation also confirms the increase of the angular momenta of galaxies with cluster mass. Moreover, the latter comparison confirms the power law relation with a coefficient very close to  $5/3$ , which is the value favored by most popular theoretical predictions; see, for instance, Stephanovich & Godłowski (2015, 2017). This suggests that the approach of Stephanovich & Godłowski (2015, 2017) correctly reflects the main features of the formation of galaxies and their clusters.

Let us finally note that, as we have shown above, our results are in close conformity with the commonly preferred model of galaxy formation, i.e. the so-called hierarchic clustering model (Peebles 1969), improved recently by taking into account a tidal torque scenario.

## REFERENCES

- Abell, G. O., Corwin, H. G. Jr., & Olowin, R. P. 1989, *ApJS*, 70, 1
- Abramowitz, M. & Stegun, I. A. 1972, *Handbook of Mathematical Functions with Formulas, Graphs, and Mathematical Tables* (New York, NY: Dover)
- Aryal, B., Paudel, S., & Saurer, W. 2007, *MNRAS*, 379, 1011
- Bartolo, N., Komatsu, E., Matarrese, S., & Riotto, A. 2004, *PhR*, 402, 103
- Bett, P., Eke, V., Frenk, C. S., Jenkins, A., & Okamoto, T. 2010, *MNRAS*, 404, 1137
- Carter, D. & Metcalfe, N. 1980, *MNRAS*, 191, 325
- Catelan, P. & Theuns, T. 1996, *MNRAS*, 282, 436
- \_\_\_\_\_. 1996, *MNRAS*, 282, 455
- Chandrasekhar, S. 1943, *RvMP*, 15, 1
- Codis, S., Dubois, Y., Pichon, C., Devriendt, J., & Slyz, A. 2016, *The Zeldovich Universe: Genesis and Growth of the Cosmic Web*, *IAUS*, 308, 437
- Codis, S., Jindal, A., Chisari, N. E., et al. 2018 *MNRAS*, 481, 4753
- Davis, M., Efstathiou, G., Frenk, C. S., & White, S. D. M. 1985, *ApJ*, 292, 371

- Dekel, A. 1985, *ApJ*, 298, 461
- Dolag, K., Borgani, S., Murante, G., & Springel, V. 2009, *MNRAS*, 399, 497
- Doroshkevich, A. G. 1970, *Afz*, 6, 581
- \_\_\_\_\_. 1973, *ApL*, 14, 11
- Efstathiou, G. A. & Silk, J. 1983, *The Formation of Galaxies*, *FCPh*, 9, 1
- Flin, P. & Godłowski, W. 1986, *MNRAS*, 222, 525
- Garbaczewski, P. & Stephanovich, V. A., 2009, *PhRvE*, 80, 1113
- \_\_\_\_\_. 2011, *PhRvE*, 84, 1142
- Giahi-Saravani, A., & Schäfer, B. M. 2014, *MNRAS*, 437, 1847
- Godłowski, W., Szydłowski, M., & Flin, P. 2005, *ReGr*, 37, 615
- Godłowski, W., Piwowarska, P., Panko, E., & Flin, P. 2010, *ApJ*, 723, 985
- Godłowski, W. 2011, *JMPD*, 20, 1643
- \_\_\_\_\_. 2012, *ApJ*, 747, 7
- Hahn, O., Carollo, C. M., Porciani, C., & Dekel, A. 2007, *MNRAS*, 381, 41
- Hawley, D. L. & Peebles P. J. E. 1975, *AJ*, 80, 477
- Heavens, A., Refregier A., & Heymans, C. 2000, *MNRAS*, 319, 649
- Heymans, C., Brown, M., Heavens, A., et al. 2004, *MNRAS*, 347, 895
- Hwang, H. S. & Lee M. G. 2007, *ApJ*, 662, 236
- Illustris Project <http://www.illustris-project.org>
- Jarvis, J. F. & Tyson, J. A. 1981, *AJ*, 86, 476
- Joachimi, B., Cacciato, M., Kitching, T. D., et al. 2015, *SSSRv*, 193, 1
- Kiessling, A., Cacciato, M., Joachimi, B., et al. 2015, *SSSRv*, 193, 67
- Kimm, T., Devriendt, J., Slyz, A., et al. 2011, *arXiv:1106.0538*
- Kravtsov, A. V. & Borgani, S. 2012, *ARA&A*, 50, 353
- Lee, J. & Pen, U. 2000, *ApJ*, 532, 5
- \_\_\_\_\_. 2001, *ApJ*, 555, 106
- \_\_\_\_\_. 2002, *ApJ*, 567, 111
- Li, Li-Xin. 1998, *GReGr*, 30, 497
- Longair, M. S. 2008, *Galaxy Formation*, (Berlin: Springer)
- Navarro, J. F., Abadi, M. G., & Steinmetz, M. 2004, *ApJ*, 613, 41
- Öepik, E. J. 1970, *IrAJ*, 9, 211
- Okabe, T., Nishimichi, T., Oguri, M., et al. 2018, *MNRAS*, 478, 1141
- Pajowska, P., Godłowski, W., Zhu, Z. H., et al. 2019, *JPAC*, 02, 005
- Panko, E. & Flin, P. 2006, *JAD*, 12, 1
- Paz, D. J., Stasyszyn, F., & Padilla, N. D. 2008, *MNRAS*, 389, 1127
- Paz, D. J., Sgró, M. A., Merchan, M., & Padill, N. 2011, *MNRAS*, 414, 2029
- Peebles, P. J. E. 1969, *ApJ*, 155, 393
- Peebles, P. J. E. & Yu, J. T. 1970, *ApJ*, 162, 815
- Pereira, M. J., Bryan, G. L., & Gill, S. P. D. 2008, *ApJ*, 672, 825
- Press, W. H. & Shechter, P. 1974, *ApJ*, 187, 425
- Romanowsky, A. J. & Fall, S. M. 2012, *ApJS*, 203, 17
- Schäfer, B. M. 2009, *IJMPD*, 18, 173
- Schäfer, B. M. & Merkel, P. M. 2012, *MNRAS*, 421, 2751
- Schmitz, D. M., Hirata, C. M., Blazek, J., & Krause, E. 2018, *JCAP*, 07, 030
- Schneider, M. D. & Bridle, S. 2010, *MNRAS*, 402, 2127
- Shandarin, S. F. 1974, *SvA*, 18, 392
- Shandarin, S. F. & Zeldovich, Y. B. 1989, *RvMP*, 61, 185
- Shandarin, S. F., Habib, S., & Heitmann, K. 2012, *PhRvD*, 85, 3005
- Shechter, P. 1976, *ApJ*, 203, 297
- Silk, J. 1968, *ApJ*, 151, 459
- Springel, V., White, S. D. M., Tormen, G., & Kauffmann, G., 2001, *MNRAS*, 328, 726
- Springel, V. 2010, *MNRAS*, 401, 791
- Stephanovich, V. A. & Godłowski, W. 2015, *ApJ*, 810, 167
- \_\_\_\_\_. 2017, *RAA*, 17, 119
- Struble, M. F. & Rood, H. J. 1999, *ApJS*, 125, 35
- Sunyaev, R. A. & Zeldovich, Y. B. 1970, *Ap&SS*, 7, 3
- \_\_\_\_\_. 1972, *A&A*, 20, 189
- Tovmassian, H. M. 2015, *Ap*, 58, 471
- Trujillo, I., Carretero C., & Patri, G. 2006, *ApJ*, 640, 111
- Varela, J., Betancort-Rijo, J., Trujillo, I., & Ricciardelli, E. 2012, *ApJ*, 744, 82
- Vogelsberger, M., Genel, S., Sijacki, D., et al. 2013, *MNRAS*, 436, 3031
- Wang, J., Tsang, W. W., & Marsaglia, G. 2003, *J. of Statistical Software*, 8 (18), 1
- Zhang, Y., Yang, X., Wang, H., et al. 2013, *ApJ*, 779, 160
- Zeldovich, Y. B. 1970, *A&A*, 5, 84
- Zjupa, J. & Springel, V. 2017, *MNRAS*, 466, 1625

## INFRARED TRANSITIONS OF DIATOMIC MOLECULES AND THE TELLURIC LINES

Daniel Lozano-Gómez<sup>1</sup>, Alejandro García-Varela<sup>2</sup>, and Beatriz Sabogal<sup>2</sup>

Received September 19 2019; accepted May 13 2020

### ABSTRACT

We present a simple model, as a pedagogical exercise, in order to obtain infrared transition energies for heteronuclear diatomic molecules, based on rotational and vibrational Hamiltonians. Our calculations allow us to identify CO absorption lines that are present in the atmosphere spectra acquired in astronomical observatories.

### RESUMEN

Presentamos un modelo sencillo, a manera de ejercicio pedagógico, con el fin de obtener las energías de transición en infrarrojo de moléculas heteronucleares, basados en Hamiltonianos de rotación y vibración. Nuestros cálculos permiten identificar líneas de absorción de CO presentes en los espectros de la atmósfera, adquiridos en observatorios astronómicos.

*Key Words:* line: identification — methods: analytical — molecular data

### 1. INTRODUCTION

Infrared (IR) spectroscopy is a useful tool in studying systems at temperatures around  $10^2$  K. Objects at these temperatures such as protoplanetary, accretion, and protostellar disks, significantly radiate in this region of the electromagnetic spectrum. Commonly, IR studies are conducted in ground-based observatories; thus, the observed spectrum presents lines of both the astronomical source and the terrestrial atmosphere. Therefore, including the atmospheric absorption is a crucial step towards any study involving IR astronomical spectra in order to avoid misidentifications with the atmospheric absorption lines. This implies dealing with the atmosphere, which is made up of a large quantity of gas molecules at temperatures of the same order as those of the observed sources.

The Earth's atmosphere is mostly composed of  $N_2$  (78.09 %) and  $O_2$  (20.95 %), both accounting for almost 99% of the average composition of the dry atmosphere (Cox 2000). These homonuclear<sup>3</sup> diatomic molecules are inactive in the IR because of their null electric dipole moment. In fact, ac-

ording to Gross selection rules (Atkins & de Paula 2014), fundamental vibrational transitions are forbidden for these molecules and no IR contribution is observed. On the other hand, atmospheric heteronuclear molecules such as CO,  $CO_2$  and  $H_2O$ , are some of the ones responsible for the major features of the IR absorption atmospheric spectrum, due to rotational and vibrational transitions.

The spectrum theory of diatomic molecules is presented in detail in classical books (Kronig 1930; Herzberg 1950) and also in physical chemistry texts (Atkins & de Paula 2014). As the atmosphere is composed of diatomic and polyatomic gases, aerosols, dust, pollutants and other constituents, studying its spectrum is a complex task. The variable concentration of CO and  $CO_2$  due to its major sources: anthropogenic, biological, oceanic, combustion, photochemical, and the strongly variable concentration of the water vapor due to atmospheric and oceanic conditions, cause the IR spectrum of the terrestrial atmosphere, called the *telluric*<sup>4</sup> spectrum, to change in time scales of seconds and up to months. Currently, simulating the atmospheric molecular transitions requires the development of complex algorithms<sup>5</sup> which consider

<sup>1</sup>Department of Physics and Astronomy, University of Waterloo, Canada.

<sup>2</sup>Universidad de los Andes, Departamento de Física, Colombia.

<sup>3</sup>A molecule composed of only one type of chemical element.

<sup>4</sup>In latin *tellus* mean "Earth".

<sup>5</sup>In this regard, HITRAN is one of the databases with greater use. <https://hitran.org/>.

the different quantum interactions present in these molecules (Rudolf et al. 2016; Ulmer-Moll et al. 2019, and references therein).

The aim of the present work is to obtain, as a pedagogical exercise, analytical expressions for the IR transition energies of heteronuclear atmospheric molecules using undergraduate quantum mechanics, and to show that these transitions produce bands in the IR spectra. The organization of this study is as follows: in § 2 we present the Hamiltonians that describe the simplest approximation to the vibrational and rotational transitions of molecules. In § 3 we compute vibration and rotation transitions, using a more realistic Hamiltonian through a Morse potential. In § 4 we present our results, showing that CO IR transitions form bands. Finally, in the last section we give the main conclusions of this work.

## 2. MODELING VIBRATION AND ROTATION OF DIATOMIC MOLECULES

To describe the energy spectrum of a diatomic molecule the vibrational and rotational degrees of freedom are considered. Studies of degrees of freedom considering complex models are discussed by Stuart (2004). In this section, we present the vibrational and rotational Hamiltonians for a system without and with an interaction term between each degree of freedom.

### 2.1. Vibrational Hamiltonian

A diatomic gas molecule has a spectrum originated in part by the vibrational motion. Because these vibrations are not completely harmonic, there must be introduced correction terms that account for the non-harmonic behavior of the molecule. As a first approximation, one can add to the potential an extra term proportional to  $\hat{x}^3$ . This procedure is similar to taking a smooth potential and performing a Taylor expansion around its minimum value, as made frequently in the quantum mechanics text books (see for example Cohen-Tannoudji et al. 1977). This correction is known as the anharmonic oscillator potential. Following this approximation, the vibrational Hamiltonian can be written as:

$$\hat{H}_{vib} = \frac{\hat{p}^2}{2\mu} + \frac{1}{2}\mu\omega^2\hat{x}^2 + \frac{1}{2}G_1\mu\omega^2\hat{x}^3 + \dots, \quad (1)$$

where  $\mu$  is the reduced mass of the system,  $\omega$  is the oscillation frequency and  $G_1$  is a *small* parameter

related to the first correction of the potential. Higher order correction terms are described by the factors  $G_{i>1}$ .

Remembering the results for the regular quantum harmonic oscillator, we use the creation  $\hat{a}$ , annihilation  $\hat{a}^\dagger$  and number  $\hat{N} = \hat{a}^\dagger\hat{a}$  operators, with their usual commutation relations. The canonical definition of this operators is given by the following relations:

$$\hat{a} = \sqrt{\frac{\mu\omega}{2\hbar}} \left( \hat{x} + \frac{i}{\mu\omega}\hat{p} \right), \quad \hat{a}^\dagger = \sqrt{\frac{\mu\omega}{2\hbar}} \left( \hat{x} - \frac{i}{\mu\omega}\hat{p} \right),$$

$$\hat{x} = \sqrt{\frac{\hbar}{2\mu\omega}} \left( \hat{a} + \hat{a}^\dagger \right).$$

For the anharmonic Hamiltonian, the term corresponding to  $\hat{x}^3$  can be computed:

$$\begin{aligned} (\hat{a} + \hat{a}^\dagger)^3 &= (\hat{a} + \hat{a}^\dagger)(\hat{a}^2 + (\hat{a}^\dagger)^2 + 1 + 2\hat{N}) \\ &= \hat{a}^3 + (\hat{a}^\dagger)^3 + \hat{a} + 2\hat{a}^\dagger + (\hat{a} + \hat{a}^\dagger)(2\hat{N}) \\ &\quad + \hat{N}(\hat{a} + \hat{a}^\dagger). \end{aligned}$$

Hence, the cubic term given by equation (1) can be rewritten in the following way:

$$\begin{aligned} \frac{1}{2}G_1\mu\omega^2\hat{x}^3 &= \left[ \frac{1}{2}G_1\mu\omega^2 \left( \frac{\hbar}{2\mu\omega} \right)^{3/2} \right] \left( \hat{a}^3 + (\hat{a}^\dagger)^3 + \hat{a} \right. \\ &\quad \left. + 2\hat{a}^\dagger + (\hat{a} + \hat{a}^\dagger)(2\hat{N}) + \hat{N}(\hat{a} + \hat{a}^\dagger) \right). \end{aligned}$$

To continue, the action of the correction term over  $|n\rangle$  is obtained:

$$\begin{aligned} \hat{x}^3 |n\rangle &\propto \sqrt{n(n-1)(n-2)} |n-3\rangle \\ &\quad + \sqrt{(n+1)(n+2)(n+3)} |n+3\rangle \\ &\quad + (\sqrt{n} + 2n\sqrt{n} + (n-1)\sqrt{n}) |n-1\rangle \\ &\quad + (2\sqrt{n+1} + 2n\sqrt{n+1} + (n+1)\sqrt{n+1}) |n+1\rangle. \end{aligned}$$

Given the small size of the correction  $G_1$  term, perturbation theory can be applied. Notice that this Hamiltonian does not present a first order correction to its energy levels. We invite the readers to calculate the second order perturbation theory correction (see Cohen-Tannoudji et al. 1977) to find the following results for the energy:

$$\begin{aligned} E &\propto \frac{n(n-1)(n-2)}{3\hbar\omega} - \frac{(n+1)(n+2)(n+3)}{3\hbar\omega} \\ &\quad + \frac{9n^3}{\hbar\omega(n-n+1)} + \frac{9(n+1)^3}{\hbar\omega(n-n-1)}, \\ E &\propto -\left[ \frac{1}{\hbar\omega} \right] \left( 30n^2 + 30n + 11 \right). \end{aligned} \quad (2)$$

Plugging back these correction terms into the corrected energy term, a new energy spectrum is found.

$$\hat{H}_{vib} | n \rangle = \hbar\omega \left( n + \frac{1}{2} \right) | n \rangle - \left[ \frac{1}{\hbar\omega} \right] \left( \frac{1}{2} G_1 \mu \omega^2 \left( \frac{\hbar}{2\mu\omega} \right)^{3/2} \right)^2 \left( 30n^2 + 30n + 11 \right) | n \rangle. \quad (3)$$

This Hamiltonian describes the degrees of freedom corresponding to the vibrational nature of molecules.

### 2.2. Rotational Hamiltonian

When a molecule rotates, the centrifugal force pulls the atoms apart causing an increase in its moment of inertia and decreasing the rotational constant associated to this energy term. This effect couples both types of interactions, vibration and rotation. In order to understand this interaction, the following analogy can be useful: a pair of masses (atoms of a diatomic molecule) are attached at the ends of a spring, so that the masses can vibrate along the line between them. The spring is fixed at some point to the center of a rotating disk. The system has no friction. Due to rotation, the Coriolis force deflects the masses, changing the vibration frequency of the spring, reflecting an interaction between rotation and vibration in this mechanical system. This is analogous to the interaction between rotation and vibration in diatomic molecules.

Returning to the effect of the centrifugal force on the coupling of the rotation and vibration interactions and, therefore, on the rotational Hamiltonian, a term named centrifugal diatomic distortion is defined as

$$D = \frac{4}{\omega^2} \left( \frac{B}{\hbar c} \right)^3, \quad \text{with } B = \frac{\hbar^2}{2\mu r^2}.$$

The  $r$  variable describes the inter-nuclear distance between the atoms composing the molecule. The rotational Hamiltonian is now the following:

$$\hat{H}_{rot} = \frac{1}{2I} \hat{L}^2 + D \hat{L}^4, \quad (4)$$

where  $\hat{L}$  is the angular momentum operator ( $\hat{L} = \hat{r} \times \hat{p}$ ) and  $I$  is the moment of inertia. The corrected Hamiltonian in equation (4) shares the same eigenstates  $| l, m \rangle$  that are used in the rotational uncorrected Hamiltonian, where  $D = 0$ . Thus the action of the Hamiltonian over these eigenstates produces:

$$\hat{H}_{rot} | l, m \rangle = Bl(l+1) | l, m \rangle + l^2(l+1)^2 D | l, m \rangle. \quad (5)$$

## 3. HAMILTONIANS FOR DIATOMIC MOLECULES

### 3.1. Model 1: Combined Hamiltonian

Before using the vibration and rotation Hamiltonians given by equations (1) and (4), it is necessary to find an appropriate basis which diagonalizes the Hamiltonians in the corresponding Hilbert space. If these Hamiltonians are defined as  $\hat{H}_{rot}(L_i)$  and  $\hat{H}_{vib}(p_i, x_i)$ , we can ensure the commutation relation  $[\hat{H}_{rot}, \hat{H}_{vib}] = 0$ . Hence we can simply add both terms and describe the total eigenvectors as a tensor product  $| n, l \rangle = | n \rangle \otimes | l \rangle$ . The quantum number  $m$  has been left out since the total Hamiltonian does not present a dependency on it. The energy of such a system is given by:

$$\begin{aligned} \hat{H}_{total} | n, l \rangle &= \left( \hat{H}_{rot} + \hat{H}_{vib} \right) | n, l \rangle \\ &= \left[ \hbar\omega \left( n + \frac{1}{2} \right) - \frac{G_1^2 \hbar^2}{32\mu} (30n^2 + 30n + 11) \right. \\ &\quad \left. + Bl(l+1) + l^2(l+1)^2 D \right] | n, l \rangle. \end{aligned} \quad (6)$$

This description supposes that the movement of the rotation and the vibration are described in the same coordinates where the Hamiltonians commute. If the vibrations were considered along a different direction, these would affect the separation radius of the molecule, changing the moment of inertia of the system. These corrections cannot be ignored and correction terms must be added. This coupling is studied in the following section.

By taking into account both interaction terms, rotation and vibration, a net Hamiltonian can be studied. This Hamiltonian is fully described by the quantum numbers  $n$  and  $l$ . This fact is a consequence of the commutation relation  $[\hat{H}_{rot}, \hat{H}_{vib}] = 0$ , which states that a common basis describes the eigenstates of both terms. Through this identification, the energy levels are found to be:

$$\begin{aligned} E_{n,l} &= \hbar\omega \left( n + \frac{1}{2} \right) - \frac{G_1^2 \hbar^2}{32\mu} (30n^2 + 30n + 11) \\ &\quad + Bl(l+1) + l^2(l+1)^2 D. \end{aligned} \quad (7)$$

Tables 1 and 2 give the vibrational and rotational transitions for an initial state  $| n, l \rangle$ . The energy transitions displayed above only show a change of state in a single Hamiltonian (vibrational or rotational). All the other transitions are described by the

TABLE 1  
ALLOWED TRANSITIONS FOR VIBRATIONAL  
HAMILTONIAN

$\Delta n$ ( $\Delta l = 0$ )	$\Delta E = E_f - E_i$
$\Delta n = -2$	$-2\hbar\omega + (G_1^2\hbar^2/32\mu)(-120n + 60)$
$\Delta n = -1$	$-\hbar\omega + (G_1^2\hbar^2/32\mu)(60n)$
$\Delta n = +1$	$+\hbar\omega - (G_1^2\hbar^2/32\mu)(60n + 60)$
$\Delta n = +2$	$+2\hbar\omega + (G_1^2\hbar^2/32\mu)(120n + 180)$

combination of transitions between both quantum numbers given by the selection rules  $\Delta n = \pm 1, \pm 2$  and  $\Delta l = \pm 1, \pm 2$ .

Notice that each initial state  $|n, l\rangle$  has 24 possible final states given the corrections proposed by this model. It is worth mentioning that this correction is very restrictive as the rotation is fully confined to one direction. Moreover, the energy constant associated with this rotational degree of freedom is greater than that found in any other direction.

### 3.2. Model 2: Morse Potential

The Morse potential is commonly used to describe the vibrational behavior of diatomic molecules. Its asymptotic behavior, given by the maximum energy of vibrations (the dissociation energy,  $D_E$ , related to the depth of the potential well) more accurately describes the physics of diatomic molecules than the quantum harmonic oscillator.

$$V(\mathbf{r}) = D_E \left(1 - e^{-a(r-r_0)}\right)^2. \quad (8)$$

In the above expression,  $r_0$  is the equilibrium bond distance and  $a$  is a constant related to the strength of the bond. By using this expression, the Schrödinger equation can be perturbatively solved obtaining the following  $n$ -dependent energy spectrum

$$E_n = \hbar\omega \left(n + \frac{1}{2}\right) - \frac{\hbar^2\omega^2}{4D_E} \left(n + \frac{1}{2}\right)^2. \quad (9)$$

### 3.3. Rotation-Vibration Interaction

In § 3.1 we have described the energy spectrum of a diatomic molecule when both vibrations and rotations are present in the system. In such a way, the Hamiltonian can be split into two non-interacting terms, which share a common basis. However, this

is not the general case as vibrations can affect the way the rotational spectrum is defined. This effect can be understood by considering the moment of inertia of a single molecule: given the vibration of the molecule, the length of the bond separating the molecules will change. Therefore, in order to introduce the radial separation ( $r$ ), the constants  $B$  and  $D$  appearing in the rotational Hamiltonian are now considered as functions of this variable:

$$B(r) = \frac{\hbar}{4\pi c\mu r^2}, \quad (10)$$

$$D(r) = \frac{\hbar^3}{4\pi c k \mu^2 r^6}. \quad (11)$$

Under the assumption that the vibration frequency is much greater than the rotational frequency, the average separation radius can be computed, and the effective separation can be described. To compute this effective separation, we consider the average radius in the wave function describing the oscillatory movement:

$$\langle r \rangle = \int \psi_{vib}^\dagger r \psi_{vib} dr. \quad (12)$$

Following the same procedure, the quantities  $B(r)$  and  $D(r)$  are defined through their mean values in a full period of oscillation:

$$\begin{aligned} \left\langle \frac{1}{r^2} \right\rangle &= \int \psi_{vib}^\dagger \frac{1}{r^2} \psi_{vib} dr, \\ \left\langle \frac{1}{r^6} \right\rangle &= \int \psi_{vib}^\dagger \frac{1}{r^6} \psi_{vib} dr. \end{aligned}$$

Through this approximation, one obtains the following new constants related to the unperturbed terms,  $B_e$  and  $D_e$ , presented in § 2.2 for the rotational Hamiltonian:

$$\begin{aligned} B_n &= \langle B(r) \rangle = B_e - \alpha_e \left(n + \frac{1}{2}\right), \\ D_n(r) &= \langle D(r) \rangle = D_e - \beta_e \left(n + \frac{1}{2}\right), \end{aligned} \quad (13)$$

where the subindex  $e$  refers to the constants given in the equation (4). The new constants,  $\alpha_e$  and  $\beta_e$ , are the ones which introduce the interaction of these two Hamiltonians. These values have been reported by Le Floch (1991).

### 3.4. Rotational and Vibrational Hamiltonian with Morse Potential

To better describe the energy spectrum of a diatomic molecule, we should use a total Hamiltonian that includes a term related to the Morse potential (given in

TABLE 2  
ALLOWED TRANSITIONS FOR ROTATIONAL HAMILTONIAN

$\Delta n, \Delta l$	$\Delta E = E_f - E_i$
$\Delta n = 0, \Delta l = -2$	$B(-4l + 2) + D(-10l^3 + 11l^2 - 12l + 4)$
$\Delta n = 0, \Delta l = -1$	$-2Bl - 4Dl^3$
$\Delta n = 0, \Delta l = +1$	$B(2l + 2) + D(4l^3 + 12l^2 + 12l + 4)$
$\Delta n = 0, \Delta l = +2$	$B(4l + 6) + D(12l^3 + 47l^2 + 72l + 36)$

equation 8) and other term related to the rotational and vibrational coupling (involving the expressions given in equation 13). Obtaining this total Hamiltonian,  $\hat{H}_{total} = \hat{H}_{morse} + \hat{H}_{rot}$  is left as an exercise for the reader, as well as the equation for energy in terms of the quantum numbers  $n$  and  $l$ :

$$E_{n,l} = \hbar\omega \left( n + \frac{1}{2} \right) - \frac{\hbar^2\omega^2}{4D_E} \left( n + \frac{1}{2} \right)^2 + B_n l(l+1) + D_n l^2(l+1)^2, \quad (14)$$

where the first two terms are the given by equation (9) and the last two terms are the rotational-vibrational energy discussed in § 3.3. Reordering terms, we obtain:

$$E_{n,l} = \left[ \hbar\omega \left( n + \frac{1}{2} \right) + B_e l(l+1) \right] - \left[ \hbar^2\omega_\chi \left( n + \frac{1}{2} \right)^2 + D_e l^2(l+1)^2 \right] - \left( n + \frac{1}{2} \right) (\alpha_e l(l+1) + \beta_e l^2(l+1)^2), \quad (15)$$

where  $\omega_\chi = \omega^2(4D_E)^{-1}$ . In the expression above, the first term corresponds to the energies of the harmonic oscillator and rigid rotor, the second one reflects corrections to the energy given by anharmonicity and centrifugal distortion, and the last term corresponds to rotation-vibration interaction.

As an exercise, we propose that readers work on some of the following ideas that could improve the presented models:

- Include higher order correction terms in the anharmonic oscillator. (These corrections make possible several other transitions given by the selection rules).

- Include higher order corrections in the rotational Hamiltonian, which would have the same effect as the corrections of the anharmonic oscillator.

- Include molecular interactions, which would take place in a diatomic gas.

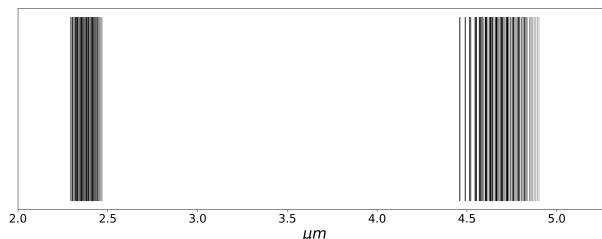


Fig. 1. Computed IR spectrum of the CO molecule. Fundamental and first overtone transitions are present around  $2.35\mu m$  and  $4.67\mu m$ , respectively. Bands are clearly appreciated.

#### 4. DISCUSSION

In the previous section we presented a model considering rotational and vibrational Hamiltonians with a Morse potential as a first approximation for diatomic molecules without molecular interactions. Using equation (14) with the transition values  $\Delta n$  and  $\Delta l$  of  $0, \pm 1, \pm 2$ , we obtained the wavelengths corresponding to IR transitions. Our calculations, in spite of not having the amplitude of probability for every transition, expose the complexity of the IR spectrum. We have used equation (14) rather than equation (7) since this model does not include the mixed energy terms.

We apply the results found to the CO molecule, as shown in Figure 1. Molecular constants for the CO were taken from Le Floch (1991) and are reported in Table 3. Experimental measurements of these constants using a near-IR spectrophotometer were presented by Mina-Camilde et al. (1996).

The CO spectrum shown in Figure 1 illustrates that IR transitions form bands. Our model illustrates how complex it is to obtain the infrared spectrum of heteronuclear diatomic molecules: every transition will depend on the initial state of vibration and rotation, i.e., both quantum numbers  $n$  and  $l$ . Note that the parameters used in the Hamiltonians depend on the moment of inertia, mass and internuclear distance and on the existence of mixed terms in the energy given by equation (15).

TABLE 3  
MOLECULAR CONSTANTS FOR CO

$B_e \times 10^1$ (cm <sup>-1</sup> )	$D_e \times 10^{-5}$ (cm <sup>-1</sup> )	$\alpha_e \times 10^{-1}$ (cm <sup>-1</sup> )
0.193128081434	0.6121593342	0.1750399404
$\beta_e \times 10^{-9}$ (cm <sup>-1</sup> )	$\omega$ (cm <sup>-1</sup> )	$\omega\chi$ (cm <sup>-1</sup> )
-0.9316227	2169.81259421	13.287834373

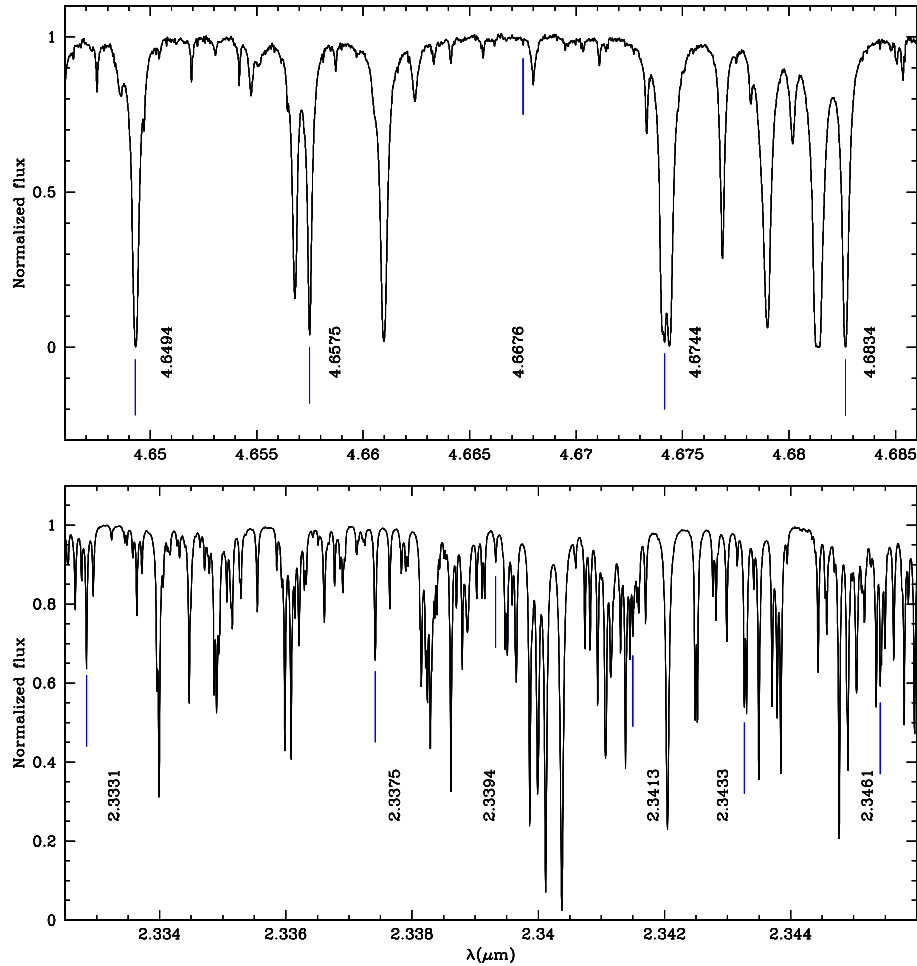


Fig. 2. Line identification.  $K_S$ - and  $M$ -band telluric spectra (black) are shown in the bottom and upper panels, respectively. In both panels we show the CO absorption lines identified with our computed wavelengths (blue). Fundamental mode transitions occur in the  $K_S$ -band. First overtone transitions are present in the  $M$ -band. The color figure can be viewed online.

We compare our theoretical CO IR wavelengths with those of the high resolution ( $R = 40000$ ) telluric spectrum<sup>6</sup> created from data made available by

<sup>6</sup>These NSO/Kitt Peak FTS IR telluric spectra produced by NSF/NOAO are available at [https://www.eso.org/sci/facilities/paranal/decommissioned/isaac/tools/spectroscopic\\_standards.html](https://www.eso.org/sci/facilities/paranal/decommissioned/isaac/tools/spectroscopic_standards.html).

the NSO/Kitt Peak Observatory, in the  $K_S$ - and  $M$ -bands.

Although the atmosphere spectrum presents multiple absorption lines of CO, CO<sub>2</sub> and H<sub>2</sub>O, we have identified several CO lines in the observed telluric spectrum using our computed CO lines as the reference spectrum. This identification was produced

by means of the IRAF<sup>7</sup> task *identify* of the package onedspec (devoted to reduction and calibration of spectra) reaching an average precision of 0.003 per cent with respect to our theoretical wavelengths. We also made a linear regression between our wavelengths and those identified in the telluric spectrum. The slope of the regression is equal to one, the intercept is zero (with a precision of  $10^{-7}$ ) and the  $R^2$  coefficient is one (with a precision of  $10^{-11}$ ). This linear regression shows that our computed CO wavelengths agree with those identified in the telluric spectrum.

Figure 2 illustrates the  $K_S-$  and  $M-$  bands IR telluric spectra, where CO absorption lines are clearly identified with our computed lines. In these regions the absorption features present in the atmosphere are caused by water vapour, carbon dioxide and greenhouse gases.

## 5. CONCLUSIONS

In order to analyse the IR spectra of astronomical sources it is important to identify the telluric features that are produced by the terrestrial atmosphere. In this work we present a quantum mechanics model, useful to obtain analytical expressions for the transition energies of heteronuclear atmospheric molecules. The Hamiltonian used includes the rotation and vibration of diatomic molecules, as well as the interactions between them. We showed that it is possible, with this model, to identify transitions of CO molecule that are present in the  $K_S-$  and  $M-$  bands.

We thank the anonymous referee for valuable corrections and comments, which have enriched this article. We also thank Javier Acevedo for help with the Python graphs and Dr. Neelima Kelkar, for comments. Both are members of the Physics Department of the Universidad de los Andes. AGV and BS also acknowledge financial support to this work by Fondo de Investigaciones de la Facultad de Ciencias de la Universidad de los Andes, Colombia, through Programa de Investigación INV-2019-84-1815 and INV-2019-84-1857. Finally, we thank NSF/NOAO for the NSO/Kitt Peak FTS IR telluric data used here.

## REFERENCES

- Atkins, P. & de Paula, J. 2014, Physical chemistry, (OUP)
- Cohen-Tannoudji, C., Diu, B., & Laloë, F. 1977, Quantum mechanics, Vols 1 & 2, (New York, NY: John Wiley & Sons)
- Cox, A. 2000, Allen's Astrophysical Quantities, (New York, NY: Springer-Verlag)
- Herzberg, G. 1950, Spectra of Diatomic Molecules, (New York, NY: D. van Nostrand Co.)
- Kronig, R. 1930, Band Spectra and Molecular Structure, (Cambridge, MA: CUP)
- Le Floch, A. 1991, A&AS, 90, 513
- Mina-Camilde, N., Manzanares, C., & Caballero, J. 1996, JChEd, 73, 804
- Rudolf, N., Günther, H., Schneider, P., & Schmitt, J. 2016, A&A, 585, 113
- Stuart, B. 2004, Infrared Spectroscopy: Fundamentals and Applications, (New York, NY: John Wiley & Sons Ltd.)
- Ulmer-Moll, S., Figueira, P., Neal, J. J., Santos, N. C. & Bonnefoy, M. 2019, A&A, 621, 79

Alejandro García-Varela and Beatriz Sabogal: Universidad de los Andes, Departamento de Física, Cra. 1 No. 18A-10, Bloque Ip, A.A. 4976 Bogotá, Colombia (josegarc, bsabogal@uniandes.edu.co).

Daniel Lozano-Gómez: Department of Physics and Astronomy, University of Waterloo, Ontario, N2L 3G1, Canada (dlozanog@uwaterloo.ca).

<sup>7</sup>IRAF is a software that was distributed by the National Optical Astronomy Observatories.

## FIRST PHOTOMETRIC INVESTIGATION OF TWO ECLIPSING BINARY SYSTEMS CRTS J213033.6+213159 AND 1SWASP J212454.61+203030.8

Massimiliano Martignoni<sup>1</sup>, Carlo Barani<sup>1</sup>, Francesco Acerbi<sup>1</sup>, and Raúl Michel<sup>2</sup>

*Received May 1 2020; accepted June 1 2020*

### ABSTRACT

The multicolour CCD light curves of the eclipsing binary systems CRTS J213033.6+213159 and 1SWASP J212454.61+203030.8 are presented for the first time, the observations are analyzed using the latest version of the Wilson-Devinney code. Both the systems are found to be W UMa contact binaries belonging to two different subtypes. All the light curves show the inverse O’Connell effect. By using our 2 times of minimum light for both the systems and the 187 and 105 ToMs extract from the SWASP observations, respectively for CRTS J213033.6+213159 and for 1SWASP J212454.61+203030.8, the orbital periods are here revised. The spectral type K of the systems and their short orbital periods ( $<0.3$  days), suggests that they are near the shortest period limit. The absolute dimensions are estimated and, from statistical diagrams, it is found that both components of the systems follow the general pattern of the relative subtype of W Ursae Majoris systems.

### RESUMEN

Se presentan las primeras curvas de luz multicolor de las binarias eclipsantes CRTS J213033.6+213159 y 1SWASP J212454.61+203030.8, analizadas con la última versión del código Wilson-Devinney. Se encuentra que ambos sistemas son binarias en contacto tipo W UMa pero de diferente subtipo. Todas las curvas de luz presentan el efecto O’Connell inverso. Con nuestros dos tiempos de mínima luz junto con los 187 y 105 tiempos, extraídos de las observaciones SWASP, de CRTS J213033.6+213159 y 1SWASP J212454.61+203030.8 respectivamente, se hace una revisión de los periodos orbitales. El tipo espectral de los sistemas (K) y sus cortos periodos orbitales ( $< 0.3$  días), sugieren que se encuentran cerca del límite inferior del periodo. También se estiman sus dimensiones absolutas y, a partir de diagramas estadísticos, se encuentra que ambas componentes de estos sistemas siguen el patrón general de los objetos W Ursae Majoris.

*Key Words:* techniques: photometric — binaries: eclipsing — stars: individual: CRTS J213033.6+213159, 1SWASP J212454.61+203030.8

### 1. INTRODUCTION

Contact binaries can be classified into four categories: A-subtype and W-subtype proposed by Binnendijk (1965) in which, in general, the A-subtype shows a transit at primary minimum with mass ratio  $q < 0.3$  and periods  $> 0.3$  days, the opposite is true for W-subtype. B-subtype proposed by Lucy & Wilson (1979) are systems in geometrical but not in thermal contact, with large surface temperature differences

between the components. H-subtype, proposed by Csizmadia & Klagyvik (2004), are systems in which the predominant characteristic is a large mass ratio  $q > 0.72$ .

Speaking generally, among the A-subtype, is possible to find the deep low-mass-ratio (DLMR) contact binaries, which are systems with a high fill out factor ( $f > 50\%$ ) and a low mass ratio ( $q < 0.25$ ) as proposed by Qian et al. (2005) and may be the progenitors of single rapidly rotating stars (Stępień 2011, Tyłenda et al. 2011, Zhu et al. 2016, Liao et al. 2017).

<sup>1</sup>Stazione Astronomica Betelgeuse, Magnago, Italy.

<sup>2</sup>Instituto de Astronomía, Universidad Nacional Autónoma de México, México.

TABLE 1  
 $UBV(RI)_C$  AND 2MASS MAGNITUDES OF THE FIELD STARS

ID	Name	RA (2000)	DEC (2000)	$U$	$B$	$V$	$R_c$	$I_c$	$J$	$H$	$K_s$
1	J213033	322.640089	+21.533081	16.218	15.597	14.623	14.030	13.497	12.662	12.174	12.039
2	2MASSJ21304078+2132332	322.669929	+21.542580	16.690	15.962	14.946	14.364	13.825	12.981	12.447	12.318
1	J212454	321.227186	+20.508471	17.334	16.763	15.808	15.211	14.642	13.494	13.039	12.849
2	2MASSJ21245253+2031522	321.218961	+20.531240	15.153	14.519	13.561	12.971	12.471	11.682	11.127	11.059

The eclipsing binary star CRTS J213033.6+213159 (hereinafter J213033,  $\alpha_{2000} = 21^h30^m33^s.6$ ,  $\delta_{2000} = +21^\circ31'59''.2$ ) is listed as a variable star with a period of 0.2246940 days and an amplitude of variation of 0.27 mag. in the Catalina Surveys Periodic Variable Star Catalog (Drake et al. 2014)

1SWASP J212454.61+203030.8 (hereinafter J212454,  $\alpha_{2000} = 21^h24^m54^s.61$ ,  $\delta_{2000} = +20^\circ30'30''.8$ ) was proposed as a short period variable star in the list of candidate eclipsing binaries published by Norton et al. (2011), with a period and amplitude of variation of 0.22783 days and 0.15 mag.

A light curve for this system was reported by Lohr et al. (2013), which presented the typical EW-type behavior.

With no previous studies on these systems, the aim of the present work is to analyze their light curves using the latest version of the Wilson-Devinney code and to understand the geometrical structure and evolutionary state of these eclipsing binaries. The determination of parameters of contact systems, though resulting only from the light curve solutions, can be useful to improve the empirical relations of overcontact W UMa systems.

## 2. CCD PHOTOMETRIC OBSERVATIONS AND DATA REDUCTION

Observations were carried out at the San Pedro Martir Observatory with the 0.84-m telescope, a filter-wheel and the *Spectral Instruments 1* CCD detector (a deep depletion e2v CCD42-40 chip with gain of  $1.39 e^-/ADU$  and readout noise of  $3.54 e^-$ ). The field of view was  $7.6' \times 7.6'$  and a binning of  $2 \times 2$  was used during all the observations. J212454 was observed on August 1 2017 for a total of 5.7 hours while J213033 was observed on the following night for a total of 6.5 hours. In both cases, alternated exposures in filters  $B$ ,  $V$ ,  $R_c$  and  $I_c$ , with exposure times of 20, 10, 6 and 6 seconds, respectively, were taken. Flat field and bias frames were also taken during both nights.

TABLE 2  
TIMES OF MINIMA OF J213033

HJD	Epoch(1)	O-C(1)	Error	Source
2457968.7484	-0.5	0.0029	0.0013	This work
2457968.8748	0	0.0017	0.0010	This work

All images were processed using IRAF<sup>3</sup> routines. Images were bias subtracted and flat field corrected before the instrumental magnitudes were computed with the standard aperture photometry method. These fields were also calibrated in the  $UBV(RI)_C$  system and the results, along with the 2MASS magnitudes, are presented in Table 1. Based on this information, we decided to use objects #2 as comparison stars, since they have magnitudes and colors similar to their respective variables, making differential extinction corrections negligible. Any part of the data set can be provided upon request.

From our observations of J213033 it was immediately clear that the period of 0.224 days proposed by the Catalina Catalog (Drake et al. 2014) was erroneous.

Using our new 2 ToMs presented in Table 2 and the 187 ToMs extracted from the 1SWASP (Butters et al. 2010) observations (more than 20000 measures, available as supplementary data, all heliocentric and determined with the polynomial fit method), we were able to refine the ephemeris of the system as follows:

$$\begin{aligned} Min.I(HJD) = & 2457968.8731(0.0177) \\ & + 0^d.2551899(0.0000011) \times E. \quad (1) \end{aligned}$$

For J212454 we used our 2 ToMs presented in Table 3 and the 105 ToMs extracted from the 1SWASP (Butters et al. 2010) observations (about 9500 measures available as supplementary data), that permitted us to refine the ephemeris, as shown in equation (2).

<sup>3</sup>IRAF is distributed by the National Optical Observatories, operated by the Association of Universities for Research in Astronomy, Inc., under cooperative agreement with the National Science Foundation.

TABLE 3  
TIMES OF MINIMA OF J212454

HJD	Epoch(2)	O-C(2)	Error	Source
2457966.8237	-0.5	-0.0003	0.0009	This work
2457966.9383	0	0.0005	0.0010	This work

$$\begin{aligned} \text{MinI}(HJD) = & 2457966.9379(0.0039) \\ & + 0^d.2278293(0.0000006) \times E + \\ & - 9.079^{-11}(2.139^{-11}) \times E^2. \quad (2) \end{aligned}$$

The ToMs used, presented in Table 3, are heliocentric and were determined with the polynomial fit method.

We used the data of Table 3 to show the behaviour of the  $O - C$  values, as shown in Figure 1. A parabolic trend can be inferred from this figure.

The data set covers only 13.2 years with a gap of 9.7 years between the last of our ToMs and the previous 1SWASP points. Bearing in mind this gap, it is impossible to see any observable manifestation due to cyclic orbital period variations, which seem to be present in many contact binaries. However, we have calculated an orbital period decrease at a rate of  $dP/dt = -2.91 \times 10^{-7}$  days  $\text{yr}^{-1}$ .

Such a variation can be explained by either mass transfer from the more massive secondary to the primary star or by angular momentum loss (AML) due to a magnetic stellar wind.

If the parabolic variation is produced by conservative mass transfer, the transfer rate is  $dM_2/dt = 2.34 \times 10^{-7} M_\odot \text{yr}^{-1}$  (Kwee 1958).

Assuming that the secondary star transfers its present mass to the less massive primary component on a thermal time scale (Paczynski 1971),  $\tau_{th} = 2 \times 10^{-7} M_2^2 (L_2 R_2)^{-1} = 4.84 \times 10^7$  years, mass is transferred to the companion at a rate of  $M_2/\tau_{th} = 1.69 \times 10^{-8} M_\odot \text{yr}^{-1}$ .

This value  $M_2/\tau_{th} M_\odot \text{yr}^{-1}$  is small compared the observed period change of  $dM_2/dt$ ; hence, a conservative mass transfer hypothesis is not confirmed.

Another possible mechanism for the parabolic variation is AML caused by magnetic braking. Guinan & Bradstreet (1988) derived an approximate formula for the period decrease rate due to spin-orbit-coupled AML of binary systems as follows:

$$\begin{aligned} dP/dt \approx & -1.1 \times 10^{-8} q^{-1} (1+q)^2 (M_1 + M_2)^{-5/3} k^2 \\ & \times (M_1 R_2^4 + M_2 R_1^4) P^{-7/3}, \quad (3) \end{aligned}$$

where  $k$  is the gyration constant. With  $k^2 = 0.1$ , (see Webbink 1976), and with the absolute dimensions of

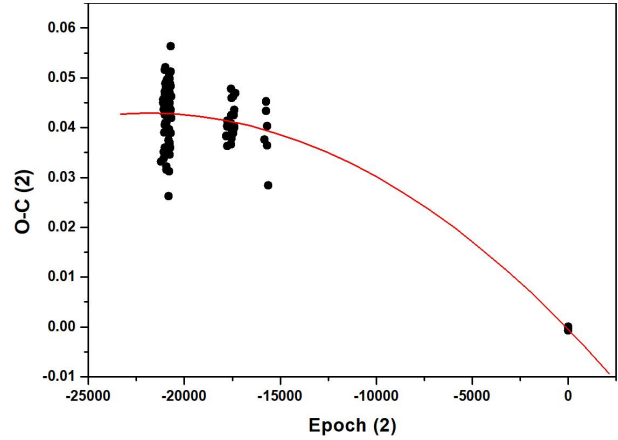


Fig. 1. The points are the data of Table 3. The solid line is the description by a second order polynomial fit to the new ephemeris in equation (2). The color figure can be viewed online.

Table 6 we computed the AML rate to be  $(dP/dt)$   $\text{AML} = -4.47 \times 10^{-8}$  days  $\text{yr}^{-1}$ , which is too small (compared with the observed value) by a factor of about 85%. Therefore, with AML alone it is difficult to fully explain the observed secular period decrease.

This means that neither mass transfer nor AML can describe the parabolic variation, indicating that the orbital period decrease could be as a combination of a downward parabola and a light-travel-time (LTT) effect due to a third body.

### 3. MODELLING THE LIGHT CURVES

Both the systems are newly discovered so there are no reported spectroscopic mass ratios for them; the latest version of the Wilson-Devinney Code (Wilson & Devinney 1971, Wilson 1990, Wilson & van Hamme 2015), was used for simultaneous modelling of our complete light curves.

The temperatures of the hotter components of both systems were estimated using the  $B - V$  index from APASS, the AAVSO Photometric All-Sky Survey (Henden et al. 2009), and interpolated from the tables of Worthey & Lee (2011).

We have taken into account the interstellar extinction using the period-color relation discovered by Eggen and revised by Wang (1994) as  $(B - V)_0 = 0.062 - 1.310 \log P$  (days). The results for both systems show that the interstellar extinction is negligible.

The atmospheric parameters adopted here were: from Lucy (1967) the gravity-darkening coefficients were taken to be 0.32 and the bolometric albedos were set to 0.5 (Ruciński 1973). The limb-darkening

TABLE 4  
DIFFERENCES IN THE HEIGHT OF THE  
MAXIMA (MAG.)

	J213033	J212454
MaxII - MaxI B	0.059	0.043
MaxII - MaxI V	0.046	0.033
MaxII - MaxI Rc	0.040	0.025
MaxII - MaxI Ic	0.038	0.016

parameters were interpolated with a square root law from the van Hamme (1993) tables for  $\log g = 4.0$  and solar abundances.

Inspection of the light curves indicates that they are similar in shape to the light curves of W UMa-type binary stars. This suggested to us to start the W-D analysis directly in Mode 3, suitable for over-contact binaries (W UMa stars).

The  $q$ -search method was applied to find the best initial value of  $q$  to be used during the light curve analysis.

A search for a solution was made for several fixed values of  $q$  using as adjustable parameters the inclination of the systems  $i$ , the mean temperature of the secondaries  $T_2$ , the surface potentials  $\Omega_1 = \Omega_2$ , and the monochromatic luminosities of the primaries  $L_1$ .

The behavior of the sum of squares of residuals,  $\Sigma(res)^2$ , was used to estimate a best value.

Then the value of  $q$  corresponding to the minimum of  $\Sigma(res)^2$  was included in the list of the adjustable parameters and a more detailed analysis was performed.

As shown in Figure 3, the light curves display an evident inverse O’Connell effect (O’Connell 1951) that should not be ignored. The maximum at phase 0.25 (Max I) is clearly fainter than that at phase 0.75 (Max II). In Table 4 we can see that the value of this asymmetry decreases from short to long wavelength; this is an indication that the spot is wavelength dependent and hotter than the surface temperature.

We therefore placed a spot at a fixed latitude  $90^\circ$  (i.e. on the equator) on the surface of the more massive component. The other spot parameters: longitude  $\phi$ , angular radius  $\gamma$  and the temperature factor  $T_s/T_*$ , were treated as free parameters and modified along with the adjustable system parameters.

The final derived photometric solution is listed in Table 5. The temperature factor of the spot suggests to us that it is possibly due to the impact from the mass transfer between the components (Lee et al. 2006).

The final synthetic light curves calculated with the whole set of parameters of Table 5 are shown in Figure 3 as continuous lines.

The observed and the theoretical light curves are in good agreement. A graphic representations and the Roche geometry of the systems is shown in Figure 4.

In this paper we use the output errors from the DC program keeping in mind that the errors here indicated are the formal errors and are unrealistically small; for a discussion see Barani et al. (2017).

The results of our analysis indicate that J213033 is an A-subtype DLMLR system with a low orbital inclination of  $62^\circ$ , while J212454 is a W-subtype shallow-contact binary with a degree of contact lower than 20% (Liu et al. 2016) and a large orbital inclination of  $88^\circ$ . This result implies that it is a totally eclipsing binary system and the photometric parameters here obtained are quite reliable (Terrell & Wilson 2005).

#### 4. EVOLUTIONARY STATE OF THE SYSTEMS

In the absence of spectroscopic elements the absolute parameters cannot be determined directly. However, preliminary absolute elements were derived for each star of both systems using the values from Table 5.

As the two systems belong to different subtypes of the W UMa contact binaries, in the estimation of the absolute parameters we used two different relationships. For J213033 we estimated the global parameters using the empirical relationship “period - total mass” by Yang & Qian (2015) for low mass-ratio binaries through the following formulae.

$$M_{total} = 0.5747(\pm 0.0160) + 2.3734(\pm 0.0331) \times P, \quad (4)$$

$$\log_{10}(R_1/R_\odot) = 0.0751(\pm 0.0014) + 0.9513(\pm 0.0086) \times \log_{10}(M_1/M_\odot), \quad (5)$$

$$\log_{10}(R_2/R_\odot) = 0.2826(\pm 0.0035) + 0.6177(\pm 0.0050) \times \log_{10}(M_2/M_\odot). \quad (6)$$

The derived mean densities of the components,  $\rho_1$  and  $\rho_2$  are estimated according to Mochnacki (1981), the luminosities are calculated using the following formula by Milano & Russo (1983).

$$L_{1,2} = R_{1,2}^2 \times (T_{1,2}/T_\odot)^4 \text{ with } T_\odot = 5780K. \quad (7)$$

While for J212454 we used the “period-semi-major axis” ( $P, a$ ) relation by Dimitrov & Kjurkchieva (2015).

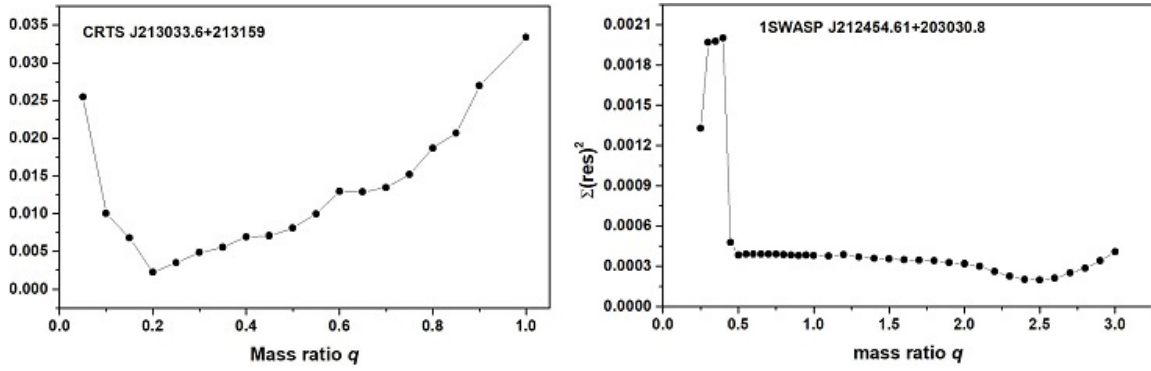


Fig. 2. The relation  $\Sigma(res)^2$  versus mass ratio  $q$  in Mode 3 for J213033 and for J212454.

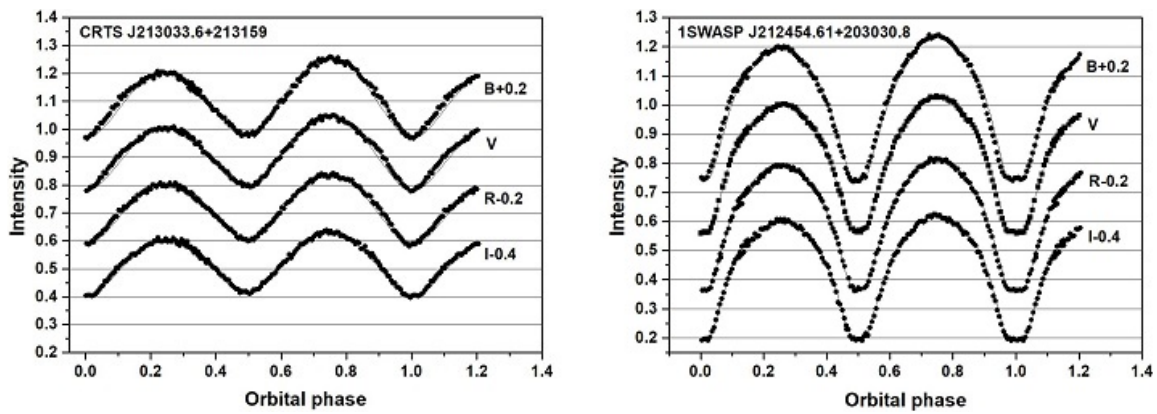


Fig. 3. CCD light curves of J2130033 and J212454. Points are the original observations and lines are the theoretical fits with the spot contribution.

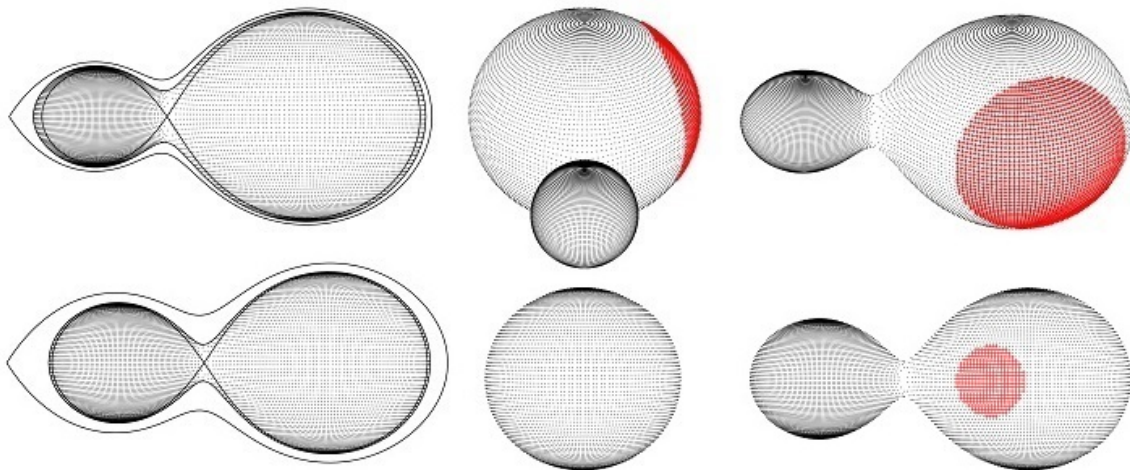


Fig. 4. Graphic representation of J313033 (up) and J212453 (down) according to our solution at quadrature (right) and at primary minimum (center). Left: the configuration of the components of the systems in the orbital plane is shown. The color figure can be viewed online.

TABLE 5

LIGHT CURVE SOLUTIONS FOR J213033  
AND J212454<sup>1</sup>

Parameter	J213033	J212454
$i$ ( $^\circ$ )	$62.022 \pm 0.272$	$88.588 \pm 0.220$
$T_1$ (K)	5200*	5190*
$T_2$ (K)	$5200 \pm 25$	$5080 \pm 12$
$\Omega_1 = \Omega_2$	$2.136 \pm 0.002$	$5.824 \pm 0.002$
$q = m_2/m_1$	$0.186 \pm 0.001$	$2.486 \pm 0.003$
$A_1 = A_2$	0.5*	0.5*
$g_1 = g_2$	0.32*	0.32*
$L_{1B}$	$0.762 \pm 0.006$	$0.321 \pm 0.002$
$L_{1V}$	$0.769 \pm 0.005$	$0.317 \pm 0.001$
$L_{1R}$	$0.769 \pm 0.004$	$0.313 \pm 0.001$
$L_{1I}$	$0.773 \pm 0.004$	$0.311 \pm 0.001$
$L_{2B}$	$0.189 \pm 0.004$	$0.629 \pm 0.003$
$L_{2V}$	$0.188 \pm 0.004$	$0.636 \pm 0.003$
$L_{2R}$	$0.187 \pm 0.003$	$0.641 \pm 0.003$
$L_{2I}$	$0.187 \pm 0.003$	$0.656 \pm 0.002$
$f$	$0.517 \pm 0.006$	$0.168 \pm 0.007$
$X_{1B} = X_{2B}$	0.789*	0.794*
$X_{1V} = X_{2V}$	0.456*	0.461*
$X_{1Rc} = X_{2Rc}$	0.268*	0.271*
$X_{1Ic} = X_{2Ic}$	0.149*	0.151*
$L_3$	0	0
$r_1$ (pole)	$0.507 \pm 0.001$	$0.291 \pm 0.001$
$r_1$ (side)	$0.559 \pm 0.001$	$0.305 \pm 0.001$
$r_1$ (back)	$0.586 \pm 0.001$	$0.343 \pm 0.002$
$r_2$ (pole)	$0.246 \pm 0.002$	$0.440 \pm 0.001$
$r_2$ (side)	$0.258 \pm 0.002$	$0.472 \pm 0.001$
$r_2$ (back)	$0.311 \pm 0.006$	$0.501 \pm 0.001$
lat spot( $^\circ$ )	90*	90*
long spot( $^\circ$ )	$110.3 \pm 3.6$	$70.3 \pm 2.2$
radius( $^\circ$ )	$50.1 \pm 2.9$	$23.4 \pm 2.2$
Temp fac.Spot	$1.025 \pm 0.006$	$1.11 \pm 0.06$
Star	secondary	primary
Sum (res)2	0.0020	0.00019

<sup>1</sup>Assumed parameters are marked with \*.Knowing the period of J212454 of  $0^d.2278293$ ,

$$a = -1.154 + 14.633 \times P - 10.319 P^2, \quad (8)$$

where  $a$  is in solar radii and  $P$  in days.

TABLE 6

PRELIMINARY ABSOLUTE ELEMENTS FOR  
THE SYSTEMS

J213033	Primary	Secondary
Mass( $M_\odot$ )	$0.995 \pm 0.001$	$0.185 \pm 0.001$
Radius( $R_\odot$ )	$1.183 \pm 0.001$	$0.676 \pm 0.002$
Luminosity( $L_\odot$ )	$0.917 \pm 0.002$	$0.3 \pm 0.002$
$\log g$ (cgs)	4.29	4.04
$\rho$ (gr/cm <sup>3</sup> )	1.47	2.27
$a$ ( $R_\odot$ )	$1.841 \pm 0.003$	
J212454	Primary	Secondary
Mass( $M_\odot$ )	$0.818 \pm 0.010$	$0.329 \pm 0.003$
Radius( $R_\odot$ )	$0.775 \pm 0.005$	$0.515 \pm 0.005$
Luminosity( $L_\odot$ )	$0.358 \pm 0.003$	$0.172 \pm 0.003$
$\log g$ (cgs)	4.57	4.53
$\rho$ (gr/cm <sup>3</sup> )	2.484	3.405
$a$ ( $R_\odot$ )	$1.644 \pm 0.002$	

The  $(P, a)$  relation (equation 8) corresponds to the following relation “period-mass” for short-period binaries

$$M = (0.0134/P^2) \times a^3, \quad (9)$$

where  $M$  is the total mass of the binary.

The full set of preliminary absolute parameters is shown in Table 6. These values can be used in statistical diagrams to understand the evolutionary state of the components.

Using the list of 46 DLMR binaries published by Yang & Qian (2015) and the seven new systems found in the literature (Table 7), we show the position of J213033 in the evolutionary diagram of Figure 5. Both components of our system follow the general pattern of the DLMR shown in the example: the primaries are evolved or slightly evolved from the ZAMS, and the secondary stars are not evolved.

In Figure 6 we plot the components of J212454 together with other W- and A-type W UMa systems collected by Yankut & Eggleton (2005) and Li et al. (2008) on the logarithmic mass-luminosity ( $M-L$ ) relationship, along with the ZAMS and TAMS computed by Girardi et al. (2000).

It is clear from this figure that both components of J212454 are in good agreement with the well known W-type W UMa systems on the  $\log M - \log L$  plane.

TABLE 7

## PHOTOMETRIC AND ESTIMATED ABSOLUTE ELEMENTS OF SEVEN NEW DLMR SYSTEMS

System	Period (days)	$T_1$ (K)	$T_2$ (K)	$q$	$f$ (%)	$M_1$ ( $M_\odot$ )	$M_2$ ( $M_\odot$ )	$R_1$ ( $R_\odot$ )	$R_2$ ( $R_\odot$ )	$L_1$ ( $L_\odot$ )	$L_2$ ( $L_\odot$ )	Ref.
ASAS 050334-2521.9	0.41407	6347	5925	0.133	53	1.260	0.168	1.540	0.600	3.450	0.400	1
ASAS 063546-1928.6	0.475515	6229	6072	0.173	58	1.190	0.206	1.630	0.700	3.600	0.600	1
TYC 1174-344-1	0.3887	6500	6357	0.187	51.8	1.381	0.258	1.449	0.714	3.310	0.736	2
TYC 2058-753-1	0.3532	5370	5394	0.103	64	1.030	0.110	1.270	0.460	1.200	0.160	3
TY Pup	0.8192	6900	6915	0.184	84.3	1.650	0.303	2.636	1.373	14.112	3.862	4
V53-M4	0.3084	7415	6611	0.078	69.1	1.470	0.115	1.383	0.481	7.306	0.465	5
V658 Lyr	0.330257	5752	5628	0.179	50.1	1.180	0.210	1.240	0.600	1.520	0.330	6

Ref. (1) Gezer & Bozkurt (2016), (2) Gürol et al. (2011), (3) Alton (2018), (4) Sarotsakulchai et al. (2018), (5) Li et al. (2017), (6) Martignoni et al. (2018).

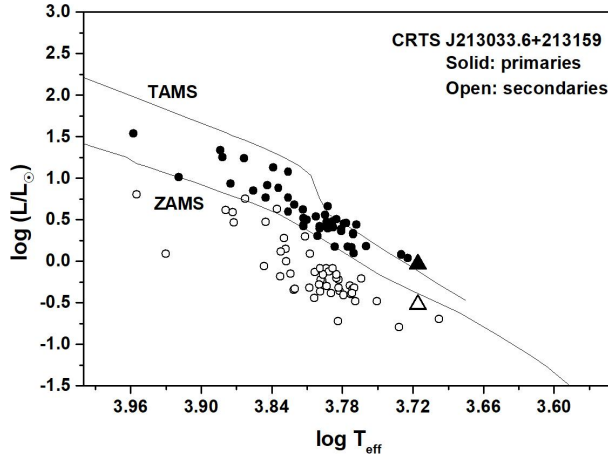


Fig. 5. Position of the components of J213033 in the  $\log T - \log L$  diagram. Zero Age Main Sequence (ZAMS) and Terminal Age Main Sequence (TAMS) are taken from Girardi et al. (2000) for solar chemical composition.

The location of the primary component of the system is near the ZAMS line; that means that is not yet evolved. On the other hand, the secondary component deviates significantly from the ZAMS.

With the absolute elements of Table 6 we can infer the dynamical evolution of the binary orbit of the systems using the orbital angular momentum  $J_0$  (Eker et al. 2006). In their paper, Eker et al. investigated 119 chromospherically active binaries (CAB) and 102 W UMa stars by means of the orbital angular momentum (OAM,  $J_0$ ) and systemic mass ( $M$ ): they found in the  $\log J_0 - \log M$  diagram a curved borderline separating the detached and the contact systems. The physical significance of this line is that it marks the maximum OAM for a contact system

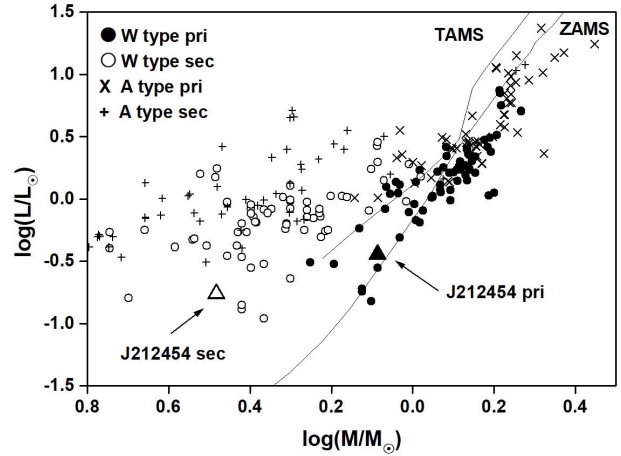


Fig. 6. Location of the components of J212454 on the  $\log M - \log L$  diagram.

to survive. If the OAM of a contact system is more than  $J_{lim}$  the contact configuration breaks.

The values of  $\log J_0 = 51.14$  obtained for J213033 and  $\log J_0 = 51.39$  for J212454 place our systems in the region of contact stars in the  $\log J_0 - \log M$  diagram shown in Figure 7.

## 5. DISCUSSION AND CONCLUSION

CRTS J213033.6+213159 is found to be an A-subtype contact binary with a low mass ratio of  $q = 0.186 \pm 0.001$  and showing a high fill-out parameter of  $f = 51.7 \pm 0.6\%$ . With these characteristics the system belongs to the class of the deep low mass ratio (DLMR) eclipsing binaries as proposed by Qian et al. (2005).

TABLE 8  
PARAMETERS OF THE PROGENITORS OF J212454

Mass parameter	Value
Current mass of the secondary $M_2$	$0.818M_{\odot} \pm 0.010$
Initial mass of the secondary $M_{2i}$	$0.426M_{\odot} \pm 0.090$
Current mass of the primary $M_1$	$0.329M_{\odot} \pm 0.003$
Initial mass of the primary $M_{1i}$	$1.223M_{\odot} \pm 0.090$
Orbital period of the first overflow PFOF	$0^d.85409 \pm 0.049$
Semi-major axis at the first overflow	$4.552R_{\odot} \pm 0.070$
J current angular momentum	$1.95^{51} \text{ cgs} \pm 0.050$
$J_{fof}$ angular momentum at the first overflow	$5.59^{51} \text{ cgs} \pm 0.049$
Mlost	$0.594M_{\odot} \pm 0.010$

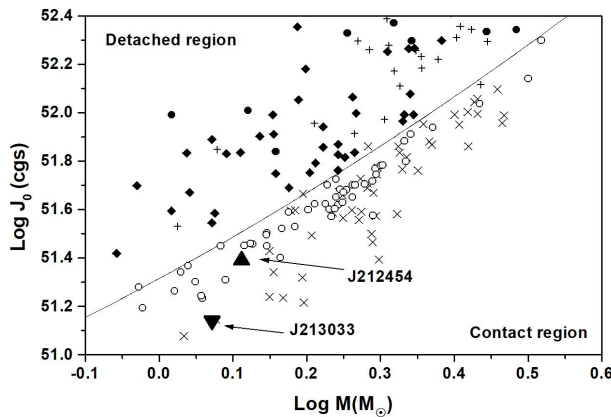


Fig. 7. The position of our systems in the  $\log J_0 - \log M$  diagram. Symbols are described in Figure 1 of the original paper of Eker et al. (2006).

1SWSP J212454.61+203030.8 is found to be an W-subtype with a mass ratio of  $q = 2.486 \pm 0.002$  ( $q_{inv} = 0.402$ ) and a shallow fill-out parameter of  $f = 16.8 \pm 0.7\%$ . Note that most of the W-subtype contact systems have shallow contact characteristics. The high orbital inclination  $i = 88.6^\circ$  tell us that the system is totally eclipsed and that the photometric parameters here obtained are reliable.

Yildiz & Dogan (2013) developed a method for the computation of initial masses of contact binaries based on the assumption that the mass transfer starts near or after the TAMS phase of the initially massive component, which is the currently less massive component.

They discovered that binary systems with an initial secondary mass higher than  $1.8 \pm 0.1M_{\odot}$  become A subtype, while systems with initial masses lower than this become W subtype.

We can apply the method to J212454, to be able to calculate the absolute parameters of the detached system, progenitor of the contact system, as shown in Table 8.

We found that the initial mass of the secondary component would be  $0.426M_{\odot}$ , that means, J212454 has evolved to a W subtype, as predicted.

The results show that the angular momentum has decreased from  $5.51 \times 10^{51}$  cgs at the first overflow (FOF) to  $1.95 \times 10^{51}$  cgs at the present time, concurrently with a mass lost by the system of  $0.594M_{\odot}$ . Consequently, the orbital period and the semi-major axis have decreased from 0.7673105 days and  $4.555R_{\odot}$  to 0.22278293 days and  $1.841R_{\odot}$ , respectively.

Initially, the binary J212454, in the detached phase, consisted of two main sequence stars. The more massive component (the progenitor of the secondary component) evolved to the TAMS. In combination with the AML, the Roche surface was filled by the evolved secondary component, allowing the mass transfer to begin. Since the FOF until the present time, the orbit has decreased by the AML and mass loss. The angular momentum has been lost to 74.6% of  $J_{fof}$  from the stage at the FOF to the present time, producing a smaller orbit.

Two possible mechanisms were examined and we concluded that the continuous period decrease of J212454 is maybe not caused by a thermal mass transfer from the primary to the secondary component, but rather by angular momentum loss due to a magnetic stellar wind.

According to the parameters obtained for the system, we have drawn the configuration of the components using the Binary Maker 3.0 software (Bradstreet & Steelman 2002), which is shown in Figure 3.

For both the systems the small difference in temperature between the components suggest to us that they are in good thermal contact in spite of their different masses and radii.

The light curves of J213033 and J212454 exhibit the inverse O'Connell effect (O'Connell 1951) with the maximum at phase 0.25 (Max I) slightly fainter than that at phase 0.75 (Max II). For this reason a hot spot was placed on the surface of the more massive component.

While for J212454 the hot spot may indicate a probable impact from mass transfer between the components, for J213033 according to Sarotsakulchai et al. (2019), how large a hot spot ( $50^\circ$ ) should appear on the contact binary system is still unknown.

Both systems belong to spectral type K and are short period ( $< 0.3$  days) contact binaries.

The systems of spectral K-type are important to explain the period cutoff phenomenon, as argued by Liu et al. (2014), and to test the thermal relaxation oscillation theory (TRO theory Lucy 1976, Flannery 1976, Robertson & Eggleton 1977, Yankut & Eggleton 2005, Li et al. 2008).

Presumably, J213033 should be in an extreme phase of contact of the TRO cycle while the opposite should hold for J212454, due to its low fill-out value. However, the available observations are insufficient to reveal any period changes that could explain the behaviour of the mass ratio of the binary system.

Absolute parameters were estimated for the components. Based on these, we discussed the evolutionary status of the systems and concluded that the components of J213033 follow the general pattern of other DLMR, with the primary component evolved or slightly evolved from ZAMS and the secondary situated on the ZAMS, as an unevolved star.

The primary component of J212454 is an unevolved ZAMS star, while the secondary component deviates significantly from ZAMS.

Following the study of Eker et al. (2006) our systems, as expected, are located in the contact region of the  $\log J_0 - \log M$  diagram.

This research has made use of the International Variable Star Index (VSX) database, operated at AAVSO, Cambridge, Massachusetts, USA; of the VizieR catalogue access tool, CDS, Strasbourg, France. The original description of the VizieR service was published in A&AS 143, 23.

We acknowledge our anonymous referee for comments that helped to improve this work.

## REFERENCES

- Alton, K. B. 2018, JAVSO, 46, 1  
 Barani, C., Martignoni, M., & Acerbi, F. 2017, *NewA*, 50, 73  
 Binnendijk, L. 1965, *VeBam*, 27, 36  
 Bradstreet, D. H. & Steelman, D. P. 2002, *AAS*, 201, 7502  
 Butters, O. W., West, R. G., Anderson, D. R., et al. 2010. *A&A* 520, 10  
 Csizmadia, Sz. & Klagyvivik, P. 2004, *A&A*, 426, 1001  
 Dimitrov, D. P. & Kjurkchieva, D. P. 2015, *MNRAS*, 448, 2890  
 Drake, A. J., Graham, M. J., Djorgovski, S. G., et al. 2014, *ApJS*, 213, 9  
 Eker, Z., Demircan, O., Bilir, S., & Karataş, Y. 2006, *MNRAS*, 373, 1483  
 Flannery, B. P. 1976, *ApJ*, 205, 217  
 Gezer, İ. & Bozkurt, Z. 2016, *NewA*, 44, 40  
 Girardi, L., Bressan, A., Bertelli, G., & Chiosi, C. 2000, *A&AS*, 141, 371  
 Guinan, E. F. & Bradstreet, D. H. 1988, in *Kinematic Clues to the Origin and Evolution of Low Mass Contact Binaries*, eds. A. K. Dupree and M. T. V. T. Lago, (Springer, Dordrecht), 345  
 Gürol, B., Derman, E., Saguner, T., et al. 2011, *NewA*, 16, 242  
 Henden, A. A., Welch, D. L., Terrell, D., & Levine, S. E. 2009, *AAS*, 41, 669  
 Kwee, K. K. 1958, *BAN*, 14, 131  
 Lee, J. W., Lee, Ch., Kim, Ch., & Kang, Y. W. 2006, *JKAS*, 39, 41  
 Li, K., Hu, S., Chen, X., & Guo, D. 2017, *PASJ*, 69, 79  
 Li, L., Zhang, F., Han, Z., Jiang, D., & Jiang, T. 2008, *MNRAS*, 387, 97  
 Liao, W.-P., Qian, S.-B., Soonthornthum, B., et al. 2017, *PASP*, 129, 124204  
 Liu, N.-P., Qian, S.-B., Soonthornthum, B., et al. 2014, *AJ*, 147, 41  
 Liu, L., Qian, S. B., He, J. J., et al. 2016, *NewA*, 43, 1  
 Lohr, M. E., Norton, A. J., Kolb, U. C., et al. 2013, *A&A*, 549, A86  
 Lucy, L. B. 1967, *ZA*, 65, 89  
 \_\_\_\_\_. 1976, *ApJ*, 205, 208  
 Lucy, L. B. & Wilson, R. E. 1979, *ApJ*, 231, 502  
 Martignoni, M., Barani, C., & Acerbi, F. 2018, *NewA*, 62, 121  
 Milano L. & Russo G. 1983, *MNRAS*, 203, 235  
 Mocknacki, S. W. 1981, *ApJ*, 245, 650  
 O'Connell, D. J. K. 1951, *PRCO*, 2, 85  
 Norton, A. J., Payne, S. G., Evans, T., et al. 2011, *A&A*, 528, 90  
 Paczyński, B. 1971, *ARA&A*, 9, 183  
 Qian, S.-B., Yang, Y.-G., Soonthornthum, B., et al. 2005, *AJ*, 130, 224  
 Robertson, J. A. & Eggleton, P. P. 1977, *MNRAS*, 179, 359  
 Ruciński, S. M. 1973, *AcA*, 23, 79

- Sarotsakulchai, T., Qian, S.-B., Soonthornthum, B., et al. 2018, *AJ*, 156, 199
- Sarotsakulchai, T., Qian, S.-B., Soonthornthum, B., et al. 2019, *PASJ*, 71, 81
- Stępień, K. 2011, *AcA*, 61, 139
- Terrell, D. & Wilson, R. E. 2005, *Ap&SS*, 296, 221
- Tylenda, R., Hajduk, M., Kamiński, T., et al. 2011, *A&A*, 528, 114
- van Hamme, W. 1993, *AJ*, 106, 2096
- Wang, J.-M. 1994, *ApJ*, 434, 277
- Webbink, R. F. 1976, *ApJ*, 209, 829
- Wilson, R. E. & Devinney, E. J. 1971, *ApJ*, 166, 605
- Wilson, R. E. 1990, *ApJ*, 356, 613
- Wilson, R. E. & van Hamme, W. 2015, Computing binary stars observables, ([ftp.astro.ufl.edu](ftp://ftp.astro.ufl.edu)), directory [pub/wilson/lcdc2015](http://pub/wilson/lcdc2015)
- Worthey, G. & Lee, H. C. 2011, *ApJS*, 193, 1
- Yang, Y.-G. & Qian, S.-B. 2015, *AJ*, 150, 69
- Yankut, K. & Eggleton, P. P. 2005, *ApJ*, 629, 1055
- Yildiz, M. & Doğan, T. 2013, *MNRAS*, 430, 2029
- Zhu, L.-Y., Zhao, E.-G., & Zhou, X. 2016, *RAA*, 16, 68

- F. Acerbi: Via Zoncada 51, Codogno, LO, 26845, Italy ([acerbifr@tin.it](mailto:acerbifr@tin.it)).
- C. Barani: Via Molinetto 35, Triulza di Codogno, LO, 26845, Italy ([cvbarani@alice.it](mailto:cvbarani@alice.it)).
- M. Martignoni: Via Don G. Minzoni 26/D, Magnago, MI, 20020, Italy ([massimiliano.martignoni@alice.it](mailto:massimiliano.martignoni@alice.it))
- R. Michel: Universidad Nacional Autónoma de México. Observatorio Astronómico Nacional. Apartado Postal 877, C.P. 22800, Ensenada, B.C., México ([rmm@astro.unam.mx](mailto:rmm@astro.unam.mx)).

## THE ADF AND THE $t^2$ FORMALISM IN H II REGIONS BASED ON THE UPPER MASS LIMIT OF THE IMF FOR THE MW

L. Carigi, A. Peimbert, M. Peimbert, and G. Delgado-Inglada

Instituto de Astronomía, Universidad Nacional Autónoma de México, México.

*Received April 9 2020; accepted June 8 2020*

### ABSTRACT

We study in depth the abundance discrepancy problem in H II regions, this time from a different perspective than the usual one: by studying the effect of the upper mass limit ( $M_{up}$ ) of the initial mass function (IMF) on the O, C, and He predicted by chemical evolution models for the Milky Way. We use abundances determined with the direct method (DM) and with the temperature independent method (TIM). We compare the predicted abundances at the present time with observations of Orion, M17, and M8 to determine the  $M_{up}$  value of the galactic IMF. From the DM abundances, the models predict an  $M_{up} = 25 - 45 M_{\odot}$ , while from the TIM, CEMs derive an  $M_{up} = 70 - 110 M_{\odot}$ . Spiral galaxies with the stellar mass and star formation rate of the MW are predicted to have an  $M_{up} \approx 100 M_{\odot}$ . These results support that abundances derived from the TIM are better than those derived from the DM.

### RESUMEN

Estudiamos el problema de la discrepancia de abundancias en regiones H II a partir del efecto que tiene la masa superior ( $M_{up}$ ) de la función inicial de masa (IMF) en la producción de O, C y He obtenida por modelos de evolución química de nuestra galaxia. Comparamos las abundancias determinadas por el método directo (DM) y por el método independiente de la temperatura (TIM) en Orión, M17 y M8 con las abundancias modeladas actuales para determinar el valor de la  $M_{up}$  de la IMF Galáctica. Al usar las abundancias a partir del DM se requiere que  $25 < M_{up} < 40 M_{\odot}$ , mientras que con las abundancias obtenidas a partir del TIM se requiere que  $70 < M_{up} < 110 M_{\odot}$ . Para galaxias espirales con masa estelar y tasa de formación estelar similar a la VL se ha predicho una  $M_{up} \approx 100 M_{\odot}$ . Este resultado implica que las abundancias obtenidas por el TIM son más adecuadas que las obtenidas por el DM.

*Key Words:* Galaxy: evolution — H II regions — ISM: abundances

### 1. INTRODUCTION

The study of the chemical composition of H II regions is crucial for the understanding of the chemical composition of the universe; it can provide observational constraints required by models of galactic chemical evolution. The proper determination of the oxygen abundance in H II regions is critical to be able to compare our determinations with other branches of astrophysics, as well as to be able to present a coherent model of the evolution of the universe.

Although a comprehensive chemical composition is desired, frequently studies are only able to determine a few chemical elements; in fact many works

focus only on the oxygen abundance. A single well determined element can be quite useful, since most elements are expected to behave in an orchestrated fashion, and oxygen is the ideal candidate, since it is expected to comprise about half of the heavy element abundance; not only that, but is the easiest element to study since it is the only element that produces bright optical lines for each of its main ionic species.

There are three competing methods to derive ionic  $O^+$  and  $O^{++}$  abundances, relative to the  $H^+$  abundance, in H II regions: (i) The use of [O II] and [O III] collisionally excited lines (CELs) together with the H Balmer lines; these lines are relatively

easy to observe. Unfortunately their emissivities depend strongly on the local temperature (in fact, this specific characteristic of CELs is used to determine the characteristic temperature of photoionized regions); this is known as the direct method (DM). (ii) The use of O I and O II recombination lines (RLs) together with the H Balmer lines (which are also RLs); this strategy has the advantage that the ratios of any pair of RLs are almost independent of the temperature structure; however, RLs of heavy elements are quite faint and harder to work with. (iii) The use of CELs with the  $t^2$  formalism introduced by Peimbert (1967); Peimbert & Costero (1969) in which the effect of the temperature structure on the emission lines is taken into account. Recent reviews of these methods have been presented by Pérez-Montero (2017); Peimbert et al. (2017); Peimbert (2019); García-Rojas (2020).

Abundances derived from either RLs or the  $t^2$  formalism usually agree with each other and are usually 0.2 to 0.3 dex higher than those determined using the DM (e.g. Esteban et al. 2009; Peimbert et al. 2017; Peimbert 2019; Carigi et al. 2019a). We have defined the temperature independent method (TIM) as abundances derived from either RLs, the  $t^2$  formalism, or their average (Carigi et al. 2019a). On the other hand, the ratio between RL abundances and DM abundances (TIM abundances to DM abundances) is called the abundance discrepancy factor (ADF):  $ADF(X^{+i}) = X_{RLs}^{+i}/X_{CELs}^{+i}$  (Tsamis et al. 2003).

Whether the origin of the abundance discrepancy is (only) due to temperature fluctuations (Peimbert 1967) or to chemical inhomogeneities (first proposed by Torres-Peimbert et al. 1990) is still under discussion (see e.g., Esteban, Toribio San Cipriano & García-Rojas 2018; García-Rojas et al. 2019). Other hypotheses have not been very successful and have been proposed over the years, such as the  $\kappa$  distribution of electrons (Nicholls, Dopita & Sutherland 2012), or uncertainties in the atomic data (e.g., Rodríguez & García-Rojas 2010), but have been discarded (García-Rojas et al. 2019). Anyway, it is beyond the scope of this paper to discuss the origin of this long-standing problem.

Oxygen observations of H II regions are limited to the O<sup>+</sup> and O<sup>++</sup> gaseous components. In general, it is not necessary to correct for other ionization stages where O<sup>+3</sup> is limited to  $\approx$  1-2% and O<sup>0</sup> is considered to be outside the relevant volume of the H II region; and, when comparing abundances between several H II regions, this is enough. However, when comparing with other types of objects,

or when trying to model the evolution of a galaxy, it is of critical importance to correct for oxygen atoms trapped in dust grains, which are estimated to be  $\approx$  25% of the total oxygen in H II regions (i.e. an additional  $\approx$  35%, when compared to the gaseous component; Mesa Delgado et al. 2009; Peimbert & Peimbert 2010; Espíritu et al. 2017).

Here we study the discrepancy between TIM and DM abundances from a different perspective. We will compute chemical evolution models adopting the initial mass function (IMF) by Kroupa (2002) with different  $M_{up}$  values, where  $M_{up}$  is the upper mass limit of the IMF. The  $M_{up}$  value is not the maximum stellar mass present in a given H II region, but the maximum mass of the IMF averaged over the age of the Galaxy.

In order to be able to study in depth as many details as possible, in this paper we will do a deeper study for a few of H II regions only. We selected the Orion Nebula because it is, by far, the most studied Galactic H II region. For our second object we selected M17 because it is the second most studied Galactic H II region, it is relatively close by, yet it has an appreciably different galactocentric distance; also it is a high-ionization H II region and thus we need not worry about the possible presence of neutral helium. Our last object is M8; it is one of the most studied Galactic H II regions, it has approximately the same galactocentric radius as M17.

Chemical evolution models for the MW have been built to reproduce robust observational constraints of the Galaxy. Some authors (e.g., Prantzos et al. 2018; Romano et al. 2010) constrain their CEMs by trying to fit the solar abundances at the Sun's age; other authors (e.g., Spitoni et al. 2019; Mollá et al. 2015) constrain their models by trying to reproduce the  $[\alpha/Fe] - [Fe/H]$  trend shown by stars at the solar vicinity. Most of these models reproduce the current slope of the  $\alpha/H$  gradients, but the predicted absolute values are different and, consequently, the predicted  $\alpha$  enrichment efficiencies are different during the last few Gyrs of the evolution.

Unfortunately, the chemical gradients of H II regions cannot be used as solid constraints because, while the slope of the chemical gradient is widely accepted, the absolute values of H II region gradients found in the literature present a large dispersion; this becomes more pronounced when combined with gradients derived from other young objects.

To improve the quality of the models, it is important to fit the absolute value of the element abundances at the present time, not only the slope. These absolute values become critical to place restrictions

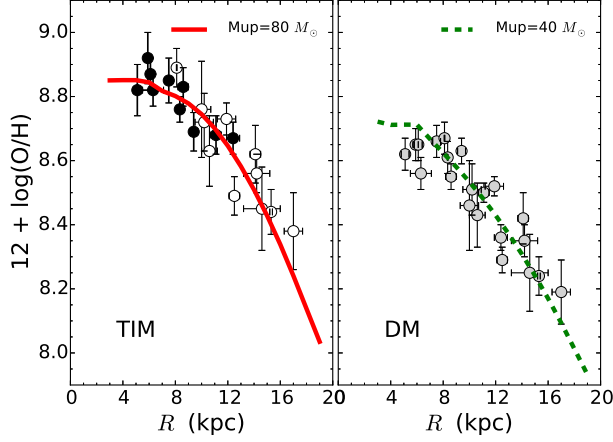


Fig. 1. Values of O/H as a function of the distance to the galactic center. Models for  $t^2 = 0.00$  and for observed  $t^2$  values versus two chemical evolution models with different  $M_{up}$  values. The filled and dashed lines represent the radial distribution obtained with the TIM ( $M_{up} = 80M_{\odot}$ ) and DM ( $M_{up} = 40M_{\odot}$ ) models, respectively. The circles represent the values derived from observations: TIM values based on recombination lines (black), TIM values based on the calibration by Peña-Guerrero et al. 2012 (empty), and DM values (grey). For further discussion, see Carigi et al. (2019a). The color figure can be viewed online.

on the CEMs. For example: since O, and other  $\alpha$  elements, are mainly produced by massive stars, the absolute values of the gradient are critical to determine the  $M_{up}$  value of the IMF.

For simplicity we will use H, He, C, and O to represent the abundances by number, and  $X$ ,  $Y$ ,  $C$ , and  $O$  to represent the abundances by mass of these elements;  $Z$  represents the total heavy element abundance by mass.

## 2. H II REGIONS ABUNDANCES AND CHEMICAL EVOLUTION MODELS

### 2.1. O/H vs. Distance to the Galactic Center

In Figure 1 we present two sets of H II region data for O/H, one based on the TIM and the other based on the DM, as well as the best fit models to each data set. The observational data were compiled from Esteban et al. (2004, 2013, 2016, 2017); Fernández-Martín et al. (2017); García-Rojas et al. (2004); García-Rojas et al. (2005, 2006); García-Rojas et al. (2007); García-Rojas, Simón-Díaz & Esteban (2014). The models, built to reproduce the O/H gradient, come from Carigi et al. (2019a). For a more detailed description of the data selection, the model, and the fit see Carigi et al. (2019a). All abundances have been

corrected by the fraction of O trapped in dust grains (Peimbert & Peimbert 2010; Peña-Guerrero et al. 2012; Espíritu et al. 2017). The figure illustrates very well that the curves required to fit the TIM and the DM data are quite different; it is thus no surprise that the  $M_{up}$  required by the models to fit the TIM data and the DM data are very different: while the  $M_{up}$  used to fit the TIM data amounts to  $80 M_{\odot}$ , the value used to fit the DM data amounts to  $40 M_{\odot}$ .

When comparing these values with the ones observed for young objects (B-stars, Cepheids), we find that the model based on the TIM values produces an excellent fit between 5 and 17 kpc, while the model based on the DM values fails to reproduce the observations (Carigi, Peimbert, & Peimbert 2019b).

### 2.2. Representation of the Chemical Evolution Models

We compute a set of nine chemical evolution models (CEMs) for MW like galaxies based on the work by Carigi et al. (2019a); these models differ only in the adopted  $M_{up}$  value. We present the output of these models for 6.2 kpc, corresponding to the average galactocentric distance of M17 (6.1 kpc) and M8 (6.3 kpc), and for 8.34 kpc, corresponding to the galactocentric distance of the Orion Nebula.

The initial abundances of our models are:  $X(0) = 0.7549$ ,  $Y(0) = 0.2451$ ,  $C(0) = 0$ , and  $O(0) = 0$ , where  $Y(0) = 0.2451 \pm 0.0026$  is the primordial helium abundance derived by Valerdi et al. (2019). Their  $Y(0)$  result is in good agreement with the value derived by Planck Collaboration (2018) that amounts to  $Y(0) = 0.24687 \pm 0.00076$ .

We explore the  $M_{up}$  effects on the predicted value of  $Y$ ,  $C$ , and  $O$  during the whole evolution. The galaxies are formed in an inside-out scenario of primordial infall, with the halo component formed from 0 to 1 Gyr and the disk component formed from 1 to 13 Gyr.

In Figures 2 and 3 we present the  $\Delta O$  vs  $\Delta Y$  evolution for  $R = 6.2$  and 8.34 kpc, respectively. Moreover, in Figures 4 and 5 we show  $\Delta O$  vs  $\Delta C$  evolution curves computed for the same radii. The evolution curves are presented for nine CEMs that consider  $M_{up} = 25, 30, 35, 40, 50, 60, 80, 100, 150 M_{\odot}$ . For comparison, we present observational data for M17, M8, and Orion, using the DM and the TIM.

In Carigi et al. (2019a), models were built to reproduce the radial behavior of the total O/H from 21 H II regions. To fit a representative absolute value of the gradient, they inferred two  $M_{up}$  values: one if the gaseous O/H values were determined

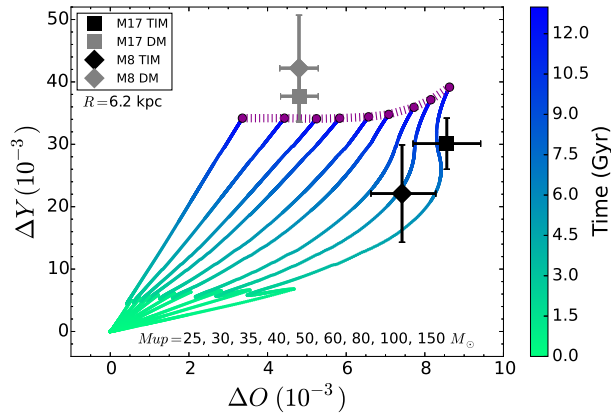


Fig. 2. Chemical evolution for  $Y$  and  $O$  at a galactocentric distance of 6.2 kpc (approximately the distance of M17 and M8). The curves cover the entire evolution from the beginning (0 Gyr) to the present time (13 Gyr, magenta points), and each curve corresponds to a model with a different  $M_{up}$ . The squares represent the  $O$  and  $He$  abundances derived for M17 using the DM (grey) and the TIM (black); the diamonds represent the abundances derived for M8 using the DM (grey) and the TIM (black). The dotted magenta line connects the present-time values predicted by the models. Note that, the observed values should be compared with this magenta line to choose the better  $M_{up}$  values. The color figure can be viewed online.

from the DM ( $M_{up} = 40 M_{\odot}$ ) and the other if the gaseous  $O/H$  values were determined from the TIM ( $M_{up} = 80 M_{\odot}$ ), see Figure 1.

Also, for NGC 6822 (an irregular galaxy), Hernández-Martínez et al. (2011) built chemical evolution models to reproduce  $O/H$  values determined from DM and TIM, and obtained  $M_{up} = 40 M_{\odot}$  and  $M_{up} = 80 M_{\odot}$ , respectively, in agreement with the values found for the MW.

In this work, we will obtain uncertainty bars for the  $M_{up}$  values, comparing the present-time abundances computed by models using different  $M_{up}$  values, with the  $O/H$ ,  $He/H$ , and  $C/H$  abundances (and their error bars) for M17, M8, and Orion.

### 2.3. Object Selection

The approach in this study is to put quality over quantity; thus, we only use three objects: the Orion Nebula, M17, and M8, since they are the most studied Galactic H II regions. One very important characteristic of the Orion Nebula and M17 is that they are very bright (hence their many studies); as a consequence of this they have arguably the best  $O/H$  abundance ratio determinations. Another reason

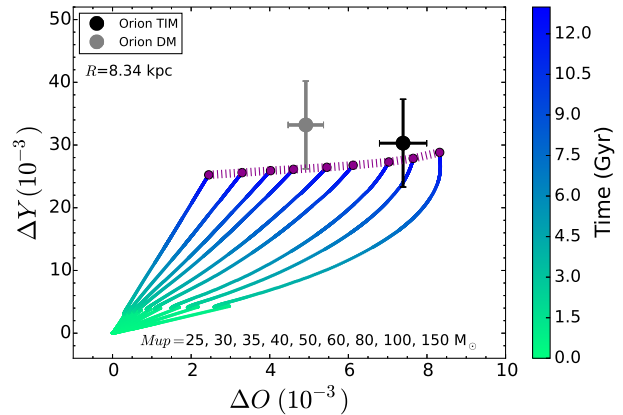


Fig. 3. Chemical evolution for  $Y$  and  $O$  at a galactocentric distance of 8.34 kpc (Orion). The curves cover the entire evolution from the beginning (0 Gyr) to the present time (13 Gyr, magenta points), and each curve corresponds to a model with a different  $M_{up}$ . The circles represent the  $O$  and  $He$  abundances derived for Orion using the DM (grey) and the TIM (black). Note that the Orion data should be compared with the magenta line (theoretical present-time values). The color figure can be viewed online.

to select them is that they have noticeable different galactocentric radii. While the Orion Nebula is, by far, the best studied H II region, M17 has the advantage of being a high ionization H II region and thus we do not need to worry about an uncertain ICF(He). Unfortunately, there are no UV observations of M17 (probably due to its relatively high  $c(H\beta) = 1.17$ ) and it is therefore not possible to derive  $C$  abundances using CELs and the direct method. We selected M8 because it is also nearby and very bright, its galactocentric distance is very similar to that of M17 (allowing us to present both of them using the same simulation and figures), it is the 4th most observed Galactic H II region, and probably the 3rd best suited for a study such as the one we present.

Tables 1, 2, and 3 show the total abundances (gas + dust) by mass derived for M17, M8, and Orion, respectively. The values were derived by transforming the abundances by number obtained by García-Rojas et al. (2007); Esteban et al. (2005) for  $O/H$ ,  $He/H$ , and  $C/H$  and assuming that  $O$  is approximately 45% of  $Z$ . The first column of these tables shows the abundances derived through the DM (from CELs) and assumes a constant temperature over the observed volume, whereas the second column shows the abundances derived through the TIM (from RLs).

TABLE 1

M17: OBSERVED  $\Delta Y$ ,  $O$ , AND  $C$  VALUES<sup>a</sup>

	DM	TIM
$\Delta Y$ ( $10^{-3}$ )	37.7 $\pm$ 4.2	30.1 $\pm$ 4.1
$O$ ( $10^{-3}$ )	4.81 $\pm$ 0.48	8.56 $\pm$ 0.86
$C$ ( $10^{-3}$ )	...	6.27 $\pm$ 0.63
$\Delta Y/\Delta O$	7.86 $\pm$ 1.39	3.52 $\pm$ 0.72
$\Delta C/\Delta O$	...	0.73 $\pm$ 0.10

<sup>a</sup>Observations from García-Rojas et al. (2007).

TABLE 2

M8: OBSERVED  $\Delta Y$ ,  $O$ , AND  $C$  VALUES<sup>a</sup>

	DM	TIM
$\Delta Y$ ( $10^{-3}$ )	42.2 $\pm$ 8.5	22.1 $\pm$ 7.8
$O$ ( $10^{-3}$ )	4.80 $\pm$ 0.49	7.42 $\pm$ 0.79
$C$ ( $10^{-3}$ )	1.50 $^{+0.30}_{-0.75}$	5.30 $^{+1.07}_{-2.65}$
$\Delta Y/\Delta O$	8.80 $\pm$ 1.99	2.84 $\pm$ 1.06
$\Delta C/\Delta O$	0.31 $^{+0.07}_{-0.16}$	0.68 $^{+0.15}_{-0.35}$

<sup>a</sup>Observations from García-Rojas et al. (2007).

As mentioned above, the line of sight in the direction of M17 has a relatively high reddening, and the  $\lambda\lambda$  1906-1909 Å [C III] lines are too obscured to have been observed. One might be interested in using the  $\lambda$  4267 Å C II line to complete the DM determination; but  $\lambda$  4267 Å C II cannot be used as part as the DM for the same reasons that the  $\lambda$  4650 Å O II multiplet cannot be used (since it corresponds to the TIM). Therefore, while widely used, it should not be considered as part of the DM (and one should beware of authors that use it as part of the DM without a clear and consistent explanation on the ADF origin and its consequences).

#### 2.4. $O/H$ vs. $He/H$

Gaseous O/H abundances are readily available from many observational sources. However, they are frequently not converted to the total ISM O/H; to do this, it is necessary to include the fraction of O trapped in dust grains. It is estimated that this correction is between 0.07 and 0.13 dex for most H II regions (Mesa Delgado et al. 2009; Peimbert & Peimbert 2010; Espíritu et al. 2017); the exact value depends on the metallicity and on the efficiency of the dust destruction present within each H II region. Here we will include a correction of 0.12 dex for the Orion Nebula (Mesa Delgado et al.

TABLE 3

ORION NEBULA: OBSERVED  $\Delta Y$ ,  $O$ , AND  $C$  VALUES<sup>a</sup>

	DM	TIM
$\Delta Y$ ( $10^{-3}$ )	33.2 $\pm$ 7.1	30.3 $\pm$ 7.0
$O$ ( $10^{-3}$ )	4.92 $\pm$ 0.45	7.39 $\pm$ 0.60
$C$ ( $10^{-3}$ )	1.35 $^{+0.55}_{-0.40}$	2.81 $^{+0.42}_{-0.32}$
$\Delta Y/\Delta O$	6.75 $\pm$ 1.45	4.10 $\pm$ 1.01
$\Delta C/\Delta O$	0.27 $^{+0.12}_{-0.08}$	0.38 $^{+0.06}_{-0.05}$

<sup>a</sup>Observations from Esteban et al. (2005).

2009; Espíritu et al. 2017) and 0.11 dex for both M17 and M8 (Peimbert & Peimbert 2010).

The C/H abundance should also be corrected for dust depletion; this correction is expected to be similar or slightly smaller than the O/H correction (Esteban et al. 1998, 2009). Here we will assume a correction of 0.10 dex for all three H II regions.

Although most elements should include a correction due to dust depletion, the fact that He is an inert noble gas means that no correction will be necessary for the He/H abundances.

#### 2.4.1. $O$ vs. $Y$ for M17 and M8

In Figure 2 we present the theoretical evolution of  $\Delta O$  and  $\Delta Y$  vs time, for  $R = 6.2$  kpc. We plot nine curves that correspond to the nine  $M_{up}$  values listed in § 2.2. The curves begin at  $t = 0$  Gyr ( $\Delta O = \Delta Y = 0$ ) and end at 13 Gyr. We include the  $\Delta O$  and  $\Delta Y$  values for M17 and M8, determined from the DM and the TIM (see Tables 1 and 2). In order to choose the  $M_{up}$  values that best reproduce the observational data, the top of each curve (the predicted values at present time (shown in magenta points) should be compared with the M17 and M8 data (the observed abundances for the ISM).

The curves evolve more rapidly to the right with increasing  $M_{up}$  values, because the O production for high mass stars (HMS) increases with the stellar mass. At 1 Gyr, when the halo formation ends, the curves present a loop due to the dilution of the ISM with primordial infall ( $Y = 0.2451$ ,  $O = 0.0$  Valerdi et al. 2019) that forms the disk. The rest of the evolution depends on the lifetime and the initial metallicity ( $Z$ ) of the HMS and low-and-intermediate mass stars (LIMS), see Carigi & Peimbert (2008) and Carigi & Peimbert (2011).

Current  $Y$  values are almost constant for  $M_{up} < 50M_{\odot}$  and increase for  $M_{up} > 50M_{\odot}$  (see Table 4), because: (i) for low  $Z$  (equivalent to low  $O$ ),

TABLE 4  
PRESENT DAY VALUES IN THE ISM PREDICTED BY THE MODELS FOR  $R = 6.2$  KPC  
(M17 AND M8)

$M_{up}$	$\Delta Y$ ( $10^{-3}$ )	$O(10^{-3})$	$C(10^{-3})$	$\Delta Y/\Delta O$	$\Delta Y/\Delta C$
150	39.16	8.63	7.54	4.54	1.14
100	37.14	8.15	7.08	4.56	1.15
80	35.92	7.72	6.67	4.65	1.16
60	34.79	7.08	6.01	4.91	1.18
50	34.40	6.57	5.47	5.24	1.20
40	34.18	5.83	4.86	5.86	1.20
35	34.09	5.24	4.50	6.51	1.16
30	34.19	4.43	4.28	7.72	1.04
25	34.19	3.36	4.24	8.06	0.79

HMS in the 8-25  $M_{\odot}$  range are much more efficient to produce He than those in the 25-150  $M_{\odot}$  range, (ii) for high  $Z$ , HMS in the 50-150  $M_{\odot}$  range are very efficient to produce He, and (iii) for LIMS, the He contribution is not strongly  $Z$ -dependent.

A peculiarity of Figure 2 is the shape of the  $M_{up} = 150 M_{\odot}$  curve, where the oxygen abundance diminishes between 7.8 and 10.0 Gyrs. This O dilution is caused by the huge amount of C ejected by very massive stars of high  $Z$  (see the description of the carbon evolution in § 2.5.1).

When comparing the observed O and He values for M17 with those derived from our models we find: (i) for the  $\Delta O$  value determined with the DM, an IMF with a galactic  $M_{up}$  of 30 - 36  $M_{\odot}$ , while (ii) for the  $\Delta O$  value determined with the TIM, an  $M_{up} > 75 M_{\odot}$ , (iii) for the  $\Delta Y$  value determined with the DM, all values of  $M_{up}$  are allowed (the  $\Delta Y$  value is not very restrictive), and (iv) for the  $\Delta Y$  value determined with the TIM, an  $M_{up} < 70 M_{\odot}(1\sigma)$  (allowing for all possible values at the  $2\sigma$  level).

From the M8 values we find: (i) the  $\Delta O$  value determined with the DM is nearly identical to the one determined for M17; therefore, the range determined for  $M_{up}$  is also of 30 - 36  $M_{\odot}$ , (ii) the  $\Delta O$  value determined with the TIM suggests  $M_{up}$  in the 52 - 120  $M_{\odot}$  range, (iii) for the  $\Delta Y$  value determined with the DM, all values of  $M_{up}$  are allowed (the  $\Delta Y$  value is not very restrictive), and (iv) for the  $\Delta Y$  value determined with the TIM there is no solution at the  $1\sigma$  level, yet at the  $2\sigma$  level all solutions are allowed; this shows both the uncertainty of the  $ICF(\text{He})$  and the lack of restriction produced by  $\Delta Y$ .

#### 2.4.2. $O$ vs. $Y$ for the Orion Nebula

In Figure 3 we present curves of the theoretical evolution of  $\Delta O$  and  $\Delta Y$  vs time for  $R = 8.34$  kpc, corresponding to nine  $M_{up}$  values listed in § 2.2. Moreover, we include the  $\Delta O$  and  $\Delta Y$  values for Orion, determined from the DM and the TIM (see Table 3). As in Figure 2, the top of each curve (in magenta) corresponds to the end of evolution (i.e. the present time; see Columns 2 and 3 of Table 5), and should be compared with the Orion data to choose the  $M_{up}$  values that best reproduce the observations.

In Figure 3, for any given  $M_{up}$ , the evolutionary curves reach lower  $\Delta O$  and  $\Delta Y$  values than the corresponding coeval values in Figure 2, because the O/H gradient is negative for all MW-like models. Therefore, for any given time, the  $\Delta O$  value (and  $Z$  value) for  $R = 8.34$  kpc is lower than the  $\Delta O$  value for  $R = 6.2$  kpc. Consequently, very few massive stars of high  $Z$  form and, since they are more efficient He producers, the reached  $Y$  values are lower. In this figure, for the  $M_{up} = 150$  curve, the O dilution is lower, due to the relative lack of massive stars of high  $Z$  (highly-efficient C producers).

When comparing the observed O and He values for Orion with those derived from our models, we find: (i) for the  $\Delta O$  value determined with the DM, an  $M_{up}$  of 38 - 50  $M_{\odot}$ ; (ii) for the  $\Delta O$  value determined with the TIM, an  $M_{up}$  of 75 - 130  $M_{\odot}$ , (iii) for the  $\Delta Y$  value determined with the DM, an  $M_{up} > 35 M_{\odot}(1\sigma)$  (allowing for all possible values at the  $1.2\sigma$  level), and (iv) for the  $\Delta Y$  value from the TIM, again, all values of  $M_{up}$  are allowed.

#### 2.5. $O$ vs. $C$

##### 2.5.1. $O$ vs. $C$ for M17 and M8

In Figure 4 we show the curves of theoretical evolution of  $\Delta O$  and  $\Delta C$  vs time, for  $R = 6.2$  kpc, ob-

TABLE 5  
PRESENT DAY VALUES IN THE ISM PREDICTED BY THE MODELS FOR  $R = 8.34$  KPC  
(ORION NEBULA)

$M_{up}$	$\Delta Y (10^{-3})$	$O (10^{-3})$	$C (10^{-3})$	$\Delta Y / \Delta O$	$\Delta Y / \Delta C$
150	28.82	8.32	5.22	3.46	5.52
100	27.87	7.65	4.84	3.64	5.76
80	27.30	7.03	4.54	3.88	6.01
60	26.77	6.12	4.10	4.37	6.53
50	26.45	5.45	3.77	4.85	7.02
40	26.12	4.60	3.42	5.68	7.64
35	25.91	4.02	3.24	6.45	8.00
30	25.50	3.30	3.11	7.73	8.20
25	25.24	2.45	3.04	10.30	8.30

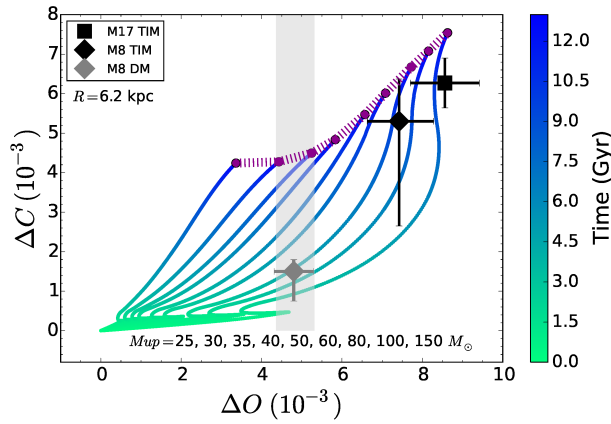


Fig. 4. Chemical evolution for  $C$  and  $O$  at a galactocentric distance of 6.2 kpc (approximately the distance of M17 and M8). The curves and points are similar to those in Figure 2. Notice, however, that there are only 3 points in this figure instead of the 4 in Figure 2: unfortunately there is no restriction on  $C$  for the DM of M17 and, instead of the fourth point the shaded vertical band is the  $\Delta O$  predicted by the DM. Again, the observed values should be compared with the magenta curve. The color figure can be viewed online.

tained from our nine CEMs. The current values, at the top end of the curves, are presented in Columns 3 and 4 of Table 4. We include the observed  $\Delta O$  and  $\Delta C$  values for M17 and M8 determined from the TIM. The gray diamond represents the  $\Delta O$  and  $\Delta C$  values determined for M8, while the shaded vertical bar represents the  $\Delta O$  for M17 using the DM combined with the lack of a  $C$  determination available from the DM (see Table 1).

A remark on the  $\Delta C$  determination for M8: according to the recent ICFs computed for giant H II regions (Amayo, Delgado-Inglada, Stasińska, 2020, in prep.), the use of  $C/O = C^{++}/O^{++}$  in M8 may

underestimate the real  $C/O$  value by up to  $\approx 0.3$  dex. However, these ICFs may not be adequate for Galactic H II regions where only a small area is observed. We decided not to change the value of  $C/H$  but to increase the associated error bars.

Current  $C$  values are almost constant for  $M_{up} \lesssim 35 M_{\odot}$  and increase significantly for  $M_{up} \gtrsim 40 M_{\odot}$  (see Table 4); this happens for two main reasons: (i) stars in the 40-150  $M_{\odot}$  range produce much more  $C$  when they are more metal rich, and (ii) stars in the 1-3  $M_{\odot}$  range produce more  $C$  when they are metal poor. Due to the the LMS enrichment contribution, HMS of high  $Z$  contribute at times similar than LMS of low  $Z$  (e.g. Akerman et al. 2004; Carigi et al. 2005; Carigi & Peimbert 2011).

When comparing the observed  $\Delta C$  value for M17 determined with the TIM with those derived from the CEMs, we find an  $M_{up}$  in the 55 - 95  $M_{\odot}$  range. Using the determination from the M8's  $\Delta C$  measurements obtained with the TIM, we only find an upper limit  $M_{up} < 72 M_{\odot}$ ; the lack of a lower limit is due to the large uncertainty on the lower limit of the ICF. When determining a  $\Delta C$  value for M8 using the DM, the value is not compatible with our models, as the DM falls short of our models by a factor of at least 2.5 (for the lowest  $M_{up} = 30 M_{\odot}$ ), and probably by a factor of about 3.5 or more (for a more reasonable  $M_{up} \gtrsim 70 M_{\odot}$ ). Finally, regarding the DM determination for M17: due to the high reddening of M17, it has not been observed in the UV, and therefore it has not been possible to obtain [C III] intensities, nor to determine DM abundances. The  $\Delta O$   $M_{up}$  determinations are the same as those in Figure 2.

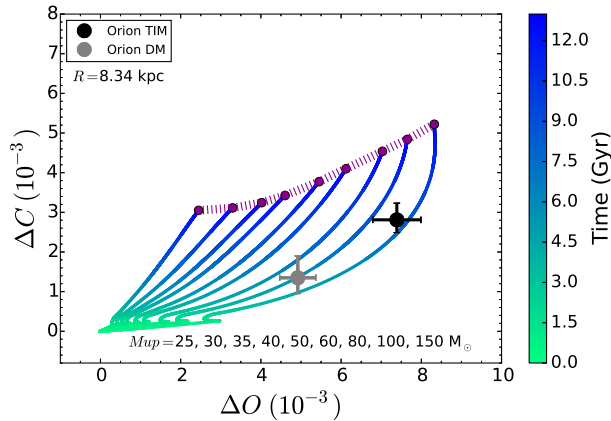


Fig. 5. Chemical evolution for  $C$  and  $O$  for a galactocentric distance of 8.34 kpc (Orion). The curves and points are similar to those in Figure 3. The Orion data should be compared with the magenta line. The color figure can be viewed online.

### 2.5.2. $O$ vs. $C$ for Orion

In Figure 5 we show the theoretical evolution of  $\Delta O$  and  $\Delta C$  vs time for  $R = 8.34$  kpc, for each of our nine  $M_{up}$  values. Moreover, we include the  $\Delta O$  and  $\Delta C$  values for Orion, determined from the DM and the TIM (see Table 3). In this figure, for any given  $M_{up}$ , the evolutionary curves reach lower  $O$  and  $C$  values than the coeval values in Figure 4, because the  $O/H$  and  $C/H$  gradients are negative for all the MW-like models.

By comparing the observed  $C$  values for Orion with the current values derived from our models (see Table 5), we find that neither set of observed  $\Delta C$  abundances (neither DM nor TIM) are consistent with the theoretical predictions. Since the  $\Delta O$  values and determinations are the same as those in Figure 3 it seems that the  $C$  abundance in Orion is lower than expected; however, the  $C/H$  abundance in the Orion nebula is noticeable smaller (about 0.1 dex) than in NGC 3603 ( $R = 8.65$  kpc) and NGC 3576 ( $R = 7.46$  kpc), which are the two H II regions with a galactocentric distance closest to the one of the Orion nebula (Esteban et al. 2004; García-Rojas et al. 2004; García-Rojas et al. 2006). There are two causes that may explain this low value. The first one is the use of an inadequate ionization correction factor (ICF); but according to a recent study on ICFs for giant H II regions (Amayo et al. (2020) in prep.) it is adequate to use  $C/O = C^{++}/O^{++}$  to compute  $C$  abundances. The second one is the possibility of this nebula having more  $C$  atoms deposited in dust grains and thus, a lower gaseous abundance of  $C$ ; a clue that the dust properties in Orion are

different than in other H II regions is the high total to selective absorption ratio present in Orion, that amounts to about  $R_V = E_V/E_{B-V} \approx 5.5$  (Peimbert & Costero 1969; Esteban et al. 2004), while for most other objects it amounts to about  $R_V = 3.1$  (Cardelli et al. 1989). If we consider that Orion could have a slightly higher (0.1 dex) total  $C$  abundance, we find, for the TIM, the total gas plus dust ratio of  $C/H$  for the Orion nebula to be  $12 + \log(C/H) \approx 8.53 \pm 0.08$ ; this value represents a slightly lower  $M_{up}$  than the one derived from  $O/H$ . On the other hand, we find, for the DM, the total  $C/H$  to be  $12 + \log(C/H) \approx 8.22 \pm 0.10$ , still 0.1 dex less than our lowest model, approximately 0.2 dex lower than the  $M_{up} \approx 40 M_\odot$  favored by the  $O/H$  determinations of the DM, and approximately 0.3 dex lower than what is required to be consistent with the more favored  $M_{up} \lesssim 80 M_\odot$  values.

### 3. THE CHEMISTRY HAS A BETTER MEMORY THAN THE LIGHT

The lifetime of massive stars (few Myr) is very short compared to the age of galaxies (several Gyr); consequently, massive stars are not an important component of the light of the majority of the observed galaxies; yet, when massive stars die, their contributions are quickly incorporated into the chemistry of the ISM.

The chemical composition of an H II region is the result of the whole history of the chemical evolution of any given galaxy; therefore the chemical composition of H II regions can be compared with estimates of the present day chemistry derived from galactic CEMs; and we can infer the amount of formed massive stars (equivalently, the  $M_{up}$  value), comparing the chemical abundances in the ISM with those obtained from CEMs.

To study the most massive stars in the MW by looking for them at present has several major inconveniences: there are very few of these stars, this is compounded by the fact that they must be formed in very massive giant molecular clouds (GMCs), and they are the first ones to evolve (first shedding mass in strong stellar winds, and then going supernova, all this before the GMC is dissipated by the combined effect of the stars that are evolving inside it). Thus, they are usually obscured and very difficult to observe during their short lifespan. Moreover, most massive stars that can be observed today may not be representative of the most massive stars that have existed during the evolution of the Galaxy, i.e. the stars that have contributed to the evolution of the

chemistry of the present day ISM as well as the chemistry available during the most recent star formation.

Based on the  $\Delta Y$  comparison, between the observed values (from TIM or DM) and the preset-time predicted values (from CEMs), we cannot exclude any  $M_{up}$  value in the 25 - 150  $M_{\odot}$  range. However, from the  $\Delta O$  comparison, we find agreement for  $M_{up}$  values in the  $30 < M_{up} < 50 M_{\odot}$  range for the DM, and in the  $75 < M_{up} < 120 M_{\odot}$  range for the TIM. Moreover, from the  $\Delta C$  comparison, we find agreement in the  $55 < M_{up} < 95 M_{\odot}$  range for the TIM, and a suggestion of a very small  $M_{up}$  for the DM ( $M_{up} < 25 M_{\odot}$ ). Therefore, by comparing TIM with CEMs, the best  $M_{up}$  values are in the  $70 \lesssim M_{up} \lesssim 100 M_{\odot}$  range; and by comparing DM with CEMs, the best  $M_{up}$  values are in the  $25 \lesssim M_{up} \lesssim 45 M_{\odot}$  range.

Weidner et al. (2013) in their Figure 3 showed the dependence of the star formation rate (SFR) on the integrated galactic stellar initial mass function (IGIMF, called IMF in our CEMs) for different power-law indexes,  $\alpha$ , (for initial stellar masses between 1.3  $M_{\odot}$  and  $M_{up}$ ). They noted that IMF for a SFR  $\approx 1 M_{\odot}/\text{yr}$  corresponds to an  $\alpha = 2.6$  and to an  $M_{up} \approx 100 M_{\odot}$ ; and that these values are in agreement with the MW (we use  $\alpha = 2.7$  for our CEMs). On the other hand, the SFR required to obtain  $M_{up} \approx 40 M_{\odot}$  is SFR  $\approx 10^{-2} M_{\odot}/\text{yr}$  (as well as an  $\alpha \approx 2.8$ ).

Regarding the observational determinations of the SFR: (i) the MW, a spiral galaxy (Sbc) with total stellar mass  $\approx 10^{11} M_{\odot}$ , presents a galaxy-wide SFR  $\approx 0.7 - 2.3 M_{\odot}/\text{yr}$  (Robitaille & Whitney 2010; Chomiuk & Povich 2011); (ii) NGC 300, a small spiral galaxy (Sd) with total stellar mass =  $1.9 \times 10^9 M_{\odot}$ , presents a galaxy-wide SFR =  $0.08 - 0.30 M_{\odot}/\text{yr}$ , approximately an order of magnitude smaller than the SFR in the MW (e.g. Kang et al. 2016, and references therein).

Moreover, based on spatially-resolved spectroscopic properties of low-redshift star-forming galaxies, Sánchez (2019) showed in his Figure 7 a difference of approximately 1 order of magnitude between the SFR of Sbc galaxies with stellar mass  $\approx 10^{11} M_{\odot}$  (as the MW galaxy) and the SFR of Sd galaxies with stellar mass  $\approx 2 \times 10^9 M_{\odot}$  (as NGC 300).

Therefore, the  $M_{up}$  values we derive from the TIM are consistent with the SFR of the MW galaxy, while the  $M_{up}$  values derived from the DM are consistent with a galaxy with a mass and SFR similar to those of NGC 300, but not with the mass and SFR of the MW.

Moreover the abundances derived from the TIM are consistent with those derived from observation of other young objects in the MW (Cepheids, B stars), while the abundances derived from the DM are approximately 0.25 dex too small.

The chemical composition of a given H II region is the result of the evolution of the ISM throughout the history of our Galaxy. Therefore, the chemical abundances of an H II region do not depend on the IMF of the observed H II region. In particular the most massive star of a given H II region is not representative of the most massive stars of the galactic IMF.

#### 4. CONCLUSIONS

We have computed nine chemical evolution models (CEM) of a MW like galaxy; the only difference among these models is the IMF, specifically its  $M_{up}$  value, that ranges between 25 and 150  $M_{\odot}$ . We compare the model predictions with the O/H, He/H, and C/H values derived for three Galactic H II regions: M17, M8, and Orion. We compute the abundances by two different methods: the DM (direct method) and the TIM (temperature independent method); these methods have always given different results. We selected these objects because they probably have the best O/H determinations, and because their galactocentric radii are different enough to be useful as independent constraints for the CEMs (6.2 and 8.34 kpc, respectively). The comparison between models and observations tells us which is the  $M_{up}$  that better fits each set of observations.

It is useful to remember that the chemistry has a better memory than the observed UV light. In other words: the chemistry will explore the average  $M_{up}$  over the lifespan of the MW, while any measurement of the UV radiation or of the most massive stars observed can only be a reflection of the present day  $M_{up}$  (and can potentially have significant biases toward lower masses).

When comparing the models with the DM abundances we find: for  $\Delta O$ , a  $30 < M_{up} < 50 M_{\odot}$  range; for  $\Delta C$ ,  $M_{up} < 25 M_{\odot}$ , while  $Y$  does not provide a significant restriction. Overall, the DM produces preferred values in the  $25 < M_{up} < 45 M_{\odot}$  range. On the other hand, when using the TIM abundances we find: for  $\Delta O$ , a  $52 < M_{up} < 150 M_{\odot}$  range; for  $\Delta C$ , a  $25 < M_{up} < 95 M_{\odot}$  range, while  $Y$  suggests a smaller value, but does not provide a significant restriction. Overall the TIM produces preferred values in the  $70 < M_{up} < 100 M_{\odot}$  range.

Moreover the  $M_{up}$  in a given galaxy is directly related to the SFR, and the SFR is directly related to

the mass of any given galaxy. A MW like galaxy, with a SFR  $\approx 1 M_{\odot}/\text{yr}$ , is expected to have an  $M_{\text{up}} \approx 100 M_{\odot}$ , in good agreement with the TIM determination, but not with the DM determination (which would be more consistent with an Sd galaxy with a SFR  $\approx 0.01 M_{\odot}/\text{yr}$ ).

We are grateful to the referee for excellent suggestions. The authors acknowledge support from PAPIIT (DGAPA-UNAM), grants No. IA-100420, IA-101517, IG-100319, IN-100519, and IN-103820. L.C. is thankful for financial support by CONACYT grant FC-2016-01-1916.

#### REFERENCES

- Akerman, C. J., Carigi, L., Nissen, P. E., et al. 2004, *A&A*, 414, 931
- Carigi, L., & Peimbert, M. 2008, *RMxAA*, 44, 341
- \_\_\_\_\_. 2011, *RMxAA*, 47, 139
- Carigi, L., Peimbert, M., Esteban, C., & García-Rojas, J. 2005, *ApJ*, 623, 213
- Carigi, L., Peimbert, M., & Peimbert, A. 2019a, *ApJ*, 873, 107
- \_\_\_\_\_. 2019b, arXiv:1906.07804
- Cardelli, J. A., Clayton, G. C., & Mathis, J. S. 1989, *ApJ*, 345, 245
- Chomiuk, L., & Povich, M. S. 2011, *AJ*, 142, 197
- Espíritu, J. N., Peimbert, A., Delgado-Inglada, G., & Ruiz M. T. 2017, *RMxAA*, 53, 95
- Esteban, C., Bresolin, F., Peimbert, M., et al. 2009, *ApJ*, 700, 654
- Esteban, C., Carigi, L., Copetti, M. V. F., et al. 2013, *MNRAS*, 433, 382
- Esteban, C., Fang, X., García-Rojas, J., & Toribio San Cipriano, L. 2017, *MNRAS*, 471, 987
- Esteban, C., García-Rojas, J., Peimbert, M., et al. 2005, *ApJ*, 618, 95
- Esteban, C., Mesa-Delgado, A., Morisset, C., & García-Rojas, J. 2016, *MNRAS*, 460, 4038
- Esteban, C., Peimbert, M., García-Rojas, J., et al. 2004, *MNRAS*, 355, 229
- Esteban, C., Peimbert, M., Torres-Peimbert, S., & Escalante, V. 1998, *MNRAS*, 295, 401
- Esteban, C., Toribio San Cipriano, L., & García-Rojas, J. 2018, *cagn.conf*, 23
- Fernández-Martín, A., Pérez-Montero, E., Vílchez, J. M., & Mampaso, A. 2017, *A&A*, 597, 84
- García-Rojas, J. 2020, Reviews in “Frontiers of Modern Astrophysics: From Space Debris to Cosmology” (eds Kabath, Jones and Skarka; publisher Springer Nature) funded by the European Union Erasmus + Strategic Partnership grant “Per Aspera Ad Astra Simul” 2017-1-CZ01-KA203-035562
- García-Rojas, J., Esteban, C., Peimbert, A., et al. 2005, *MNRAS*, 362, 301
- García-Rojas, J., Esteban, C., Peimbert, A. et al. 2007, *RMxAA*, 43, 3
- García-Rojas, J., Esteban, C., Peimbert, M. et al. 2004, *ApJS*, 153, 501
- García-Rojas, J., Esteban, C., Peimbert, M., et al. 2006, *MNRAS*, 368, 253
- García-Rojas, J., Simón-Díaz, S., & Esteban, C. 2014, *A&A*, 571, 93
- García-Rojas, J., Wesson, R., Boffin, H. M. J., et al. 2019, arXiv:190406763
- Hernández-Martínez, L., Carigi, L., Peña, M., & Peimbert, M. 2011, *A&A*, 535, 118
- Kennicutt, R. C. & Evans, N. J. 2012, *ARA&A*, 50, 531
- Kang, X., Zhang, F., Chang, R., Wang, L., & Cheng, L. 2016, *A&A*, 585, 20
- Kroupa, P. 2002, *Sci*, 295, 82
- Mesa Delgado, A., Esteban, C., García-Rojas, J., et al. 2009, *MNRAS*, 395, 855
- Mollá, M., Cavichia, O., Gavilán, M., & Gibson, B. K. 2015, *MNRAS*, 451, 3693
- Nicholls, D. C., Dopita, M. A., & Sutherland R. S. 2012, *ApJ*, 752, 148
- Peimbert, A. & Peimbert, M. 2010, *ApJ*, 724, 791
- Peimbert, M. 1967, *ApJ*, 150, 825
- \_\_\_\_\_. 2019, arXiv: 1905.01244
- Peimbert, M. & Costero, R. 1969, *BOTT*, 5, 3
- Peimbert, M., Peimbert, A., & Delgado-Inglada, G. 2017, *PASP*, 129, 2001
- Peña-Guerrero, M. A., Peimbert, A., & Peimbert, M. 2012, *ApJ*, 756, 14
- Pérez-Montero, E. 2017, *PASP*, 129, 3001
- Planck Collaboration 2018, arXiv:1807.06209
- Prantzos, N., Abia, C., Limongi, M., Chieffi, A., & Cristallo, S. 2018 *MNRAS*, 476, 3432
- Robitaille, T. P. & Whitney, B. A. 2010, *ApJ*, 710, 11
- Rodríguez, M. & García-Rojas, J. 2010, *ApJ*, 708, 1551
- Romano, D., Karakas, A. I., Tosi, M., & Matteucci, F. 2010, *A&A*, 522, 32
- Sánchez, S. F. 2019, arXiv:1911.06925
- Spitoni, E., Silva Aguirre, V., Matteucci, F., Calura, F., & Grisoni, V. 2019, *A&A*, 623, 60
- Torres-Peimbert, S., Peimbert, M., & Peña, M. 1990, *A&A*, 233, 540
- Tsamis, Y. G., Barlow, M. J., Liu, X. W., Danziger, I. J., & Storey, P. J. 2003, *MNRAS*, 338, 687
- Valerdi, M., Peimbert, A., Peimbert, M., & Sixtos, A. 2019, *ApJ*, 876, 98
- Weidner, C., Kroupa, P., Pflamm-Altenburg, J., & Vazdekis, A. 2013, *MNRAS*, 436, 3309

Carigi, L., Delgado-Inglada, G., Peimbert, A., and Peimbert, M.: Instituto de Astronomía, Universidad Nacional Autónoma de México, Apdo. Postal 70-264, México, C.P. 04510, CdMx, México (carigi, gdelgado, antonio, peimbert@astro.unam.mx).

## AN ASTROMETRIC AND PHOTOMETRIC STUDY OF THE INTERMEDIATE-AGE OPEN CLUSTER NGC 2158 AND ITS ECLIPSING BINARY [NBN2015]78

A. E. Abdelaziz<sup>1</sup>, Y. H. M. Hendy<sup>1</sup>, A. Shokry<sup>1</sup>, S. M. Saad<sup>1,2</sup>, F. Y. Kamal<sup>3</sup>, and K. A. Edris<sup>3</sup>

*Received February 24 2020; accepted July 2 2020*

### ABSTRACT

We present a photometric and astrometric analysis of the NGC 2158 cluster using Gaia DR2 and 2MASS data. The cluster age, color excess, intrinsic distance modulus and distance are calculated to be  $t = 2.240 \pm 0.260$  Gyr,  $E(B - V) = 0.420 \pm 0.050$  mag,  $(m - M)_{\odot} = 12.540 \pm 0.130$  mag and  $d_{\odot} = 3224 \pm 200$  pc respectively. The photometric analysis and light curve modelling of the proposed eclipsing binary member [NBN2015]78 is performed using the latest version of the Wilson-Devinney (W-D) code. The solutions show that the system is an over-contact binary with a secondary component filling its Roche lobe, with a mass ratio  $q = 0.262$ . The primary and the secondary components of the system consist of two late spectral types K1 and K2 respectively. The membership of [NBN2015]78 is discussed using two independent methods, and we find that [NBN2015]78 is an interloper and not a member of NGC 2158.

### RESUMEN

Presentamos un análisis fotométrico y astrométrico del cúmulo NGC 2158 con datos de Gaia DR2 y 2MASS. Calculamos la edad del cúmulo, el exceso de color, el módulo intrínseco de distancia y la distancia como  $t = 2.240 \pm 0.260$  Giga-años,  $E(B - V) = 0.420 \pm 0.050$  mag,  $(m - M)_{\odot} = 12.540 \pm 0.130$  mag y  $d_{\odot} = 3224 \pm 200$  pc, respectivamente. Mediante la última versión del código Wilson-Devinney modelamos la curva de luz de la binaria eclipsante [NBN2015]78 propuesta como miembro del cúmulo. Las soluciones muestran que el sistema es una binaria en sobre-contacto, cuya secundaria llena el lóbulo de Roche; el cociente de masas es  $q = 0.262$ . Las dos componentes del sistema son de tipo espectral tardío, K1 y K2. Discutimos la pertenencia de [NBN2015]78 al cúmulo mediante dos métodos independientes, y encontramos que no pertenece a él.

*Key Words:* astrometry — binaries: eclipsing — open clusters and associations: individual: NGC 2158 — stars: individual: [NBN2015]78 — techniques: photometric

### 1. INTRODUCTION

Photometric studies of open clusters in the optical and infrared are fundamental tools for determining their structural parameters. These parameters play an important role towards understanding galactic structure and evolution. NGC 2158 [Melotte 40] is a rich northern open cluster of in-

termediate age, located in the constellation Gemini (Carraro et al. 2002). It has a diameter of about 5' (Lynga et al. 1987). Anderson et al. (2013) estimated a core radius  $R_{cor} = 1'.7$  and a limiting radius  $R_{lim} = 18'.60$ . Bedin et al. (2010) estimated  $\log(\text{age})=9.301$ ,  $E(B - V) = 0.420$  mag,  $(m - M)_{\odot} = 12.980$  mag. Kharchenko et al. (2013) determined  $\log(\text{age}) = 9.330$ ,  $E(B - V) = 0.333$  mag and a heliocentric distance of  $d_{\odot} = 4770$  pc. NGC 2158 is centered at (RA=06:07:25.00, DE=+24:05:48.00) and the eclipsing binary [NBN2015]78 is located at (RA=06:07:38.02, DE=+24:07:24.94), Figure 1 dis-

<sup>1</sup>Astronomy Department, National Research Institute of Astronomy and Geophysics (NRIAG), Helwan, Cairo, Egypt.

<sup>2</sup>Kottamia Center of Scientific Excellence for Astronomy and Space Sciences (KCSSE), STDF No. 5217.

<sup>3</sup>Department of Astronomy and Meteorology, Faculty of Science, Al-Azhar University, Cairo, Egypt.

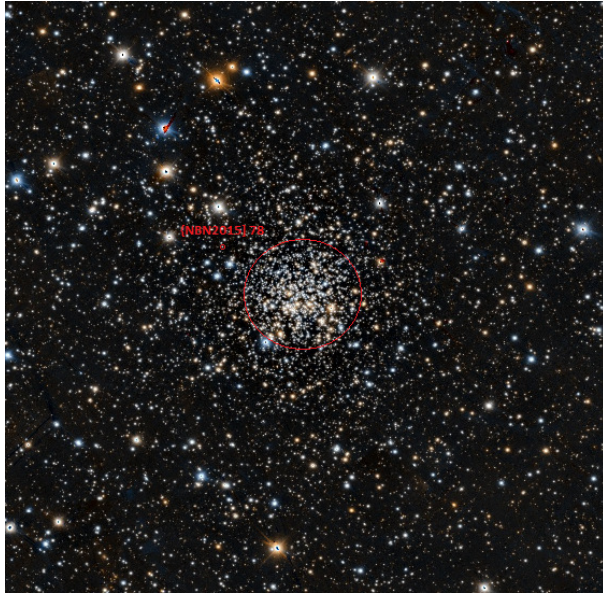


Fig. 1. Color image of the open cluster NGC 2158 from the Pan-STARRS survey (Panoramic Survey Telescope and Rapid Response System). The size of the field of view is  $21' \times 21'$ . The large red circle marks the region of the open cluster NGC 2158, while the small red circle gives the position of the eclipsing binary [NBN2015]78. The color figure can be viewed online.

plays the color image of the cluster using ALADIN (Bonnarel et al. 2000).

Studying eclipsing binary systems in the field and clusters gives valuable information about the physical and absolute parameters of the stars, such as masses and radii. Eclipsing binaries of the W UMa type are very important objects to study the evolutionary state of close binary stars and to characterize their formation. When they are members of a stellar cluster, the distance, age and metallicity of these stars are known independently, which makes them an ideal test for theories of binary structure and evolution. [NBN2015]78 is a poorly studied early-type eclipsing binary star which is located in the field of the open cluster NGC 2158. The designation comes from Nardiello et al. (2015), as it is the number 78 in their catalogue. It is also known as NGC 2158 MSS V60, NGC 2168 HIZ V6, and 2MASS J06073800 +2407249. It is a short period (0.341325 days) eclipsing binary system (Nardiello et al. 2015).

The main aim of this work is to present the photometric and astrometric parameters for the open cluster NGC 2158 and to perform a light curve analysis and modelling of the eclipsing binary [NBN2015]78. This paper is organized as follows: the photometric

and astrometric study of the open cluster NGC 2158 is presented in § 2. The photometric study of the eclipsing binary [NBN2015]78 is presented in § 3. Finally, discussions and conclusions are summarized in § 4.

## 2. PHOTOMETRIC AND ASTROMETRIC STUDY OF THE OPEN CLUSTER NGC 2158

### 2.1. Data and Analysis

In the present work, we use both the GAIA DR2 and 2MASS databases. Astrometric, photometric and spectroscopic measurements of the entire sky have been obtained by the ESA mission Gaia (Gaia Collaboration et al. 2016). The latest version of the Gaia data (Gaia DR2) contains over 1.3 billion sources in three photometric bands ( $G$ ,  $G_{BP}$ ,  $G_{RP}$ ), in addition to their proper motion and parallax (Gaia Collaboration et al. 2018, Lindegren et al. 2018). The limiting  $G$ -band magnitude of Gaia DR2 data is 21 mag. At the bright end ( $G < 14$  mag), the uncertainties reach 0.02 mas in parallax and 0.05 mas/yr in proper motions, while for sources near  $G \sim 21$  mag the uncertainties reach 2 mas and 5 mas/yr respectively. The 2MASS survey is the catalog of choice for astronomical studies near the Galactic plane (Skrutskie et al. 2006). The limiting magnitudes of 2MASS data  $J$  (1.25  $\mu\text{m}$ ),  $H$  (1.65  $\mu\text{m}$ ) and  $K$  (2.17  $\mu\text{m}$ ) are 15.8, 15.1 and 14.3 mag, respectively.

We extracted the data around NGC 2158 inserting the coordinates of the cluster NGC 2158 as RA=06h 07m 25s.00, DEC=+24° 05' 48"00,  $\ell$ =186°634 and  $b$ =+1°781 (Dias et al. 2002) in the Virtual Observatory tool TOPCAT (Taylor 2005), within a radius of  $30'$ . Cross-matching the Gaia DR2 and 2MASS data we obtain a matched number of stars of 17977.

To obtain the best astrometric precision of the proper motions, we used the sources brighter than  $G = 18$  mag, which correspond to typical astrometric uncertainties smaller than 0.3 mas/yr in proper motion (Cantat-Gaudin et al. 2018, Lindegren et al. 2018). Using the Vector Point Diagram (VPD) of the proper motions in RA and DEC, we select the over-density in the cluster region, obtaining 2103 stars (red region on the left panel, Figure 2). To obtain the candidate cluster members, we removed stars from the selected cluster region (red region) if their proper motions in RA and DEC were inconsistent with a median proper motion by more than three median absolute deviations (MAD). The color magnitude diagram (CMD) in the right panel of Figure 2 shows that the candidate members (red dots) fall on

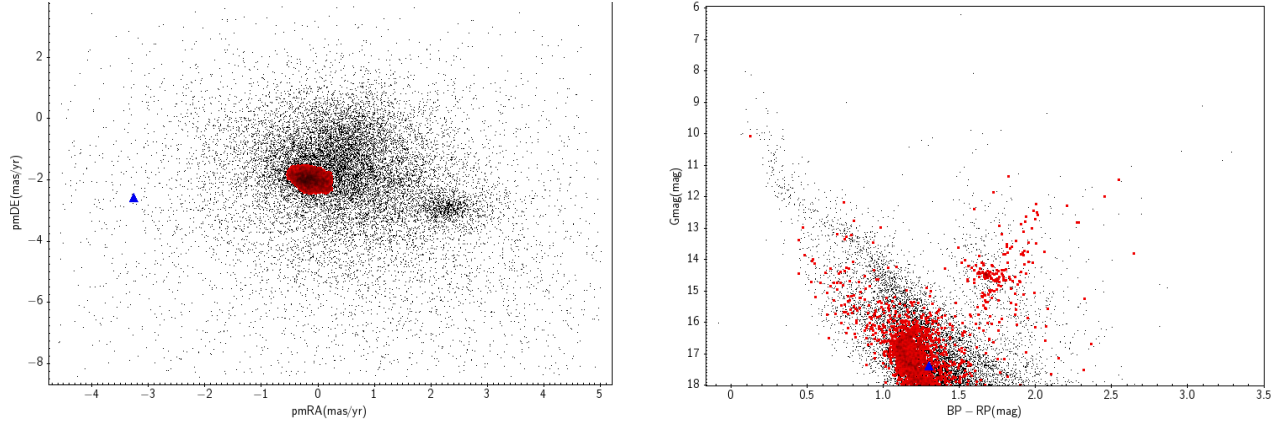


Fig. 2. The left panel shows the Vector Point Diagram (VPD), and the right panel shows the Color Magnitude Diagram (CMD) of the open cluster NGC 2158. The selected red region from the VPD marks the candidate member stars. The blue triangle and the black dots represent the eclipsing binary [NBN2015]78 and the field stars respectively. The red dots on the CMD represent candidate members. The color figure can be viewed online.

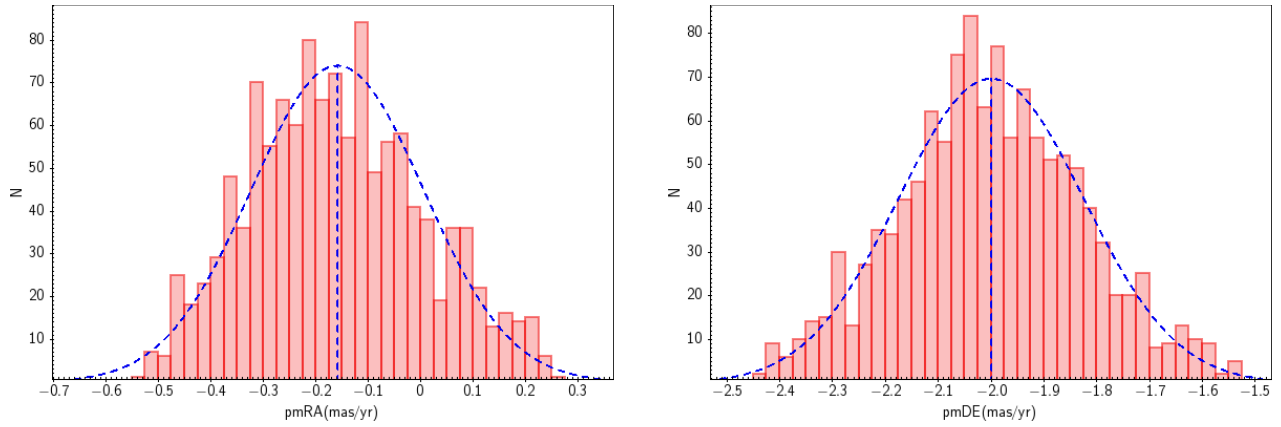


Fig. 3. The histograms of the proper motion in RA (mas/yr) and DEC (mas/yr), and the Gaussian fits are shown as blue dashed lines. The color figure can be viewed online.

a well-defined main sequence. The selected cluster region of the candidate members has a nearly ellipsoidal shape. The equivalent radius  $R_e = \sqrt{a^2 + b^2}$  (with  $a$  and  $b$  the semi-major and semi-minor axes of the ellipse, respectively) of the selected cluster region is 0.7 mas/yr. This value is well within the range of the best-precision Gaia proper motions of 2 mas/yr (Ferreira et al. 2019).

Our membership criterion depends on the chosen overdensity region to define the members of the cluster from the VPD, which obviously is a compromise between losing cluster members and including field stars (see Bisht et al. 2019). To minimize the field contamination, we used the Blob subset from TOPCAT for selecting the cluster region in the VPD. Stars are considered members if they lie inside the

overdensity cluster region in VPD and have proper motions in RA and DEC within  $\pm 3$  MAD from the mean proper motion; they must also have a clear main sequence in the CMD (Figure 2). These stars must be inside the limiting radius and they should have the same direction of proper motion vectors (Figure 4). The cluster members must have the same angular speed in the space.

To determine the mean proper motion of the cluster, we constructed the histograms and made a Gaussian fitting of the proper motions in both directions RA and DEC, see Figure 3. We found that the mean proper motion of NGC 2158 is  $\text{pmRA} = -0.159 \pm 0.165$  mas/yr and  $\text{pmDEC} = -2.000 \pm 0.175$  mas/yr. These values are in good

TABLE 1  
ESTIMATION OF THE  $\text{pmRA}$  AND THE  $\text{pmDEC}$  VALUES OF THE OPEN CLUSTER NGC 2158

Parameter	Values	References
$\text{pmRA}$ (mas/yr)	$-0.159 \pm 0.165$	Present study
	$-0.177 \pm 0.185$	Cantat-Gaudin et al. (2018)
	$+0.002 \pm 0.089$	Loktin and Popova (2017)
	$-0.290$	Kharchenko et al. (2013)
	$+1.430$	Wu et al. (2009)
	$-1.220 \pm 0.190$	Dias et al. (2002)
$\text{pmDEC}$ (mas/yr)	$-2.000 \pm 0.175$	Present study
	$-2.002 \pm 0.173$	Cantat-Gaudin et al. (2018)
	$-0.849 \pm 0.089$	Loktin and Popova (2017)
	$-2.480$	Kharchenko et al. (2013)
	$-3.280$	Wu et al. (2009)
	$-3.300 \pm 0.010$	Dias et al. (2002)

agreement with the values obtained by Cantat-Gaudin et al. (2018), see Table 1.

The measured proper motions of the eclipsing binary [NBN2015]78 in Gaia DR2 are  $\text{pmRA} = -3.252 \pm 0.673$  mas/yr and  $\text{pmDEC} = -2.63 \pm 0.596$  mas/yr with relative uncertainties smaller than 20%. The position of the eclipsing binary [NBN2015]78 in VPD is found to be very far away from the cluster region, close to the main sequence of the CMD (Figure 2). It is clearly seen that the direction of the proper motion vector of [NBN2015]78 in Figure 4 is different from the direction of the cluster members. Therefore, in spite of its position in the color magnitude diagrams in the optical and IR (2MASS, Figure 7) this eclipsing binary does not seem to be a member of the cluster.

## 2.2. Cluster Center and Radius

To determine the cluster center we count the stars in right ascension (RA) and declination (DEC). The center of the open cluster NGC 2158 is calculated at the point where the maximum stellar density of the cluster's area is reached, using a Gaussian fitting. The center of the cluster NGC 2158 is found to be at  $RA = 91^{\circ}866 \pm 0^{\circ}077$  and  $DEC = 24^{\circ}109 \pm 0^{\circ}070$ , and the corresponding Galactic coordinates are  $\ell = 186^{\circ}629$  and  $b = +1^{\circ}796$  (Figure 5). We find that that the difference between our estimation of the centre of the cluster in  $RA$  and  $DEC$  and that of Cantat-Gaudin et al. (2018) is  $14''.4$  and  $0''.60$ , respectively. The difference with the values from Anderson et al. (2013); Wu et al. (2009); Dias et al. (2002) is  $43''.2$  and  $0''.72$ , respectively (Table 2).

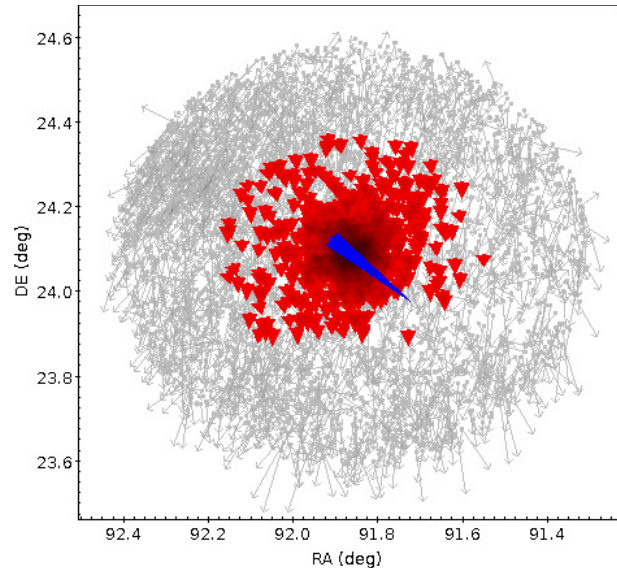


Fig. 4. Projection on the sky of the proper motion vectors. The red vectors (red triangles) represent the cluster members, the blue vector (blue triangle) represents the eclipsing binary [NBN2015]78 and the gray vectors (gray arrows) represent the field stars. The color figure can be viewed online.

To calculate the core and limiting radii, we measure the radial density profile (RDP) of the open cluster NGC 2158, extracting the brightest stars  $G \leq 18$  mag within a square region of side 2 mas/yr around the center of the overdensity in the VPD, see Figure 2. We then divide the square area around the cluster into concentric rings. The stars are counted

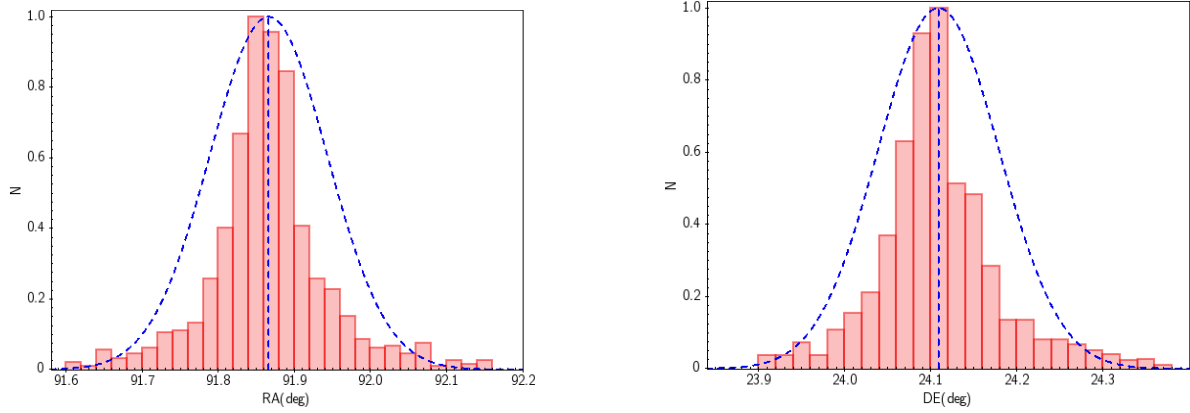


Fig. 5. Inferring the center of NGC 2158 in *RA* (left panel) and *DEC* (right panel). The blue lines are Gaussian fits. The color figure can be viewed online.

TABLE 2

ESTIMATIONS OF THE CENTER OF THE OPEN CLUSTER NGC 2158

Parameter	Values	References
RA (deg)	$91.866 \pm 0.077$	Present study
RA (hh:mm:ss)	06:07:27.84	Present study
	06:07:26.88	Cantat-Gaudin et al. (2018)
	06:07:26.40	Loktin and Popova (2017)
	06:07:25.68	Kharchenko et al. (2013)
	06:07:25.00	Anderson et al. (2013), Wu et al. (2009) Dias et al. (2002)
DEC (deg)	$24.109 \pm 0.070$	Present study
DEC (dd:mm:ss)	24:06:32.40	Present study
	24:05:56.40	Cantat-Gaudin et al. (2018)
	24:05:52.80	Loktin and Popova (2017)
	24:05:31.20	Kharchenko et al. (2013)
	24:05:48.00	Anderson et al. (2013), Wu et al. (2009) Dias et al. (2002)
$\ell$ (deg)	186.629	Present study
	186.635	Cantat-Gaudin et al. (2018)
	186.704	Loktin and Popova (2017)
	186.635	Kharchenko et al. (2013)
	186.634	Anderson et al. (2013), Wu et al. (2009) Dias et al. (2002)
b (deg)	1.796	Present study
	1.788	Cantat-Gaudin et al. (2018)
	1.786	Loktin and Popova (2017)
	1.774	Kharchenko et al. (2013)
	1.781	Anderson et al. (2013), Wu et al. (2009) Dias et al. (2002)

within each ring and their number divided by the area of each ring. A King (1966) model is then fitted to the radial density profile of NGC 2158 as shown in Figure 6.

$$\rho(R) = f_{bg} + \left[ \frac{f_0}{1 + (R/R_{core})^2} \right], \quad (1)$$

where  $f_{bg}$ ,  $f_0$  and  $R_{core}$  are the background density, the central star density and the core radius of the cluster, respectively. The best-fit values are  $f_0 = 67.06 \pm 2.47$  stars/arcmin<sup>2</sup> and  $R_{core} = 1'.70 \pm 0.08$  see Table 3. The limiting radius of NGC 2158 is estimated as  $R_{lim} = 17'.00$ , beyond which stars begin to merge with the background population (see Figure 6, Tadross and HENDY

TABLE 3  
THE RDP PARAMETERS OF THE OPEN CLUSTER NGC 2158

Parameter	Values	Reference
$R_{lim}$ (arcmin)	17.00	Present study
	15.00	Kharchenko et al. (2013)
	18.60	Anderson et al. (2013)
	07.50	Glushkova et al. (2010)
$R_{core}$ (arcmin)	01.70±0.08	Present study
	02.40	Kharchenko et al. (2013)
	01.71	Anderson et al. (2013)
Concentration parameter ( $C$ )	01.00	Present study
$f_0$ (stars/arcmin <sup>2</sup> )	67.06±2.47	Present study

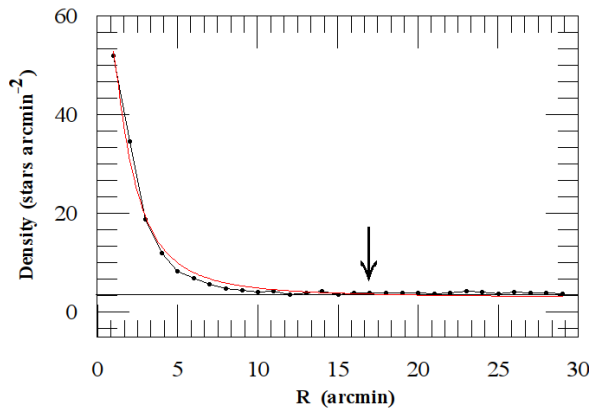


Fig. 6. The radial density profile of NGC 2158. The red curved line is our best-fit King profile). The value of the limiting radius is  $R_{lim} = 17.00$ . The solid line represents the background density. The color figure can be viewed online.

2016; Hendy 2018). Following Peterson and King (1975), we find that the concentration parameter  $C = \log s(R_{lim}/R_{cor})$  of NGC 2158 is  $C = 1.00$ .

Our estimations of the core and limiting radii are in very good agreement with the ones obtained by Anderson et al. (2013) and Kharchenko et al. (2013), see Table 3, but the limiting radius obtained by Glushkova et al. (2010) is significantly smaller than the one we find.

### 2.3. Color Magnitude Diagrams

To obtain photometric data for multi-color magnitude diagrams (MCMDs), we cross-matched our cluster members in Figure 4 with Gaia, 2MASS and  $BV$  data from Nardiello et al. (2015). We obtained 1223 common stars which are members of the cluster. The MCMDs of NGC 2158 are built using optical data from Gaia DR2 [ $G$ , ( $G_{BP} - G_{RP}$ )], Nardiello

et al. (2015) [ $V$ , ( $B - V$ )] and infrared 2MASS data [ $J$ , ( $J - H$ ) and  $J - K$ ], are shown in Figure 7.

To obtain the best fit for each CMD, we use the Padova isochrones of Marigo et al. (2017) with a solar metallicity of 0.0152 (Bressan et al. 2013). Using the turn-off point, we find an age of  $\log \text{age} = 9.350 \pm 0.050$ , that is, and age of  $2.240 \pm 0.260$  Gyr. The extinction ratios used for correcting the magnitudes come from the following transformation equations, based on the work by Cardelli et al. (1989) and O'Donnell (1994):

$$R_V = \frac{A_V}{E(B - V)} = 3.1, \quad (2)$$

$$\frac{A_G}{A_V} = 0.861, \quad (3)$$

$$\frac{A_J}{A_V} = 0.296, \quad (4)$$

$$\frac{A_K}{A_V} = 0.116, \quad (5)$$

and hence

$$\frac{E(B - V)}{E(G_{BP} - G_{RP})} = 0.785, \quad (6)$$

$$\frac{E(B - V)}{E(J - H)} = 2.842, \quad (7)$$

$$\frac{E(B - V)}{E(J - K)} = 1.792. \quad (8)$$

Table 4 lists the comparison between the fundamental parameters of NGC 2158 obtained here and those obtained in other studies. Using the inferred values of the photometric color excess of NGC 2158, we found that  $E(G_{BP} - G_{RP}) = 0.590$ ,  $E(J - H) = 0.160$  and  $E(J - K) = 0.220$ . The mean color excess  $E(B - V)$  and the intrinsic distance modulus  $(m - M)_0$  are  $0.420 \pm 0.050$  mag and

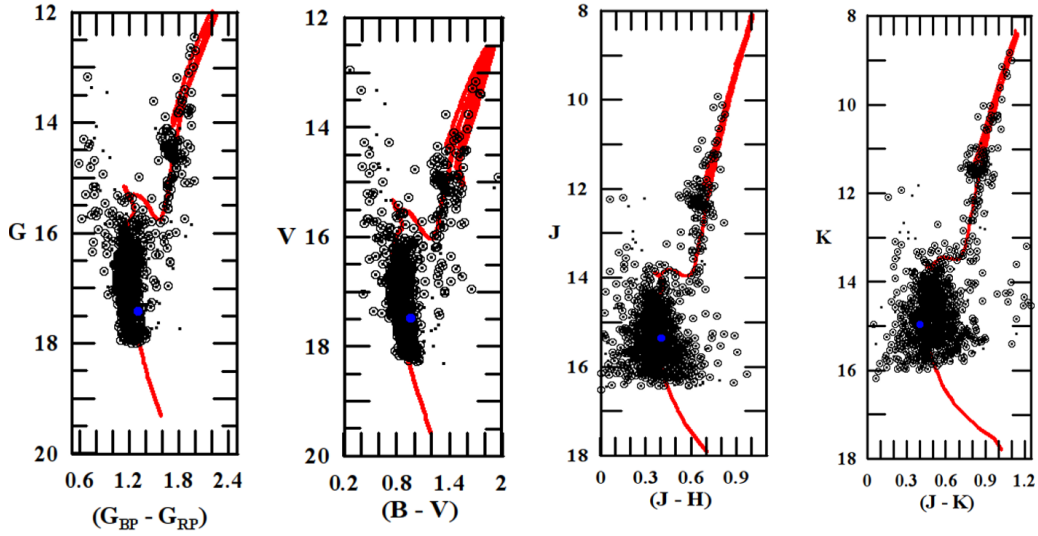


Fig. 7. CMDs of NGC 2158:  $[G - (G_{BP} - G_{RP})]$  from Gaia DR2,  $[V - (B - V)]$  from Nardiello et al. (2015) and  $[J - (J - H) \& J - (J - K)]$  from 2MASS data respectively. The blue circles in the CMDs refer to the position of the eclipsing binary [NBN2015]78. The dots represent 1223 member stars in the optical (Gaia &  $[V - (B - V)]$ ), and the 2MASS data using our criteria. The open circles represent 1031 member stars obtained by Cantat-Gaudin et al. (2018) using their UPMASK code to determine membership probabilities. The color figure can be viewed online.

$12.540 \pm 0.130$  mag respectively.  $E(B - V)$  and  $(m - M)_0$  are in a good agreement with those estimated by Glushkova et al. (2010), Tadross (2001); Loktin et al. (2001); Dias et al. (2002) and Bedin et al. (2010), see Table 4. The distance of NGC 2158 from the Sun is  $d_{\odot} = 3224 \pm 200$  pc, in good agreement with that of Glushkova et al. (2010).

Cantat-Gaudin et al. (2018) calculated the distance of 1229 open clusters by using the UPMASK code of probable cluster members with probabilities larger than 50%. Lindegren et al. (2018) found that the Gaia DR2 parallaxes are affected by a zero-point offset of  $-0.029$  mas. Cantat-Gaudin et al. (2018) reported in their Table 1 (VizieR database reference J/A+A/618/A93) the distance and its uncertainties  $d$ ,  $d_+$  and  $d_-$  as 4535.1, 3119.8 and 8301 pc respectively<sup>4</sup>. We estimate a distance of  $d_{\odot} = 3224 \pm 200$  pc using the best fit of the isochrones in the multi-color magnitude diagrams of optical and 2MASS data (Figure 7), in a good agreement with the smaller value of  $d_+ = 3119.8$  pc of Cantat-Gaudin et al. (2018).

The published parallax of the eclipsing binary [NBN2015]78 in Gaia DR2 is  $\varpi = 2.202 \pm 0.409$  mas, a relative uncertainty smaller than 20%. We determine the distance of this binary as  $d_{EB}(Gaia) =$

454.2 pc using the inverse of the Gaia parallax. This distance to [NBN2015]78 is much smaller than the mean distance to NGC 2158  $d_{\odot} = 3224 \pm 200$  pc, and therefore [NBN2015]78 is a foreground field star and not a cluster member.

Following Tadross (2011) we assume that the Sun lies at distance 8.2 kpc from the Galactic center, and find, for the following parameters: the distance of NGC 2158 from the Galactic center ( $R_{gc}$ ), the projected distances on the Galactic plane from the Sun ( $X_{\odot}$  and  $Y_{\odot}$ ) and the distance from the Galactic plane ( $Z_{\odot}$ ) the values  $R_{gc} = 11407 \pm 394$  pc,  $X_{\odot} = -3201 \pm 278$  pc,  $Y_{\odot} = -372 \pm 32$  pc and  $Z_{\odot} = 101 \pm 009$  pc, respectively. These values for  $R_{gc}$ ,  $X_{\odot}$ ,  $Y_{\odot}$  and  $Z_{\odot}$  are fully consistent with those of Cantat-Gaudin et al. (2018) using  $d_+ = 3119.8$  pc, see Table 4.

### 3. PHOTOMETRIC STUDY OF THE ECLIPSING BINARY [NBN2015]78

#### 3.1. Data Analysis

The photometric analysis of [NBN2015]78 was carried out using the data obtained by Nardiello et al. (2015), using the SBIG STL-11000M camera attached to the Asiago 67/92 cm Schmidt Telescope, available at the Astronomical Observatory of Padova (OAPD-Osservatorio Astronomico di Padova). The

<sup>4</sup> $d_+$  and  $d_-$  are the most likely distances when 0.1 mas is added or subtracted to the maximum likelihood parallax.

TABLE 4  
FUNDAMENTAL PARAMETERS OF NGC 2158

Parameter	Values	References
Solar metallicity	0.0152	Present study
Members (stars)	1223	Present study
	1380	Cantat-Gaudin et al. (2018)
	216	Dias et al. (2002)
log age (yr)	$9.350 \pm 0.050$	Present study
	9.330	Kharchenko et al. (2013)
	$9.300 \pm 0.100$	Glushkova et al. (2010)
	9.301	Chen et al. (2003) & Bedin et al. (2010)
	9.200	Tadross (2001)
$E(B - V)$	$0.420 \pm 0.050$	Present study
	$0.368 \pm 0.021$	Loktin & Popova (2017)
	0.333	Kharchenko et al. (2013)
	$0.340 \pm 0.030$	Glushkova et al. (2010)
	0.420	Bedin et al. (2010)
	0.360	Loktin et al. (2001) & Dias et al. (2002)
	0.400	Tadross (2001)
$E(G_{BP} - G_{RP})$	0.590	Present study
$E(J - H)$	0.160	Present study
	0.107	Kharchenko et al. (2013)
$E(J - K)$	0.220	Present study
	0.160	Kharchenko et al. (2013)
$(m - M)_{\odot}$	$12.540 \pm 0.130$	Present study
	$13.545 \pm 0.082$	Loktin & Popova (2017)
	$12.580 \pm 0.200$	Glushkova et al. (2010)
	12.980	Bedin et al. (2010)
$d_{\odot}$ (pc)	$3224 \pm 200$	Present study
	3119.800	Cantat-Gaudin et al. (2018)
	4770	Kharchenko et al. (2013)
	$3300 \pm 300$	Glushkova et al. (2010)
	5071	Dias et al. (2002), Wu et al. (2009) & Gozha et al. (2012)
	3600	Carraro et al. (2002) & Chen et al. (2003)
$R_{gc}$ (pc)	5012	Tadross (2001)
	$11407 \pm 394$	Present study
	11444	Cantat-Gaudin et al. (2018)
$X_{\odot}$ (pc)	13050	Gozha et al. (2012)
	$-3201 \pm 278$	Present study
	-3097	Cantat-Gaudin et al. (2018)
	-13035	Wu et al. (2009)
$Y_{\odot}$ (pc)	-5035	Gozha et al. (2012)
	$-372 \pm 032$	Present study
	-360	Cantat-Gaudin et al. (2018)
$Z_{\odot}$ (pc)	-586	Wu et al. (2009) & Gozha et al. (2012)
	$101 \pm 009$	Present study
$Z_{\odot}$ (pc)	97.300	Cantat-Gaudin et al. (2018)
	158	Wu et al. (2009) & Gozha et al. (2012)

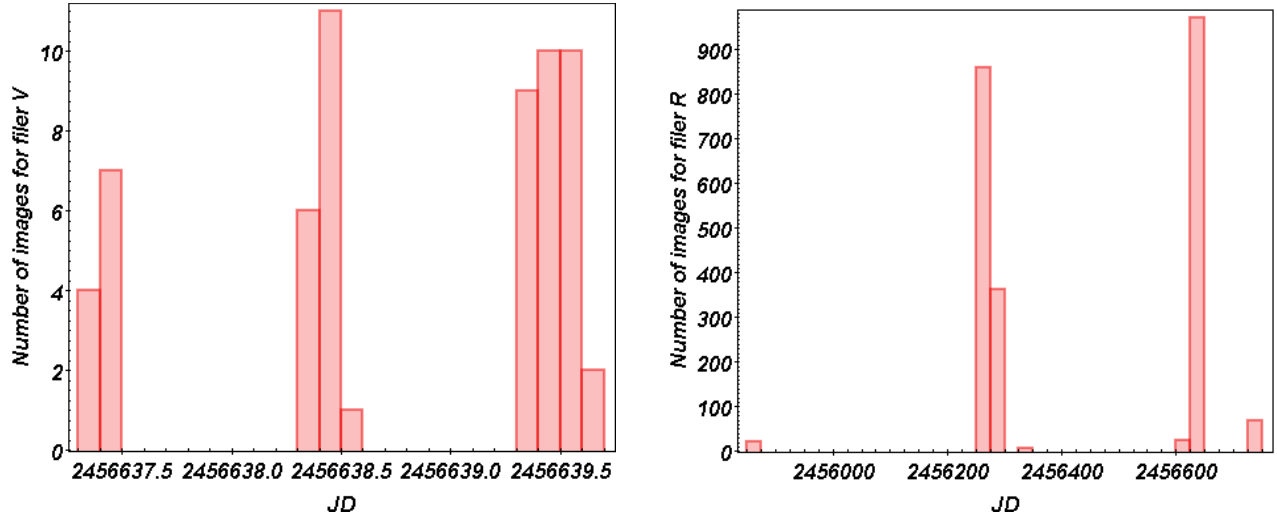


Fig. 8. Histogram of the number of images collected per night during the three campaigns. The histograms refer to observations in the  $V$  and  $R$  filters. The color figure can be viewed online.

TABLE 5  
LOG OF OBSERVATIONS

Filter	# Images	Exp. time (s)	FWHM (arcsec)	Median FWHM (arcsec)
$V$	60	180	1.24-2.05	1.43
$R$	1385	15	1.35-6.34	2.75
	27	120		
	2552	180		

$V$ ,  $R$  data were collected from a number of images gathered over the three seasons. Table 5 presents the total number of observations in each filter as obtained from Nardiello et al. (2015) and Figure 8 shows the histogram of the observations in each filter.

The period and the times of primary (I) and secondary (II) minima of [NBN2015]78 were obtained for the  $V$  and  $R$  filters (see Table 6). Using the method of Kwee and Woerden (1956), we infer that the new ephemeris for the system is given by

$$\text{HJD}(MinI) = 2456639.55464 \pm 0.0015 + 0.341325^d \times E, \quad (9)$$

where  $E$  is the integer number of cycles. This ephemeris is used to calculate the phases and to draw the light curves in the  $V$  and  $R$  bands as shown in Figure 9.

### 3.2. Light Curve Analysis

The light curve analysis of the system [NBN2015]78 is performed using the light curves in both  $V$  and

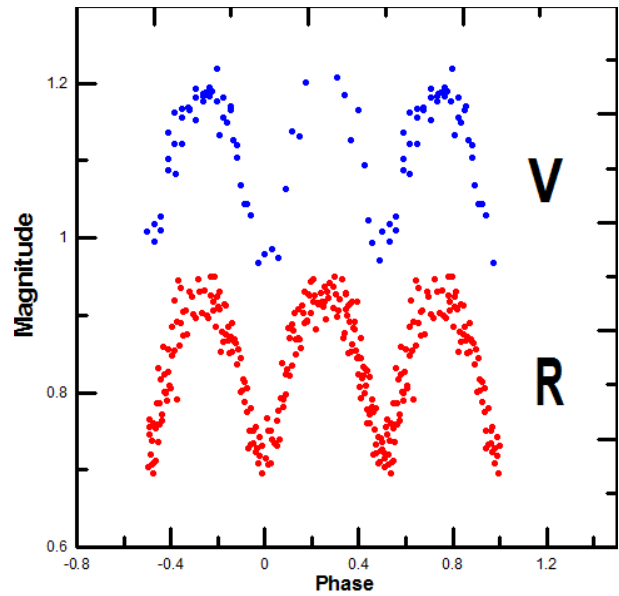


Fig. 9. The observed phase diagram of [NBN2015]78 in the  $V$  and  $R$  filters. The color figure can be viewed online.

$R$  bands and is carried out using the program of Wilson-Devinney (W-D, Nelson 2009; Wilson and Devinney 1971). We assumed gravity darkening and bolometric albedo exponents appropriate for the convective envelopes of late-type stars ( $T_{\text{eff}} < 7500 \text{ K}$ ). We adopted  $g_1 = g_2 = 0.32$  (Lucy 1967) and  $A_1 = A_2 = 0.5$  (Rucinski 1969). The limb-darkening coefficients were interpolated from the tables of van

TABLE 6  
TIMES OF PRIMARY AND SECONDARY  
MINIMA OF [NBN2015]78

Filter	MinI	MinII
V	2456639.555 ± 0.002	2456638.351 ± 0.0001
R	2456639.547 ± 0.002	2456639.384 ± 0.0002

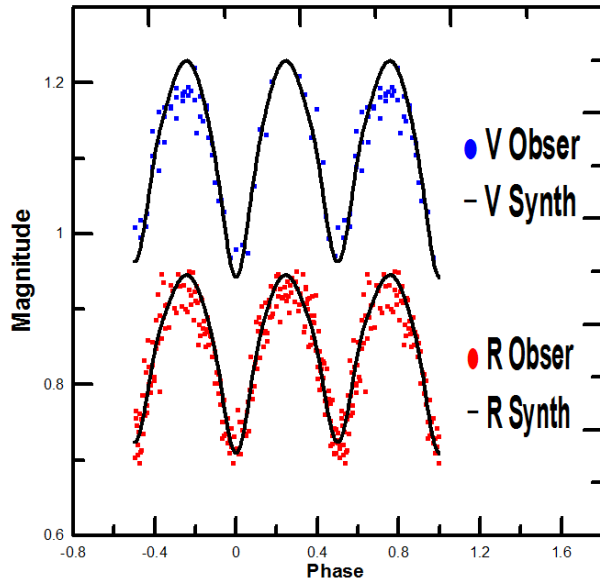


Fig. 10.  $V$ ,  $R$  filters for the system [NBN2015]78 as fitted with the synthetic model (solid line). The color figure can be viewed online.

Hamme (1993) using the logarithmic law and the values  $X_1 = X_2$  and  $Y_1 = Y_2$  for the over-contact mode. The effective temperature of the primary star ( $T_1$ ) is adopted as 4925 K (Flower 1996), corresponding to a  $B-V$  color index of 0.959 from the combined light of both components (Nardiello et al. 2015). The adjusted parameters are the orbital inclination ( $i$ ), the mean temperature of the secondary star ( $T_2$ ), the potential of the two components  $\Omega = \Omega_1 = \Omega_2$ , the mass ratio ( $q$ ), and the luminosity of the primary star ( $L_1$ ). We used Mode 3 in the Wilson-Devinney (W-D) program (over-contact mode not in thermal contact). The orbital solutions using both  $V$  and  $R$  light curves are performed and the accepted parameters are listed in Table 7. Figure 10 shows the best match between the model and the observed light curves. The solution shows that the primary component is the more massive and the hotter one, with a difference in effective temperature equal to 145 K. According to this solution, the two components of

TABLE 7  
THE ORBITAL SOLUTION FOR [NBN2015]78 IN  
 $V$  AND  $R$  BANDS

Parameter	$V$	$R$
$\lambda$ (Å)	5500	7000
$T_1$ (K)	4925	4925
$T_2$ (K)	4780 ± 107	4760 ± 062
$q$	0.263 ± 0.035	0.262 ± 0.010
$\Omega_1 = \Omega_2$	2.354 ± 0.075	2.374 ± 0.023
$g_1 = g_2$	0.320	0.320
$A_1 = A_2$	0.500	0.500
$X_1 = X_2$	0.643 ± 0.076	0.643 ± 0.028
$Y_1 = Y_2$	0.160	0.160
$i$ (°)	69.530 ± 2.900	67.500 ± 1
r pole1	0.468	0.473
r side1	0.505	0.512
r back1	0.530	0.538
r pole2	0.253	0.259
r side2	0.264	0.270
r back2	0.297	0.308
$\frac{L_1}{L_1+L_2}$	0.797 ± 0.050	0.799 ± 0.020
$\sum(o-c)^2$	0.020	0.160

TABLE 8  
ABSOLUTE PHYSICAL PARAMETERS FOR  
[NBN2015]78

Element	$M(M_\odot)$	$R(R_\odot)$	$T(T_\odot)$	$L(L_\odot)$	$M_{bol}$	$Sp.type$
Primary	0.817	0.912	0.852	0.439	5.588	K1
Secondary	0.214	0.858	0.827	0.345	5.849	K2

[NBN2015]78 are of spectral types K1 and K2 (Covey 2007).

Figure 11 shows the geometric configuration of [NBN2015]78 at different phases and the corresponding Roche lobe geometry. The absolute physical parameters of the system are calculated using the empirical relations of Harmanec (1988). The mass of the primary component  $M_1 = 0.817 M_\odot$ , while the mass of the secondary component is directly calculated from the estimated mass ratio of the system ( $q = M_2/M_1$ ) as  $M_2 = 0.214 M_\odot$ . The radii of the two components  $R_1(R_\odot)$ ;  $R_2(R_\odot)$  and the bolometric magnitudes  $M_{1bol}$  and  $M_{2bol}$  also calculated and listed in Table 8.

### 3.3. Evolutionary Status of [NBN2015]78

Using the calculated physical parameters listed in Table 8 we investigated the current evolutionary sta-

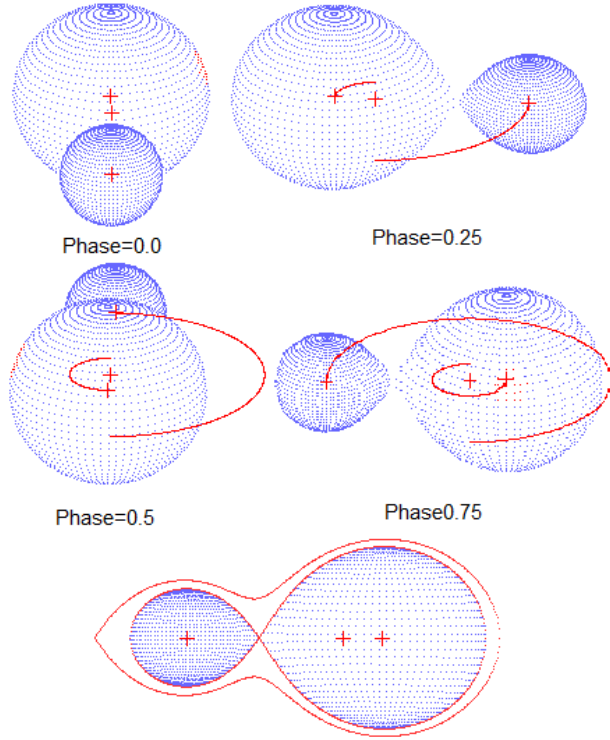


Fig. 11. Geometric configuration at different phases of [NBN2015]78. The color figure can be viewed online.

tus of the system. Figure 12 shows the components of the system in the mass-luminosity ( $M$ - $L$ , left panel), mass-radius ( $M$ - $R$ , middle panel) and mass-temperature ( $M$ - $T$ , right panel) relations, along with evolutionary tracks computed by Mowlavi et al. (2012) for both zero age main sequence (ZAMS) and terminal age main sequence (TAMS) with solar metallicity ( $Z_{\odot} = 0.014$ ).

The right panel also shows the location of the components on the empirical  $M - T_{\text{eff}}$  relation for intermediate mass stars from Malkov (2007). As it is clear from Figure 12 (left and middle panels) the primary component is lying on the ZAMS track while the secondary component is an evolved star.

#### 4. DISCUSSION AND CONCLUSIONS

Using a combination of all the available photometric and astrometric data from the Gaia DR2 and 2MASS catalogues, we presented the optical, near-IR photometric and astrometric properties of the intermediate-age open cluster NGC 2158 and an eclipsing binary system [NBN2015]78 which is found within the same field. The main results of this study can be summarized as follows:

- The cluster membership investigation was performed using a criterion based on the high-

precision Gaia proper motions. We found 1223 member stars in Gaia, 2MASS and the BV catalogue of Nardiello et al. (2015), 1031 of which being in the catalog of Cantat-Gaudin et al. (2018) with high membership probabilities, above  $> 60\%$ .

- Using multi-color magnitude diagrams (Gaia DR2, optical BV, 2MASS), we determined the age, colour excess and distance of NGC 2158 as  $2.240 \pm 0.260$  Gyr,  $0.420 \pm 0.050$  mag and  $3224 \pm 200$  pc, respectively.
- Using the high-precision Gaia proper motions, we found that the position of the eclipsing binary [NBN2015]78 in VPD is very far away from the cluster region. It is clearly seen that the direction of the proper motion vector of [NBN2015]78 is different from the direction of the cluster members.
- We analyzed the light curves in the  $V$  and  $R$  bands of the system [NBN2015]78 using the W-D code to obtain the geometric and photometric parameters of the system.
- The [NBN2015]78 system is an over-contact binary with a fill-out factor= $17.5\%$  and a low mass ratio  $q = 0.262$ .
- The system is classified as being of the A-subtype and the components have spectral types K1 and K2.
- The positions of both components of [NBN2015]78 in the mass-radius and mass-luminosity relations reveal that the primary component is a main sequence star while the secondary is an evolved component.
- The distance to [NBN2015]78 is 454.2 pc, while the mean distance to the NGC2158 is equal to  $3224 \pm 200$  pc, so we can confirm that the binary system [NBN2015]78 is definitely one of the foreground field stars.

A series of new photometric and spectroscopic observations of [NBN2015]78 is highly recommended for a detailed study of its period stability and to determine more precise physical parameters.

The research is supported by the National Research Institute of Astronomy and Geophysics (NRIAG) and the Science and Technology Development Fund (STDF No. 5217). This work also is supported by the IMHOTEP collaboration program

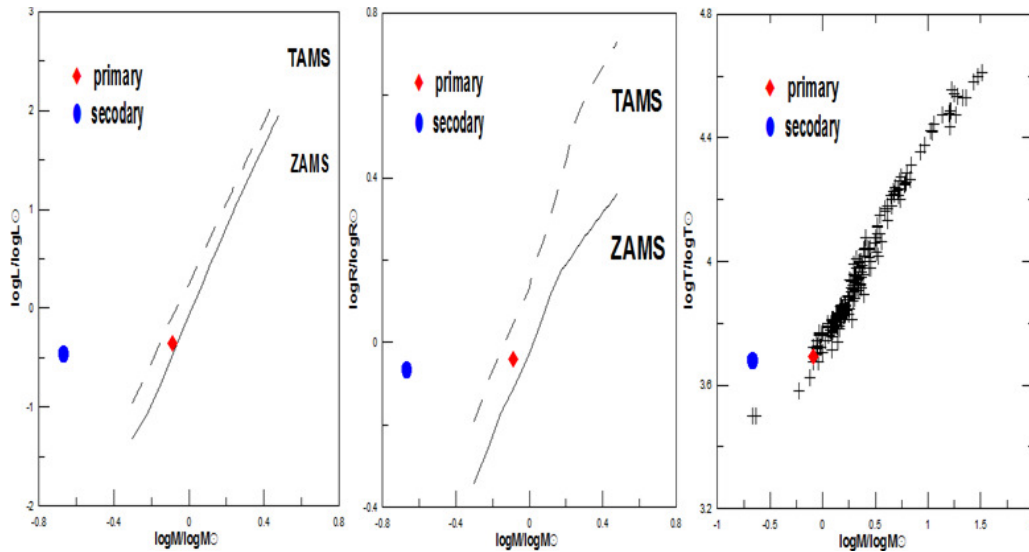


Fig. 12. The position for the components of the system on the mass-luminosity (left), mass-radius (middle) and empirical  $M - T_{\text{eff}}$  relation (right) for intermediate mass stars. The color figure can be viewed online.

No. 42088ZK between Egypt and France. We are grateful to the Academy of Scientific Research and to the Service of Scientific Cooperation in both countries for giving us the opportunity to work through this project and providing the necessary support to accomplish our scientific goals. The criticism of the first version of this article by the anonymous referee and the revision of the text done by Prof. David Valls-Gabaud greatly helped us to improve the article and the arguments, and the authors gratefully appreciate this effort. The authors also are very grateful to I. Zead and M. Darwish for helpful discussions. This work has made use of data from the European Space Agency (ESA) mission Gaia <https://www.cosmos.esa.int/gaia>, processed by the Gaia Data Processing and Analysis Consortium (DPAC, <https://www.cosmos.esa.int/web/\gaia/dpac/consortium>). Funding for the DPAC has been provided by national institutions, in particular the institutions participating in the Gaia Multilateral Agreement. This publication makes use of data products from the Two Micron All Sky Survey, which is a joint project of the University of Massachusetts and the Infrared Processing and Analysis Center/California Institute of Technology, funded by the National Aeronautics and Space Administration and the National Science Foundation. This work has made use of TOPCAT <http://www.starlink.ac.uk/topcat>. It has been developed mostly in the UK within various UK and Euro-VO projects (Starlink, AstroGrid, VOTech, AIDA, GAVO, GENIUS,

DPAC) and under PPARC and STFC grants. Its underlying table processing facilities are provided by the related packages STIL and STILTS. This research has made use of VizieR catalogue access tool, CDS, Aladin sky atlas developed at CDS, Strasbourg Observatory, France.

## REFERENCES

- Anderson, R. I., Eyer, L., & Mowlavi, N. 2013, *MNRAS*, 434, 2238
- Bedin, L. R., Salaris, M., King, I. R., et al. 2010, *ApJ*, 708, 32
- Bisht, D., Yadav, R. K. S., & Ganesh, S. 2019, *MNRAS*, 482, 1471
- Bonnarel, F., Fernique, P., Bienaymé, O., et al. 2000, *A&AS*, 143, 33
- Bressan, A., Marigo, P., Girardi, L., Nanni, A., & Rubele, S. 2013, *EPJWC*, 43, 03001
- Cantat-Gaudin, T., Jordi, C., Vallenari, A., et al. 2018, *A&A*, 618, 93
- Cardelli, J. A., Clayton, G. C., & Mathis, J. S. 1989, *ApJ*, 345, 245
- Carraro, G., Girardi, L., & Marigo, P. 2002, *MNRAS*, 332, 705C
- Chen, L., Hou, J. L., & Wang, J. J. 2003, *AJ*, 125, 1397C
- Covey, K. R., Ivezić, Ž., Schlegel, D., et al. 2007, *AJ*, 134, 2398
- Dias, W. S., Alessi, B. S., Moitinho, A., & Lepine, J. R. D. 2002, *A&A*, 389, 871
- Ferreira, Filipe A., Santos, J. F. C., Corradi, W. J. B., et al. 2019, *MNRAS*, 483, 5508F
- Flower, P. J. 1996, *ApJ*, 469, 355

- Gaia Collaboration, Prusti, T., de Bruijne, J. H. J., et al. 2016, *A&A*, 595, A1
- Gaia Collaboration, Brown, A. G. A., Vallenari, A., et al. 2018, *A&A*, 616, A1
- Glushkova, E. V., Koposov, S. E., Zolotukhin, I. Yu, et al. 2010, *AstL*, 36, 75
- Gozha, M. L., Borkova, T. V., & Marsakov, V. A. 2012, *AstL*, 38, 506
- Harmanec, P. 1988, *BAICz*, 39, 329
- Hendy, Y. H. M. 2018, *JAsGe*, 7, 180H
- Kharchenko, N. V., Piskunov, A. E., Schilbach, E., et al. 2013, *A&A*, 558, 53
- King, I. R. 1966, *AJ*, 71, 64
- Kwee, K. & Van Worden, H. 1956, *BAN*, 12, 327
- Lindgren, L., Hernandez, J., Bombrun, A., et al. 2018, *A&A*, 616, A2
- Loktin, A. V., Gerasimenko, T. P., & Malysheva, L. K. 2001, *A&AT*, 20, 607
- Loktin, A. V. & Popova, M. E. 2017, *AstBu*, 72, 257
- Lucy, L. 1967, *ZA*, 65, 89
- Lynga, G. 1987, *The Open Star Clusters Catalogue*, 5th edition: (<http://cdsarc.u-strasbg.fr/viz-bin/VizieR?-meta.foot&-source=VII/92A>)
- Malkov, O. Yu. 2007, *MNRAS*, 382, 1073
- Marigo, P., Girardi, L., Bressan, A., et al. 2017, *ApJ*, 835, 77
- Mowlavi, N., Eggenberger, P., Meynet, G., et al. 2012, *A&A*, 541, 41
- Nardiello, D., Bedin, L. R., Nascimbeni, V., et al. 2015, *MNRAS*, 447, 3536
- Nelson, R. H. 2009, *WDwint56a*, available from: (<https://www.variablestarsouth.org/bob-nelson>)
- O'Donnell, J. E. 1994, *ApJ*, 422, 158
- Peterson, C. J. & King, I. R. 1975, *AJ*, 80, 427
- Ruciński, S. M. 1969, *AcA*, 19, 125
- Saad, M. S., Darwish, M. S., Nasser, M. A., et al. 2016, *NewA*, 47, 24S
- Skrutskie, M. F., Cutri, R. M., Stiening, R., et al. 2006, *AJ*, 131, 1163
- Stassun, K. G. & Torres G. 2018, *ApJ*, 862, 61S
- Tadross, A. L. 2001, *NewA*, 6, 293
- \_\_\_\_\_. 2011, *JKAS*, 44, 1
- Tadross, A. L. & Hendy, Y. H. M. 2016, *JKAS*, 49, 53T
- Taylor, M. B. 2005, *ASPC*, 347, 29
- Van Hamme, W. 1993, *AJ*, 106, 2096
- Wilson, R. E. & Devinney, E. J. 1971, *ApJ*, 166, 605
- Wu, Z-Y., Zhou, X., Ma, J., & Du, C-H. 2009, *MNRAS*, 399, 2146

A. E. Abdelaziz, Y. H. M. Hendy, S. M. Saad, and A. Shokry: Astronomy Department, National Research Institute of Astronomy and Geophysics (NRIAG), Helwan, Cairo, Egypt (abdelazizeid3, y.h.m.hendy@gmail.com).

K. A. Edris and F. Y. Kamal: Department of Astronomy and Meteorology, Faculty of Science, Al-Azhar University, Cairo, Egypt.

S. M. Saad: Kottamia Center of Scientific Excellence for Astronomy and Space Sciences (KCSCE), STDF No. 5217.

## PHOTOMETRIC STUDY OF THREE SHORT PERIOD VARIABLE STARS<sup>1</sup>

J. H. Peña<sup>2,3,4</sup>, S. B. Juárez<sup>4</sup>, A. A. Soni<sup>2,4</sup>, H. Huepa<sup>3</sup>, A. Rentería<sup>2,3,4</sup>, and A. L. Zuñiga<sup>4</sup>

*Received November 26 2019; accepted July 29 2020*

### ABSTRACT

We have obtained *uvby*– $\beta$  photoelectric photometry with the 0.84 m telescope at the San Pedro Mártir Observatory, México, for the stars HD 115520, HD 220735 and HD 26738. The first two had been previously determined to be variables whereas the last one is being reported here as a new variable. With an extended time basis for the first two, we have determined their period of pulsation, which is found to be stable. Physical parameters are presented for the three stars.

### RESUMEN

Se obtuvo fotometría fotoeléctrica *uvby* –  $\beta$  con el telescopio de 0.84 m del Observatorio de San Pedro Mártir, México, de las estrellas HD115520, HD 220735 y HD 26738; las primeras dos ya se habían determinado como variables mientras que la última se reporta aquí por primera vez como variable. Con la base de tiempo ampliada de las dos primeras determinamos sus períodos de pulsación, que se encuentran estables. Se presentan parámetros físicos para las tres estrellas.

*Key Words:* stars: variables: delta Scuti — stars: variables: general — techniques: photometric

### 1. INTRODUCTION

Knowledge of the nature of variable stars can be achieved with only a few hours of observation, but a more profound understanding can be attained solely through continuous monitoring. For this reason it is important for them to be observed and reported. A previous study (Fox Machado et al. 2007) confirmed the variable nature of HD 115520 as a  $\delta$  Scuti star, a state which had been previously determined by Peña et al. (2007). In this paper we present unpublished observations of this star which were carried out in 2013; these data permitted the analysis of the periodic content with an extended time baseline. Analogously, HD 220735 was found to be variable, and was reported in Peña et al. (2019) with observational data from 2016. A new set of observations over two nights in 2018 is presented in the current paper. The new period analysis establishes that, as in the case of HD 115520, two close frequencies pro-

voke modulation in its light curve. HD 26738 was found to be a new, previously unreported, variable star.

### 2. OBSERVATIONS

These were all done at the Observatorio Astronómico Nacional de San Pedro Mártir, México (SPM). The 0.84 m telescope, to which a *uvby* –  $\beta$  spectrophotometer was attached, was utilized at all times. Table 1 lists the log of the observations.

#### 2.1. Data Acquisition and Reduction

A well-defined and calibrated *uvby* –  $\beta$  data set provides an efficient way to investigate the pulsational nature of the stars as well as the physical conditions, such as effective temperature and surface gravity, by comparing the unreddened indexes obtained with the theoretical models. The calibrations for unreddening have already been described and used in previous analyses (Peña & Peniche; 1994; Peña & Sareyan, 2006).

As was stated in Peña et al. (2016) reporting on BO Lyn, the observational pattern, as well as the reduction procedure, have been employed at the SPM Observatory since 1986 and hence, have been described repeatedly. A detailed description of the methodology can be found in Peña et al. (2007).

<sup>1</sup>Based on observations collected at the San Pedro Mártir Observatory, México.

<sup>2</sup>Instituto de Astronomía, Universidad Nacional Autónoma de México, México.

<sup>3</sup>Observatorio Astronómico Nacional de Tonantzintla, México.

<sup>4</sup>Facultad de Ciencias, Universidad Nacional Autónoma de México, México.

TABLE 1  
LOG OF THE OBSERVATIONS

Date YYYY/MM/DD	Target 1	Target 2	Target 3	HJD - 2450000(day)
2013/06/23	HD115520	NGC 6913	RRs	7687
2013/06/24	HD115520	NGC 6913		7688
2013/06/25	HD115520	NGC 6913		7689
2013/06/26	HD115520		RRs	7690
2018/10/28	HD220735	GP And		8419
2018/10/31	HD220735		Cephs	8422
2018/11/01	HD220735	GP And		8423
2018/11/02		GP And	Cephs	8424
2018/11/03		V479 Tau	Cephs	8425
2018/11/04	HD26738			8426

TABLE 2  
TRANSFORMATION COEFFICIENTS OBTAINED FOR THE OBSERVED SEASONS

Season	B	D	F	J	H	I	L
June 2013	-0.016	0.974	1.028	0.009	1.049	0.162	-1.345
$\sigma$	0.052	0.018	0.040	0.022	0.034	0.030	0.054
Oct 2018	0.021	0.989	1.028	-0.017	1.019	0.180	-1.398
$\sigma$	0.062	0.007	0.026	0.017	0.020	0.032	0.034

The observations were done over two different seasons. HD 115520 was observed in 2013, mostly in *uvby* without  $H\beta$  measurements, whereas the other two stars, HD 220735 and HD 26738, were observed in 2018 in *uvby* -  $\beta$ . Nevertheless, in both seasons the procedure was the same: at least five ten-second integrations of each star and one ten-second integration of the sky for the *uvby* filters as in the narrow and wide filters that define  $H\beta$  were taken for each measurement. The time difference between the two sets is 0.0006 d. What must be emphasized here are the transformation coefficients for the observed seasons (Table 2) and the season errors, which were evaluated using the observed standard stars.

The best way to determine the accuracy of our observations is through the differences in magnitude and color indexes ( $V$ ,  $b - y$ ,  $m_1$ ,  $c_1$  and  $H\beta$ ) of the standard stars. In the 2013 season, 373 data points of sixteen standard stars were measured. The corresponding standard deviations of the mean values for ( $V$ ,  $b - y$ ,  $m_1$ ,  $c_1$ ) were (0.019, 0.006, 0.007 and 0.014). In the 2018 season thirty-four standard stars were measured for a total of ninety-four points in *uvby* and 68 points in  $H\beta$ , respectively; the calcu-

lated uncertainties were (0.054, 0.012, 0.019, 0.025, 0.012), which provide a numerical evaluation of our uncertainties. Emphasis is made on the large range of the standard stars in the magnitude and color indexes values in both seasons:  $V$ :(5.62, 8.00); ( $b - y$ ): (-0.09, 0.88);  $m_1$ :(-0.09, 0.67);  $c_1$ :(-0.02, 1.32) and  $H\beta$ : (2.50, 2.90) for the 2018 season. Similar ranges were obtained in the 2013 season.

To verify the consistency of the data from our derived standard star values, mean values for each one, as well as their standard deviations were calculated. For the 2018 season these are presented in Table 3 by decreasing brightness. The last column of this table is  $N$ , the number of entries.

Table 4 lists the photometric values obtained of HD 26738. In this table Column 1 reports the time of the observation in HJD, Columns 2 to 5 list the Strömgen values  $V$ , ( $b - y$ ),  $m_1$  and  $c_1$ , respectively; Column 6,  $H\beta$ . The photometry of the other two stars has been sent to the Variable Star Index (VSX) for publication, and is also available upon request. The photometry of the light curves of the variables in the  $V$  filter is presented in Figures 1, 2 and 3.

TABLE 3  
MEAN PHOTOMETRIC VALUES AND STANDARD DEVIATIONS OF THE STANDARD STARS OF THE 2018 SEASON

ID	V	$(b - y)$	$m_1$	$c_1$	$\beta$	$\sigma V$	$\sigma(b - y)$	$\sigma m_1$	$\sigma c_1$	$\sigma \beta$	N
HR8085	5.195	0.669	0.650	0.167	2.529	0.054	0.014	0.033	0.020	0.018	6
HD013871	5.763	0.275	0.180	0.513	2.664	0.052	0.009	0.021	0.008	0.014	4
HD057006	5.887	0.354	0.111	0.525							1
HD035520	5.901	0.138	0.071	1.331	2.720	0.014	0.003	0.004	0.003	0.024	4
HD015335	5.917	0.367	0.167	0.386	2.594	0.076	0.004	0.005	0.006	0.019	4
HD224165	5.965	0.718	0.539	0.236							1
HD033203	5.996	0.619	-0.185	0.005	2.597	0.024	0.008	0.016	0.012	0.025	5
HR8086	6.053	0.811	0.636	0.102	2.513	0.104	0.006	0.014	0.009	0.016	6
HD202314	6.201	0.689	0.451	0.297	2.618	0.111	0.006	0.011	0.007	0.020	6
HD015596	6.219	0.560	0.273	0.392	2.547	0.051	0.002	0.003	0.005	0.010	4
HD221661	6.224	0.602	0.414	0.353							1
HD033632	6.480	0.340	0.146	0.353	2.647	0.033	0.006	0.011	0.009	0.027	5
HD028354	6.534	0.008	0.115	0.793	2.809	0.020	0.010	0.017	0.011	0.011	4
HR8389	6.550	0.032	0.115	1.122	2.818	0.014	0.007	0.012	0.005	0.004	6
HD013936	6.583	0.019	0.141	1.128	2.798	0.090	0.006	0.008	0.009	0.015	4
HD043461	6.617	0.015	0.063	0.583	2.668	0.042	0.009	0.016	0.012	0.027	4
HD042089	6.626	0.582	0.335	0.535	2.627	0.037	0.004	0.010	0.011	0.004	4
HD012884	6.764	0.087	0.215	0.899	2.866	0.076	0.003	0.006	0.009	0.029	4
HD018066	6.956	0.755	0.557	0.328	2.560	0.055	0.004	0.004	0.008	0.018	4
HD044812	6.998	0.667	0.455	0.300	2.589	0.033	0.004	0.004	0.004	0.029	4
HD055036	7.000	0.268	0.014	1.308							1
HD208344	7.199	0.071	0.184	1.097	2.890	0.037	0.005	0.009	0.008	0.008	6
HD049564	7.371	0.836	0.708	0.356							1
HD204132	7.542	0.368	0.068	1.327	2.755	0.034	0.003	0.005	0.010	0.024	6
HD028304	7.723	0.147	0.031	0.614	2.730	0.036	0.004	0.003	0.003	0.013	4
HD013801	7.885	0.199	0.179	0.688	2.740	0.030	0.017	0.019	0.008	0.021	4
HD031125	7.955	0.030	0.176	1.001	2.931	0.071	0.003	0.004	0.010	0.030	4
HD219364	7.958	0.679	0.541	0.376	2.593	0.026	0.024	0.023	0.009	0.021	
HD047777	7.985	-0.052	0.085	0.084	2.649	0.066	0.004	0.009	0.022	0.017	3
HD013997	8.010	0.464	0.331	0.367	2.577	0.055	0.023	0.025	0.006	0.019	4
HD207608	8.069	0.313	0.146	0.533	2.669	0.110	0.005	0.004	0.004	0.014	6
HD048691	8.212	0.144	-0.032	-0.013							2

### 3. PERIODIC CONTENT

For the two previously known variable stars, HD 115520 and HD 220735, we have significantly extended the time basis. Hence, period analysis of both should give more significant results. The numerical package of Period04 (Lenz & Breger, 2005) was used.

Searching for new short period variables, HD 26738 was found to be a new variable. This

star, according to SIMBAD (Wenger et al. 2000), has no previous reports on its variability.

A brief description for each star is presented.

#### 3.1. HD 115520

This star was first determined to be variable while it was being used as a standard star from a season in 2005. The photometric data of this star presented a large scatter in comparison with the other standard

TABLE 4  
*uvby* -  $\beta$  PHOTOELECTRIC PHOTOMETRY OF  
 HD 26738

HJD	V	(b - y)	$m_1$	$c_1$	$\beta$
425.8569	9.472			0.932	
425.9039	9.517	0.250	0.165	0.925	
425.8593	9.465	0.247	0.171		
425.8965	9.510	0.253	0.164	0.921	2.885
425.8489	9.497	0.251	0.164	0.919	2.884
425.8674	9.447	0.243	0.173		
425.8745	9.462	0.244	0.165	0.929	
425.8464	9.501			0.924	2.879
425.8649	9.454	0.244	0.163	0.939	
425.9150	9.465	0.246		0.933	2.873
425.8386	9.504	0.257	0.158	0.920	2.872
425.8411	9.509	0.256	0.158	0.929	2.870
425.8309	9.490	0.257	0.156	0.925	2.867
425.8209	9.459	0.247	0.164	0.927	2.864
425.8773	9.468	0.249	0.161	0.932	2.864
425.9069		0.247	0.170	0.912	
425.9179	9.469		0.166	0.935	2.861
425.8235	9.470	0.248	0.162	0.932	2.854
425.8333	9.495	0.256	0.156	0.926	

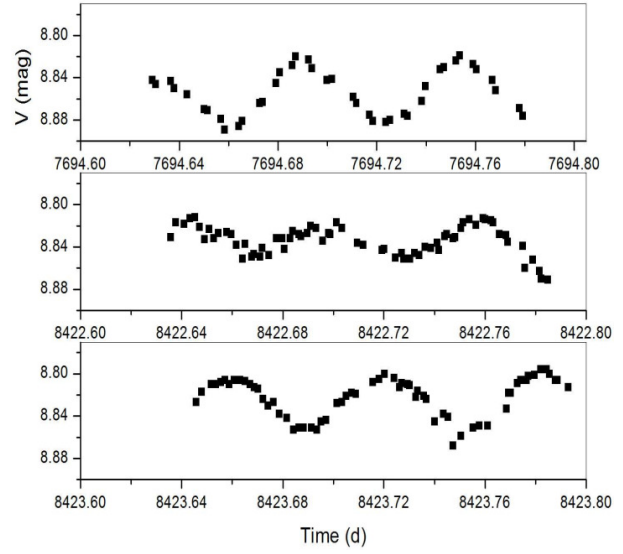


Fig. 2. Light curves of HD 220735 in the V filter obtained in *uvby* -  $\beta$  absolute photometry. At the top, the night of the previous season. To convert time shown into HJD, 2450000.00 must be added.

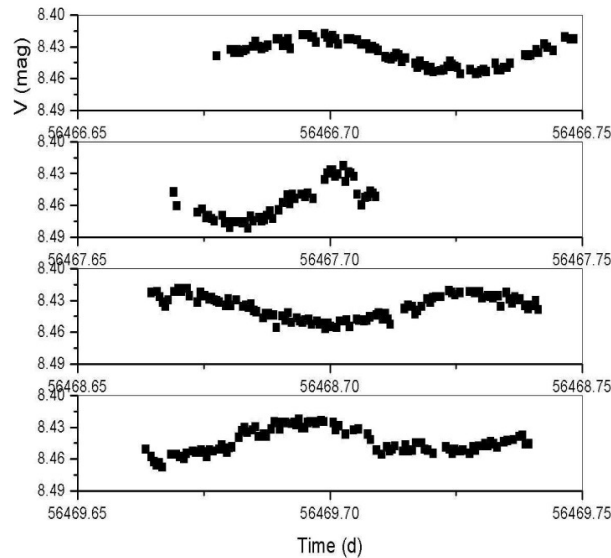


Fig. 1. Light curves of HD 115520 in the V filter obtained in *uvby* -  $\beta$  absolute photometry. Each night is shown in descending order. To obtain the adequate HJD, 2400000 must be added.

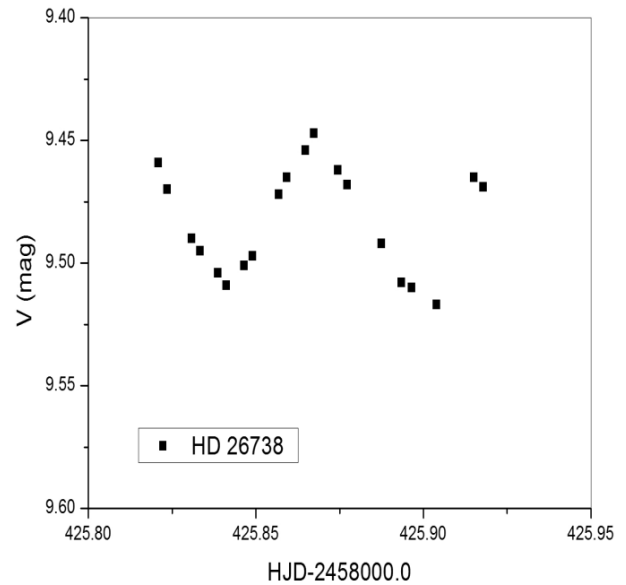


Fig. 3. Light curve of HD 26738 in the V magnitude of the *uvby* -  $\beta$  photoelectric photometry. To convert time shown into HJD, 2450000.00 must be added.

TABLE 5  
OUTPUT OF PERIOD04 CALCULATED WITH THE V MAGNITUDE OF THE STAR HD115520 WITH SEVERAL DATA SETS

Considered data	Nr.	Frequency	Amplitude	Phase
Set 1	F1	18.00	0.0130	0.2789
	F2	16.16	0.01442	0.6888
Set 2	F1	17.8375	0.0131	0.1028
	F2	14.7537	0.0108	0.2612
	F3	16.51521	0.0070	0.5646
Set 3	F1	17.6933	0.01503	0.5483
	F4	15.9967	0.00473	0.8836
	F6	14.5667	0.0063	0.0400

Notes: Set 1: data from 2005 and 2006 (Fox-Machado et al (2007)). Set 2: adds V magnitude of the *uvby* data (Peña et al. 2007). Set 3: includes the 2013 data (present paper).

stars used and this dispersion led the authors to suspect the variable nature of the star. New observations were performed in 2006 to verify its variability (Fox Machado et al. 2007) and it was observed again in 2006 to verify its variability (Fox Machado et al. 2007). It was re-observed in 2007 and the analysis published (Peña et al, 2007). Finally it was observed again in 2013. The time basis is, therefore, ten nights in 2600 days. The analysis of the shorter data groups has already been done and reported. Here we merely copy the published results in Table 5. At the bottom we add the analysis obtained when analysing the entire data, but we must keep in mind that the gap between observations is huge, six years. Figure 4 presents the periodograms of HD 115520 with the San Pedro Martir Observatory's V data.

### 3.2. HD 220735

Peña et al. (2019) reported from observations taken in 2016 that the periodic behavior of the star was determined from one night that covered a sufficient time span to cover two cycles. The difference of these maxima gave 0.0658 d, which gives a coarse period of pulsation of this star.

The other technique which was used for this star in the present work is time series analysis. These data gave the results listed in Table 6 with a zero point of 5.39 mag, residuals of 0.0049 mag and 5 iterations. This frequency coarsely agrees with that determined by the difference of the two maxima: 0.0658 d. The analysis of Period04 is presented in Figure 2. Beginning at the top is the periodogram of the original data; next are the consecutive sets of residuals. The scale of the Y axis shows the relative

TABLE 6  
OUTPUT OF PERIOD04 WITH THE V MAGNITUDE OF HD 220735 OF THE *uvby* -  $\beta^*$

Nr.	Frequency	Amplitude	Phase
F1	16.5974	0.0200	0.8674
F3	13.2807	0.0088	0.2043
F3	27.6206	0.0033	0.8021

\*Data from 2016 and present paper.

importance of the residuals. However, it is obvious that the data of only one night cannot provide an accurate period determination. To complicate things more, this preliminary analysis suggests the presence of a second frequency, a common phenomenon among  $\delta$  Scuti stars.

The star was observed again in December, 2018 for two nights. Combining the data the entire time basis is 732 days. Figure 5 presents the periodograms of HD 220735 with the SPM V data.

### 3.3. HD 26738

The star was observed on the night of Nov 3, 2018 (JD 2458424 ) for a short period of time (three hours). Although its variability is evident (Figure 3) the series analysis with Period04 gave the following results despite the shortness of the observing time span. A period of 0.15 d is determined from the consecutive minima whereas Period04 gave a frequency of 16.955 c/d with an amplitude of 0.0312 and a phase of 0.98. Prewhitening this frequency, a sec-

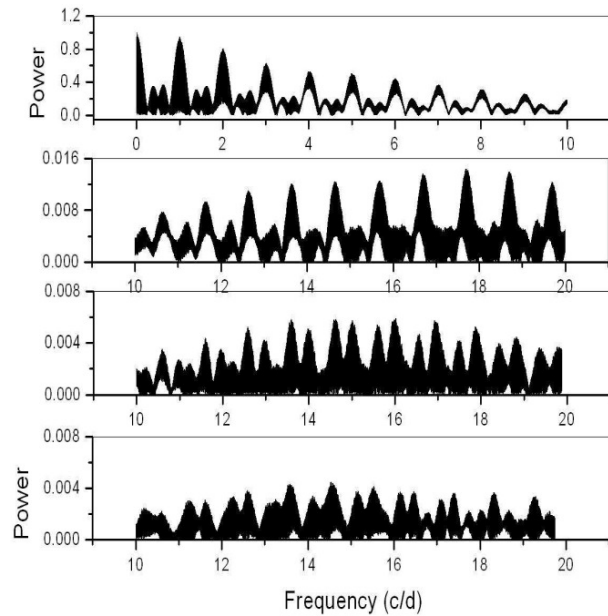


Fig. 4. Periodograms of HD 115520 with the SPM V data. At the top is the periodogram of the window; descending, the periodogram of the original data and subsequently, the periodogram of the residuals after subtracting each frequency. We call attention to the scale of the Y axis to show the relative importance of each frequency. Although the periodogram was evaluated from 0 to 50 c/d we merely present a limited frequency range, where the pulsational frequencies were found.

ond peak at 9.147 c/d with an amplitude of 0.0057 and a phase of 0.568 was obtained. The residuals were 0.00388 mag.

### 3.4. Discussion

Since their discovery neither HD 115520 nor HD 220735 had been studied for period determination. After the first report, more information was gathered, but no period analysis was done. In the present paper, two different approaches were utilized to determine the period of the pulsation.

In the first one, differences in consecutive times of maximum light were evaluated to determine a coarse period; the second method utilized was a time series analyses. The set employed was that of the V magnitude of the *wvby* -  $\beta$  photoelectric analysis in the present paper.

## 4. PHYSICAL PARAMETERS

### 4.1. Spectral Type Determination

To determine physical parameters, unreddened photometric values have to be determined through ap-

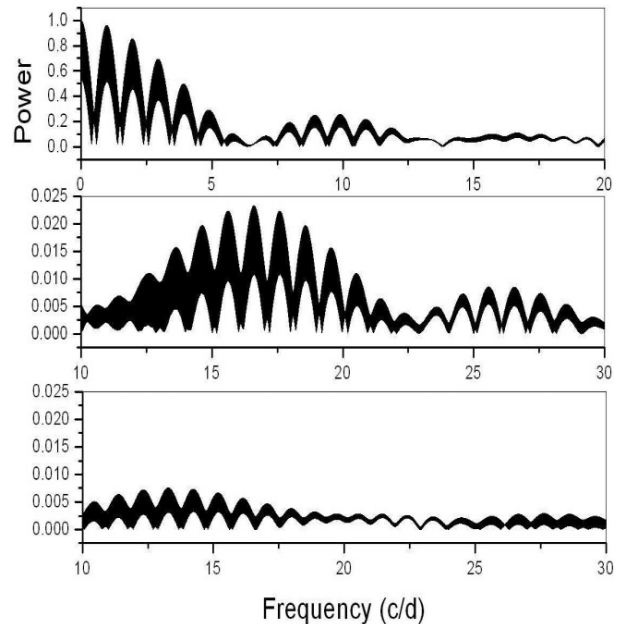


Fig. 5. Periodograms of HD 220735 with the SPM V data. Top to bottom: first is the periodogram of the window function. Middle, the output that provides the first frequency (16.597 c/d), and bottom, the result of the set of residuals subtracting this frequency at 13.280 c/d. We call attention to the scale of the Y axis to show the relative importance of each frequency.

propriate calibrations. These calibrations were proposed by Nissen (1988) for A and F type stars. Therefore, it is necessary to first determine if the range of variation in spectral class of the involved stars lies in these limits. The spectral types can be determined very accurately with the *wvby* -  $\beta$  photometric data. We determined their unreddened photometric indexes  $[m_1]$  and  $[c_1]$  and positioned them in the analogous plot determined for the open cluster Alpha Per, whose stars have well-determined spectral types and whose membership has been established.

### 4.2. HD115520

The best way to determine the accuracy of our observations is through the differences in magnitude and colors ( $V$ ,  $b - y$ ,  $m_1$ ,  $c_1$  and  $H\beta$ ) of the standard stars, where  $c_1$  and  $m_1$  are parameters defined by the well-known color indexes:  $m_1 = (v - b) - (b - y)$  and  $c_1 = (u - v) - (v - b)$ . For HD 115520 Fox Machado et al. (2007) stated that its position in the  $[m_1]$  -  $[c_1]$  diagram establishes it to be an A8V star, a classification that was corroborated in Peña et al. (2007).

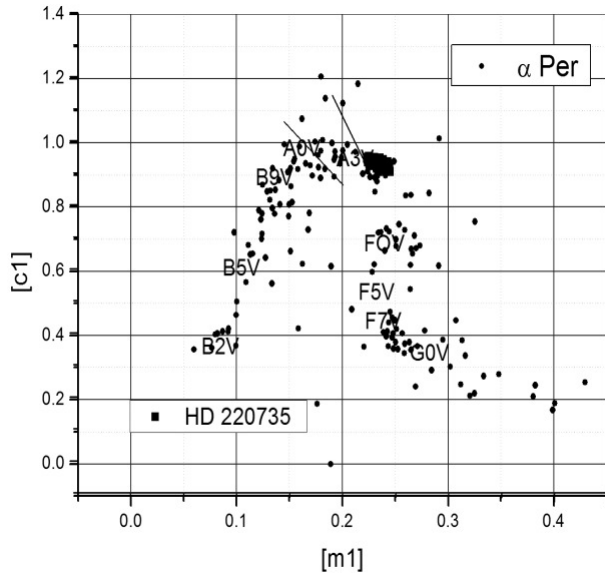


Fig. 6. Position of the HD 220735 star in the  $[m_1] - [c_1]$  diagram of the open cluster Alpha Per (Peña & Sareyan, 2006).

#### 4.3. HD 220735

The analysis of HD 220735 reported by Peña et al. (2019) stated that the spectral type of this star is A3-A4. This determination was done by locating the unreddened color indexes of the  $uvby - \beta$  photometry in the  $[m_1] - [c_1]$  diagram of this star compared to those determined for the open cluster Alpha Per (Peña et al., 2006) for which there is accurate determination of the spectral types for its stars and its photometry. This is shown schematically in Figure 6.

#### 4.4. HD 26738

Figure 7 shows the position of this star in the  $[m_1] - [c_1]$  diagram. Its spectral type corresponds to an A main sequence star around A4 or A5.

#### 4.5. Physical Parameters Determination

In view of the fact that the three stars have spectral classes typical of  $\delta$  Scuti stars, A8 for HD 115520, A3-A4 for HD 220735 and A4-A5 for HD 26738, we can apply the prescription of Nissen (1988) for the three to determine their reddening. This procedure has been explained elsewhere (see for example Peña et al. (2007)).

To determine the range of the effective temperature and surface gravity in which the stars vary,

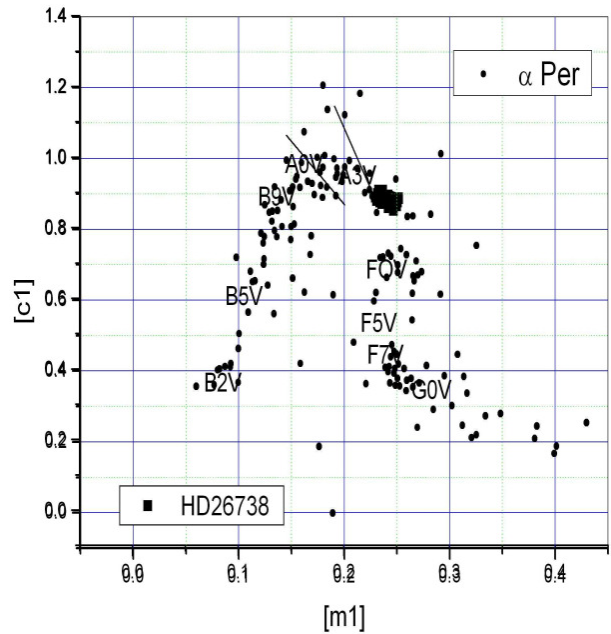


Fig. 7. Position of the HD 26738 star in the  $[m_1] - [c_1]$  diagram of the open cluster Alpha Per (Peña & Sareyan, 2006).

we must locate the determined unreddened points in some theoretical grids such as those of Lester, Gray and Kurucz (1986, hereinafter LGK86) developed for  $uvby - \beta$  photometric data for several metallicities. However, before locating the unreddened points in the theoretical grids, a metallicity for each star has to be assumed. For each star its unreddened points ( $b - y$ ), and  $m_1$  were plotted in a diagram of the LGK86 grids built for  $\log g$  of 4 and for different metallicities. The position in the ( $b - y$ ) vs.  $m_1$  diagram of the unreddened points indicates the metallicity  $[Fe/H]$  of each star. They were: for HD 115520 a metallicity of 0.0; for HD 26738, of 1.0 and for HD 220735 values spread out between 0.5 and 1.0. These are the metallicities that were assumed.

As can be seen in Figure 8, for the case of  $[Fe/H] = 1.0$ , the HD 220735 star varies between an effective temperature of 7500 K and 8200 K; the surface gravity  $\log g$  lies around 4.0. The star HD 26738 (Figure 9), on the other hand, varies between 7500 and 8100 K with a  $\log g$  slightly larger than 4.0. In the case of HD 115520 since no new  $H\beta$  observations were done in 2013 we rely on the 2007 findings for unreddening and obtained:  $T_e$  around 7700 K and  $\log g$  close to 4.0.

TABLE 7  
DETERMINED PARAMETERS FOR THE VARIABLE STARS

Parameter	HD 115520	HD 220735	HD 26738
Reddening [mag] $E(b-y)$	0.000	$0.051 \pm 0.016$	$0.173 \pm 0.011$
Distance [pc]	$119 \pm 7$	$280 \pm 35$	$205 \pm 15$
Distance modulus [mag]	$5.4 \pm 0.1$	$7.2 \pm 0.3$	$6.6 \pm 0.2$
[Fe/H]	0.0	1.0	1.0

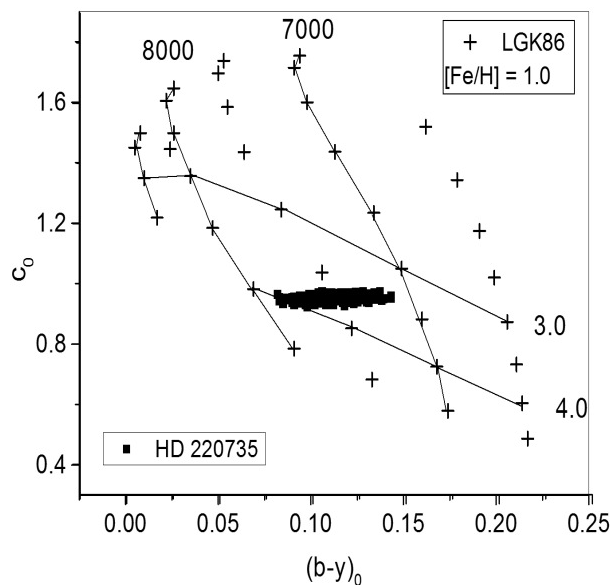


Fig. 8. Position of the HD 220735 star in the grids of LGK86 for a metallicity of 1.0.

#### 4.6. Physical Parameters Conclusions

New observations in  $uvby - \beta$  photoelectric photometry were carried out on the three variable stars.

Reddening, as well as the unreddened indexes, were determined from Nissen's (1988) calibrations. These served to determine the physical characteristics of the HD 220735 star: effective temperature in a range from 7000 K to 7700 K and  $\log g$  from 3.6 to 4.3 from two methods: (1) from the location of the unreddened indexes in the LGK86 grids and (2) through the theoretical relation (P&J72).

The application of the above mentioned numerical unreddening package of Nissen's (1988) provided the results for HD 115520 and HD 226738. The results are summarized in Table 7 which lists the reddening  $E(b-y)$ , distance modulus, DM and distance (in pc) as well as the determined metallicity.

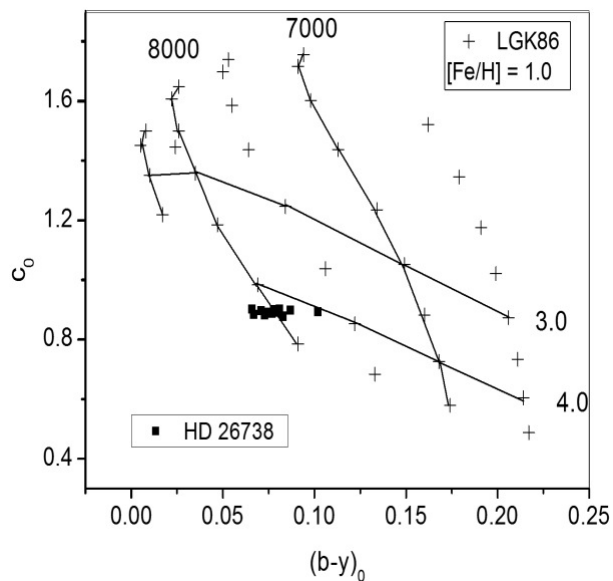


Fig. 9. Position of the HD26738 star in the grids of LGK86 for a metallicity of 1.0

## 5. CONCLUSIONS

In this study we present our findings on HD 115520 and HD 220735 which were previously reported to be variables. We confirmed their spectral types from  $uvby - \beta$  photoelectric photometry. We did the same for the unreported variable star HD 22738. The extended time basis of the observed stars served to determine their period of pulsation more accurately. Physical characteristics were calculated by determining first their reddening and plotting the unreddened indexes in the theoretical grids of LGK86. The determined values are consistent with their spectral types.

We would like to thank A. Pani, and the staff of the OAN at SPM for their assistance in securing the observations and the GAOOT group (J. Guillen and D. Segura) for fruitful discussions. This work was partially supported by PAPIIT IN104917, IG100620 and PAPIME PE113016. Proofreading and typing were done by J. Miller and J. Orta, respectively.

C. Villarreal, C. Guzmán, F. Ruiz, A. Díaz and G. Pérez assisted us at different stages. AAS, SB, HH, ARL, ALZ and AZ thank the IA for allotting the telescope time. The comments and suggestion of an anonymous referee improved this article. We have made use of the SIMBAD databases operated at CDS, Strasbourg, France and NASA ADS Astronomy Query Form.

## REFERENCES

- Fox-Machado, L., Peña, J. H., Muñoz, G., & Vargas, B. 2007, *CoAst*, 151, 26
- Lenz, P. & Breger, M. 2005, *CoAst*, 146, 53
- Lester, J. B., Gray, R. O., & Kurucz, R. L. 1986, *ApJS*, 61, 509
- Nissen, P. 1988, *A&A*, 199, 146
- Peña, J. H. & Peniche, R. 1994, *RMxAA*, 28, 139
- Peña, J. H. & Sareyan, J.-P. 2006, *RMxAA*, 42, 179
- Peña, J. H., Sareyan, P., Cervantes-Sodi, B., et al. 2007, *RMxAA*, 43, 217
- Peña, J. H., Villarreal, C., Piña, D. S., et al. 2016, *RMxAA*, 52, 385
- Peña, J. H., Soni, A., Rentería, A., & Piña, D. 2019, *IBVS*, 6260, 1
- Petersen, J. O. & Jørgensen, H. E. 1972, *A&A*, 17, 367
- Wenger, M., Ochsenbein, F., Egret, D., et al. 2000, *A&AS*, 143, 9

H. Huepa, J. H. Peña, and A. Rentería: Observatorio Astronómico Nacional de Tonantzintla, México.

S. B. Juárez, J. H. Peña, A. Rentería, A. A. Soni, and A. L. Zuñiga: Facultad de Ciencias, Universidad Nacional Autónoma de México, México.

J. H. Peña, A. Rentería, and A. A. Soni: Instituto de Astronomía, Universidad Nacional Autónoma de México, Apdo. Postal 70-264, Cd. de México (jhpena@astro.unam.mx).

## DYNAMICS AROUND AN ASTEROID MODELED AS A MASS TRIPOLE

L. B. T. Santos<sup>1</sup>, L. O. Marchi<sup>1</sup>, P. A. Sousa-Silva<sup>2</sup>, D. M. Sanchez<sup>1</sup>, S. Aljbaae<sup>1</sup>, and A. F. B. A. Prado<sup>1</sup>

*Received March 17 2020; accepted August 3 2020*

### ABSTRACT

The orbital dynamics of a spacecraft orbiting around irregular small celestial bodies is a challenging problem. Difficulties to model the gravity field of these bodies arise from the poor knowledge of the exact shape as observed from the Earth. In order to understand the complex dynamical environment in the vicinity of irregular asteroids, several studies have been conducted using simplified models. In this work, we investigate the qualitative dynamics in the vicinity of an asteroid with an arched shape using a tripole model based on the existence of three mass points linked to each other by rods with given lengths and negligible masses. We applied our results to some real systems, namely, asteroids 8567, 243 Ida and 433 Eros and also Phobos, one of the natural satellites of Mars.

### RESUMEN

La dinámica orbital de un satélite en torno a un cuerpo celeste irregular es un problema abierto. La dificultad de modelar el campo gravitatorio de esos cuerpos surge del pobre conocimiento que tenemos sobre sus formas, al observarlos desde la Tierra. Para entender el complejo entorno dinámico de los asteroides irregulares se han propuesto modelos simplistas. En este trabajo, investigamos cualitativamente la dinámica en el entorno de un asteroide en forma de arco, mediante un modelo de tripolo basado en tres puntos masa unidos por barras de longitudes determinadas y masas despreciables. Aplicamos nuestros resultados a algunos cuerpos reales, como el asteroide 8567, el 243 Ida, y el 433 Eros, así como a Phobos, uno de los satélites naturales de Marte.

*Key Words:* methods: numerical — minor planets, asteroids: general — space vehicles

### 1. INTRODUCTION

Small-body explorations, such as asteroids and comets, have become an essential subject in deep space exploration. They involve multiple disciplines, such as science and control engineering, aerospace science and technology, celestial mechanics, and astronomy, among others. The combination of non-spherical gravitational attraction together with the rapid rotation of the asteroids around their axis governs the dynamics of the spacecraft near its surface. Thus, the analysis of the orbits of a spacecraft around these bodies is one of the current challenges in astrodynamics.

Developing mathematical models to represent the gravitational field around irregular bodies is an important research topic in orbital dynamics. Often,

a spherical harmonics expansion is used to model the Earth and other Planets, as these more massive celestial bodies (when compared to asteroids) have a shape that resembles a sphere (Elife & Riaguas 2003). On the other hand, when the body does not resemble a sphere, this expansion is no longer convenient and, in some cases, convergence cannot be guaranteed (Elife & Riaguas 2003). Generally, when the field point is located within the circumscribing sphere, the series diverge (Lan et al. 2017; Elife & Riaguas 2003). Furthermore, the expansion of low-order Legendre coefficients often does not provide a good approximation for the motion of a spacecraft due to the fact that higher order terms can generate divergence after several iterations (Riaguas et al. 1999; Jiang & Baoyin 2018).

The shape of a celestial body, its rotation period, and other physical characteristics can be obtained by light curve and radar analysis. From these ob-

<sup>1</sup>National Institute for Space Research, INPE, Brazil.

<sup>2</sup>São Paulo University (UNESP), São João da Boa Vista, Brazil.

servations, it is possible to use the solid polyhedron method to determine the dynamics around irregular bodies, including gravitational fields, stationary state solutions (equilibrium points, periodic orbits, quasiperiodic orbits, and chaotic motion), stability, bifurcation, etc (Werner 1994; Scheeres et al. 1996; Jiang & Baoyin 2018; Chanut et al. 2015b; Jiang et al. 2014; Yu & Baoyin 2012; Tsoulis & Petrović 2001). However, this approach requires a large computational effort depending on the quantity of polyhedral shapes. This problem was partially solved in Chanut et al. (2015a), where the authors considerably reduced the computation time ( $\approx 30$  times) applying the Mascon gravity framework, as presented in Geissler et al. (1996), using a shaped polyhedral source to model the external gravitational field of a small celestial body. For more details about this approach we also refer the readers to Venditti (2013) and Aljbaae et al. (2017).

The gravitational potential can be obtained with high accuracy using the polyhedral model, but from this model it is difficult to understand the effect of certain parameters (mass ratio ( $\mu$ ), shape, among others) on the dynamics. This happens because, in the polyhedron model, the parameters mix and produce a mixed influence on the gravitational field of irregular bodies. Therefore, to study the effect of a single parameter, it is often necessary to model irregular bodies using simplified models.

By using simplified models, it is possible to perform semi analytical studies to understand which parameters affect stability, appearance of equilibrium points, bifurcations, etc. Thus, simplified models help to understand the dynamics around irregular bodies, and allow us to design orbits (Wang et al. 2017; Zeng & Liu 2017), feedback control schemes (Yang et al. 2017), as well as the permissible hovering regions (Zeng et al. 2016).

An effective way to analyze the surface of an asteroid is body-fixed hovering in a region close to the asteroid, where the spacecraft maintains its position constant with respect to the asteroid (Wen et al. 2020). Great locations for using the body-fixed hovering are the equilibrium points, due to the fact that they are locations that receive minimal disturbance. Jiang et al. (2014) investigated body-fixed hovering at equilibrium points and classified the manifolds close to these points into eight types. Body-fixed hovering can be used to obtain accurate measurements of a region on the surface of the target asteroid and to facilitate the descent and ascent maneuvers of a spacecraft whose mission is to return to Earth with samples (Broschart & Scheeres 2005). Such ma-

neuvers were used in the Hayabusa mission (Scheeres 2004).

Several bodies with different shapes can be described using simplified mathematical models. For example, Elife & Lara (2003); Riaguas et al. (1999, 2001), analyzed the motion of a particle under the gravitational field of a massive straight segment. A simple planar plate (Blesa. 2006), a rotating homogeneous cube (Liu et al. 2011) and a triaxial ellipsoid (Gabern et al. 2006) have also been used to model bodies with irregular shapes.

Zeng et al. (2015) proposed that certain classes of elongated small bodies can be modeled by a double-particle-linkage called the dipole model. After that, Zeng et al. (2016) investigated the dynamical properties in the vicinity of an elongated body (using the dipole model) in order to analyze the influence of the force ratio ( $k$ ), the mass ratio ( $\mu$ ) and the oblateness ( $A_2$ ) of the primary in the distribution of the equilibrium points in the  $xy$  plane. Through this dynamical analysis, Zeng et al. (2016) observed that the non-collinear equilibrium points exist only for  $0.37 < k < 2.07$ , and that these equilibria do not depend on  $\mu$ . In Zeng et al. (2016), the influence of the parameters  $k$ ,  $\mu$  and  $A_2$  (oblateness of the second primary) on the positions of the of out-of-plane equilibrium points and on the topological structure of the zero velocity curves were analyzed. Zeng et al. (2016) noted that the oblateness of the second primary greatly influences the distribution of equilibrium points outside the plane. These works, among others, showed that using that simplified model it is possible to identify the main parameters governing the dynamics around certain asteroid systems (Barbosa Torres dos Santos et al. 2017a,b; Zeng et al. 2018).

Inspired by the double-particle-linkage model, Lan et al. (2017) proposed that small arched bodies can be modeled by a triple-particle-linkage model determined by five parameters:  $M$ ,  $\omega$ ,  $l_1$ ,  $\tau$  and  $\beta$ . Analyzing asteroids 433 Eros, 243 Ida, and the Martian moon M1 Phobos, they validated the so called tripole model, by verifying that the gravitational field distribution of unstable annular regions is similar to the one found with the polyhedral model. Later, Yang et al. (2018) proposed the non-axisymmetric triple particle-linkage model as a further step to improve the modeling towards a more realistic scenario. The authors analyzed the non-axisymmetric tripole model using three different elongated asteroids (243 Ida, 433 Eros, and (8567) 1996 HW1) and verified that the asymmetrical tripole model was

more accurate than its predecessors, the dipole and the symmetrical tripole model.

We consider different geometries for the tripole to compute the gravitational potential and we compute the positions of the equilibrium points for the different combinations of relevant parameters of the model. Additionally, we analyze the conditions for linear stability. We find that the existence of some equilibrium points depends on the azimuthal angle and that the stability conditions depend on the rotation of the asteroids around their axis ( $k$ ), on the azimuthal angle ( $\Phi$ ), and on the mass ratio of the system ( $\mu^*$ ). Also, we investigate the influence of  $\Phi$  on the topological structure of the zero velocity curves. Finally, we find the relationship between the Jacobi constant and the azimuthal angle of the asteroid for all equilibrium points outside the asteroid's body.

Although the works found in the literature deal with the validation of the symmetric and the asymmetric tripole model, a semi-analytical analysis of the tripole model has not yet been performed. So, the main goal of the present work is to perform a dynamical analysis around arched asteroids and investigate which parameters ( $k$ ,  $\mu^*$  and  $\Phi$ , where  $\Phi$  determines the degree of arching of the asteroid) influence the distribution of the equilibrium points, the topological structure of the zero velocity curves as well as the stability condition of stationary solutions. The tripole model has additional degrees of freedom when compared to the dipole model. So, it is possible to identify new parameters, such as the azimuthal angle, and to investigate their influence on the dynamical properties around an arched system. With this, the results can be applied to investigate elongated natural arched bodies, such as some asteroid systems, comet nuclei and planet moons.

We note that, from a dynamical point of view, it should be interesting to explore the effect of the shape on the inner equilibria also. However, since we focus on the applicability of the solutions, we restrict the investigation to the points outside the body of the asteroid.

This article is organized as follows. The model and the methodology are discussed in § 2. The results are analyzed and discussed in § 3. In § 4, we investigate and compare the stability conditions of the model adopted in this study with real systems of small bodies. In § 5, some final considerations are made.

## 2. MATHEMATICAL FRAMEWORK

In this section, we describe the Restricted Four-Body Problem using the rotating mass tripole model. In

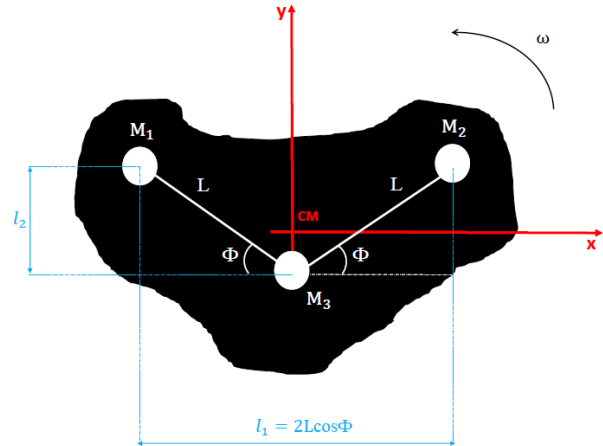


Fig. 1. Schematic representation of the asteroid modeled by a tripole. The color figure can be viewed online.

our investigations, we use the rotating mass tripole model shown in Figure 1. This model consists in three mass points,  $M_1$ ,  $M_2$ , and  $M_3$ , arranged inside an irregularly shaped asteroid. All the equations developed in this work refer to the asteroid-particle system (where the particle is a body with negligible mass), i.e., the perturbations from other bodies are not taken into account. The rods connecting  $M_1$  to  $M_3$  and  $M_2$  to  $M_3$  have negligible mass and the same length  $L = 1$ , which is the canonical unit. The distance between  $M_1$  and  $M_2$  is denoted by  $l_1$ , while the distance between  $M_2$  and the  $x$ -axis, which contains  $M_3$ , is denoted by  $l_2$ . The parameter  $\tau$  is defined as the ratio of  $l_2$  to  $l_1^*$ , where  $l_1^* = l_1/2$ , i.e.  $\tau = l_2/l_1^*$ .

The origin of the reference system ( $xy$ ) is at the center of mass of the asteroid. The angle formed by each rod with the  $x$ -axis is called the azimuthal angle and is denoted by  $\Phi$ . We assume that both rods make the same angle with the horizontal axis. The geometric configuration of the asteroid depends on this angle. The more arched the shape of the asteroid, the larger is the azimuthal angle. Note that when  $\Phi = 0^\circ$  the length of the asteroid is maximum and equals to two canonical units. The equations that describe the motion of the particle in the  $xy$  plane around the tripole are written in a rotating frame that rotates with constant angular velocity  $\omega = 1$ , in canonical units. The unit of time is defined such that the period of rotation of the tripole is equal to  $2\pi$ . We consider that  $M_1$ ,  $M_2$ , and  $M_3$  have equal masses, i.e.,  $m_1 = m_2 = m_3$ .

### 2.1. Equations of Motion

Consider that the body with negligible mass (particle) is located at  $P(x,y)$  and its motion is governed exclusively by the gravitational forces due to the primary bodies  $M_1$ ,  $M_2$ , and  $M_3$ .  $M_1$  and  $M_2$  have masses  $m_1 = m_2 = \mu^*$ , and  $M_3$  has mass  $m_3 = 1 - 2\mu^*$ , where  $\mu^*$  is mass ratio defined as

$$\mu^* = \frac{m_2}{m_1 + m_2 + m_3}. \quad (1)$$

The coordinates of the primaries, in canonical units, are, respectively, given by:

$$x_1 = -\cos(\Phi), \quad y_1 = \sin(\Phi) - 2\mu^* \sin(\Phi), \quad z_1 = 0 \quad (2)$$

$$x_2 = \cos(\Phi), \quad y_2 = \sin(\Phi) - 2\mu^* \sin(\Phi), \quad z_2 = 0 \quad (3)$$

$$x_3 = 0, \quad y_3 = -2\mu^* \sin(\Phi), \quad z_3 = 0. \quad (4)$$

Using the canonical units mentioned above the Hamilton function of the system is written as (Broucke 1968):

$$H = \frac{(p_x + y)^2 + (p_y + x)^2}{2} - \frac{x^2 + y^2}{2} - k \left( \frac{\mu^*}{r_1} + \frac{\mu^*}{r_2} + \frac{1 - 2\mu^*}{r_3} \right), \quad (5)$$

where

$$r_1 = \sqrt{(x - x_1)^2 + (y - y_1)^2 + z^2}, \quad (6)$$

$$r_2 = \sqrt{(x - x_2)^2 + (y - y_2)^2 + z^2}, \quad (7)$$

$$r_3 = \sqrt{(x - x_3)^2 + (y - y_3)^2 + z^2}, \quad (8)$$

and  $p_x$  and  $p_y$  are the components of the angular momentum of the particle with respect to the  $x$ -axis and the  $y$ -axis, respectively. The dimensionless parameter  $k$  is the force ratio, given by the ratio between the gravitational force and the centrifugal force (Zeng et al. 2018, 2016):

$$k = \frac{G^* M}{\omega^{*2} l_1^{*3}}. \quad (9)$$

The value of  $k$  depends on the angular velocity of the asteroid ( $\omega^*$ ). In the international system of units, the total mass of the body ( $M$ ), is given in kg, the length  $l_1^*$ , and the distance between  $M_1$  and  $M_2$ , in meters;  $G^*$  is the universal gravitational constant

in the international unit system. So  $k$  can be computed after obtaining the length of the segment  $l_1^*$ . (Zeng et al. 2018; Lan et al. 2017; Zeng et al. 2016).

From the Hamilton function, it is possible to obtain the equations of motion of the particle in the rotating reference system:

$$\dot{x} = \frac{\partial H}{\partial p_x} = p_x + y, \quad (10)$$

$$\dot{y} = \frac{\partial H}{\partial p_y} = p_y - x. \quad (11)$$

The remaining dynamical equations are

$$\dot{p}_x = -\frac{\partial H}{\partial x} = p_y - x + \Omega_x, \quad (12)$$

$$\dot{p}_y = -\frac{\partial H}{\partial y} = p_x - y + \Omega_y, \quad (13)$$

where  $\Omega_x$  and  $\Omega_y$  are the partial derivatives of  $\Omega$  with respect to  $x$  and  $y$ , respectively, and  $\Omega$  is given by

$$\Omega = \frac{x^2 + y^2}{2} + k \left( \frac{\mu^*}{r_1} + \frac{\mu^*}{r_2} + \frac{1 - 2\mu^*}{r_3} \right). \quad (14)$$

Equation 14 is a scalar function, also known as the pseudo-potential, which accounts for the acceleration experienced by the particle in a non-inertial reference system. The equations of motion in the  $xy$  plane in the Lagrangian formulation are (Szebehely 1967; Murray & Dermott 1999; McCuskey 1963; Scheeres 2012):

$$\ddot{x} - 2\dot{y} = \Omega_x, \quad (15)$$

$$\ddot{y} + 2\dot{x} = \Omega_y, \quad (16)$$

which have the same appearance as the equations of the Classical Restricted Three-Body Problem (CRTBP) (Moulton 1914; Szebehely 1967; Murray & Dermott 1999; McCuskey 1963).

Considering the motion in the  $xy$  plane, multiplying equation 15 by  $2x$  and equation 16 by  $2y$ , and adding all of them, we have

$$2x\ddot{x} + 2y\ddot{y} = 2\dot{x}\frac{\partial\Omega}{\partial y} + 2\dot{y}\frac{\partial\Omega}{\partial x}, \quad (17)$$

which can be rewritten as

$$\frac{d(\dot{x}^2 + \dot{y}^2)}{dt} = 2\frac{\partial\Omega}{\partial t}. \quad (18)$$

Integrating equation 18 with respect to time, we find that

$$v^2 = 2\Omega - C^*, \quad (19)$$

where  $v$  is the velocity of the particle and  $C^*$  is a constant of integration.

In this paper,  $C^*$  is called the modified Jacobi constant, where modified means that it is different from the constant studied by Jacobi for the case of the Classical Restricted Three-Body Problem. A special case occurs when  $k = 1$ , since the modified Jacobi constant has the same value as the Jacobi constant, corresponding to the CRTBP. Looking at equation 19, we note that the velocity of the particle depends only on the pseudo-potential and the integration constant  $C^*$ . The constant  $C^*$  is determined numerically in terms of the initial position and velocity of the particle.

2.2. *Equilibrium Points*

Equilibrium solutions are points in which the particle has zero acceleration and zero velocity in the rotating frame. They are good locations in space to insert the spacecraft because they are located in regions where external perturbations are minimal, reducing the fuel consumption required for station-keeping maneuvers (Barbosa Torres dos Santos et al. 2017a). The locations of the equilibrium points are explicitly defined in terms of  $\mu^*$  (and implicitly by  $\Phi$ ). Making the right side of equations 15 and 16 equal to zero, that is,  $\dot{x} = \dot{y} = 0$ , implies null accelerations:

$$\begin{aligned}
 x - \frac{\mu^*(x-x_1)}{[(x-x_1)^2+(y-y_1)^2]^{\frac{3}{2}}} - \frac{\mu^*(x-x_2)}{[(x-x_2)^2+(y-y_2)^2]^{\frac{3}{2}}} \\
 - \frac{(1-2\mu^*)(x-x_3)}{[(x-x_3)^2+(y-y_3)^2]^{\frac{3}{2}}} = 0, \\
 y - \frac{\mu^*(y-y_1)}{[(x-x_1)^2+(y-y_1)^2]^{\frac{3}{2}}} - \frac{\mu^*(y-y_2)}{[(x-x_2)^2+(y-y_2)^2]^{\frac{3}{2}}} \\
 - \frac{(1-2\mu^*)(y-y_3)}{[(x-x_3)^2+(y-y_3)^2]^{\frac{3}{2}}} = 0.
 \end{aligned}
 \tag{20}$$

The solutions of this system of equations can be determined numerically using an iterative method.

2.3. *Linear Stability Analysis*

The linear stability analysis of the equilibrium points  $(x_0, y_0)$  is performed by displacing the origin of the coordinate system to the position of the libration points, so that the equations of motion are linearized around the origin. Equation 15 and 16 can be written as, respectively

$$\begin{aligned}
 \ddot{\xi} - 2\dot{\eta} &= \Omega_{xx}(x_0, y_0)\xi + \Omega_{xy}(x_0, y_0)\eta, \\
 \ddot{\eta} + 2\dot{\xi} &= \Omega_{xy}(x_0, y_0)\xi + \Omega_{yy}(x_0, y_0)\eta,
 \end{aligned}
 \tag{21}$$

where the partial derivatives in  $(x_0, y_0)$  mean that the value is computed at the libration point that is being investigated.  $\xi$  and  $\eta$  represent the coordinates of the particle with respect to the equilibrium point  $(x_0, y_0)$ , and  $\Omega_{xx}$ ,  $\Omega_{xy}$ ,  $\Omega_{xy}$ , and  $\Omega_{yy}$  are the partial derivatives calculated at this point, given by

$$\begin{aligned}
 \Omega_{xx} &= \frac{3(1-2\mu^*)x^2}{(x^2+(y-y_3)^2)^{5/2}} - \frac{1-2\mu^*}{(x^2+(y-y_3)^2)^{3/2}} \\
 &- \frac{\mu^*}{((x-x_1)^2+(y-y_1)^2)^{3/2}} + \frac{3\mu^*(x-x_1)^2}{((x-x_1)^2+(y-y_1)^2)^{5/2}} \\
 &- \frac{\mu^*}{((x-x_2)^2+(y-y_2)^2)^{3/2}} + \frac{3\mu^*(x-x_2)^2}{((x-x_2)^2+(y-y_2)^2)^{5/2}} + 1, \\
 \Omega_{yy} &= \frac{3(1-2\mu^*)(y-y_3)^2}{(x^2+(y-y_3)^2)^{5/2}} - \frac{1-2\mu^*}{(x^2+(y-y_3)^2)^{3/2}} \\
 &+ \frac{3\mu^*(y-y_1)^2}{((x-x_1)^2+(y-y_1)^2)^{5/2}} - \frac{\mu^*}{((x-x_1)^2+(y-y_1)^2)^{3/2}} \\
 &+ \frac{3\mu^*(y-y_2)^2}{((x-x_2)^2+(y-y_2)^2)^{5/2}} - \frac{\mu^*}{((x-x_2)^2+(y-y_2)^2)^{3/2}} + 1, \\
 \Omega_{xy} = \Omega_{yx} &= \frac{3(1-2\mu^*)x(y-y_3)}{(x^2+(y-y_3)^2)^{5/2}} \\
 &+ \frac{3\mu^*(x-x_1)(y-y_1)}{((x-x_1)^2+(y-y_1)^2)^{5/2}} + \frac{3\mu^*(x-x_2)(y-y_2)}{((x-x_2)^2+(y-y_2)^2)^{5/2}}.
 \end{aligned}
 \tag{22}$$

The nontrivial roots of equations 21 are obtained from the solution of the characteristic equation of order four in  $\lambda$ :

$$\lambda^4 + (4 - \Omega_{xx}^0 - \Omega_{yy}^0)\lambda^2 + \Omega_{xx}^0\Omega_{yy}^0 - (\Omega_{xy}^0)^2 = 0.
 \tag{23}$$

In equation 23,  $\Omega_{xx}^0$ ,  $\Omega_{xy}^0$  and  $\Omega_{yy}^0$  refer, respectively, to  $\Omega_{xx}(x_0, y_0)$ ,  $\Omega_{xy}(x_0, y_0)$  and  $\Omega_{yy}(x_0, y_0)$ . The equilibrium point is linearly stable if all the four roots (or eigenvalues  $\lambda$ ) of equation 23 are purely imaginary, or complex with negative real parts (Ollé et al. 2004). However, if one or more of the eigenvalues have a positive real part, the equilibrium point is classified as unstable (Moulton 1914; Szebehely 1967; Murray & Dermott 1999; McCuskey 1963).

3. RESULTS

In this section we will show the numerical results obtained from our numerical simulations. The goal is to gain a general view of the dynamics of the problem, which will allow us to draw some conclusions.

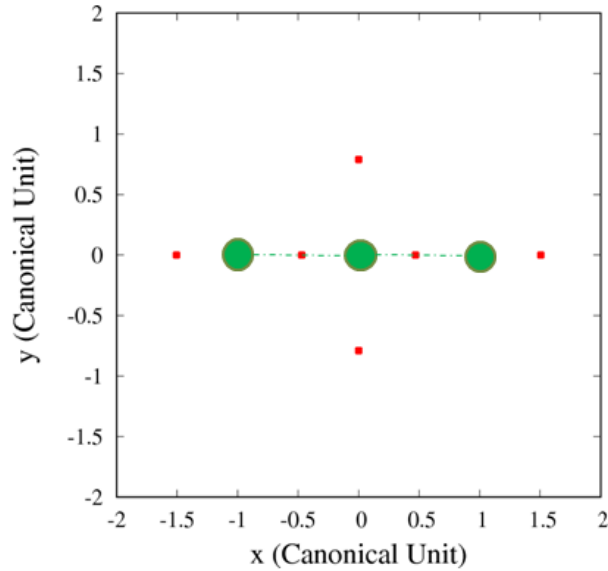
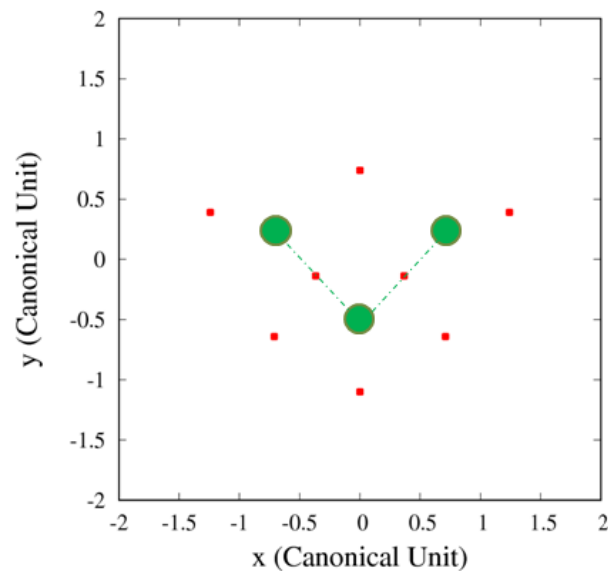
(a)  $\Phi = 0^\circ$ .(b)  $\Phi = 45^\circ$ .

Fig. 2. Equilibrium points for an azimuthal angle of (a)  $0^\circ$  and (b)  $45^\circ$ . In both cases  $\mu^* = 1/3$ . The color figure can be viewed online.

### 3.1. Influence of $[k, \mu^*, \Phi]$ on Equilibrium Points

We start by computing the equilibrium points of the system. Figure 2(a) shows the points of mass  $M_1$  (green circle on the left side),  $M_2$  (green circle on the right side) and  $M_3$  (green middle circle), and six equilibrium points (red) for  $\Phi = 0^\circ$ ,  $\mu^* = 1/3$  and  $k = 1$ . The equilibrium points between  $M_1$  and  $M_3$  and between  $M_2$  and  $M_3$  overlap with the rod that

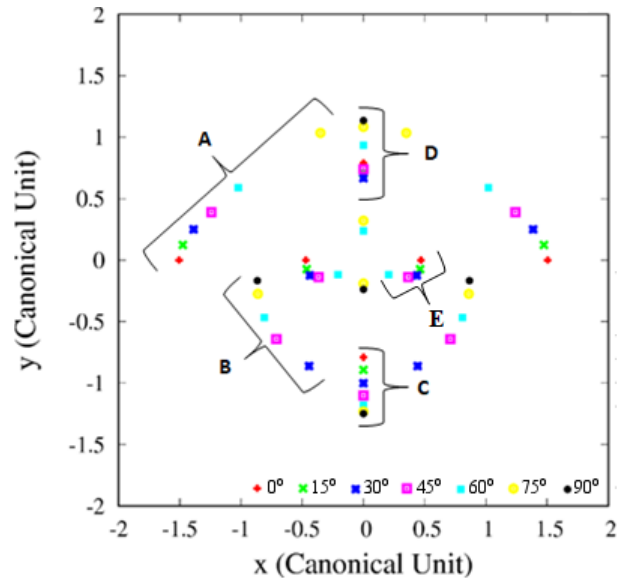
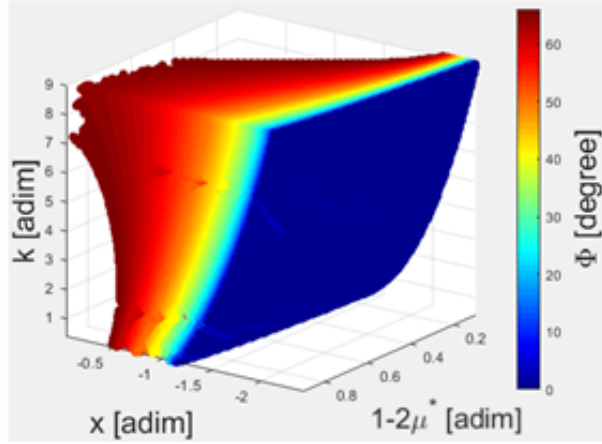


Fig. 3. Equilibrium points separated by regions A to E. The color figure can be viewed online.

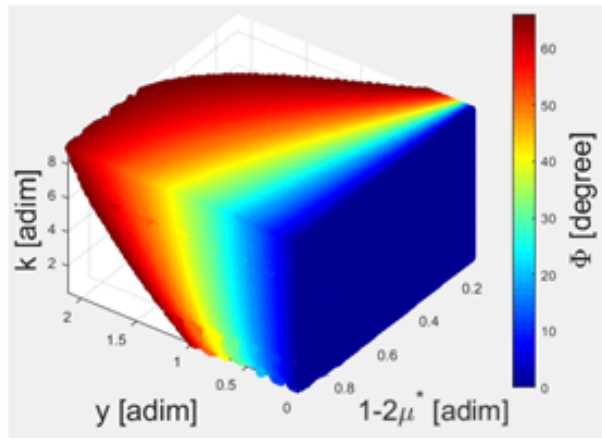
connects the spheres (see Figure 1). Therefore, we assume that these equilibrium points are inside the body of the asteroid.

Figure 2(b) is similar to Figure 2(a), with  $\mu^* = 1/3$  and  $k = 1$ , but now  $\Phi = 45^\circ$ . In this case, there are eight equilibrium points, all of them off the  $x$ -axis. The position shift occurs because a new configuration is necessary to fulfill the equilibrium conditions as the positions of the primaries change, modifying the value of the azimuthal angle.

We performed numerical investigations to understand how the coordinates of the external equilibrium points change when  $\mu^*$ ,  $k$  and  $\Phi$  are varied. To facilitate this analysis, we identified five regions, A, B, C, D, and E, as shown in Figure 3. We note that the regions are symmetric with respect to the  $y$ -axis. Observe that regions A, B and E are symmetric with respect to the  $y$ -axis, i.e., if the equilibrium point (in regions A, B or E) has coordinates  $(x, y)$ , then there will be another equilibrium point in the coordinates  $(-x, y)$ . Due to this symmetric property of the regions, we will only analyze the situations for which  $x$  is negative. Figure 3 displays the equilibrium points when  $\mu^* = 1/3$ ,  $k = 1$  and  $\Phi$  is varying. It illustrates how the equilibrium points move as this parameter is varied. The corresponding azimuthal angles are given in the caption of the plot. One can note the “path” followed by the equilibrium points as  $\Phi$  increases. For  $\Phi = 90^\circ$ , the equilibrium points are equivalent to those of a dipole aligned at  $x = 0$ .



(a)



(b)

Fig. 4. Coordinates of the equilibrium points in region A as a function of  $k$ ,  $\mu^*$  and  $\Phi$ . (a) Position of the equilibrium points on the  $x$ -axis. (b) Position of equilibrium the points on the  $y$ -axis. The color figure can be viewed online.

For region A, we plot the behavior of the equilibrium points in the  $x$  and  $y$  plane as a function of  $\mu^*$ ,  $k$  and  $\Phi$ , as shown in Figure 4.

Figure 4 shows how the coordinates of the equilibrium points vary with  $k$ ,  $\mu^*$  and  $\Phi$ . Note that the graphs show the variation in the mass of the body  $M_3$ , given by  $1-2\mu^*$ . That is, if the mass of  $M_3$  increases, consequently the mass of  $M_1$  (and  $M_2$ ), given by  $\mu^*$ , decreases. The color bar represents the value of the azimuthal angle. First, we investigate the solutions when we vary  $k$  and keep  $\mu^*$  and  $\Phi$  constant. Note from Figure 4 that as the rotation of the asteroid decreases, that is, as  $k$  becomes larger, the equilibrium points move away from the center of mass of the system. This is because increasing  $k$  im-

plies decreasing the angular velocity of the asteroid around its own axis (see equation 9), thus making the value of the centrifugal force smaller. The condition of existence of an equilibrium point is that the resulting force at one point in space is zero, that is, the gravitational force and the centrifugal force must have the same value (in the module) but in opposite directions. So, to keep the centrifugal force at a value that counteracts the gravitational force, the distance from the center of mass to the position of the equilibrium points must increase. As  $k$  increases, the equilibrium points appear farther from the center of mass.

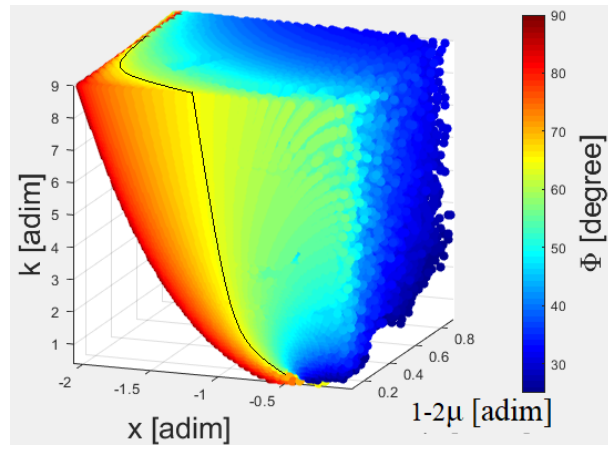
Next, keeping the values of  $k$  and  $\Phi$  constant and varying  $\mu^*$ , Figure 4 shows that, as  $\mu^*$  becomes smaller, the equilibrium points on the  $x$ -axis inside region A approach the center of mass of the system. On the other hand, as  $1-2\mu^*$  decreases (i.e.  $\mu^*$  increases), the equilibrium points move away from the asteroid. This happens because, as the mass of the bodies  $M_1$  and  $M_2$  becomes smaller, the gravitational force on the asteroid edge decreases on the  $x$ -axis, making it necessary to reduce the centrifugal force of the system on this axis. Conversely, the positions of the libration points move away from the center of mass along the  $y$ -axis as the gravitational force on this axis becomes larger due to the increase in the mass of  $M_3$ .

Finally, in region A as we increase  $\Phi$ , the equilibrium points along the  $x$ -axis come nearer to the center of mass of the system, while the ones along the  $y$ -axis move away from the center of mass of the system. These equilibrium points only exist when the azimuthal angle is between  $0^\circ$  and  $76^\circ$ . Beyond this value, the configuration of the tripole does not allow the existence of equilibrium points in region A.

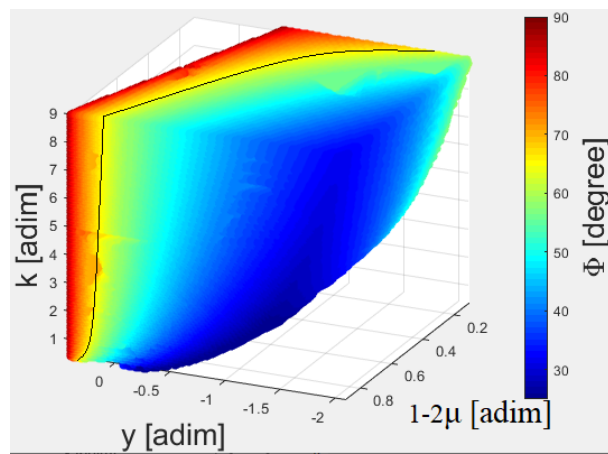
For region B, the variations of the  $x$  and  $y$  coordinates of the equilibrium points as a function of  $k$ ,  $\mu^*$  and  $\Phi$  are shown in Figures 5(a) and (b), respectively. For a better view of the path taken by the equilibrium points when we vary the parameters  $k$ ,  $\mu^*$  and  $\Phi$ , we insert a curve (black line) in the yellow region ( $\Phi = 65^\circ$ ).

We note that, as  $k$  becomes smaller, the positions of the equilibrium points in region B shift away from the center of mass of the system. This is true for the equilibrium points on both the  $x$ -axis and the  $y$ -axis and it occurs for the same reason as for the equilibrium points in region A.

The equilibrium points in region B occur for  $\Phi > 26^\circ$ . When the mass  $m_3$  increases, the equilibrium points tend to move away from primary body on both the  $x$  and  $y$  axis.



(a)



(b)

Fig. 5. Coordinates of the equilibrium points in region B as a function of  $k$ ,  $\mu^*$  and  $\Phi$ . (a) Position of the equilibrium points on the  $x$ -axis. (b) Position of equilibrium the points on the  $y$ -axis. The color figure can be viewed online.

Analyzing the positions of equilibrium points in region B as we increase  $\Phi$ , we find that the equilibrium points move upwards along the  $y$ -axis and may cross over to the positive semi-plane. Unlike what happens for solutions in region A, the equilibrium points in region B move away from the system's center of mass along the  $x$ -axis.

Table 1 summarizes the direction of the displacement of the equilibrium points in region A and B with respect to the body's center of mass as  $k$ ,  $\mu^*$  and  $\Phi$  vary. The symbol  $\nearrow$  indicates that the corresponding parameter is increasing, while  $\equiv$  is used to indicate parameters that are fixed. Directional arrows denote the direction of the displacement of the equilibrium points. For example, when we keep

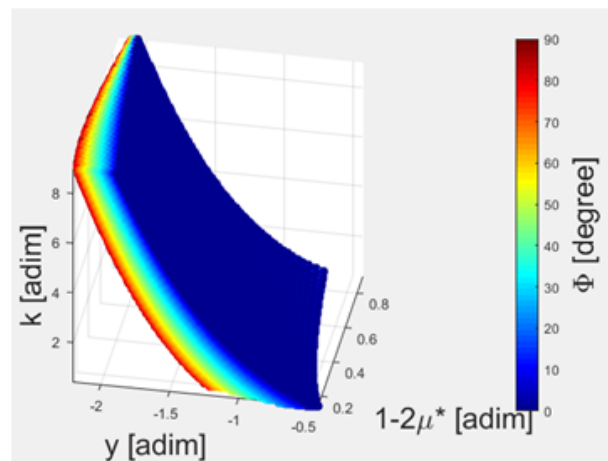


Fig. 6. Behavior of the equilibrium points on the  $y$ -axis of region C as a function of parameters  $k$ ,  $\mu^*$  and  $\Phi$ . The color figure can be viewed online.

fixed the values of  $k$  and  $\mu^*$ , and increase  $\Phi$ , the equilibrium points of region A,  $x$  and  $y$ , move to the right (approaching the system center of mass) and up (moving away from the system center of mass), respectively.

Next, we investigate regions C and D. In these two regions, the coordinate of the equilibrium points on the  $x$ -axis is zero for all points.

Figure 6 shows the  $y$  coordinate of the equilibrium points as a function of  $k$ ,  $\mu^*$  and  $\Phi$ . When  $k$  increases the centrifugal force becomes smaller, so the equilibrium points move downwards, away from  $M_3$ . As the mass of  $M_3$  increases, the gravitational force in the  $y$  direction becomes stronger, causing the positions of the equilibrium points to change. As  $\mu^*$  decreases and  $(1-2\mu^*)$  becomes larger, the equilibrium points in region C move in the negative direction of the  $y$ -axis.

Finally, as  $\Phi$  increases, the equilibrium points move in the downwards along the  $y$ -axis. Figure 6 illustrates that the  $y$  coordinate of the equilibrium points of the C region depends on  $\Phi$ , and that  $y_C(\Phi)$  becomes smaller as we increase the azimuthal angle. This happens because, as we increase  $\Phi$ ,  $M_1$  and  $M_2$  move upwards along the  $y$ -axis. Then, to keep the center of mass of the system at the origin,  $M_3$  must be in the semiplane with negative  $y$ -axis. Moreover, as  $\Phi$  increases, the coordinate of  $M_3$  becomes increasingly negative, so the equilibrium points in region C move away from  $M_3$  in the negative direction, to maintain the balance between the gravitational and centrifugal forces.

TABLE 1  
 VARIATION TRENDS OF COORDINATES FOR THE EQUILIBRIUM POINTS OF THE A AND B REGIONS

Summary, variation of parameters.	Equilibrium point motion. A region		Equilibrium point motion. B region	
	$x_0$	$y_0$	$x_0$	$y_0$
$k \nearrow, 1-2\mu^* \equiv, \Phi \equiv$	$\leftarrow$	$\uparrow$	$\leftarrow$	$\downarrow$
$k \equiv, 1-2\mu^* \nearrow, \Phi \equiv$	$\rightarrow$	$\uparrow$	$\leftarrow$	$\uparrow$
$k \equiv, 1-2\mu^* \equiv, \Phi \nearrow$	$\rightarrow$	$\uparrow$	$\leftarrow$	$\uparrow$

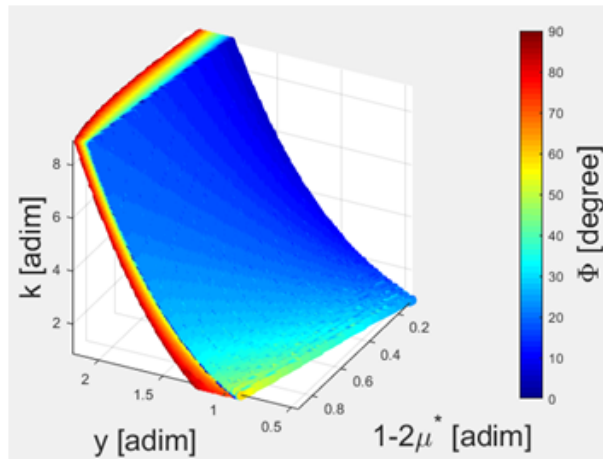


Fig. 7. Behavior of the equilibrium points on the  $y$ -axis of region D as a function of parameters  $k$ ,  $\mu^*$  and  $\Phi$ . The color figure can be viewed online.

Figure 7 shows how the equilibrium points in region D depend on  $k$ ,  $\mu^*$  and  $\Phi$ . As  $k$  increases, the equilibrium points move upwards, away from the center of mass of the system. As the mass of  $M_3$  increases, the gravitational force in the  $y$  direction becomes larger, changing the positions of the equilibrium points. As  $(1-2\mu^*)$  becomes larger, the equilibrium points in region D move in the positive direction of the  $y$ -axis, away from the center of mass of the system.

Finally, we investigated the behavior of the equilibrium points on the  $y$ -axis when we increase  $\Phi$ . Initially, when we increase  $\Phi$ , the equilibrium points on the  $y$ -axis approach the center of mass of the system. This happens because, as we increase the azimuthal angle,  $M_3$  moves downward; consequently, the gravitational force on the positive  $y$ -axis becomes weaker. In contrast, as we increase  $\Phi$ , the bodies  $M_1$  and  $M_2$  move upward with respect to the  $y$ -axis. This causes the gravitational force to increase in region D, now causing the equilibrium points to move upwards. For

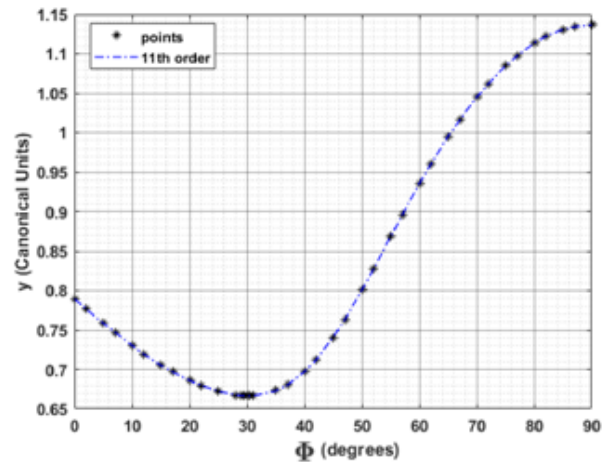


Fig. 8.  $y$ -coordinate of the equilibrium points in region D as a function of  $\Phi$  for  $[\mu^*, k] = [1/3, 1]^T$ . The color figure can be viewed online.

a better understanding, we constructed a figure using  $[\mu^*, k] = [1/3, 1]^T$ , which shows the equilibrium point behavior in the D region when we vary  $\Phi$ , as shown in Figure 8.

Then, as we increase the value of  $\Phi$ , the equilibrium point values in region D decrease, approaching the center of mass of the system; they reach a minimum for  $\Phi_D = 30.32^\circ$ , and the  $y$  position of the D region that depends on  $\Phi$  is  $y(\Phi)_{D-min} = 0.6664$ . Then they increase again, moving away from the center of mass of the system.

Table 2 summarizes the direction of the displacement of the equilibrium points in region D relative to the asteroid's center of mass when  $k$ ,  $\mu^*$  and  $\Phi$  vary.

### 3.2. Influence of the Azimuthal Angle on the Zero Velocity Curves

The azimuthal angle is one of the main parameters that govern the topological structure of the zero ve-

TABLE 2  
 VARIATION TRENDS OF COORDINATES FOR THE EQUILIBRIUM POINTS OF THE C AND D  
 REGIONS

Summary, variation of parameters.	Equilibrium point motion. C region		Equilibrium point motion. D region	
	$x_0$	$y_0$	$x_0$	$y_0$
$k \nearrow, 1-2\mu^* \equiv, \Phi \equiv$	0	$\downarrow$	0	$\uparrow$
$k \equiv, 1-2\mu^* \nearrow, \Phi \equiv$	0	$\downarrow$	0	$\uparrow$
$k \equiv, 1-2\mu^* \equiv, \Phi \nearrow$	0	$\downarrow$	0	$\downarrow \uparrow$

locity curves around the tripole system. In this section, this effect is investigated. For the numerical simulations we keep  $[k, \mu^*]^T = [1, 1/3]^T$  and we vary the angle  $\Phi$  in the interval  $[0, 90^\circ]$ .

Equation 19 relates the square of the velocity and the position of the infinitesimal mass body in a rotating coordinate system. Note that when the integration constant  $C^*$  is numerically determined by the initial conditions, equation 19 gives the speed with which the infinitesimal mass body moves.

In particular, if  $v$  is zero, equation 19 defines the curves at which the velocity is zero. The equation that gives the zero velocity curves, in Cartesian coordinates, is:

$$x^2 + y^2 + \frac{2\mu^*}{r_1} + \frac{2\mu^*}{r_2} + \frac{2(1-2\mu^*)}{r_3} = C^*, \quad (24)$$

where  $r_1$ ,  $r_2$  and  $r_3$  are as shown in equations 6, 7 and 8. The zero velocity curves in the  $xy$  plane for six different values of  $\Phi$  are shown in Figure 9. Each curve in frames (a) to (f) of Figure 9 corresponds to the value of the Jacobi constant for which the contacts between the ovals occur and the equilibrium points appear. The tripole is not illustrated in the figure.

Figure 9(a) shows the zero velocity curves when the azimuthal angle is  $0^\circ$ . Note that, for this azimuthal angle,  $M_1$ ,  $M_2$ , and  $M_3$  are aligned on the  $x$ -axis. On the other hand, Figure 9(b) shows the zero velocity curves when the azimuthal angle is  $20^\circ$ . For small values of  $x$  and  $y$  that satisfy equation 24, the first two terms are virtually irrelevant and the equation can be written as:

$$\frac{\mu^*}{r_1} - \frac{\mu^*}{r_2} - \frac{2(1-2\mu^*)}{r_3} = \frac{C^*}{2} - \frac{(x^2 + y^2)}{2} = \frac{C^*}{2} - \epsilon. \quad (25)$$

This equation gives the equipotential curves for the three centers of force  $\mu^*$ ,  $\mu^*$  and  $1-2\mu^*$ , as shown in Figure 9(a) and (b). For large values of  $C^*$ , ovals consist of closed curves around each of the body. If

we decrease  $C^*$ , the ovals around  $M_1$ ,  $M_2$  and  $M_3$  (inner ovals) expand, and the outer contours (outer ovals) move towards the center of mass of the system. The inner ovals connect with the outer ovals, resulting in the equilibrium points in region A (black curve) and the ovals between the bodies also connect, resulting in the equilibrium points in region E (red curve). See Figures 9(a) and (b).

If  $C^*$  is further decreased, the regions where movement is allowed become larger. This happens because the oval around the masses increases and merges with the outer oval, leaving only a small confined area (regions C and D), where the movement is impossible. Note from Figure 9(a) that, due to the symmetry of the problem, equilibrium points in regions C and D appear for the same value of  $C^*$  (green curve). On the other hand, when the azimuthal angle is different from  $0^\circ$ , the equilibrium points in the C and D regions appear for different Jacobi constant values (green and blue curves, respectively) shown in Figure 9(b).

Figure 9(c) shows the zero velocity curves when the azimuthal angle is  $40^\circ$ . The change in the topological structure of the zero velocity curves is evident as the azimuthal angle is varied. Note from Figure 9(c) that, in addition to the contact points shown in Figures 9(a) and (b), new contact points emerge (red curves), in region B. Through numerical simulations, we observe that the B region arises when the azimuthal angle is greater than  $26^\circ$ .

When we consider an azimuthal angle of  $60^\circ$ ,  $M_1$ ,  $M_2$  and  $M_3$  form an equilateral triangle relative to the rotating reference system. Thus, the zero velocity curves have a symmetrical shape. When the azimuthal angle is  $60^\circ$ , the equilibrium points in regions A and C arise for  $C_{A-C} = 2.946725190$ . Likewise, the ( $C_{B-D} = 3.35803516$ ) is required for contacts between ovals in regions B and D. If the masses of  $M_1$  and  $M_2$  are different, the symmetric property of the equilibrium points and the zero velocity curves with respect to the  $xy$  axis is not valid. Figure 9(e)

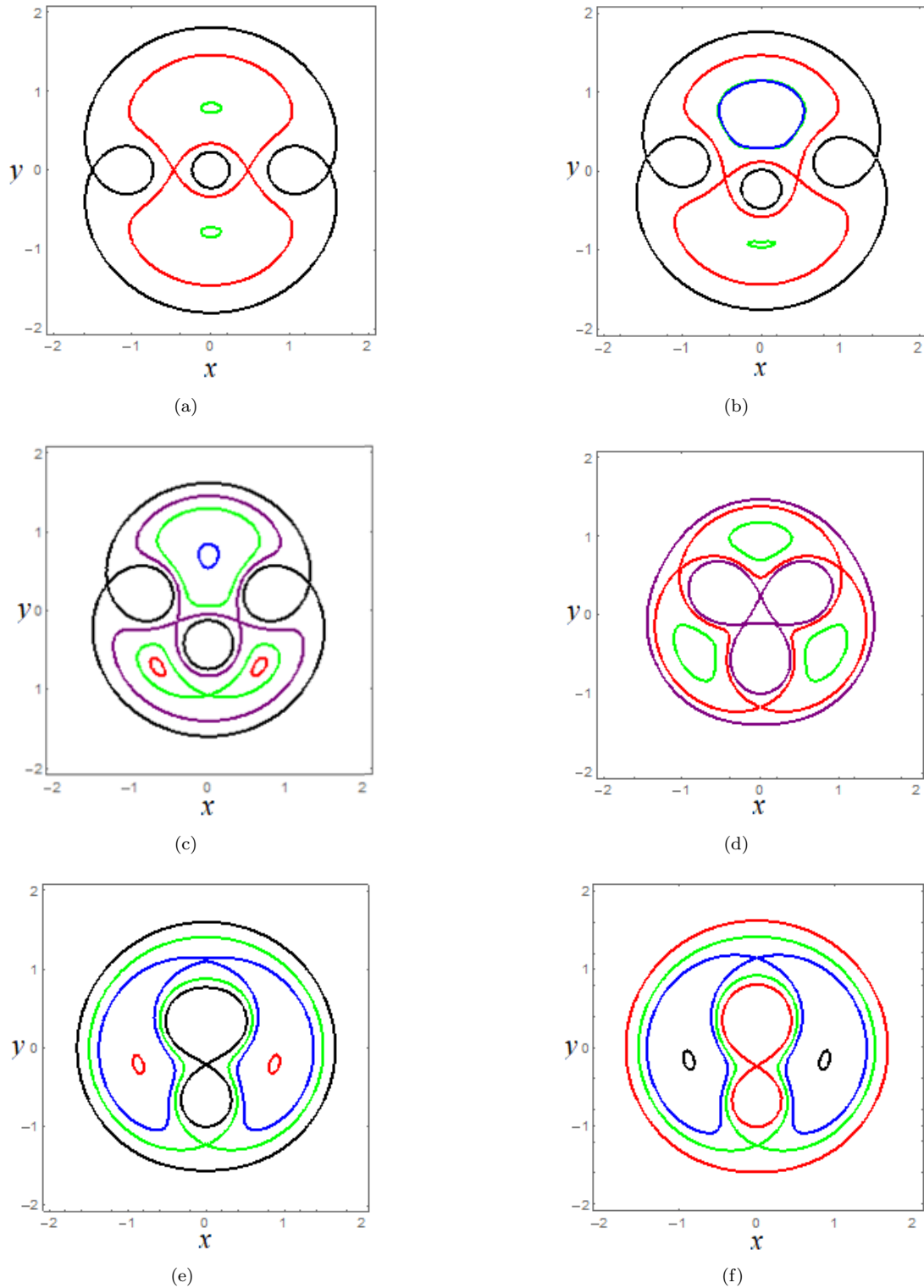


Fig. 9. Influence of the azimuthal angle on the zero-velocity curves in the  $xy$  plane. (a) Zero velocity curves for a  $0^\circ$  azimuthal angle. (b) Zero velocity curves for a  $20^\circ$  azimuthal angle. (c) Zero velocity curves for a  $40^\circ$  azimuthal angle. (d) Zero velocity curves for a  $60^\circ$  azimuthal angle. (e) Zero velocity curves for an  $80^\circ$  azimuthal angle. (f) Zero velocity curves for a  $90^\circ$  azimuthal angle. The color figure can be viewed online.

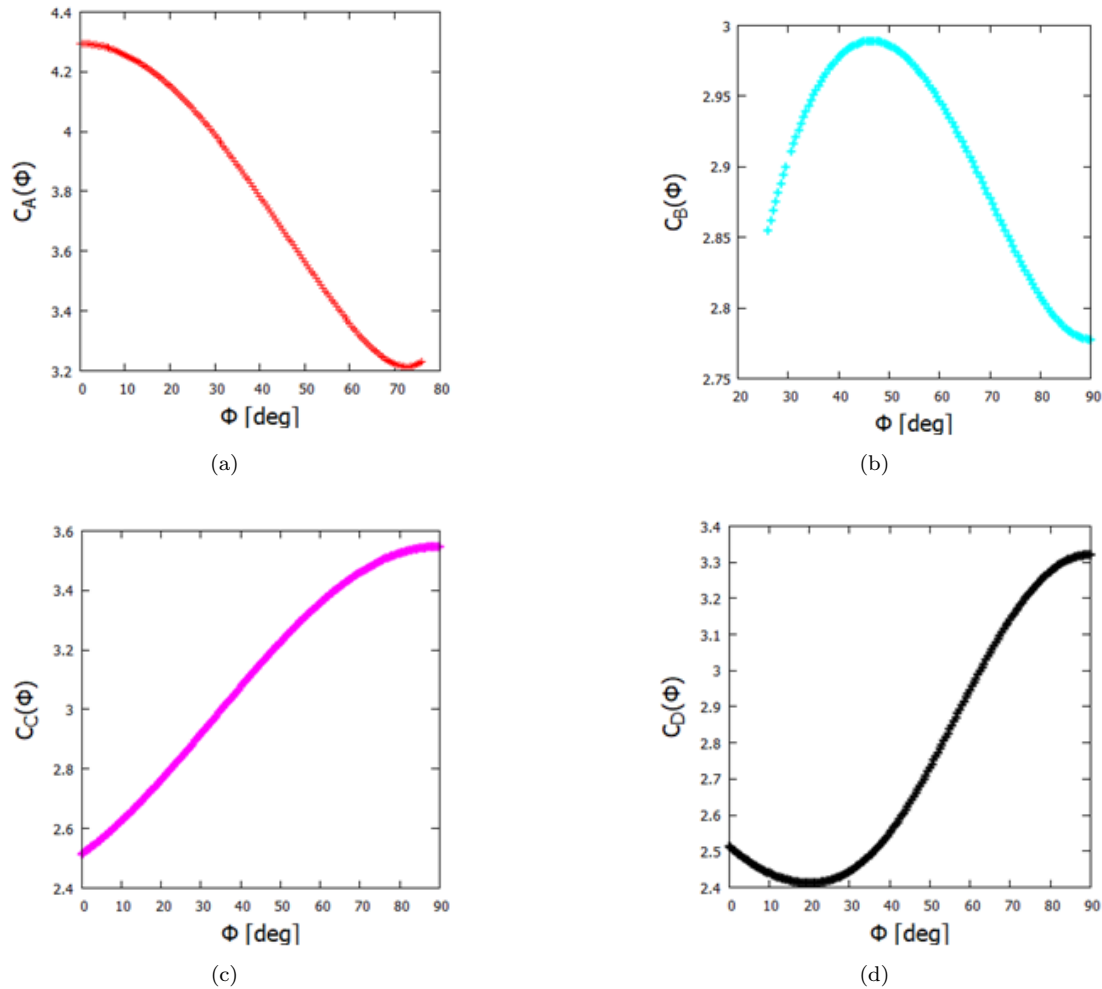


Fig. 10. Jacobi constant behavior in regions A, B, C and D, respectively, as a function of azimuthal angle. (a) Values of the Jacobian constant ( $C_A$ ) at the equilibrium points versus  $\Phi$ . (b) Values of the Jacobian constant ( $C_B$ ) at the equilibrium points versus  $\Phi$ . (c) Values of the Jacobian constant ( $C_C$ ) at the equilibrium points versus  $\Phi$ . (d) Values of the Jacobian constant ( $C_D$ ) at the equilibrium points versus  $\Phi$ . The color figure can be viewed online.

shows the zero velocity curves for an azimuthal angle of  $80^\circ$ . In Figure 9(e), we observe that the regions A cease to exist, leaving only regions B, C, D and E. This means that, just as regions B depend on the azimuthal angle to emerge or disappear, so do regions A. Regions A cease to exist for  $\Phi > 76^\circ$ .

Finally, considering an azimuthal angle of  $90^\circ$ ,  $M_1$  and  $M_2$  overlap, which means that they behave as a single body with mass  $m = m_1 + m_2$ . For this configuration, the system is similar to the Classical Restricted Three-body Problem with a mass ratio of  $\mu^* = 1/2$ .

Note from Figures 9(a) - (f) that, as we increase the azimuthal angle from 0 to  $90^\circ$ , noticeable changes in the zero velocity curves can be observed near the arched asteroid. Note that the regions that connect

the ovals move along the  $xy$  plane as we vary the azimuthal angle. Some fixed points also emerge or disappear.

The values of the modified Jacobi constants at the contact points in each region in Figure 9 are shown in Figure 10. Figures 10(a) - (d) show how the values of the Jacobi constant at regions A, B, C, and D ( $C_A$ ,  $C_B$ ,  $C_C$ , and  $C_D$ , respectively) vary as a function of the azimuthal angle  $\Phi$ . In Figure 10(a), we see that the values of the Jacobi constant  $C_A(\Phi)$  decrease as the azimuthal angle  $\Phi$  increases. For  $C_B(\Phi)$ , one notes that initially the value of the Jacobi constant increases with increasing azimuthal angle, and then it decreases, as shown in Figure 10(b). This behavior causes a maximum value for  $C_B(\Phi)$ , which happens at  $C_B = 2.989303755$ , for

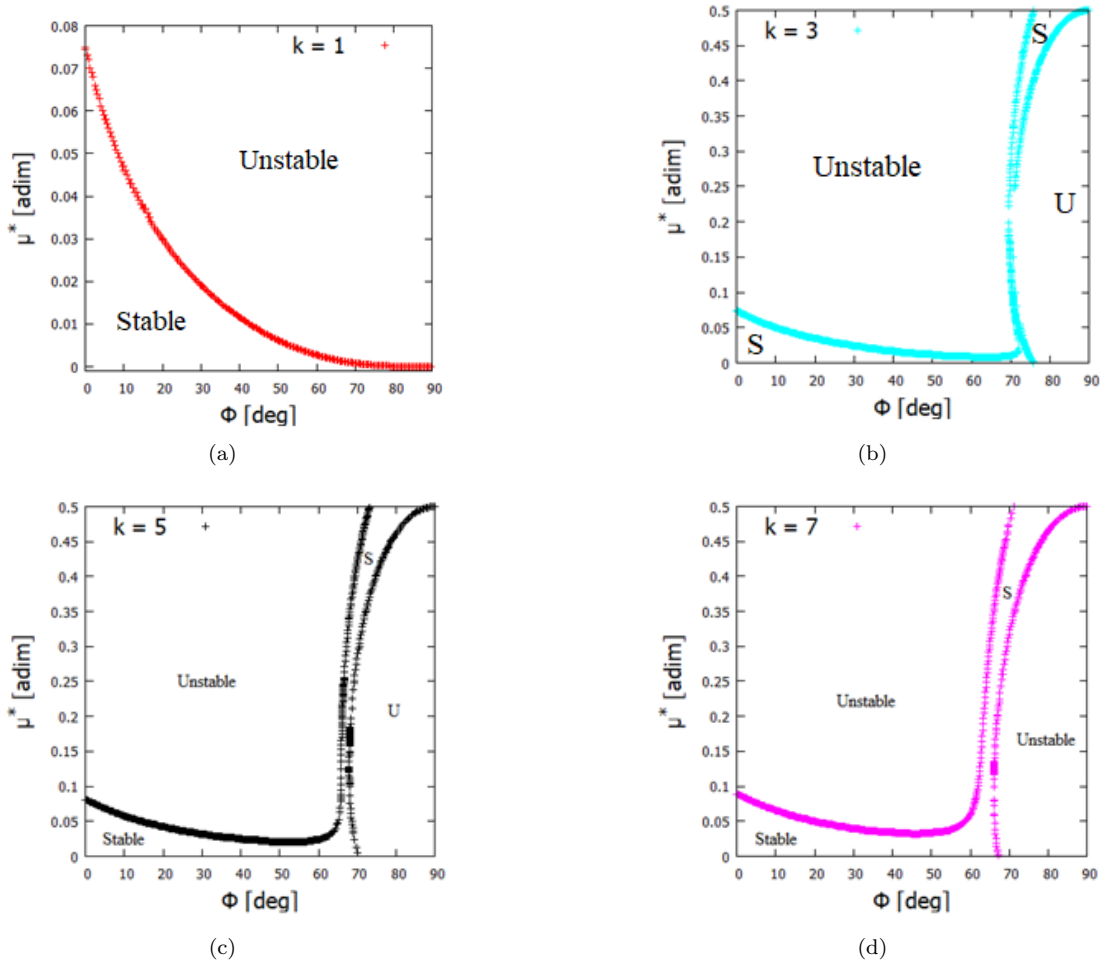


Fig. 11. Values of the mass ratio ( $\mu^*$ ) versus the azimuthal angle ( $\Phi$ ) for the stability condition of the equilibrium point  $L_D$  considering different values of  $k$ . (a) Values of the mass ratio ( $\mu^*$ ) versus the azimuthal angle ( $\Phi$ ) when  $k = 1$  for the stability condition of the equilibrium point  $L_D$ . (b) Values of the mass ratio ( $\mu^*$ ) versus the azimuthal angle ( $\Phi$ ) when  $k = 3$  for the stability condition of the equilibrium point  $L_D$ . (c) Values of the mass ratio ( $\mu^*$ ) versus the azimuthal angle ( $\Phi$ ) when  $k = 5$  for the stability condition of the equilibrium point  $L_D$ . (d) Values of the mass ratio ( $\mu^*$ ) versus the azimuthal angle ( $\Phi$ ) when  $k = 7$  for the stability condition of the equilibrium point  $L_D$ . The color figure can be viewed online.

$\Phi = 46.524234^\circ$ . On the other hand, the values of the function  $C_C(\Phi)$  increase as we increase  $\Phi$ . Finally, for  $C_D$ , as we increase  $\Phi$ , initially the values of  $C_D$  become smaller, reaching a minimum value of  $C_D = 2.4120014$  when the azimuthal angle is approximately  $\Phi = 19.987^\circ$ , and then they increase.

### 3.3. Stability Conditions

Now, we focus on the analysis of the stability conditions for the equilibrium points in regions D and C, ( $L_D$  and  $L_C$ ), respectively, i.e., points that have null  $x$  coordinate. We describe how the stability conditions for the equilibrium points  $L_D$  (and  $L_C$ ) depend on the azimuthal angle ( $\Phi$ ), the force ratio ( $k$ ) and

the mass ratio ( $\mu^*$ ). Indeed, if any of these parameters are changed, the stability condition (unstable or stable) of these equilibrium points may also change.

First let us look at the stability condition for region D. Figure 11 displays plots of  $\Phi$  versus  $\mu^*$ , showing the stability transition. We see from Figure 11(a) that, when the azimuthal angle increases and  $k = 1$ , the mass ratio required to maintain the equilibrium point  $L_D$  stable decreases. When the angle is  $0^\circ$ , the maximum mass ratio to allow linear stability of the system studied is  $\mu^* = 0.0742683$ . If the mass ratio is greater than this value, the system is unstable for every azimuthal angle. Note that, when  $\Phi \rightarrow 90^\circ$ , the two masses of the tripole ( $m_1$  and  $m_2$ ) collapse

into a mass point with a mass ratio  $2\mu^*$ . In this case, the point  $L_D$  is similar to the equilibrium point  $L_3$  of the Classical Restricted Three-Body Problem. Therefore this equilibrium point is linearly unstable for any mass ratio, which is in agreement with the literature (Moulton 1914; Szebehely 1967; Murray & Dermott 1999; McCuskey 1963).

Figures 11(b) to (d) show  $\Phi$  versus  $\mu^*$ , illustrating the stability regions when  $k > 1$ . We see from Figure 11(b) that, for  $\Phi < 70^\circ$ , the stability transition is similar to the case when  $k = 1$ , but the bifurcation occurs when  $\Phi \approx 70^\circ$ . Notice in the graph that a narrow vertical strip appears, causing the  $L_D$  equilibrium point to be stable for any value of  $\mu^*$ . As  $\Phi$  increases, the stability conditions change again, making the equilibrium point stable only for high values of  $\mu^*$ . So, observe that when the system has small values of  $\mu^*$ , the equilibrium points are linearly stable for  $\Phi < 76^\circ$ . On the other hand, for a very arched asteroid ( $\Phi > 76^\circ$ ), the equilibrium point  $L_D$  is linearly stable when the mass ratio of the system is large.

Figure 11(c) shows the stability transition curve for  $k = 5$ . We observe that when  $\Phi < 60^\circ$ , the stability transition curve is similar to the previous cases. We also notice that a narrow vertical strip appears (around  $\Phi \approx 65^\circ$ ) and has a larger area with respect to the previous case. This means that we can also find stable regions when we consider large values of  $\Phi$  ( $\Phi > 60^\circ$ ) and  $\mu^*$ . As we increase the value of  $\Phi$  (when  $\Phi > 70^\circ$ ), the equilibrium point  $L_D$  becomes linearly stable only for large values of  $\mu^*$ . For small values of  $\mu^*$ , the equilibrium point  $L_D$  is stable when  $\Phi < 70^\circ$ . The letters S and U shown in Figure 11(c) are abbreviations for stable and unstable condition, respectively.

Finally, Figure 11(d) shows the stability transition when  $k = 7$ . Note that, as in the previous cases, when we consider  $k = 7$  a narrow vertical strip appears (around  $\Phi 60^\circ$ ), allowing the equilibrium point  $L_D$  to be linearly stable for any value of  $\mu^*$ . If we gradually increase  $\mu$  and  $\Phi$ , the stable regions remain until  $\Phi = 89.6^\circ$ . On the other hand, if we decrease  $\mu$  as we increase  $\Phi$  (from  $66^\circ$ ), the stable region extends to  $\Phi = 67^\circ$ . Note in Figures 11(b) to (d) that the area of the narrow vertical strip becomes larger as we increase the  $k$  value. This means that, the larger the value of  $k$ , the larger the region that allows linear stability of the equilibrium point  $L_D$  for any values of  $\mu^*$ .

A similar analysis was performed for the equilibrium point  $L_C$  and the results are shown in Figure 12. Unlike Figure 11(a), when  $k = 1$ , Fig-

ure 12(a) shows that there are two stability transition limits. The first limit (lower transition, left-hand curve) exists for small azimuthal angles, starting at  $0^\circ$ , with a mass ratio of 0.07427949. Above  $18.351^\circ$ , numerical evidence shows that another stability transition arises, as shown by the right-hand curve in Figure 11(a).

Figures 12(b) - (d) show  $\Phi$  versus  $\mu^*$ , which illustrates the stability regions, when  $k > 1$ . Figure 12(b) shows two stability transitions. Note that the first transition starts when  $\Phi = 0^\circ$  and  $\mu^*$  is approximately 0.074.

The second stability transition starts when  $\Phi = 25^\circ$ , when the asteroid is  $8^\circ$  more arched than in the previous case, so the equilibrium point  $L_C$  has a wider stable region compared to when  $k = 1$ . For  $\Phi > 57.5^\circ$ , the equilibrium point  $L_C$  is unstable for any mass ratio.

If we further increase the value of  $k$  to  $k = 5$ , the stability region becomes even larger, as shown in Figure 12(c). The first stability transition arises when  $\Phi = 0^\circ$  and  $\mu^* = 0.08$ . In contrast, the second curve arises when  $\mu^* = 0$  and  $\Phi = 28^\circ$ , thus limiting the region that allows the equilibrium point  $L_C$  to be stable. If the azimuthal angle is greater than  $68^\circ$ , the equilibrium point  $L_C$  becomes unstable for any mass ratio.

Finally, we made an analysis considering  $k = 7$ . Note from Figure 12(d) that, due to the slow rotation of the asteroid, now a larger area on the graph makes the  $L_C$  equilibrium point linearly stable. For  $k = 7$ , the first transition starts when  $\Phi = 0^\circ$  and  $\mu^* = 0.09$ . In contrast, the second stability transition starts when  $\Phi = 29^\circ$  and  $\mu^* = 0$ . This shows that when we increase the value of  $k$  (ie, the angular velocity of the asteroid becomes slower), the two stability transition curves intersect at a larger azimuthal angle, ranging from approximately,  $\Phi = 35^\circ$  when  $k = 1$ , to  $\Phi = 75^\circ$  when  $k = 7$ . This shows that, as we increase the force ratio  $k$ , the stability region becomes larger.

#### 4. APPLICATION

To validate the equations and results developed in this article, we compared the results obtained with four celestial bodies, (i) 243 Ida, (ii) 433 Eros, (iii) 1996(HW1) and (iv) M1 Phobos.

The parameters  $k$ ,  $\Phi$  and  $\mu^*$  were taken from Lan et al. (2017) (for Ida and M1 Phobos) and Yang et al. (2018) (for Eros and 1996 HW1). The linear stability of the equilibrium points of the celestial bodies mentioned above was obtained by Wang et al. (2014)

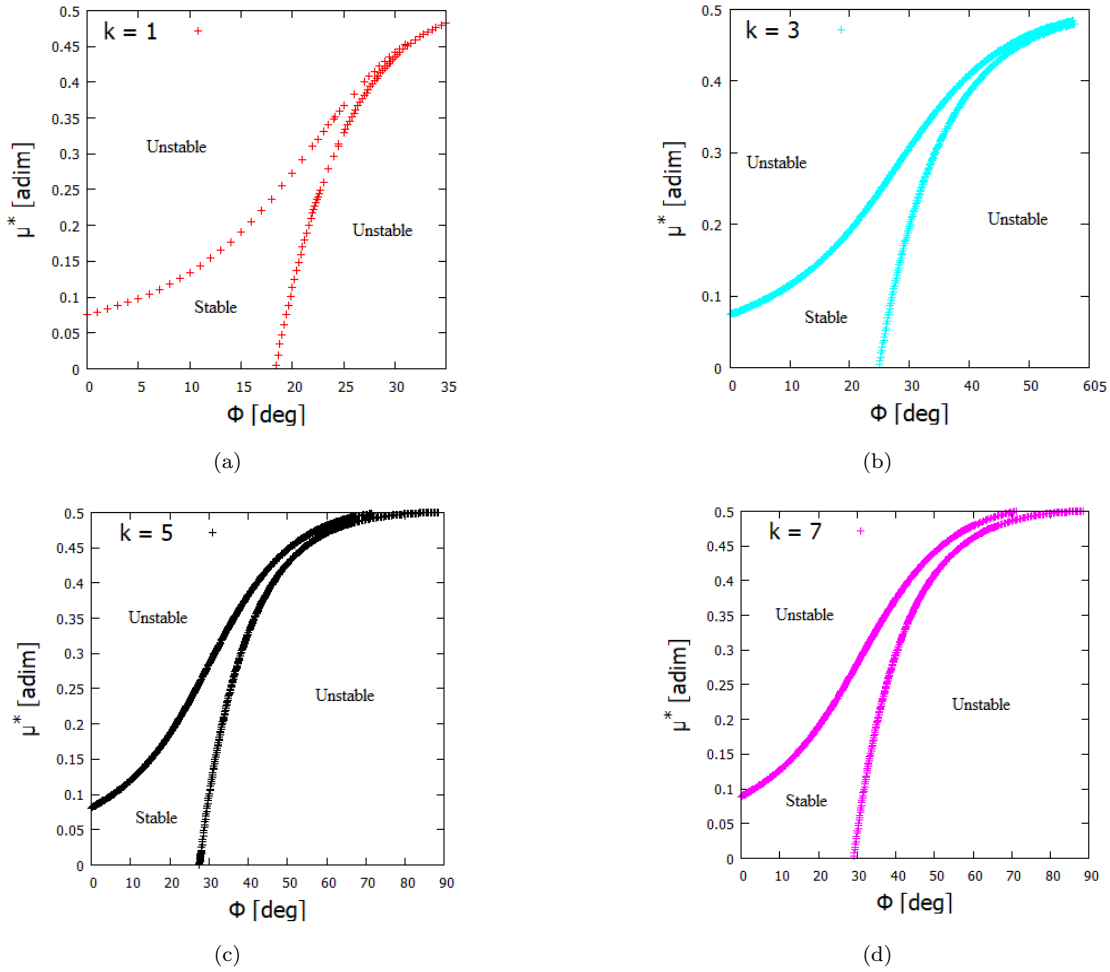


Fig. 12. Values of the mass ratio ( $\mu^*$ ) versus the elevation angle ( $\Phi$ ) for the stability condition of the equilibrium point  $L_C$  considering different values of  $k$ . (a) Values of the mass ratio ( $\mu^*$ ) versus the azimuthal angle ( $\Phi$ ) when  $k = 1$  for the stability condition of the equilibrium point  $L_C$ . (b) Values of the mass ratio ( $\mu^*$ ) versus the azimuthal angle ( $\Phi$ ) when  $k = 3$  for the stability condition of the equilibrium point  $L_C$ . (c) Values of the mass ratio ( $\mu^*$ ) versus the azimuthal angle ( $\Phi$ ) when  $k = 5$  for the stability condition of the equilibrium point  $L_C$ . (d) Values of the mass ratio ( $\mu^*$ ) versus the azimuthal angle ( $\Phi$ ) when  $k = 7$  for the stability condition of the equilibrium point  $L_C$ . The color figure can be viewed online.

and used in this study for comparison purposes. In Wang et al. (2014), regions  $C$  and  $D$  are the equilibrium points  $E_4$  and  $E_2$ , respectively.

The optimized parameters of the bodies under analysis in this article are shown in Table 3, where  $\Phi$  is determined by setting  $\Phi = \arctan(2\sigma)$  in which  $\sigma$  is given by  $l_2/l_1$  and was determined in Lan et al. (2017) and Yang et al. (2018).

Knowing the parameters for each celestial body, it is possible to find the stability conditions for the equilibrium points  $E_4$  and  $E_2$  from equations 22 and 23.

TABLE 3

THE OPTIMAL PARAMETERS FOR THE TRIPOLE MODELS

Asteroid	$k$	$\mu^*$	$\Phi$
243 Ida	0.402	0.237	19.94°
M1 Phobos	22.003	0.396	56.09°
433 Eros	0.434	0.260	18.95°
1996 (HW1)	3.158	0.443	27.43°

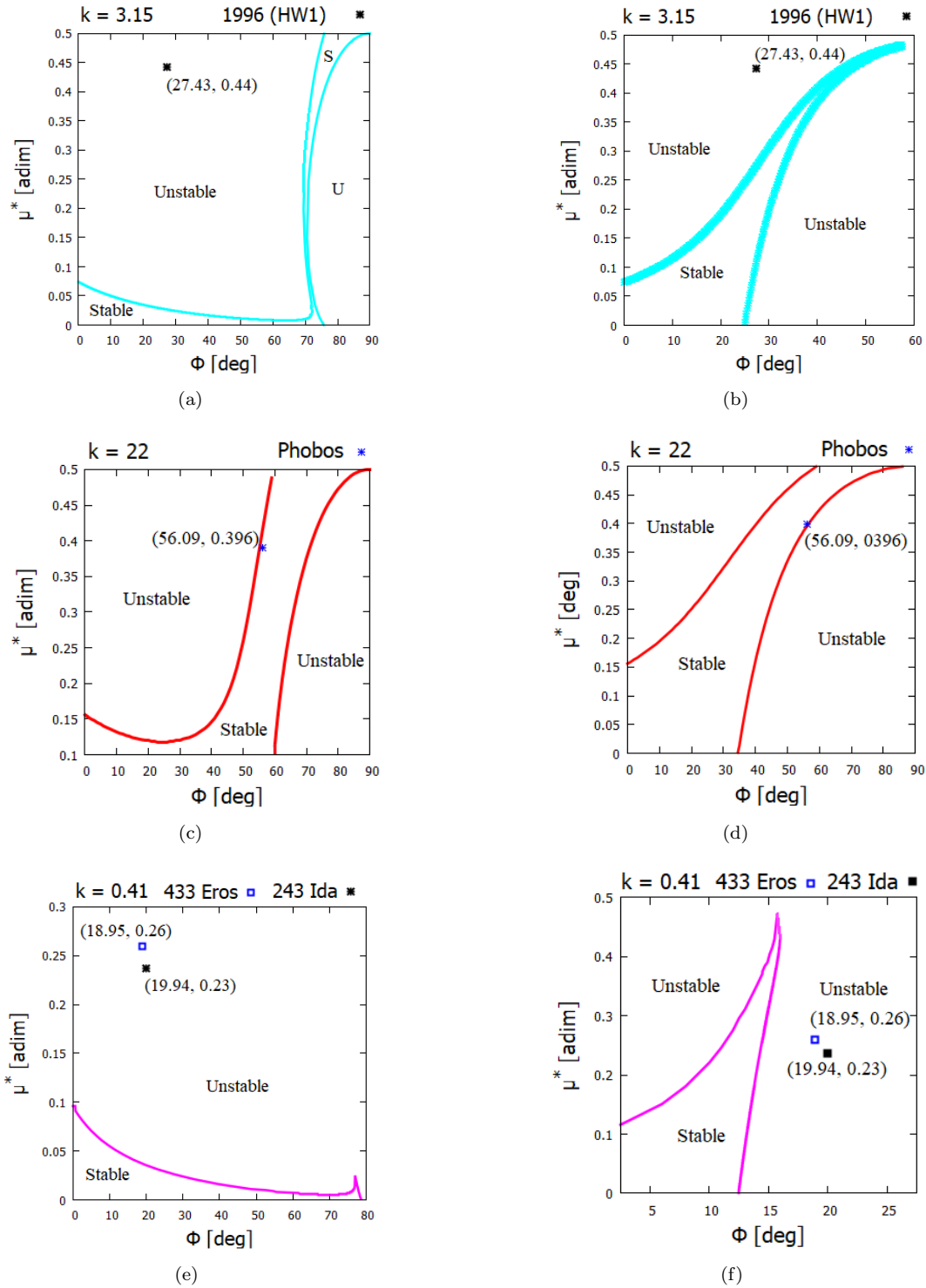


Fig. 13. Values of the  $\mu^*$  versus  $\Phi$  for the stability condition of the equilibrium point  $L_D$  ( $E_2$ ) and  $L_C$  ( $E_4$ ) for a specific  $k$  value. (a)  $k = 3.15$  for the equilibrium point  $L_D$  ( $E_2$ ) of the 1996 HW1 asteroid. (b)  $k = 3.15$  for the equilibrium point  $L_C$  ( $E_4$ ) of the 1996 HW1 asteroid. (c)  $k = 22$  for the equilibrium point  $L_D$  ( $E_2$ ) of M1 Phobos. (d)  $k = 22$  for the equilibrium point  $L_C$  ( $E_r$ ) of M1 Phobos. (e)  $k = 3.15$  for the equilibrium point  $L_D$  ( $E_2$ ) of the 243 Ida and 433 Eros asteroids. (f)  $k = 3.15$  for the equilibrium point  $L_C$  ( $E_4$ ) of the 243 Ida and 433 Eros asteroids. The color figure can be viewed online.

Figure 13 shows  $\mu^*$  versus  $\Phi$  and illustrates the stability regions for the equilibrium points  $L_C$  and  $L_D$  for asteroids 1996 HW1, 243 Ida and 433 Eros and M1 Phobos.

Figure 13(a) and (b) plot  $\Phi$  vs.  $\mu^*$  (27.43, 0.44) for the asteroid 1996 HW1. We observe that the point is outside the region that allows stability of the equilibrium points  $E_2$  and  $E_4$ , showing that these equilibrium points are unstable, a result that coincides with the results obtained by Wang et al. (2014).

Figures 13(c) and (d) show the stability region of the equilibrium points  $E_2$  and  $E_4$  when  $k = 22$ . We plotted the ordered pair (56.09, 0.396) for M1 Phobos. Due to the characteristics (shape, density and rotation) of M1 Phobos, the equilibrium points  $E_2$  and  $E_4$  are within the stability region, making these equilibrium points linearly stable.

The stability of the equilibrium points depends on the bulk density, the shapes, and the angular velocities of the asteroids. The bulk density is obtained from the composition of the asteroid, a characteristic that is hard to change. The asteroids are shaped in the long-term in space. On the other hand, the angular velocities of asteroids are altered due to the accelerations caused by the YORP effect (Paddack 1969).

Observe that the equilibrium points  $E_2$  and  $E_4$  of M1 Phobos are close to the boundary that guarantees the condition of stability (see Figure 13(c) and (d)). If the angular velocity of this body increases, as predicted by the YORP effect,  $k$  will decrease, making the equilibrium point unstable. This result shows the importance of carrying out a generalized analysis with the aim of globally understanding the dynamical properties in the vicinity of celestial bodies.

Finally, Figure 13(e) and (f) provide information regarding the stability condition for 243 Ida and 433 Eros asteroids. In Table 3 we see that  $k$  for asteroids 243 Ida and 433 Eros are very close. Because of this, we will show the results for these two asteroids on the same graph, in Figures 13(e) and (f). We plotted  $(\phi, \mu^*) = (18.95, 0.26)$  and  $(\phi, \mu^*) = (19.94, 0.23)$  for 433 Eros and 243 Ida asteroids, respectively.

We observe that the equilibrium points  $E_2$  and  $E_4$  (Figure 13(e) and (f), respectively) of asteroids 243 Ida and 433 Eros are unstable due to their physical and dynamical characteristics.

These results show that our generalized analysis coincides with the results obtained for asteroids that can be modeled as rotating mass tripoles.

## 5. CONCLUSION

Dynamical properties of the rotating mass tripole were addressed in this article. The rotating mass tripole consists of three point masses whose geometric configuration depends on the shape of the asteroids under analysis.

We observed that the gravitational potential depends on three free parameters, which are: the force ratio, the mass ratio and the azimuthal angle. We note that the number of equilibrium points that arise depends on the combination of these free parameters. It can be from five to eight equilibrium points. The tendency to vary the location of the equilibrium points according to the free parameters was studied.

We also analyzed the topological structure of the zero velocity curves with respect of the azimuthal angle. We observed that the zero velocity curves around the rotating mass tripole have significant changes due to the arched shape of the asteroid.

Analyzing the linearized equations, we observed that the condition of stability of the equilibrium points in regions C and D depends on  $k$ ,  $\mu^*$  and  $\Phi$ . For region C, we observed the appearance of bifurcations when  $k > 1$ . On the other hand, the equilibrium points in region D show two stability transition limits for any value of  $k$ . For both regions (C and D), it was observed that as we increased the value of  $k$  the region of stability became larger.

Understanding the dynamics of a particle subject to the gravitational field of an elongated asteroid is extremely important for the exploration of these bodies. The results presented here provide a global characterization of the dynamical behavior of an infinitesimal mass body around an asteroid modeled as a rotating mass tripole. This allows a better understanding of the main factors that influence the topological structure of the gravitational field in the vicinity of asteroids with an arched shape. More complex models, such as the polyhedral method, are much more accurate and are widely used in the analysis of a specific asteroid, but the present model proved to be useful in providing general information about families of asteroids similar to the tripole model.

The authors wish to express their appreciation for the support provided by: grants 406841/2016-0, 140501/2017-7, 150678/2019-3, 422282/2018-6259 and 301338/2016-7 from the National Council for Scientific and Technological Development (CNPq); grants 2016/24561-0, 2018/00059-9 and 2016/18418-0, from São Paulo Research Foundation (FAPESP); grant 88887.374148/2019-00 from

the National Council for the Improvement of Higher Education (CAPES) and to the National Institute for Space Research (INPE).

## REFERENCES

- Aljbaae, S., Chanut, T. G. G., Carruba, V., et al. 2017, *MNRAS*, 464, 3552
- Barbosa Torres dos Santos, L., Prado, A. F. B. de A., & Merguizo Sanchez, D. 2017, *Ap&SS*, 362, 61
- Barbosa Torres dos Santos, L., Prado, A. F. B. de A., & Sanchez, D. M. 2017, *Ap&SS*, 362, 202
- Blesa, F. 2006, *Monografías del Seminario Matemático García de Galdeano*, 33, 67
- Broschart, S. B. & Scheeres, D. J. 2005, *JGCD*, 28, 343
- Broucke, R. A. 1968, *Periodic Orbits in the Restricted Three-Body Problem with Earth-Moon Masses* (Pasadena, CA: California Institute of Technology)
- Chanut, T. G. G., Aljbaae, S., & Carruba, V. 2015, *MNRAS*, 450, 3742
- Chanut, T. G. G., Winter, O. C., Amarante, A., & Araújo, N. C. S. 2015, *MNRAS*, 452, 1316
- Elipe, A. & Lara, M. 2003, *The Journal of the Astronautical Sciences*, 51, 391
- Elipe, A. & Riaguas, A. 2003, *Intern. Math. Journal*, 3, 3435
- Gabern, F., Koon, W. S., Marsden, J. E., & Scheeres, J. D. 2006, *JADS*, 5, 252
- Geissler, P., Petit, J.-M., Durda, D. D., et al. 1996, *Icar*, 120, 140
- Jiang, Y., Baoyin, H., Li, J., & Li, H. 2014, *Ap&SS*, 349, 83
- Jiang, Y. & Baoyin, H. 2018, *AdSpR*, 62, 3199
- Lan, L., Yang, H., Baoyin, H., & Li, J. 2017, *Ap&SS*, 362, 169
- Liu, X., Baoyin, H., & Ma, X. 2011, *Ap&SS*, 333, 409
- McCuskey, S. W. 1963, *Introduction to celestial mechanics* (Reading, MA: Addison-Wesley Pub. Co.)
- Moulton, F. R. 1914, *An Introduction to celestial mechanics* (New York, NY: The Macmillan company)
- Murray, C. D., & Dermott, S. F. 1999, *Solar System Dynamics* (Cambridge, UK: CUP)
- Ollé, M., Pacha, J. R., & Villanueva, J. 2004, *CeMDA*, 90, 87
- Paddack, S. J. 1969, *J. Geophys. Res.*, 74, 4379
- Riaguas, A., Elipe, A., & Lara, M. 1999, *CeMDA*, 73, 169
- Riaguas, A., Elipe, A., & López-Moratalla, T. 2001, *CeMDA*, 81, 235
- Scheeres, D. J., Ostro, S. J., Hudson, R. S., & Werner, R. A. 1996, *Icar*, 121, 67
- Scheeres, D. J. 2004, *AIAA*, 1445
- \_\_\_\_\_. 2012, *CeMDA*, 113, 291
- Szebehely, V. 1967, *Theory of orbits. The restricted problem of three bodies* (New York, NY: Academic Press)
- Tsoulis, D., & Petrović, S. 2001, *Geop*, 66, 535
- Venditti, F. C. F. 2013, *Orbital Maneuvres around Irregularly shaped bodies*, Ph.D. Thesis, INPE
- Wang, X., Jiang, Y., & Gong, S. 2014, *Ap&SS*, 353, 105
- Wang, W., Yang, H., Zhang, W., et al. 2017, *Ap&SS*, 362, 229
- Weng, T., Zeng, X., Circi, C., et al. 2020, *JGCD*, 43, 1269
- Werner, R. A. 1994, *CeMDA*, 59, 253
- Yang, H.-W., Li, S., & Xu, C. 2018, *RAA*, 18, 084
- Yang, H., Baoyin, H., Bai, X., & Li, J. 2017, *Ap&SS*, 362, 27
- Yu, Y. & Baoyin, H. 2012, *AJ*, 143, 62
- Zeng, X., Jiang, F., Li, J., et al. 2015, *Ap&SS*, 356, 29
- Zeng, X., Baoyin, H., & Li, J. 2016, *Ap&SS*, 361, 15
- \_\_\_\_\_. 2016, *Ap&SS*, 361, 14
- Zeng, X., Zhang, Y., Yu, Y., et al. 2018, *AJ*, 155, 85
- Zeng, X., Gong, S., Li, J., et al. 2016, *JGCD*, 39, 1223
- Zeng, X. & Liu, X. 2017, *ITAES*, 53, 1221

S. Aljbaae, L. Barbosa T. dos Santos, L. O. Marchi, A. F. B. A. Prado, and D. M. Sanchez: Division of Space Mechanics and Control - National Institute for Space Research (INPE), CEP 12227-010, São José dos Campos - SP, Brazil (leonardo.btorres@inpe.br).

Priscilla A. de Sousa-Silva: Department of Aeronautical Engineering - São Paulo University (UNESP), CEP 13876-750, Campus of São João da Boa Vista - SP, Brazil (priscilla.silva@unesp.br).

## ANALYSIS OF A SHORT PERIODIC PULSATOR: SX PHOENICIS STAR XX CYG

Mohamed Abdel-Sabour<sup>1</sup>, Ahmed Shokry<sup>1</sup>, and Ahmed Ibrahim<sup>2,3</sup>

*Received May 5 2020; accepted August 7 2020*

### ABSTRACT

Photometric observations were made of the SX Phoenicis star XX Cyg between September and October 2019, using the 1.88-m Kottamia reflector telescope in Egypt. We used 340 CCD observations with blue-visible-red (BVR) filters to derive light curves. In addition, we obtained 9540 visual magnitudes for XX Cyg from the literature to prepare an observed-minus-calculated (O-C) diagram. 85 new times of maximum for XX Cyg are presented. We did not detect a bump in the descending portion of the light curve of maximum light for XX Cyg. However, we did detect a secular bump in the phased light curves, which changes with phase in some SuperWASP observations. We found the change in period of XX Cyg to be  $dP/dt = 15.5 \times 10^{-5}$  s/yr, with its amplitude decreasing at a rate of 0.7 mmag/year. Stellar parameters of XX Cyg and its position in the instability strip of the Hertzsprung Russell stellar evolution diagram are presented.

### RESUMEN

Se realizaron observaciones fotométricas de la estrella tipo SX Phoenicis XX Cyg entre septiembre y octubre de 2019 con el telescopio de 1.88 m Kottamia, en Egipto. Mediante 340 observaciones con CCD en los filtros BVR derivamos curvas de luz. También obtuvimos 9540 magnitudes visuales para XX Cyg de la literatura, para preparar un diagrama O-C. Presentamos 85 nuevos tiempos del máximo para XX Cyg. No detectamos una protuberancia en la parte descendiente del máximo de la curva de luz de XX Cyg. Sin embargo, encontramos una protuberancia secular en las curvas de luz en fase, la cual cambia con la fase en algunas observaciones del SuperWASP. Encontramos que el cambio del período de XX Cyg es  $dP/dt = 15.5 \times 10^{-5}$  s/yr, y que la amplitud decrece a una tasa de 0.7 mmag/year. Presentamos los parámetros estelares y el estado evolutivo de XX Cyg, que se encuentra en la franja de inestabilidad del diagrama de Hertzsprung Russell.

*Key Words:* stars: evolution — stars: individual: XX Cyg — stars: variables: general

### 1. INTRODUCTION

The evolution of stars with 0.9 to  $120 M_{\odot}$  is well described theoretically by Schaller et al. (1992). After leaving the main sequence, they evolve to the right in the Hertzsprung-Russell (H-R) diagram. Then, they pass through the instability strip and evolve toward cooler temperatures. The rate of period change for pulsating variable stars is of great value for establish-

ing both their evolutionary status and their position in the instability strip, as well as for testing stellar evolutionary models (Turner et al. 1998).

SX Phoenicis variables are analogues of Delta Scuti stars and are located below the classical Cepheid variable stars in the instability strip, closer to the main sequence. In general, SX Phoenicis variables have periods ranging between 30 minutes and six hours. SX Phe stars are interesting because they often pulsate in so-called non-radial modes, they have a lower luminosity and are more metal poor than Delta Scuti stars (Frolov, 1974).

<sup>1</sup>National Research Institute of Astronomy and Geophysics (NRIAG), Cairo, Egypt.

<sup>2</sup>Dept. of Astronomy and Meteorology, Faculty of Science, Al-Azhar University, Nasr City, Cairo, Egypt.

<sup>3</sup>King Saud Univ, Dept. Phys & Astron, Coll. Sci, Saudi Arabia.

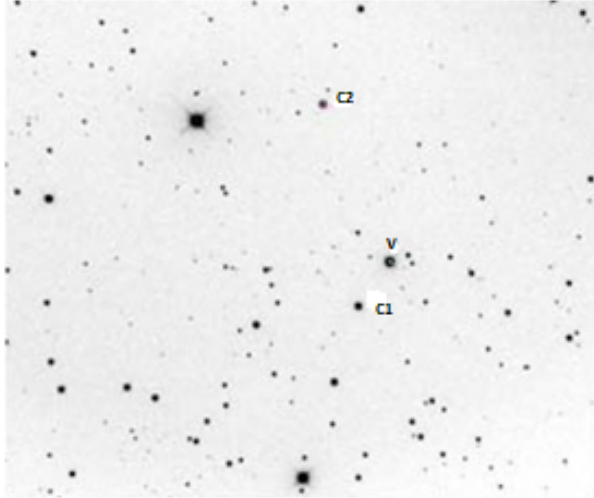


Fig. 1. XX Cyg variable star ( $V$ ) with comparison star ( $C1$ ) and check star ( $C2$ ), as seen from the CCD camera at KAO.

XX Cyg is a Population-II variable star, which has a fundamental radial mode, excited with a high velocity ( $V = -108$  km/s; Joneer 1982); see Figure 1. It has a visual magnitude of  $V = 11.7$  mag with an amplitude in this band of  $\Delta V = 0.80$  mag (Kiss and Derakas 2000) and a radial-velocity amplitude of 37 km/s (Joneer 1982). Its classification changed from a dwarf Cepheid (Joneer 1982, McNamara and Feltz 1980) to the more modern classification as a Population-II SX Phoenicis-type variable star. Our study examines the amplitude stability of XX Cyg and investigates the dependence of the pulsation amplitude on its location within the instability strip.

## 2. OBSERVATIONS AND DATA REDUCTION

### 2.1. Observations

To investigate the variability of our target star (XX Cyg), photometric observations from the archives of the All-Sky Automated Survey for Supernovae (ASAS-SN), Wide Angle Search for Planets (SuperWASP), and American Association of Variable Star Observers (AAVSO) provided new maximum-light times for our target. The data, span a time interval of over 110 years, from the early twentieth century to the present, as shown in the references. We acquired four nights' observations on September 24/25 and October 8/9, 9/10, and 20/21, 2019, as displayed in Figure 2. The observations were obtained through standard Johnson blue-visible-red ( $BVR$ ) filters; and the exposure times ranged from 20 to 60 seconds, depending on the atmospheric conditions and background

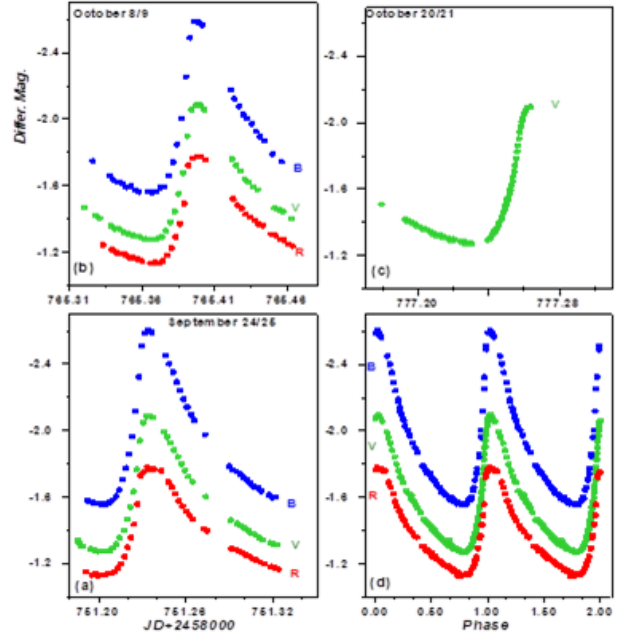


Fig. 2. Differential instrumental magnitude in  $BVR$  colors ( $\Delta B$ ,  $\Delta V$ , and  $\Delta R$ ) (a,b,c) and the phases in three colors (d) of XX Cyg. The color figure can be viewed online.

contribution. All observations from the Kottamia Observatory (KAO) were made using a 2048x2048-pixel EEV CCD 42-40 camera, cooled by liquid nitrogen and attached to the Newtonian focus of the 1.88-m Kottamia reflector telescope in Egypt. The Kottamia Observatory is located at a latitude of  $29^{\circ}56'02.43''$  N, a longitude of  $31^{\circ}49'40.1''$  E, and a height of 467 m. Figure 1 shows one of the  $V$ -band images of the variable XX Cyg, along with comparison and check stars. The comparison star has coordinates  $\alpha_{2000} = 20^{\text{h}}03^{\text{m}}18^{\text{s}}$  and  $\delta_{2000} = +58^{\circ}55.6'6.9''$ . All times were corrected to Heliocentric Julian Date (HJD). Standard data reduction processes (i.e., dark and bias removal, flat-field correction) and aperture photometry have been applied to the present observations, using the free data reduction software (MuniWin) from the website (<http://c-munipack.sourceforge.net/>). We obtained differential instrumental magnitudes for each filter and constructed the present light curves of the system XX Cyg.

### 2.2. Methods of Reduction

We used two methods to determine the period and amplitude variations. The first one originated with Hertzsprung (Hertzsprung, 1928) and the second one is the Fourier decomposition method. Modern usage

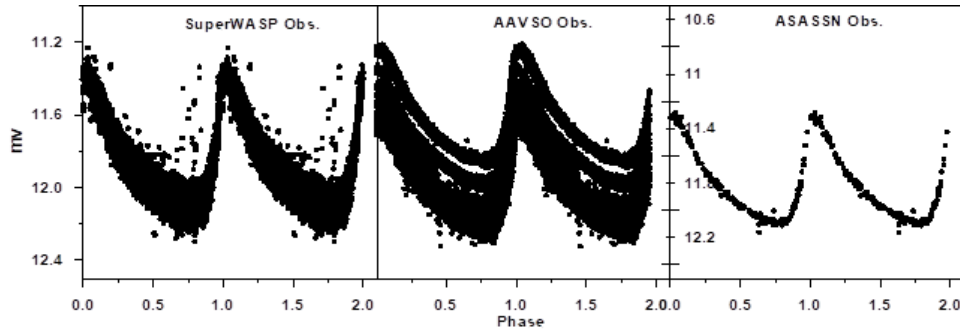


Fig. 3. Phase observations from the ASAS, AAVSO, and SuperWASP archives.

of the first method has been described by Berdnikov (1992), Turner and Berdnikov (2001), and Turner (2003). The observed-minus-calculated (O-C) technique is used to study changes in the periods of Cepheids with high accuracy. The phased data were used to construct seasonal light curves, which were matched to a standard light curve to detect phase shifts, indicating a period change. An alternative procedure used by Abdel-Sabour et al. (2015) relies on a set of high-quality light curves as a standard, to which independent data sets are matched in magnitude and phase space using least-squares techniques. In the second method, we use Fourier decomposition (FD) as a tool for variable-star diagnostics. As the light curves of pulsating variable stars are periodic, they can be written as shown in the following equations;

$$f(x) = A_0 + \sum_{n=1}^N A_n \cos(i\omega(t_0 - t_i) + \varphi_i). \quad (1)$$

Or

$$f(x) = A_0 + \sum_{n=1}^N A_n \cos(i\omega(t_0 - t_i)) + \sum_{n=1}^N B_n \sin(i\omega(t_0 - t_i)), \quad (2)$$

where  $A_i = \sqrt{a^2 + b^2}$ ,  $\tan \Phi_i = -b_i/a_i$ . Because the period is known from the respective databases, the observation time can be folded into the phase ( $\varphi_i$ ) (Ngeow et al. 2003).

The relative Fourier parameters are  $\varphi_{i1} = \varphi_i - i\varphi_1$  and  $R_{i1} = A_i/A_1$ , where  $i > 0$ . We used the above equations to calculate the Fourier parameters from 85 light curves of XX Cyg. The combination of coefficients,  $R_{i1}$  and  $\varphi_{i1}$ , where  $i = 2, 3, 4, \dots$ , can be used to describe the progression of the light-curve shape, as seen in Figure 5 for the visual amplitude  $A_v$ . We can also use these coefficients for variable-star classification (Deb and Singh 2009).

### 3. RESULTS AND DISCUSSION

#### 3.1. O-C Light Curve and Period Change of XX Cyg

Comparing the observed time with the calculated time of maximum brightness (O-C method) is the classical method for studying period changes in variable stars, because it is sensitive to the accumulated effects of the period changes. We used all of the data published in the literature to fill the gaps in the O-C diagram. Light curves with a large scatter in the observations were removed from our analysis. i.e. If the scatter in the phased light curve was about the same as the scatter in the raw data (usually about 0.2 mag. or less) we used it in the O-C diagram. All of the maximum-light times used to study the period change of XX Cyg are presented in Figure 4. The computed time of maximum was measured using the linear ephemeris of Szeidl and Mahdy (1981). The time of maximum brightness ( $HJD_{Max}$ ) can be modeled as a function of epoch ( $E$ ) using the following quadratic equation:

$$HJD_{max} = M_0 + PE + QE^2. \quad (3)$$

Here,  $M_0$  is a new epoch,  $P$  is the new period, and  $Q$  is used to measure the period change ( $dP/dt$ ) in seconds per year given by;  $dP/dt = (2Q/P)(32,557,600)$  s/yr. The evolution of the period over time was investigated by means of the classic O-C method and Fourier transforms, as mentioned in the last section. The O-C behavior of XX Cyg was observed from November 1905 to October 2019. A fit to the O-C diagram was made using a quadratic polynomial, which corresponds to a constantly changing period. After analysis, we found the following ephemeris:

$$HJD_{max} = 2430671.103 - 0.1349E - 2.82 \times 10^{-13} E^2. \quad (4)$$

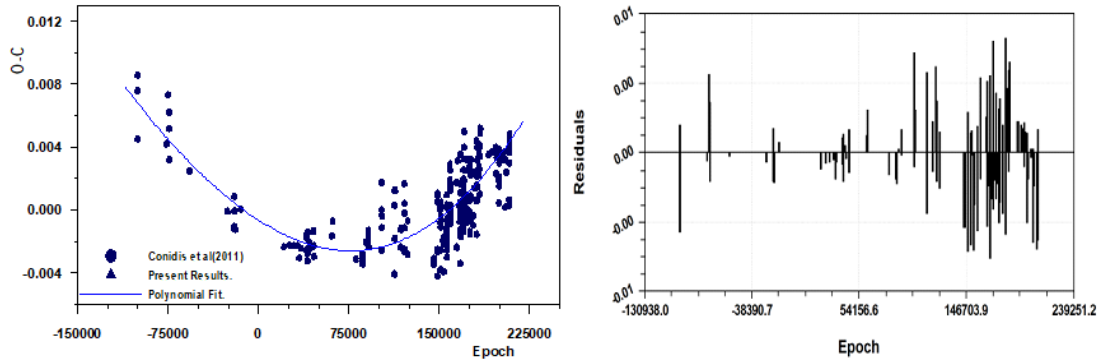


Fig. 4. O-C diagram for XX Cyg and the best fitted parabola, plotted as a function of the observed maximum-light epoch (left panel) and the O-C residuals (right). The color figure can be viewed online.

The parabolic trend in the O-C data reflects a regular period decrease or increase. From this analysis we find that the period is increasing at a rate of  $dP/dt = (15.50 \pm 1.10) \times 10^{-5}$  s/yr or  $([1/P]dP/dt = 1.33 \times 10^{-8} \text{yr}^{-1})$ . Our rate of period change agrees with an earlier estimate by Conidis et al. (2011) ( $1.337 \times 10^{-8} \text{yr}^{-1}$ ) but differs slightly from Blake, et al. (2003) ( $1.13 \times 10^{-8} \text{yr}^{-1}$ ) because we used extra data at recent epochs, including our KAO observations.

### 3.2. Amplitude Variation in XX Cyg

Variations in the amplitude, period, and shape of the light curves are known as the Blazhko Effect. This phenomenon can be seen easily in RR Lyrae variables. A frequency analysis of XX Cyg was performed with a package of computer programs, employing single-frequency (Fourier) and multiple-frequency least-squares techniques (PERIOD04, Breger 1990). The technique fits a number of simultaneous sinusoidal variations in the magnitude domain and does not rely on prewhitening. We analyzed the stellar light curves using the PERIOD04 program and FORTRAN programs to evaluate the Fourier parameters for all available observations. The amplitude behavior in the visible band is presented in Figure 5. Linearly fitting the variations resulted in the following equation:  $A_V = 0.1165^m - (7.544^m \times 10^{-7})\text{Epoch}$ , which indicated a decreasing rate of 0.7 mmag/yr. If we use only our recent observations ( $E > 50000$ ) we find approximately the same results, 0.56 mmag/yr, as presented in Figure 5. The results for the Fourier amplitudes agree with those derived using wavelet analysis by Zhou et al. (2002). These results indicate that there is a relation between pulsation amplitude and rate of period change.

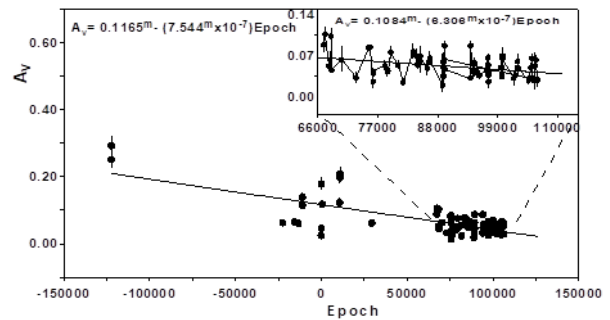


Fig. 5. Time evolution for the AV amplitude of the fundamental frequency of XX Cyg, determined by Fourier analysis. The trend of the variations is shown by a linear-fitted line. The inset shows a fit to only epochs  $E > 50,000$  and shows approximately a similar decreasing trend.

### 3.3. Ambiguity in the Light Curves

When we tried to test the amplitude stability of our system we noticed a damping in the light curves in some observations, as presented partially in Figure 6, from phase 0.1 to 0.8. These observations are from the SuperWASP Camera#145 on nights 2454613.59, 2454629.565, 2454631.54, 2454632.54, 2454659.46, and 2454660.46. These may be the same light curve bumps described by Blake et al. (2003) and Sadun and Ressler (1986). However, we did not detect the bump in our BVR observations. Also, we failed to observe similar bumps in the other automated surveys (Northern Sky Variability Survey (NSVS), Hipparcos Catalogue (HIP), Kamogata/Kiso/Kyoto Wide-field Survey (KWS), and ASAS SN). The SuperWASP bump detections are significant because the bump amplitudes are more than three times larger than the photometric errors of the dataset. Also, we noticed the positions and effects of the bumps changes with phases. i.e. a smaller bump

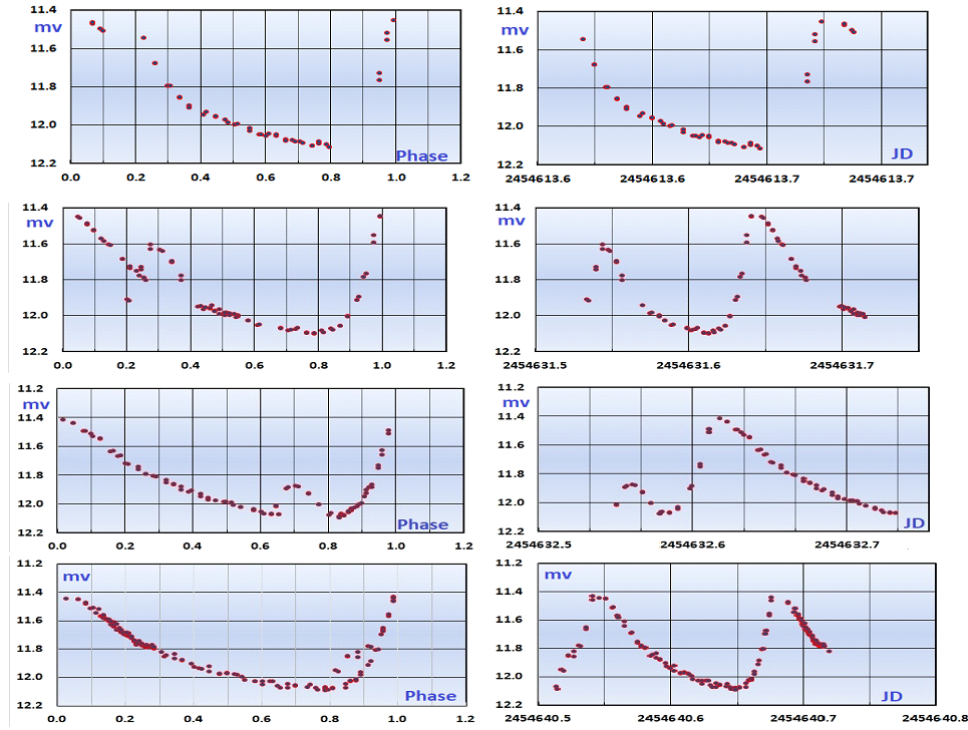


Fig. 6. Six nights: 2454613.59, 2454631.54, 2454632.54, and 2454640.46 Light curves and phases from SuperWASP observations with Camera#145. The color figure can be viewed online.

with a dip of amplitude approximately 0.1 magnitude, which peaks at a phase of 0.15 and a larger bump occurring with ascending phases towards the brightness minimum (as seen at one phase in Figure 6). This damping in the light curve or bump in phase may be a result of magnetic activity or shock waves (Gillet, D. 1988, Balona et al. 2015).

#### 4. ABSOLUTE PARAMETERS OF SYSTEM XX CYG

Spectroscopic observations are an important source for estimating physical parameters. At present, no spectroscopic observations are available for XX Cyg except for the radial velocities reported by Jøner (1982), which yield a mean  $RV$  of  $-108$  km/s. So, the absolute parameters cannot be determined directly. Therefore, we used simple approximation formulae (Harmanec, 1988), which relate the effective temperature to other basic physical parameters (mass, radius, luminosity, and bolometric magnitude).

##### 4.1. Physical Parameters and Evolutionary State of XX Cyg

If the effective temperature ( $T_{eff}$ ) and bolometric magnitude ( $M_{bol}$ ) are known, as well as the period and pulsation mode, the pulsation mass ( $M_{puls}$ ) follows directly from the fundamental equation of stellar pulsation,  $Q = \sqrt{(M/R^2)}$ , where  $P$  is the period in days,  $M$  and  $R$  are the mass and radius in solar units, respectively, and  $Q$  is the pulsation constant. The physical parameters, absolute magnitude ( $M_V$ ), relative radius ( $R/R_\odot$ ), relative luminosity ( $L/L_\odot$ ), surface gravity ( $g$ ), and pulsation constant ( $Q$ ), were calculated using standard stellar-structure equations (Gray 2005 equation 3, Reed Cameron 1998, Collier Cameron et al. 2011, and Breger 1990) assuming the effective temperature of XX Cyg ( $T_{eff} = 7530$  K) from Zhou et al. (2002),  $\log g_\odot = 4.44$ , and  $M_{bol_\odot} = 4.74$ . To see the location of XX Cyg in the Hertzsprung-Russell diagram, we calculated the parameters using the equations of Reed (1998), Torres (2010), and Flower (1996). The results are presented in Table 1.

These results are in good agreement with a thesis by Bowman (2016) (see his Figure 4.12 for low-frequency pulsations,  $\nu \leq 25d^{-1}$ ). The evolu-

TABLE 1

PHYSICAL PARAMETERS: MASS, LUMINOSITY, RADIUS, BOLOMETRIC MAGNITUDE, STELLAR GRAVITY, AND AGE OF XX CYG

Ref.	$M/M_{\odot}$	$L/L_{\odot}$	$R/R_{\odot}$	$M_{bol}$	$\log g$	Age(yr) $\times 10^9$
Our results	1.955 (0.164)	1.038 (0.026)	1.944 (0.343)	1.688 (0.164)	4.086 (0.079)	0.949 (0.064)
Zhou (2002)	1.0 (0.5)		2.400	1.700	3.660	1.00
Yang et al. (2012)	1.7(0.1)			1.700		0.90(0.30)

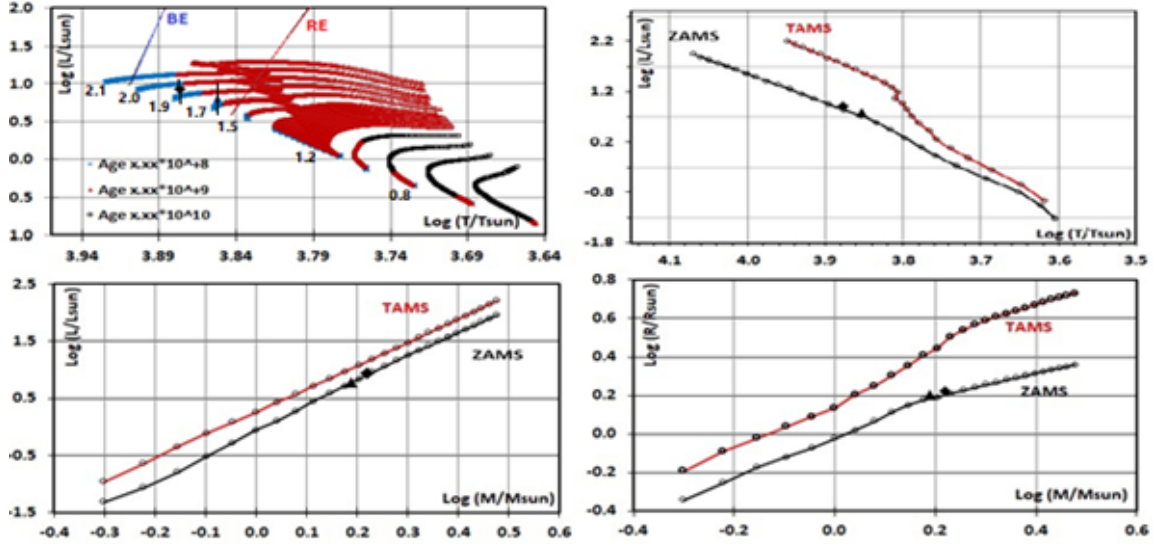


Fig. 7. Position of XX Cyg (square) and the Cepheid variable GSC 02444-00241 (triangle) in temperature-luminosity (HR diagram), mass-luminosity and mass-radius diagrams. The top left plot shows theoretical mass tracks from Mowlavi et al. (2012) for  $Z=0.014$  over a range of ages (in Gyr). The blue (BE) and red (RE) edges of the instability strip are marked. The color figure can be viewed online.

tionary tracks for the non-rotating model, as computed by Mowlavi et al. (2012), for both zero-age main-sequence stars (ZAMS) and terminal-age main-sequence stars (TAMS) with a metallicity of  $Z = 0.014$  (solar metallicity), are presented in Figure 7. The absolute physical parameters of XX Cyg, are plotted as mass-luminosity ( $M-L$ ), mass-radius ( $M-R$ ), and H-R diagrams at Figure 7. The parameters are in good agreement with those expected for SX Phe variables in the  $\log M - \log L$  plane. XX Cyg is close to, or on, the ZAMS in all the diagrams of Figure 7 and lies halfway between the blue edge (BE) and red edge (RE) of the instability strip, as shown in the  $L-T$  relation (H-R diagram). To estimate the age of the system, we plotted theoretically calculated models (Mowlavi et al. 2012) for temperature versus luminosity ( $T-L$ ) (Figure 7). From this diagram, and from McNamara and Feltz (1980), the age of XX

Cyg should be approximately  $(0.949 \pm 0.064) \times 10^9$  years, It is close to the age predicted by Zhou (2002) and Yang et al. (2012), which is  $(0.9 \pm 0.3) \times 10^9$  years as shown in Table 1. The location of XX Cyg in the H-R diagram is shown in Figure 7. These parameters would explain the position of the star at or near the main sequence (Rodríguez and Breger 2001).

## 5. CONCLUSION

The following conclusions were drawn:

1. Photometric observations from the archives of the ASAS-SN, SuperWASP and AAVSO provided 85 new times of maximum-light for XX Cyg.

2. From the O-C result (Figure 4), we estimated the period change rate for XX Cyg; the result was  $(dP/dt) = (15.248 \pm 1.092) \times 10^{-5}$  s/yr and/or  $(1/P)dP/dt = 1.33 \times 10^{-8}$  yr $^{-1}$ .
3. We also found that the amplitude was decreasing over time.
4. The amplitude behavior in the visible band is decreasing at a rate of 0.7 mmag per year. This variation of amplitude is not at all understood and is one of the open questions about SX Phe stars.
5. As noticed from the period change and amplitude variations, there seems to be a correlation between the two quantities: the amplitude decreases with increasing period.
6. The existence of a bump in the light curve is still uncertain. However, a bump in the amplitude was observed in an automated SuperWASP survey, as noted in the text. Maybe there are large magnetically active regions on the surface, or shock waves from the stellar interior, which are responsible for the bump.
7. Multi-wavelength and radial-velocity observations of XX Cyg are required to determine the reason for this bump.
8. We calculated the physical parameters for XX Cyg, and the results were found as  $L/L_{\odot} = 1.038(0.026)$ ,  $M/M_{\odot} = 1.955(0.164)$ ,  $R/R_{\odot} = 1.944(0.343)$ ,  $\log g = 4.086$ ; in addition to an age ( $\tau$ ) equal to  $0.949(0.064) \times 10^9$  year.

The authors would like to extend their sincere appreciation to the Deanship of Scientific Research (DSR) and College of Science Research Center at King Saud University, Saudi Arabia for their financial support. Also, the authors are thankful to the Egyptian Science and Technology Development Fund (STDF) for funding the Kottamia Faint Imaging Spectro-Polarimeter (KFISP), STDF 2531 and the Kottamia Center of Scientific Excellence for Astronomy and Space Science (KCSce), STDF 5217, as well as the support of the KAO team and the funding from NRIAG, Egypt. Also, we would like to

thank Dr. A. Essam and Dr. M. Nouh for enlightening discussions.

## REFERENCES

- Abdel-Sabour, M., Ibrahim, A., Essam, A., & Elkhateeb, M. M. 2015, *RoAj*, 25, 157
- Balona, L. A., Broomhall, A.-M., & Kosovichev, A., et al. 2015, *MNRAS*, 450, 956
- Berdnikov, L. N. 1992, *A&AT*, 2, 43
- Blake, R. M., Delaney, P., Khosravani, H., Tome, J., & Lightman, M. 2003, *PASP*, 115, 212
- Bowman, D. M. 2016, *Amplitude Modulation and Energy Conservation of Pulsation Nodes in Delta Scuti Stars*, PhD, Thesis, University of Central Lancashire, UK, 267B
- Breger, M. 1990, *ASPC*, 11, 263
- Collier, C. A., Wilson, D. M., West, R. G., Hebb, L. et al. 2007, *MNRAS*, 380, 1230
- Deb, S. & Singh, H. P. 2009, *A&A*, 507, 1729
- Eddington, A. S. and Plakidis, S. 1929, *MNRAS*, 90, 65
- Flower, P. J. 1996, *ApJ*, 469, 355
- Frolo, M. S. 1974, *Sci. Inform. Astron. Council USSR Acad. Sci.*, 33, 29
- García, J. 2012, *JAAVSO*, 40, 272
- Gillet, D. & Crowe, R. A. 1988, *A&A*, 199, 242
- Gray, D. F. 2005, *The Observation and Analysis of Stellar Photospheres*, (Cambridge, UK: CUP)
- Harmanec, P. 1988, *AICz*, 39, 329
- Hertzsprung, E. 1928, *BAN*, 4, 178
- Joner, M. D. 1982, *PASP*, 94, 289
- Kiss, L. L. & Derekas, A. 2000, *IBVS*, 4950, 1
- McNamara, D. H. & Feltz, K. A. Jr. 1980, *PASP*, 92, 195
- Mowlavi, N., Eggenberger, P., Meynet, G., et al. 2012, *A&A*, 541, 41
- Ngeow, C. C., Kanbur, S. M., Nikolaev, S., Tanvir, N. R., & Hendry, M. A. 2003, *ApJ*, 586, 959
- Reed, B. C. 1998, *JRASC*, 92, 36
- Rodríguez, E. & Breger, M. 2001, *A&A*, 366, 178
- Sadun, A. C. & Ressler, M. 1986, *PASP*, 98, 504
- Schaller, G., Schaerer, D., Meynet, G., & Maeder, A. 1992, *A&AS*, 96, 269
- Szeidl, B. & Mahdy, H. A. 1981, *MiUng*, 75, 1
- Torres, G. 2010, *AJ*, 140, 1158
- Turner, D. G. & Berdnikov, L. N. 2001, *OAP*, 14, 170
- \_\_\_\_\_. 2004, *A&A*, 423, 335
- Turner, D. G. 2003, *JAVSO*, 31, 160
- Turner, D. G., Horsford, A. J., & MacMillan, J. D. 1998, *JRASC*, 92, 320
- Yang, X. H., Fu, J. N., & Zha, Q. 2012, *AJ*, 144, 92
- Zhou, A.-Y. 2002, *ASPC*, 259, 332

Mohamed Abdel-Sabour and Ahmed Shokry: National Research Institute of Astronomy and Geophysics (NRIAG), 11421 Helwan, Cairo, Egypt (sabour2000@hotmail.com).

Ahmed Ibrahim: Dept. of Astronomy and Meteorology, Faculty of Science, Al-Azhar University, Nasr City, Cairo, Egypt.

Ahmed Ibrahim: King Saud Univ, Department of Physics & Astronomy, Coll. Sci, Riyadh 11451, Saudi Arabia (ahabdalla@ksu.edu.sa).

## THIRTEEN YEARS OF WEATHER STATISTICS AT SAN PEDRO MARTIR OBSERVATORY

I. Plauchu-Frayn<sup>1</sup>, E. Colorado<sup>1</sup>, M. G. Richer<sup>1</sup>, and C. Herrera-Vázquez<sup>2</sup>

*Received June 10 2020; accepted August 10 2020*

### ABSTRACT

We present weather statistics for thirteen years of data gathered with the meteorological stations at Observatorio Astronómico Nacional in the Sierra San Pedro Mártir (OAN-SPM) over the period 2007–2019. These weather stations include sensors that measure various climatological variables. The median values of the air temperature are 10.3° C and 7.0° C for daytime and nighttime, respectively. The relative humidity follows a seasonal variation with April–June being the driest months. The median values for the sustained wind speed are 11 and 14 km hr<sup>-1</sup> for daytime and nighttime data, respectively. Preferred wind directions are SSW and North. Sustained winds are stronger at night and during December, January and February. The annual mean rain precipitation is 313 mm, most of which occurs during the summer season as afternoon thunderstorms.

### RESUMEN

Presentamos la estadística del clima para trece años de datos obtenidos con las estaciones meteorológicas en el Observatorio Astronómico Nacional en la Sierra San Pedro Mártir (OAN-SPM) durante el período 2007–2019. Estas estaciones meteorológicas incluyen sensores que miden diferentes variables climatológicas. Los valores medianos de la temperatura del aire son 10.3° C y 7.0° C, para el día y la noche, respectivamente. La humedad relativa sigue una variación estacional, siendo los meses de abril a junio los más secos. Los valores medianos de la velocidad del viento son 11 y 14 km hr<sup>-1</sup>, para el día y la noche, respectivamente. Las direcciones del viento dominantes son el SSW y el Norte. Los vientos sostenidos son más fuertes por la noche y durante los meses de diciembre, enero y febrero. El promedio anual de precipitación de lluvia es 313 mm, gran parte de la cual ocurre durante las tardes del verano en forma de tormentas eléctricas.

*Key Words:* methods: data analysis — site testing

### 1. INTRODUCTION

The Observatorio Astronómico Nacional in the Sierra San Pedro Mártir (hereinafter OAN-SPM) is located on the top of Sierra San Pedro Mártir in Baja California, México (2800 m, +31° 02' 40" N, 115° 28' 00" W). The site excels in sky darkness (Tovmassian et al. 2016; Plauchu-Frayn et al. 2017) and an absence of cloud cover, with approximately 70% and 80% photometric and spectroscopic time, respectively (Tapia et al. 2007). The median seeing measured at zenith at 5000Å varies from 0.55" to 0.79", depending upon the study (Echevarría et al.

1998; Echevarría 2003; Bohigas et al. 2008; Skidmore et al. 2009; Sánchez et al. 2012; Ávila et al. 2019) with the most recent measurements favoring a median value near 0.79". Similar seeing seems to be the rule at nearby sites (Bohigas et al. 2008). Atmospheric extinction is typically 0.13 mag airmass<sup>-1</sup> in the V band (Schuster & Parrao 2001). Due to these excellent atmospheric conditions and favorable location away from large urban areas, the OAN-SPM is an excellent site for optical and infrared facilities.

In the early 1960's, a search was begun to find the best site for optical astronomical observations in Mexico (Mendoza 1973). The site was chosen, using, among other information, satellite photographs and on-site testing, as recounted by Mendoza et al.

<sup>1</sup>Instituto de Astronomía, Universidad Nacional Autónoma de México (IA-UNAM), México.

<sup>2</sup>Centro de Investigación Científica y Educación Superior de Ensenada (CICESE), México.

(1972). Subsequent studies during the first years of the observatory's operation validated the choice of the site (e.g., Walker 1971; Mendoza et al. 1972; Álvarez & Maisterrena 1977). The OAN-SPM was formally inaugurated in 1979.

Tapia (1992) presented a study of ten years (1982–1992) of weather and observing statistics at OAN-SPM site, based upon data reported by the telescope operators. He found that the mean relative humidity was 54% and that the best seasons in terms of cloudlessness and low humidity were spring and autumn. Tapia (2003) and Tapia et al. (2007) updated these results, based upon data spanning 22 years (1982–2002), finding that the fraction of photometric nights was close to 70% for the most recent data and the fraction of spectroscopic nights was approximately 80%.

Michel et al. (2003) presented a four year study with a weather station installed at the 1.5 m telescope. They estimated that air temperatures were in the range of  $-15$  to  $20^\circ\text{C}$ , the relative humidity showed a seasonal dependence with short variations on short time scales, especially during summer nights. Also, this study reported a range of 733 to 753 mb for the atmospheric pressure. Daytime and nighttime wind speeds had median values of 14 and  $19\text{ km hr}^{-1}$  with strong winds coming from the SSW direction.

Hiriart (2003) studied the precipitable water vapor above the site over an eight year period (1995–2002) by measuring the optical depth of the atmosphere at 210 GHz, finding a clear peak corresponding to the summer “monsoon” as well as year-to-year variations, e.g., “El Niño” events and the like. Subsequent analysis (Otárola et al. 2009; Otárola et al. 2010) indicated a median precipitable water vapor below 4 mm, except in summer.

Here, we continue the tradition of characterizing the site of the OAN-SPM by presenting an analysis of weather variables acquired with the observatory's weather stations. Since 2006, the OAN-SPM installed weather stations and has operated them continuously as facility instruments. This study describes the data gathered in a consistent and continuous manner by the weather stations during the last thirteen years of operation of the observatory (2007–2019). These stations include sensors for measuring air temperature, atmospheric pressure, relative humidity, wind conditions, water precipitation, solar radiation, evapotranspiration, and the UV index. The equipment used to measure weather conditions is described in § 2, we present our results in § 3 and finally, our conclusions are given in § 4.

## 2. WEATHER DATA ARCHIVE AND ANALYSIS

The data were acquired with two sets of instrumentation. From mid-2006 to mid-2013, a Davis Instruments weather station (hereinafter DI; Colorado & Hiriart 2007) model Vantage Pro2 Plus was used. From mid-2013, a Vaisala Weather Transmitter (hereinafter VWT) model WXT520 with a Vaisala WINDCAP sensor was installed at OAN-SPM. The DI weather station has a mechanical cup anemometer (instant readings: 2.5–3 secs.), while the Vaisala WINDCAP sensor of the VWT weather station is ultrasonic (instant readings: 0.25 secs.). The weather data recorded by these stations is currently available from the OAN-SPM homepage<sup>3</sup>. The basic data that we consider in this paper are air temperature, relative humidity, precipitation, atmospheric pressure, and wind speed and direction. All meteorological variables are monitored continuously. Every five minutes the mean value of the air temperature, relative humidity and atmospheric pressure and the total accumulated precipitation are recorded on the hard disk of the control computer. For the sustained wind speed, the mean value of all instant readings within a five minute interval is determined, while for the gust wind speed, the maximum value in this interval is determined. A systematic error of  $\pm 5^\circ$  degrees is estimated in the alignment process of the station with respect to the true North pole. In Table 1 we present the parameter accuracies for each station as indicated by the manufacturer.

The two weather stations are quite similar, with the main difference being a better precision in the wind speed and direction for the VWT station. These two stations have been located at three different sites within the OAN-SPM. The DI station was located on a 6 m mast erected upon a rock outcrop about 3 m high between the 1.5 m and 0.84 m telescopes (site 1). The VWT station was first installed on a 6 m mast near the Cabaña Azul from August 2013 to November 2015 (site 2), and subsequently on a 6 m mast to the west of the 1.5 m telescope (site 3). These three different locations are shown in Figure 1.

For this study, we retain thirteen whole years of data (2007–2019), representing  $\approx 97\%$  of the time span available ( $\approx 1.3$  million 5-minute data points). Table 2 presents a summary of the data. The principal gaps in the data are as follows. There are gaps of approximately two weeks in December 2007 and December 2008, corresponding to the staff holiday period, and there is a gap of several weeks in January 2010, when the observatory was evacuated due to a severe snow storm. During these periods, the

<sup>3</sup><http://www.astrossp.unam.mx>.

TABLE 1  
WEATHER STATION PARAMETER ACCURACY

Parameter	DI	VWT
Wind speed	$\pm 5\%$ ( $< 241 \text{ km hr}^{-1}$ )	$\pm 3\%$ ( $< 136 \text{ km hr}^{-1}$ )
Wind direction	$\pm 7^\circ$	$\pm 3^\circ$
Temperature	$\pm 0.5^\circ \text{ C}$ ( $< 43^\circ \text{ C}$ )	$\pm 0.2 - 0.3^\circ \text{ C}$ ( $-20$ to $20^\circ \text{ C}$ )
Humidity	$\pm 3\%$ (0 to 90%)	$\pm 3\%$ (0 to 90%)
	$\pm 4\%$ ( $> 90\%$ )	$\pm 5\%$ ( $> 90\%$ )
Pressure	$\pm 0.3 \text{ mb}$	$\pm 0.5 \text{ mb}$ (0 to $30^\circ \text{ C}$ )
Precipitation	$\pm 4\%$	$\pm 5\%$

TABLE 2  
WEATHER DATA ARCHIVE

Year	N of days	% of the year	Location	Comments
2007	319	87.4%	site 1	The barometer calibration was incorrect.
2008	344	94.0%	site 1	–
2009	365	100%	site 1	–
2010	351	96.2%	site 1	–
2011	365	100%	site 1	The pluviometer was not working.
2012	366	100%	site 1	Only 67% of wind data. The anemometer was broken.
2013	350	95.9%	site 1 & 2	The wind direction is not reliable for site 2.
2014	364	99.7%	site 2	The wind direction is not reliable for site 2.
2015	352	96.4%	site 2 & 3	The wind direction is not reliable for site 2.
2016	363	99.2%	site 3	–
2017	351	96.2%	site 3	–
2018	363	99.4%	site 3	–
2019	361	98.9%	site 3	–

weather station was switched off. In addition, there were periods when some of the individual sensors were not functioning, as noted in Table 2.

Also, the data available concerning the precipitation during winter should be considered a lower limit. The pluviometers for both weather stations are unreliable at sub-zero temperatures (they freeze) and under-record the precipitation that falls as snow. We shall address this limitation in § 3.4.

As a first step in our study, we compare each of the weather parameters collected by the weather stations at the three sites. The distributions of air temperature and relative humidity for both weather stations are similar with no shift between them. On the other hand, for the distribution of the atmospheric pressure, we find a shift of  $\approx 1 \text{ mb}$  in the distribution of the VWT station compared to the DI station. In addition, when we compare the distributions of the accumulated precipitation of two stations, we find similar distributions, with the VWT distribu-



Fig. 1. This aerial view of the OAN-SPM indicates the locations of the DI (site 1) and VWT (site 2 and later site 3) weather stations during period 2006–2019. The photo is courtesy of Eduardo López Ángeles. The color figure can be viewed online.

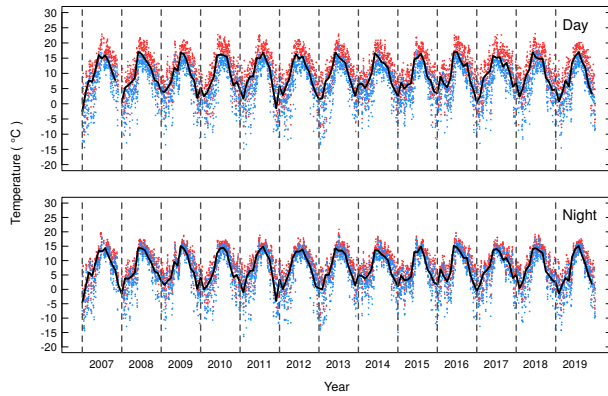


Fig. 2. We present the daily maximum (red) and minimum (blue) air temperature for daytime and nighttime data for the thirteen year time span of our data (2007–2019). In each panel the black line represents the median monthly air temperature, while the vertical dashed lines indicate the first day of each year. The color figure can be viewed online.

tion slightly shifted to larger values compared to the DI distribution. Because these two weather stations never run simultaneously, we cannot rule out that the differences found are due to an increase of these variables over time. When we compare the distributions for the wind conditions, we find that the only difference among sites was for the wind direction, which lead us to not use the wind direction data collected at site 2, a topic we shall address further in § 3.5.

For the analysis of the data and presentation of the results, we have constructed two data sets: one for daytime and one for nighttime. The nighttime data set includes only data collected when the Sun was  $\geq 6^\circ$  below the horizon (i.e., the period between two consecutive civil twilights) while the daytime data set consists of the data collected during the rest of the day. Both data sets, originally gathered in 5 minute intervals, have been reduced to hourly, daily, monthly, seasonal and annual means, medians, modes or sums depending upon the weather parameter or the issue to be studied. Finally, we define the seasons as follows: winter includes January, February, and March; spring, April, May, and June; summer, July, August, and September, and autumn, October, November, and December.

### 3. RESULTS

#### 3.1. Air Temperature

The daily maximum and minimum values of the air temperature from 2007 to 2019 are plotted in Fig-

TABLE 3  
MONTHLY MEAN AIR TEMPERATURE

Month	Day	Night	Day + Night
	(° C)		
January	$2.9 \pm 4.7$	$1.3 \pm 4.4$	$2.1 \pm 4.5$
February	$3.0 \pm 5.0$	$1.1 \pm 4.8$	$2.1 \pm 4.9$
March	$5.1 \pm 4.1$	$3.0 \pm 3.9$	$4.2 \pm 4.0$
April	$6.9 \pm 4.1$	$4.4 \pm 3.8$	$6.0 \pm 3.9$
May	$9.4 \pm 4.2$	$6.8 \pm 4.1$	$8.5 \pm 4.1$
June	$15.4 \pm 2.9$	$12.8 \pm 3.0$	$14.5 \pm 2.9$
July	$15.7 \pm 1.8$	$13.9 \pm 1.7$	$15.1 \pm 1.7$
August	$15.5 \pm 1.8$	$13.8 \pm 1.6$	$14.8 \pm 1.7$
September	$13.3 \pm 2.3$	$11.3 \pm 2.1$	$12.5 \pm 2.2$
October	$10.4 \pm 3.3$	$8.3 \pm 3.2$	$9.4 \pm 3.2$
November	$6.5 \pm 4.2$	$5.0 \pm 3.8$	$5.9 \pm 4.0$
December	$3.3 \pm 5.1$	$1.8 \pm 4.7$	$2.5 \pm 4.9$

ure 2. The air temperature spans the range from  $-17^\circ\text{C}$  to  $23^\circ\text{C}$  over the course of the entire study period. From Figure 2, it can be seen that the daytime temperatures cover a wider range than the temperatures at night. Also, there is a larger dispersion in the temperature during the winter (the valleys in the curves).

The cumulative distribution of daytime and nighttime air temperatures based upon 5 minute averages is shown in Figure 3a. The median daytime and nighttime air temperatures are  $10.3^\circ\text{C}$  and  $7.0^\circ\text{C}$ , respectively. From Figure 3a, it can be seen that 90% of the time the air temperature is below  $17^\circ\text{C}$ , both day and night. The minimum temperature registered is  $-16.7^\circ\text{C}$ , with temperatures below  $0^\circ\text{C}$  and  $-4^\circ\text{C}$  occurring only 11% and 4% of the time, respectively. In Figure 3b, we present the cumulative distribution of air temperatures by season for daytime and nighttime. From Figure 3b, it can be seen that the warmest season is summer with a median value of the air temperature of  $15.1^\circ\text{C}$  and  $13.2^\circ\text{C}$ , for daytime and nighttime, respectively. The coldest season is winter with median values of  $4.7^\circ\text{C}$  and  $2.7^\circ\text{C}$ , for daytime and nighttime, respectively. Spring is the season with the largest difference between daytime and nighttime temperatures, with median values of the air temperature  $11.1^\circ\text{C}$  and  $7.9^\circ\text{C}$ , respectively. In autumn, median values of the air temperature are  $8.0^\circ\text{C}$  for daytime and  $6.0^\circ\text{C}$ , for nighttime.

We present the monthly means of the air temperature for daytime and nighttime in Table 3 and later in Figure 24 and for each year, the monthly medians

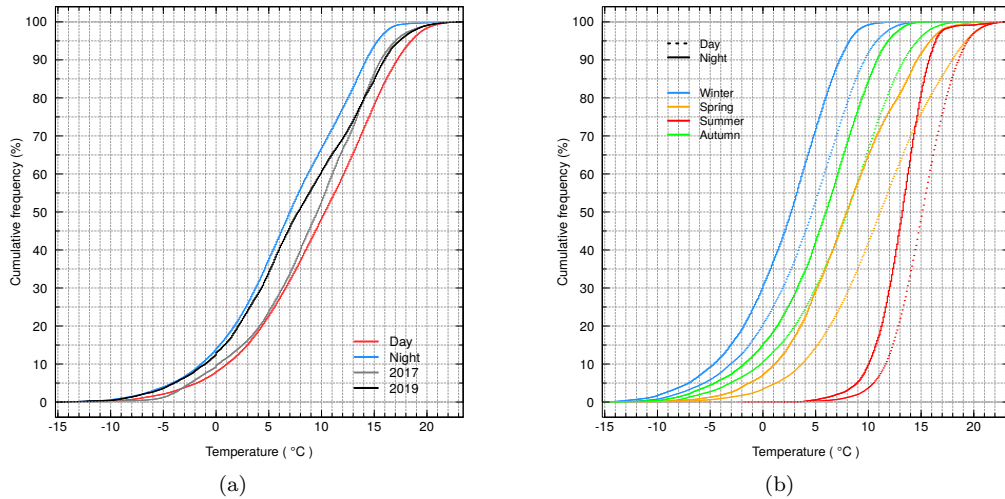


Fig. 3. We present (a) the cumulative distribution of the daytime and nighttime air temperature obtained in the period 2007–2019, based upon the 5 minute averages. The blue line stands for nighttime data, the red line for daytime data, the gray line for 2017 (warmest year, day+night) data, and the black line for 2019 data (coldest, day+night). In (b) we present the cumulative distribution of air temperature by season in the same period for daytime (dotted line) and nighttime (solid line). The blue line stands for winter, the orange line for spring, the red line for summer and the green line for autumn. In both plots, the x-axis does not cover the extremes of total temperature range ( $-17$  to  $23^{\circ}\text{C}$ ). Values below  $-10^{\circ}\text{C}$  and above  $20^{\circ}\text{C}$  represent only 0.4% and 1.0% of the data, respectively. The color figure can be viewed online.

are presented in Table 4. The mean temperature at the OAN-SPM has a very clear seasonal variation as can also be seen in Figure 3b. The warmest months are June, July and August and the coldest are December, January and February. The variation between the warmest and coldest months is  $13^{\circ}\text{C}$  (see Table 3). The dispersion about the mean temperatures in Table 3 confirms the impression from Figure 2 that there is more dispersion in temperature in winter and during the day. In Figure 4, we compare the monthly mean of the air temperatures obtained here with those from Álvarez & Maisterrena (1977), Álvarez et al. (2007), and Bohigas & Núñez (2010). All of the data sets are quite similar, except for one point in the 1969–1974 data set, due to a very cold March in 1973 ( $-3.1^{\circ}\text{C}$ ; see Table 1 from Álvarez et al. 2007).

In the last three rows of Table 4 we report the median annual total (day + night), daytime and nighttime air temperature, which are determined as the median value of the distribution of the daily mean temperatures for each year. By this measure, 2017 was the warmest year in the last thirteen years (see Figure 3a) with daytime and nighttime median air temperatures of  $10.7^{\circ}\text{C}$  and  $8.2^{\circ}\text{C}$ , respectively. The coldest year was 2019 (see Figure 3a) with daytime and nighttime median air temperatures

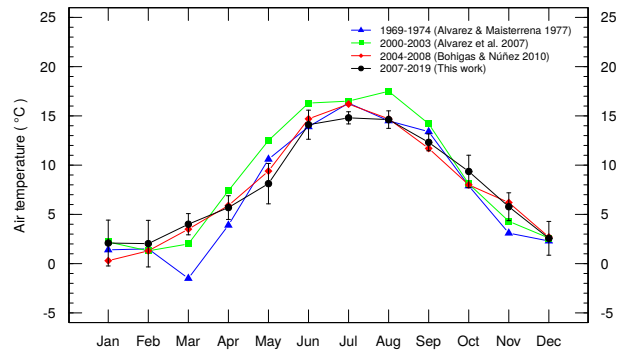


Fig. 4. We compare the monthly mean of the air temperatures from this study with data from Álvarez & Maisterrena (1977), Álvarez et al. (2007) and Bohigas & Núñez (2010) and this work. The agreement is generally very good. The color figure can be viewed online.

of  $8.4^{\circ}\text{C}$  and  $6.0^{\circ}\text{C}$  respectively. Note that 2007 and 2008 have missing data for the coldest months, so their median temperatures are likely biased to slightly warmer temperatures than the true values.

In Figure 5, we show the cumulative distribution of the daily daytime, nighttime, and day-to-night air temperature variations. We define these temperature variations as the difference between the max-

TABLE 4  
MONTHLY MEDIANS OF AIR TEMPERATURE

	2007	2008	2009	2010	2011	2012	2013	2014	2015	2016	2017	2018	2019
Month	(° C)												
Jan	−3.4	−0.9 <sup>b</sup>	3.6	4.2 <sup>d</sup>	3.4	4.2	0.9	5.5	1.4	2.5	0.1	6.1	3.3
Feb	1.9	4.8	2.6	1.1	0.7	1.8	1.0	5.9	6.0	8.1	1.9	1.4	−0.1
Mar	6.7	5.2	4.2	2.7	5.9	4.7	6.2	4.3	4.3	5.6	7.1	3.4	2.6
Apr	6.1	6.0	5.9	5.3	7.8	7.6	6.9	6.3	5.2	4.4	8.7	8.4	6.1
May	10.3	7.5	11.0	7.9	8.3	12.7	11.3	8.9	5.8	7.0	9.9	10.4	4.5
Jun	15.2	16.0	10.0	14.7	14.0	15.3	16.0	15.7	14.0	16.4	15.0	16.0	12.9
Jul	14.3 <sup>a</sup>	15.7	16.0	15.4	14.5	14.2	15.2	14.8	14.5	16.4	14.7	14.8	15.2
Aug	15.4	14.5	15.3	15.3	16.1	14.9	14.3	13.2	16.1 <sup>e</sup>	13.7	14.2	14.4	16.3
Sep	13.0	12.3	12.8	14.4	13.1	11.8	13.0	12.1	12.9	11.4	11.1	14.1	12.9
Oct	10.1	10.7	8.3	9.1	10.9	10.0	8.6	10.8	8.2	12.6	12.2	7.6	10.5
Nov	7.3	7.1	6.9	5.1	4.1	5.9	5.6	6.0	6.2	6.5	9.6	6.0	5.3
Dec	...	6.2 <sup>c</sup>	0.8	6.3	−3.0	2.2	1.8	3.5	2.9	3.1	4.8	3.5	2.4
Total	9.6 <sup>f</sup>	8.7 <sup>f</sup>	8.2	8.2	8.4	9.0	8.4	8.8	7.6	8.4	9.4	8.4	7.5
Day	10.6	9.6	9.3	9.3	9.7	9.9	9.3	9.9	8.5	9.5	10.7	9.3	8.4
Night	8.2	7.5	6.7	7.1	7.1	7.8	7.4	8.0	6.6	7.2	8.2	7.3	6.0

<sup>a</sup>No data for the 3–17th of the month.

<sup>b</sup>No data for 10–15th of the month.

<sup>c</sup>No data for the 14–28th of the month.

<sup>d</sup>No data for the 20–30th of the month.

<sup>e</sup>No data for 26–31th of the month.

<sup>f</sup>< 95% of data (see Table 2).

imum and minimum temperatures during daytime, nighttime and over a 24 hour day. In a single day, the maximum air temperature variation is smaller than 8° C 90% of the time with a daily median air temperature variation of 5.4° C. During daytime this variation is larger than at night, with median values of 4.8° C and 2.4° C for the day and night, respectively.

Figure 6 presents the diurnal variation of the temperature by season. For each season, we determine the mean temperature of the entire day (24 hours) and subtract this temperature from the temperature at a given hour. Values below zero indicate that the temperature is cooler than the daily mean temperature. During daytime (≈06:00 to 12:00 hrs), the air temperature variation is large, typically  $\Delta T \approx 3^\circ \text{C}$ , with the most extreme variation in the spring, ( $\Delta T \approx 5^\circ \text{C}$ ). The air is heated after sunrise with the most rapid phase occurring before 10:00 local time. There is less variation during the middle 4-6 hours of the day. The last four hours before sunset see rapid cooling. From Figure 6, we can see that during the night the air temperature varies little in all seasons.

In order to estimate how little the air temperature varies during the night, we have estimated the rate of change of the air temperature during nighttime. These rates of change are defined as the air temperature at a given hour minus the air temperature an hour before. According to this definition, positive rates indicate heating, while negative rates indicate cooling. In Figure 7a, we present the density functions of the rate of change of the air temperature for 1, 2, 3 hours after the beginning of the night (BoN; Sun is 6° below the horizon, i.e., 24 minutes after sunset) and the period of time between three hours after BoN and three hours before the end of the night (EoN, i.e., 24 minutes before sunrise). We refer to this period simply as “Night” in Figure 7a and 7b. From Figure 7a, it can be seen that after the first hour after the BoN there is a rapid cooling with median value of  $-0.08^\circ \text{C hr}^{-1}$ . Later, the cooling continues in the second and third hour after the BoN ( $\approx -0.015^\circ \text{C hr}^{-1}$ ), although it is not as rapid as in the first hour after de BoN. In the “Night” period, the cooling has a median value of  $-0.06^\circ \text{C hr}^{-1}$ . In addition, in Figure 7b, we present the density functions of the air temperature gradi-

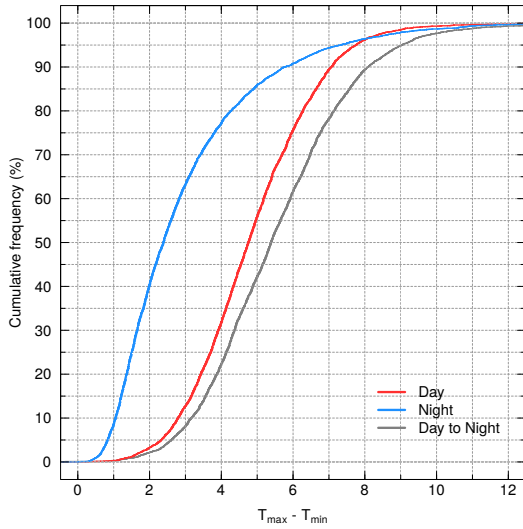


Fig. 5. We present the cumulative distributions of the difference between the maximum and minimum air temperatures during an entire day (gray), during daytime (red), and nighttime (blue). Clearly, the temperature varies substantially less at night than during the day. The color figure can be viewed online.

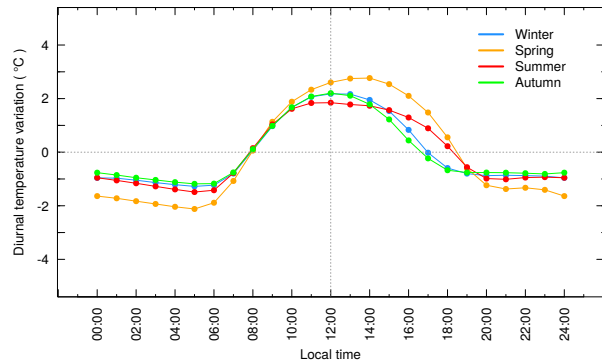


Fig. 6. We present the diurnal air temperature variation by season. To construct these curves, the mean temperature for each entire day (24 hours) is subtracted from the mean temperature for each hour, and the values for the days in a given season are averaged. Again, we see that there is little temperature variation at night. The greatest diurnal temperature variation occurs in spring. The color figure can be viewed online.

ents 1, 2, 3 hours before the end of the night (EoN) and the “Night” period previously defined. From Figure 7b, it can be seen that in three hours before the EoN, the cooling is the most rapid with a median value of  $-0.11\text{ }^{\circ}\text{C hr}^{-1}$ . This cooling continues with a median value of  $-0.09\text{ }^{\circ}\text{C hr}^{-1}$  two hours before the EoN and  $-0.05\text{ }^{\circ}\text{C hr}^{-1}$  one hour

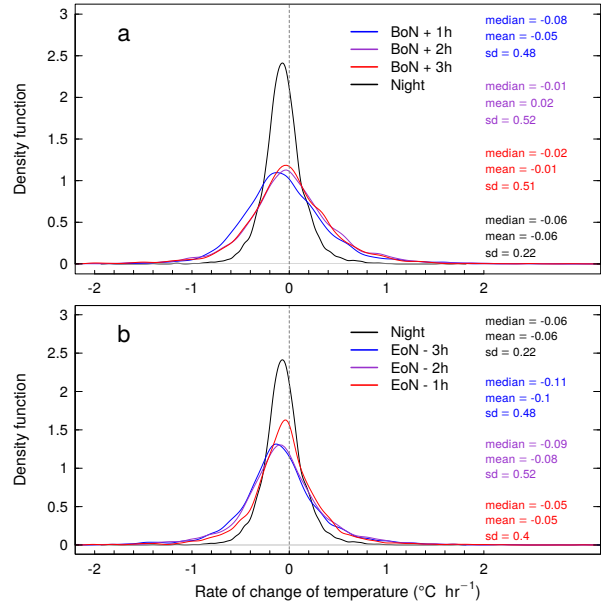


Fig. 7. We present the kernel density plots of the rate of change of the air temperature for: (a) 1h, 2h, 3h after the beginning of the night (BoN) and the period of time including 3 hours after BoN and 3 hours before the end of the night (EoN) or simply “Night” and (b) 1h, 2h, 3h before the end of night and the “Night” period. In each panel, we indicate the median, mean, and standard deviation for each distribution of rates of change with the same color as its respective curve. Negative values of the rates of change of the air temperature gradient indicate cooling, while positive rates indicate heating. The color figure can be viewed online.

before the EoN. Overall, the air temperature gradually decreases throughout the night at a mean rate of  $-0.06\text{ }^{\circ}\text{C hr}^{-1}$ , with the most rapid cooling one hour after the BoN and the three hours before the EoN.

In Table 5, we present the dates with the lowest temperatures recorded in the last thirteen years. We have searched for dates where the daytime or nighttime mean temperature was  $\leq -10\text{ }^{\circ}\text{C}$ . From this table it can be seen the lowest temperatures occur from December to March, usually at night and when the relative humidity is high, perhaps due to the presence of sleet and/or snow. Such conditions are unusual, since the median relative humidity in Table 5 is 70%, which occurs less than 15% of the time (see § 3.2).

Table 6 presents the dates where the daytime mean temperature was  $\geq 20\text{ }^{\circ}\text{C}$ . As expected, all of these extreme temperatures take place in June and

TABLE 5  
LOWEST MEAN TEMPERATURES

Date	Day/Night	Temperature		RH
		mean	min	mean
		(° C)		(%)
Jan 13, 2007	D	-10.2	-12.2	80
Jan 13, 2007	N	-10.4	-13.6	31
Jan 15, 2007	D	-10.2	-12.5	36
Jan 18, 2007	N	-10.2	-12.7	69
Jan 19, 2007	D	-11.1	-12.4	92
Jan 19, 2007	N	-11.6	-13.2	97
Jan 22, 2007	D	-10.7	-14.4	82
Jan 22, 2007	N	-11.1	-14.4	78
Mar 16, 2008	N	-10.0	-10.7	89
Feb 2, 2011	N	-10.5	-15.8	21
Feb 3, 2011	D	-10.3	-14.9	6
Feb 3, 2011	N	-10.9	-16.4	13
Mar 18, 2012	N	-10.7	-11.9	86
Jan 11, 2013	N	-13.1	-14.1	75
Jan 12, 2013	D	-10.3	-13.4	70
Jan 12, 2013	N	-11.3	-13.7	66
Jan 14, 2013	N	-11.0	-13.1	26
Dec 31, 2014	D	-10.8	-13.3	84
Dec 26, 2015	D	-12.8	-14.1	50
Dec 26, 2015	N	-12.9	-13.9	47
Dec 29, 2018	N	-10.5	-13.9	37
Jan 1, 2019	N	-10.7	-14.2	64
Feb 18, 2019	N	-10.1	-14.2	84
Feb 22, 2019	N	-11.3	-12.3	83

July during daytime. When these temperatures occur, the relative humidity is typically below its median value (see § 3.2).

Studies of global warming (IPCC–SR15 2018<sup>4</sup>), performed over long periods of time ( $\approx 30$  years to correct for short-term natural fluctuations), have shown an increase in the temperature of 0.1–0.3° C per decade. However, this value has been found to be higher in Earth’s land regions than at sea, because oceans lose more heat by evaporation. Also, higher values are measured in the Northern Hemisphere compared to the Southern Hemisphere, because the former has more land surface to absorb more sunlight and more heat. Similarly, there is a seasonal dependence, with higher values for colder seasons. Some Northern Hemisphere mid-latitude

<sup>4</sup>The Intergovernmental Panel on Climate Change. <https://www.ipcc.ch/sr15/>.

TABLE 6  
HIGHEST MEAN TEMPERATURES

Date	Day/Night	Temperature		RH
		mean	max	mean
		(° C)		(%)
Jul 1, 2007	D	20.4	22.9	18
Jul 2, 2007	D	20.5	22.2	17
Jul 2, 2011	D	20.0	22.4	19
Jun 28, 2013	D	20.2	22.2	31
Jun 29, 2013	D	21.2	22.5	24
Jun 30, 2013	D	20.8	22.9	27
Jun 20, 2015	D	20.1	21.8	10
Jun 19, 2016	D	20.9	22.1	17
Jun 20, 2016	D	20.5	22.1	24
Jul 7, 2017	D	20.0	22.7	35
Jun 22, 2018	D	20.5	23.1	9

winter locations are experiencing a regional warming of more than double the global average.

Álvarez et al. (2007) found an increase in temperature at the OAN-SPM site. They found that temperature increased by 1.3° C from 1969–1974 to 2000–2003 (or 0.4° C per decade). We searched for a trend in temperature as a function of time in our data. The best linear fit to the mean yearly temperature data in the 2009–2019 period does not give a significant variation of the temperature at a 95% confidence level. We present the coefficients of the linear regression fit in Table 7. (We do not include the years 2007 and 2008 since their temperatures are likely biased, as noted earlier.) If we consider data from Álvarez et al. (2007) and perform a linear regression fit to the data for 1969–1974, 2000–2003, and 2009–2019 (a 50 year interval), we obtain an increase in temperature of  $\approx 1^\circ\text{C}$  (or 0.2° C per decade see Table 7), but this variation is also not significant at the 95% confidence level.

Additionally, we searched for a change in the number of cold days (daily mean temperature  $\leq 0^\circ\text{C}$ ) or the number of warm days (mean temperature  $\geq 17^\circ\text{C}$ ). These two extreme temperatures occur less than 10% of the time. We present these statistics in Table 8. Once again, the linear fits to these data are not statistically significant.

### 3.2. Relative Humidity

We present the daily maximum and minimum values of the relative humidity from 2007 to 2019 in Figure 8 for daytime and nighttime data. In this fig-

TABLE 7  
PARAMETER VARIATIONS (2009–2019)

Parameter	Coeff. <sup>a</sup>		P <sup>c</sup>	Variation (per decade)
	a ± σ	b ± σ		
Temperature	7.94 ± 0.30 (° C)	0.03 ± 0.04 (° C yr <sup>-1</sup> )	0.48	Not significant
Temperature <sup>b</sup>	7.29 ± 0.40 (° C)	0.02 ± 0.01 (° C yr <sup>-1</sup> )	0.06	Not significant
Relative Humidity	34.71 ± 1.33 (%)	0.05 ± 0.20 (% yr <sup>-1</sup> )	0.82	Not significant
Atmospheric pressure	728.88 ± 0.27 (mb)	0.12 ± 0.05 (mb yr <sup>-1</sup> )	0.03	1.1 ± 0.3 mb
Precipitation	124 ± 62 (mm)	32 ± 9 (mm yr <sup>-1</sup> )	0.01	286 ± 63 mm

<sup>a</sup>Coefficients of the linear regression  $a + bx$  ( $x = 1, 2, \dots, N$  years.).

<sup>b</sup>Using data from 1969–2019 period.

<sup>c</sup>P value of the slope coefficient of the linear regression.

TABLE 8  
NUMBER OF WARM AND COLD DAYS  
(2009–2019)

Year	Num. cold	Num. warm
	$T \leq 0^\circ \text{C}$	$T \geq 17^\circ \text{C}$
2009	40	10
2010	39	15
2011	56	14
2012	40	11
2013	40	10
2014	19	9
2015	28	16
2016	32	20
2017	34	7
2018	28	18
2019	42	17

ure, daily maximum and minimum relative humidity values and the monthly median relative humidity for each year are shown. The relative humidity covers a range from 0 to 100 % and shows a seasonal variation due to the North American monsoon (Douglas et al. 1993), with summer months being the most humid on average.

Figure 9a presents the cumulative distribution of the daytime and nighttime relative humidity based upon 5 minute averages. The OAN-SPM is indeed a low humidity site, with a median relative humidity of 30% during the day and 27% at night. Though the distributions are very similar, a Wilcoxon-Mann-Whitney test confirms that they differ significantly (P value =  $8.9 \times 10^{-9}$ ), with the median daytime relative humidity (30%) being slightly greater than the median nighttime value (27%).

The drier conditions at night might seem counterintuitive, but they are mostly due the so called mountain thermal circulation. In their study of the hourly temperature and relative humidity variations at different altitudes at the Kilimanjaro, Duane et al. (2008) found that at low altitudes the relative humidity increases during the night, while at high altitudes this increase is seen during the day (see their Figure 9b). According to these authors, the diurnal variation in humidity it is the outcome of strong upslope moisture transport during the day (via anabatic winds), counterbalanced by downslope transport and drying at night (via katabatic winds). This moisture is produced by the evapotranspiration process of the forest vegetation. At the OAN-SPM site, this effect has also been observed. In their characterization of the Vallecitos site (a valley at an altitude of 2435 m and  $\approx 3.5$  km away from the OAN-SPM site), Tovmassian et al. (2016) found that at Vallecitos site the humidity is much higher at night than in the day, while for the OAN-SPM site it is slightly higher during the day (see their Figure 12). These authors suggest that this might be the result of anabatic and katabatic winds (see their Figure 16). From Figure 9a, it can be seen that 75% of the time, the relative humidity at night is lower than in the day, the rest of the time it is quite similar. The standard requirement for the use of the telescopes is that the relative humidity be  $\leq 85\%$  (and that there be no condensation). At the OAN-SPM, such humid conditions ( $>85\%$ ) occur during only 6.5% of daytime (300 hours per year) and 7.1% of nighttime (273 hours per year).

In Figure 9b we present the cumulative distribution by season. From this figure, it can be seen that summer is the most humid season with a median value of the relative humidity of 51%, and the

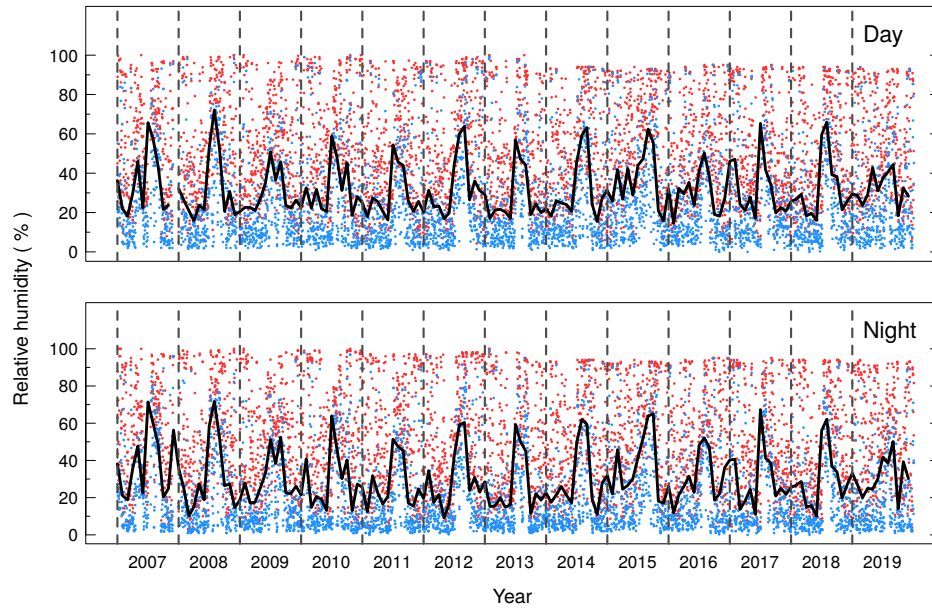


Fig. 8. We present the thirteen year evolution (2007–2019) of the daily maximum (red) and minimum (blue) relative humidity for daytime and nighttime data. In each panel, the black line represents the median monthly relative humidity, while the vertical dashed lines indicate the first day of each year. The monthly median relative humidity peaks in summer due to the North American monsoon. The color figure can be viewed online.

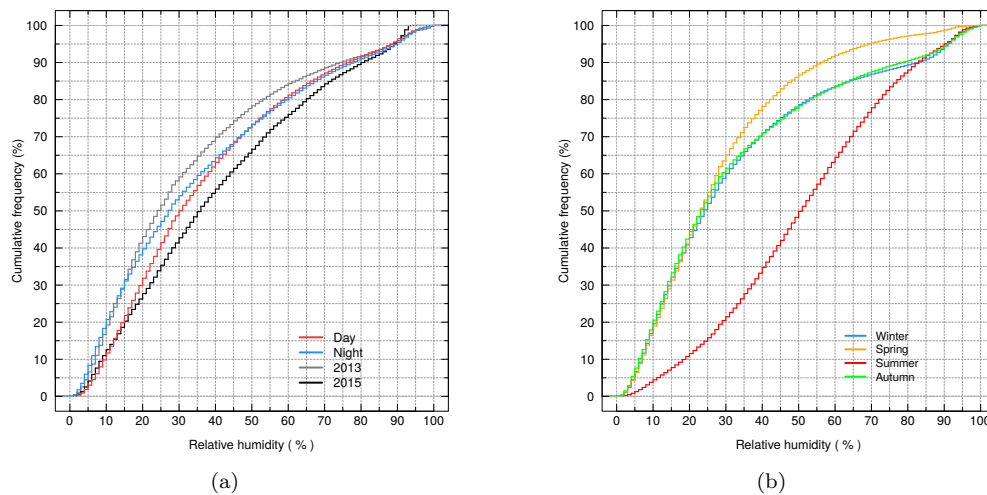


Fig. 9. We present (a) the cumulative distribution of the daytime and nighttime relative humidity obtained in the period 2007–2019, based upon the 5 minute averages. The blue line is for nighttime data, red line is for daytime data, gray line is for 2013 (driest year) data and black line is for 2015 data (most humid year), both data sets include day and night data. There is an excess of low humidity values at night compared to during the day. In (b) we present the cumulative distribution by season in the same period. The blue line is for winter, orange line for spring, red line for summer and green line for autumn. The color figure can be viewed online.

driest is spring with a median value of 23%. This is also shown in Table 9, where we present monthly mean values of the relative humidity. April to June

(spring) is the driest period at OAN-SPM site while July to September (summer) is the most humid period (see Figure 24).

TABLE 9  
MONTHLY MEAN RELATIVE HUMIDITY

Month	Day	Night	Day + Night
	(%)		
January	36 ± 25	36 ± 26	36 ± 26
February	34 ± 27	32 ± 26	33 ± 27
March	31 ± 21	27 ± 23	29 ± 21
April	28 ± 18	26 ± 20	27 ± 18
May	31 ± 19	27 ± 20	29 ± 18
June	25 ± 14	23 ± 16	24 ± 15
July	52 ± 21	52 ± 21	52 ± 21
August	53 ± 21	52 ± 21	52 ± 20
September	48 ± 24	47 ± 25	47 ± 24
October	33 ± 22	30 ± 25	31 ± 23
November	31 ± 23	29 ± 24	30 ± 23
December	35 ± 28	33 ± 26	34 ± 27

TABLE 10  
ANNUAL MEDIAN RELATIVE HUMIDITY

Year	Day	Night	Day + Night
	(%)		
2007 <sup>a</sup>	33	32	34
2008 <sup>a</sup>	28	28	28
2009	27	27	27
2010	31	26	29
2011	27	27	26
2012	30	28	28
2013	26	22	24
2014	27	26	27
2015	36	32	35
2016	30	30	29
2017	29	28	28
2018	28	27	27
2019	31	29	29

<sup>a</sup> < 95% of data (see Table 2).

In Table 10, we present the annual median relative humidity for the years 2007 to 2019. Considering day and night data, the driest year was 2013 and the most humid 2015, with relative humidities of 24 % and 35 %, respectively. This can be seen in Figure 9a, where we show the 2013 and 2015 cumulative distribution of the relative humidity.

Figure 10 presents the hourly relative humidity and its variation by season. The first panel (a) makes clear that summer is by far the most humid season. There is little difference in the relative humidity between the other seasons. In the second panel (b), for

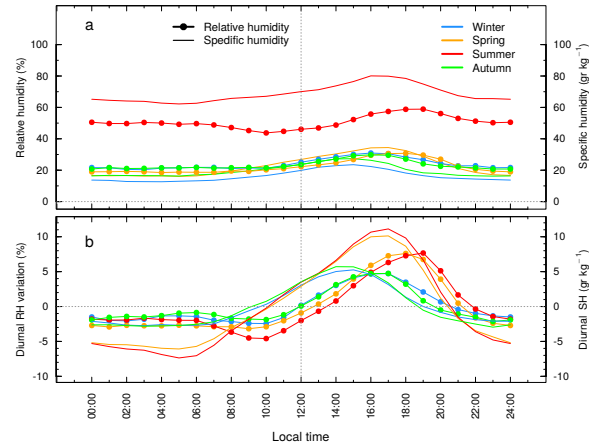


Fig. 10. We present the relative and specific humidity (upper panel) and the diurnal relative and specific humidity variation (bottom panel) by season. Summer is the most humid season (50% relative humidity), with the others all being substantially lower (30% relative humidity). The diurnal variation of the humidity is highest (and similar) in spring and summer while autumn and winter have a smaller diurnal variation. The color figure can be viewed online.

each season, we subtract the mean relative humidity of the day from the relative humidity at a given hour during the day. At a given hour, values below the zero line indicate that the relative humidity is lower than the mean relative humidity of the day.

In general, for all seasons, the relative humidity first decreases as the atmosphere warms up during the first hours after sunrise (morning warming), but then increases throughout the rest of the day (via anabatic winds). As the atmosphere cools at sunset, the relative humidity reaches its maximum value, before rapidly falling over the next few hours (via katabatic winds) and reaching a stable value shortly before midnight. Figure 10b indicates that the most extreme (and similar) diurnal variation in relative humidity occurs during the spring and summer seasons.

The relative humidity provides only a partial picture of the water content of the atmosphere at the OAN-SPM. Figure 10 also presents the specific humidity, the amount of water vapor (in grams) present in an air volume of 1 kg, which depends on air temperature, relative humidity and atmospheric pressure. The hourly specific humidity is plotted in absolute value in Figure 10a, while its diurnal variation is plotted in Figure 10b with continuous lines.

Based upon the specific humidity, there is a much greater amount of water vapor in the atmosphere in the summer than in the other seasons (3 times more; Figure 10a). This is not surprising given that both the temperature and the relative humidity are highest in summer, the two factors most affecting the specific humidity. The specific humidity is especially low in winter.

The diurnal variation in summer and spring are quite similar (see Figure 10b), with the only difference being a lower minimum at sunrise ( $\approx 05:00$  hours) for the summer. In detail, the specific humidity depends upon the relative humidity, the atmospheric pressure and the temperature, but temperature provokes variations of the largest absolute magnitude for the typical conditions at the OAN-SPM. Hence, the diurnal variation of the specific humidity is mostly driven by the diurnal variation of the temperature, though also scaled by the relative humidity. There is a greater diurnal temperature variation in spring than in summer (see Figure 6), but both a lower relative humidity (Table 9) and a smaller amplitude of its diurnal variation. These factors conspire to produce a similar diurnal variations of the specific humidity in spring and summer. As for autumn and winter, their diurnal temperature variations are similar, as are their relative humidities, so they too have similar diurnal variations of the specific humidity.

To investigate whether the relative humidity varies with time, we fit the mean annual values. We find no significant variation as a function of time (see Table 7).

### 3.3. Atmospheric Pressure

The daily median values of the atmospheric pressure are plotted in Figure 11. Note that we have no data from 2007, when the barometer was not working properly (Table 2). There is a clear seasonal variation of the atmospheric pressure, with high values in summer and lower values in winter. The atmospheric pressure has a median value of 730 mb, but varies within the range of 713–737 mb (534–552 mm-Hg) during the entire period (see Figure 24). As for the air temperature, there is much more variation in the atmospheric pressure in winter than in summer.

In Figure 12a, we present the cumulative distribution of the daytime and nighttime atmospheric pressure obtained in the period 2008–2019, based upon the 5 minute averages. The median atmospheric pressure during the day is 730.1 mb while at night it is 729.6 mb. Although the distributions

for the day and night are similar, there is a systematic shift. A Wilcoxon-Mann-Whitney test confirms that both distributions are statistically different ( $P = 8.4 \times 10^{-10}$  that the two distributions arise from the same parent distribution), with the median daytime atmospheric pressure value exceeding the nighttime median value by 0.5 mb. As we show later, this difference is mainly due to the thermal atmospheric tides phenomenon.

In Figure 12b, we present the cumulative distribution of atmospheric pressure by season. From this figure, it can be seen that the season with the highest atmospheric pressure is summer with a median value of 733.1 mb. On the other hand, winter has the lowest atmospheric pressure, with a median value of 727.7 mb.

In Table 11, we present the monthly mean values of the atmospheric pressure. The seasonal variation seen in Figure 11 appears in the run of the values. During the summer months (July to September), the atmospheric pressure is the highest ( $\approx 733$  mb). This occurs because the OAN-SPM samples the mid-layers of the low atmosphere air. In summer, the air at lowest altitudes is heated most and so expands, which raises a greater fraction of the lower atmosphere to greater heights and raises the air pressure at middle heights in the process. The rest of the year, the median atmospheric pressure is below  $\approx 730$  mb (see Figure 12b). As a comparison, at the sea level (e.g. Ensenada, B.C.), the atmospheric pressure ranges between 1002 – 1025 mb and the annual pattern is the inverse, with highest atmospheric pressure during the winter ( $\approx 1016$  mb) and the lowest during the summer ( $\approx 1011$  mb)<sup>5</sup>.

Figure 13 presents the variation of the atmospheric pressure throughout the day. Here, we bin the data by season and subtract the daily mean value. The atmospheric pressure varies through two cycles per day whose shape varies seasonally. These variations, also known as thermal atmospheric tides, are complex and not fully understood, but their main cause is the absorption of the solar radiation by the ozone in the stratosphere, aided by water vapor (Siebert 1961; Chapman & Lindzen 1970; Haurwitz & Cowley 1973; Pugh 1987). In the upper atmosphere, the diurnal heating cycle gives rise to diurnal pressure waves, but the dynamic structure of the atmosphere causes the semidiurnal harmonic to be dominant (Pugh 1987; Le Blancq 2011). Hence, we observe two cycles per day.

<sup>5</sup>Data in the 2012-2019 period from CICESE weather stations <http://redmar.cicese.mx/>.

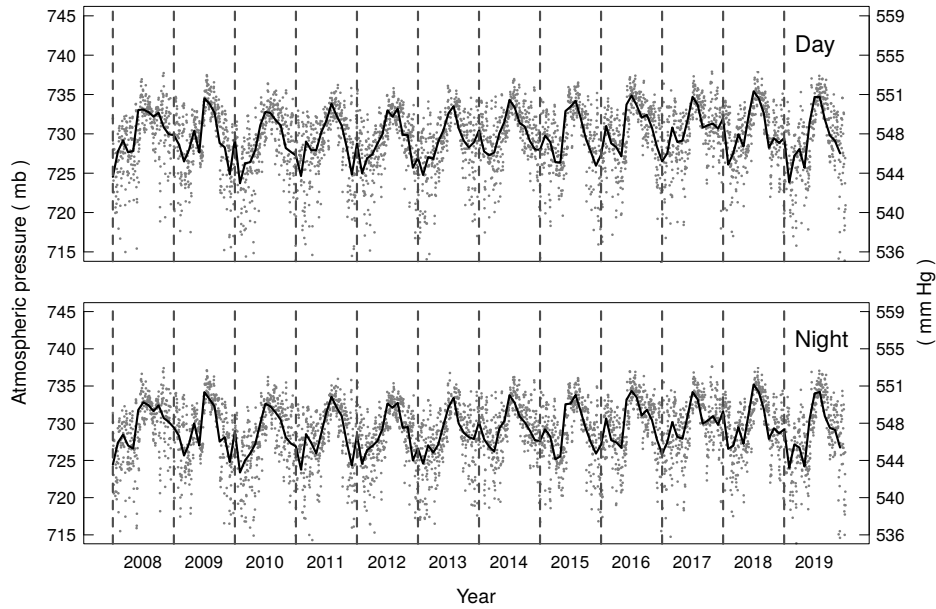


Fig. 11. We present the variation of the daily mean atmospheric pressure for daytime and nighttime data as a function of time (2008–2019). In each panel, the black curve represents the median monthly atmospheric pressure and the vertical dashed lines indicate the first day of each year. There is a clear seasonal variation, with the highest atmospheric pressure in summer and the lowest in winter. There is also a greater variation in the atmospheric pressure in winter.

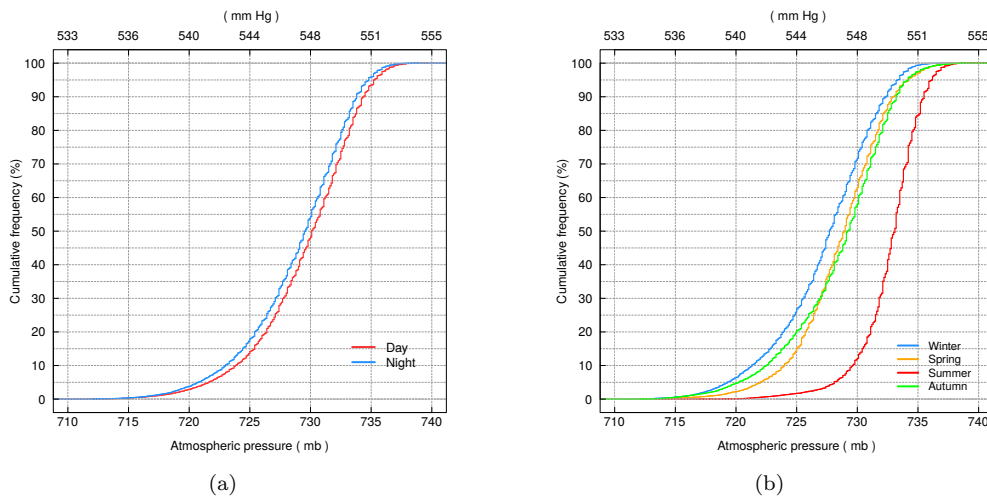


Fig. 12. We present (a) the cumulative distribution of the daytime and nighttime atmospheric pressure obtained in the period 2008–2019, based upon the 5 minute averages. The blue line stands for the nighttime data and the red line for the daytime data. There is a statistically-significant shift between the two distributions, with the daytime values shifted to higher values. In (b) we present the cumulative distribution by season in the same period. The blue line stands for winter, the orange line for spring, the red line for summer and the green line for autumn. The color figure can be viewed online.

The diurnal pressure variation has a minimum and a maximum that occurs at the same time each day in all seasons. In Figure 13, the diurnal min-

imum (main minimum) occurs at 04:00 hrs while the diurnal maximum (secondary maximum) occurs around 22:00 hrs. On the other hand, the semi-

TABLE 11  
MONTHLY MEDIAN ATMOSPHERIC  
PRESSURE

Month	Day	Night	Day + Night
	(mb)		
January	728	728	728
February	727	727	727
March	728	727	728
April	728	727	728
May	728	727	728
June	731	730	731
July	734	733	734
August	734	733	733
September	732	732	732
October	730	730	730
November	729	729	729
December	728	727	728

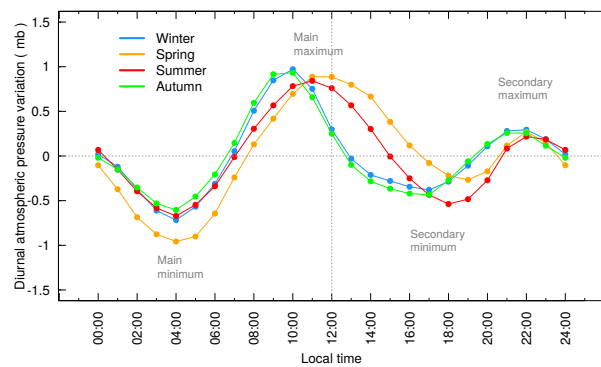


Fig. 13. We present the diurnal and semidiurnal atmospheric pressure variation by season. To construct these curves, we subtract the daily mean value from the hourly means and then average all of the data by season and hour. The diurnal atmospheric pressure variation consists of the main maximum and secondary minimum, while the semidiurnal variation consists of the main minimum and the secondary maximum. The color figure can be viewed online.

urnal pressure variation varies seasonally. Its maximum (main maximum) happens earlier in winter and autumn (10:00 hrs) compared to spring and summer (12:00 hrs) and, likewise, its minimum (secondary minimum) also occurs earlier in winter and autumn (16:00 hrs) than in spring and summer (19:00 hrs). Overall, the net effect of the atmospheric tides is a lower atmospheric pressure at night compared to the day. The atmospheric pressure variation during the

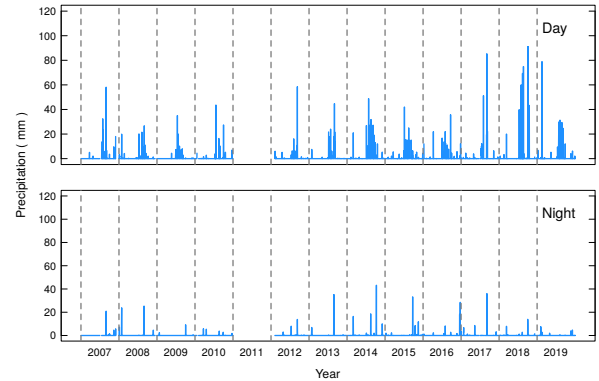


Fig. 14. We present the records (2007–2019) of the daily accumulated precipitation for daytime and nighttime data. The vertical dashed lines indicate the first day of each year. No data were recorded for 2011. These data indicate that there is more precipitation during the day than at night. The color figure can be viewed online.

night has a mean value of  $-0.64$ , while this value is  $0.25$  during the day.

Studies indicate that the amplitude of atmospheric tides varies with latitude, from about  $0.3$  mb in polar regions to  $3.0$  mb in the tropics (Le Blancq 2011). The amplitude of the tides seen at the OAN-SPM fits this pattern, since we find an amplitude of  $\approx 2$  mb. Also, there is evidence that the amplitude varies seasonally (Le Blancq 2011). Our results support this finding, since the amplitude is approximately  $1.7$  mb in winter,  $1.8$  mb in spring, and  $1.5$  mb in summer and autumn.

Over the last ten years, the fit to our data shows that the annual mean atmospheric pressure increased by  $1.1$  mb (see Table 7).

### 3.4. Precipitation

Previous studies of the climate at the OAN-SPM did not include precipitation. These studies relied upon measurements obtained at weather stations in the region of the observatory, at distances up to around  $150$  km (Álvarez et al. 2007) in order to understand the precipitation regime at the top of the mountain. Here, we include rain precipitation data recorded over the last thirteen years. As noted earlier, our data underestimate the precipitation from snowfall since the pluviometers are unreliable in sub-zero temperatures. Hence, our precipitation data should be treated as a lower limit to the true total precipitation. As mentioned in § 2, we have no data for 2011.

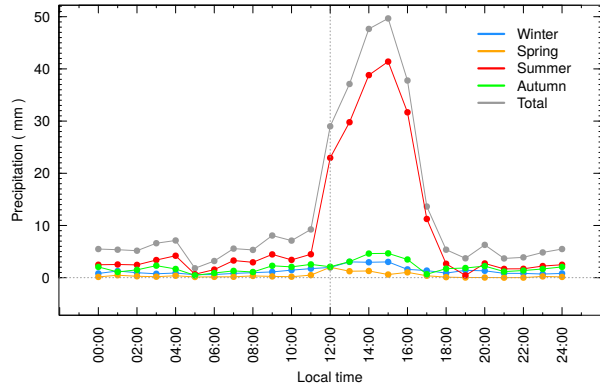


Fig. 15. We present the hourly accumulated precipitation by season as a function of time throughout the day. Except in summer, there is no preferred time for precipitation. In summer, most of the precipitation falls as afternoon thunderstorms. The color figure can be viewed online.

In Figure 14, we show the daily accumulated precipitation for the period 2007 to 2019 for daytime and nighttime data. It is clear that rain is more common during the day than at night. Overall, our records indicate that there is four times more rain during the day than at night.

Two factors affect the precipitation at the OAN-SPM. On the one hand, the rainy season in the northwest coastal region of Mexico occurs during the winter and it is primarily caused by the southern tails of North Pacific winter storms reaching Southern California and Northern Baja California. On the other hand, in the area surrounding the north end of the Mar de Cortés (Gulf of California), heavy rainstorms occur during the summer, when the precipitation rises to a maximum in August due to the water vapor carried by the North American monsoon (Higgins et al. 1997). Since the Sierra San Pedro Mártir, where the OAN-SPM is located, occupies the highest reaches of the mountain range dividing these two regimes, it is affected by both.

In Table 12, we present the monthly mean accumulated precipitation for daytime and nighttime, which is also plotted in Figure 24. In Table 13, we present the monthly accumulated precipitation for every year. Both Tables 12 and 13, as well as Figure 24, demonstrate that the summer months dominate our precipitation data, though we should keep in mind that we are missing an important fraction of the winter precipitation.

TABLE 12  
MONTHLY MEAN ACCUMULATED PRECIPITATION

Month	Day	Night	Day + Night
	(mm)		
January	6	7	13
February	11	3	14
March	4	2	5
April	3	1	5
May	2	1	2
June	3	0	3
July	76	2	77
August	80	13	92
September	44	10	54
October	20	8	27
November	5	4	9
December	5	8	12

In Figure 15, we plot the accumulated precipitation according to the hour of the day for each season. There is no noticeable trend, except for summer. In summer, we find that the heaviest rains occur preferentially between 12:00 to 17:00 hrs, which is to be expected since afternoon thunderstorms dominate the precipitation in summer. In other seasons, the precipitation is similar for daytime and nighttime. Since the precipitation in other seasons is determined by larger-scale weather systems, this suggests that the snowfall in winter, largely absent in our data, is similar during the day and night. Hence, we expect the true trend for winter in Figure 15 to be a scaled version of the trend shown.

In the last three rows of Table 13, we present the total (day + night), daytime and nighttime accumulated precipitation for 2007–2019. The annual mean rain precipitation at the OAN-SPM is  $313 \pm 125$  mm, with  $\approx 70\%$  (220 mm) falling between July and September. From Table 13, the total is clearly very variable. 2018 had double the annual mean, in part due to abundant rains in October and more than usual during the summer, while 2009 was a year characterized by little precipitation.

Álvarez et al. (2007) reported an annual rain precipitation of 449 mm using a CONAGUA station (Comision Nacional del Agua) located at the National Park (13 km southwest at an altitude of 2080 m) during the period 1977–2007, but only 173 mm at the OAN-SPM. They reported that 77% of the precipitation at the National Park station occurred during winter time and the rest during spring

TABLE 13  
MONTHLY ACCUMULATED PRECIPITATION (2007–2019)

	2007 <sup>a</sup>	2008 <sup>a</sup>	2009	2010	2011 <sup>b</sup>	2012	2013	2014	2015	2016	2017	2018	2019
Month	(mm)												
Jan	0	72.7	3.2	4.4	...	0	30.3	0.1	4.1	14.2	14.6	2.4	8.5
Feb	0	4.8	0	0.4	...	13.1	0	36.1	0.1	0.1	7.7	3.9	100.0
Mar	7.5	0	0	5.6	...	0	0	3.4	14.5	1.5	0.8	25.7	1.0
Apr	2.7	0.30	0	9.0	...	8.4	0	1.6	0.1	26.5	3.9	0	2.1
May	0	0	5.8	0.2	...	0.9	1.2	0.1	3.9	0.1	8.8	0	5.2
Jun	0	0.9	12.2	0	...	0	0	0	9.3	16.7	0	0.3	0
Jul	69.5	26.6	97.2	56.6	...	19.7	73.3	105.4	78.4	67.0	55.5	188.0	92.5
Aug	112.0	129.6	28.4	44.8	...	49.3	178.8	85.7	68.5	46.2	70.8	197.9	92.8
Sep	7.6	17.8	6.4	9.0	...	94.2	59.4	75.7	71.0	44.5	151.5	15.8	89.9
Oct	7.2	2.0	9.8	38.6	...	1.8	0.4	75.4	19.5	2.0	0	169.4	0
Nov	39.5	7.6	0	0	...	1.2	0.9	0	23.5	8.8	6.6	0.3	14.7
Dec	...	0	2.2	10.2	...	1.2	0.3	27.3	6.0	71.9	4.6	3.4	17.1
Total	246.0	262.3	165.2	178.8	...	189.8	344.6	410.8	298.9	299.5	324.8	607.1	423.8
Day	224.5	184.6	152.2	159.8	...	159.2	247.1	294.6	224.9	222.3	259.3	573.5	389.7
Night	21.5	77.7	13.0	19.0	...	30.6	97.5	116.2	74.0	77.2	65.5	33.6	34.1

<sup>a</sup>< 95% of data (see Table 2).

<sup>b</sup>Pluviometer not working.

and summer (see their Figure 2 and Table 3). They also included weather data for a station to the east of the Sierra San Pedro Mártir at a similar latitude as the other two stations. There, precipitation almost only falls in summer, as a result of summer thunderstorms, and the yearly total amounts to 147 mm. Therefore, there is clearly a regime change in the precipitation in the vicinity of the OAN-SPM.

At the OAN-SPM, we find at least 50% more rainfall in summer (223 mm; Table 12) than reported for the station further east, and double that reported by Álvarez et al. (2007) for the National Park weather station. Even if all of the winter precipitation recorded at the National Park station fell at the OAN-SPM, it would amount to only about half the total at the OAN-SPM. If so, the total annual precipitation at the OAN-SPM is likely in the 400–450 mm range.

Considering that the rainy days have, on average, a daily accumulated precipitation of 10 mm, a heavy precipitation day could be one with  $\geq 30$  mm. In Table 14 we present the dates with heavy accumulated precipitation in the 2007–2019 period. From this table it can be seen that heavy precipitation days occur always during the summer days and in general are characterized by high temperatures  $\geq 10^\circ\text{C}$ , high relative humidity ( $> 70\%$ ) and

high atmospheric pressure ( $\geq 730$  mb). On the other hand, heavy precipitation days where the relative humidity is low ( $< 70\%$ ) have the highest temperatures  $> 13^\circ\text{C}$ . However, there were four dates with heavy precipitation, but low temperature ( $< 9^\circ\text{C}$ ) and low atmospheric pressure ( $< 728$  mb). These might be the result of cold fronts, which produced the abundant precipitation recorded.

Our findings are undoubtedly biased as a result of our partial winter precipitation records. Clearly, our total annual precipitation must be an underestimate of the true value. Correcting for this would increase the total precipitation in winter. However, given the different nature of the storms, due to weather systems rather than thunderstorms, this winter precipitation is unlikely to be biased to daytime or nighttime. Hence, we expect the true winter precipitation in Figure 15 to be enhanced overall.

The yearly totals in Table 13 show a clear increase in precipitation in recent years compared to the years up to 2012. Alternatively, if we fit these data as a linear trend, we find an annual increase in precipitation, on average, of 30 mm more precipitation per year for the 2009–2019 period (99% confidence level). The values and uncertainties of the coefficients of the linear fit are shown in Table 7. In Figure 16 we present the linear fit to our data in the

TABLE 14  
HEAVY PRECIPITATION<sup>a</sup>

Date	Day/Night	Daily precip. (mm)	T mean (° C)	RH mean (%)	Atmosph. pressure (mb)
Jul 29, 2007	D	32	14.4	66	–
Aug 31, 2007	D	58	12.9	93	–
Jul 15, 2009	D	35	16.4	58	737
Jul 20, 2010	D	44	16.4	67	733
Sep 9, 2012	D	59	10.7	98	731
Aug 26, 2013	N	35	10.0	95	730
Aug 31, 2013	D	45	13.1	67	734
Jul 25, 2014	D	49	15.8	62	734
Aug 17, 2014	D	32	14.3	70	735
Oct 8, 2014	N	43	8.0	91	728
Jul 4, 2015	D	42	14.9	61	732
Sep 21, 2015	N	33	9.7	93	729
Sep 19, 2016	D	36	10.1	94	734
Aug 1, 2017	D	51	13.1	85	734
Sep 2, 2017	D	85	10.8	94	729
Sep 3, 2017	N	36	10.1	95	730
Jul 10, 2018	D	40	11.6	88	734
Jul 29, 2018	D	60	13.7	85	735
Aug 11, 2018	D	69	12.6	82	734
Aug 20, 2018	D	75	15.3	74	735
Oct 1, 2018	D	117	8.4	94	728
Oct 15, 2018	D	43	2.1	67	727
Feb 14, 2019	D	79	4.5	94	723
Ago 6, 2019	D	31	15.3	57	735

<sup>a</sup>Accumulated precipitation ( $\geq 30$  mm).

2009-2019 period (blue line). In addition, we have included the linear fit for the 2007-2019 period (2007 and 2008 are years with  $<95\%$  of data; see Table 2) to verify if this increase in precipitation over the years is also maintained in this period. We find that this trend continues, although it is slightly lower, with 20 mm per year (99% confidence level). Álvarez et al. (2007) presented a weather model (see their Figure 7) that predicted that precipitation would increase from 2007, equalling its long-term average around 2015 and increasing to a maximum between 2020 and 2035. Hence, the increase in total annual precipitation that we find supports their scenario.

Studies of global warming have shown that regions with the largest increases in heavy precipitation events include several high-latitude regions, mountainous regions, eastern Asia and eastern North America (IPCC–SR15 2018). We count the number of days per year with measurable daily precipitation

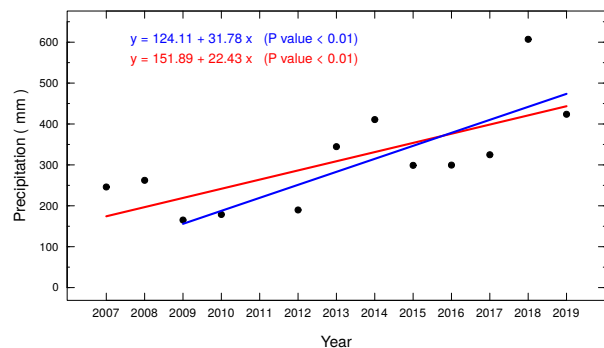


Fig. 16. We present the linear fits to annual precipitation data for the 2009–2019 period (blue line) and 2007–2019 period (red line). Both linear fits have a confidence level of 99%. The color figure can be viewed online.

TABLE 15  
NUMBER OF DAYS WITH PRECIPITATION  
(2009–2019)

Year	Number of days	
	$P \geq 1$ mm	$P \geq 10$ mm
2009	20	5
2010	23	5
2011	...	...
2012	23	4
2013	25	13
2014	31	14
2015	35	9
2016	31	11
2017	28	7
2018	25	13
2019	35	12

( $P \geq 1$  mm) and the number of days with daily heavy precipitation ( $P \geq 10$  mm) for the 2009–2019 period (only years with  $\geq 95\%$  data) and present this information in Table 15. We do not find any significant variation in the number of days with precipitation or heavy precipitation, but rather a correlation with the total precipitation.

### 3.5. Wind Speed and Direction

The DI and VWT weather stations deliver two wind speeds: the sustained wind speed and the wind gust speed. For a description of how these two parameters are determined, we refer the reader to § 2.

The DI and VWT stations were installed at different heights in the three sites, so we have normalized all wind speeds (both sustained and gusts) to a common 7 m height using equation (1) of Bohigas & Núñez (2010) (hereinafter referred to as BN10). Their fit to the median value of the wind speed as a function of height,  $h$ , is

$$V(h)/V(7) = 1.0103 + 0.4293 \ln(h/7). \quad (1)$$

While equation 1 was derived for another nearby site, a relation of this form is expected generally (e.g., Stull 1988). In Figure 17, we present the cumulative distributions of the sustained wind speed for the three sites before and after applying the normalization from BN10. Clearly, equation 1 is reasonably effective at matching the three wind speed distributions from the three sites, especially since our focus is

upon the general conditions at the OAN-SPM. The small residual differences are presumably due to differences in the vertical variation of the wind speed at the three sites relative to that at the site studied by BN10. It is likely that the smaller differences between sites 1 and 3 reflect that these sites, like that studied by BN10, are on the south side of the ridge whereas site 2 is on the north side. Since the strongest winds come predominantly from southerly directions (e.g., Figure 22), site 2 should be somewhat more protected by the local terrain than are sites 1 and 3. This may explain why the wind speed distribution for site 2 has a slightly lower proportion of the highest wind speeds.

As noted in § 2, the distribution of wind directions for site 2 seems to be rotated by  $45^\circ$  when compared to sites 1 and 3, probably due to an error in the orientation of the sonic anemometer at site 2. Alternatively, the orography or buildings around site 2 may be to blame. On the other hand, the cumulative distribution for the wind speed does not appear anomalous. Given the discrepancy with its wind directions, we discard the wind direction data gathered at site 2 from this study. But when only the wind speed is needed, we include the data from site 2. When both the wind speed and direction are needed, we discard the data from site 2 because its wind direction parameter it is not reliable.

The daily maximum and minimum values of the sustained wind speed are plotted in Figure 18 for daytime and nighttime. There are gaps in the data for the years 2007, 2008, 2009 and 2010 winters because the DI wind vane froze, and in 2012 the anemometer was broken (see Table 2). From Figure 18, it is also clear that the sustained wind speed is lowest in summer.

In Figure 19a and Table 16, we present the cumulative distribution of sustained wind and wind gust speeds for daytime and nighttime data. From this figure, it is clear that the wind speeds, both sustained and gusts, are stronger at night. The median sustained wind speed for daytime is  $10.6 \text{ km hr}^{-1}$  ( $2.9 \text{ m s}^{-1}$ ) and at nighttime  $12.9 \text{ km hr}^{-1}$  ( $3.6 \text{ m s}^{-1}$ ), while the median wind gust speeds are  $20.1 \text{ km hr}^{-1}$  ( $5.6 \text{ m s}^{-1}$ ) and  $21.5 \text{ km hr}^{-1}$  ( $\approx 6.0 \text{ m s}^{-1}$ ) for daytime and nighttime, respectively.

The cumulative distributions for the speed of the daytime and nighttime sustained winds differ greatly in shape. In Figure 19a, we also indicate the speed limit of  $45 \text{ km hr}^{-1}$  ( $12.5 \text{ m s}^{-1}$ ) for the sustained wind at which the OAN-SPM's telescope domes are closed. The fraction of time with the sustained wind

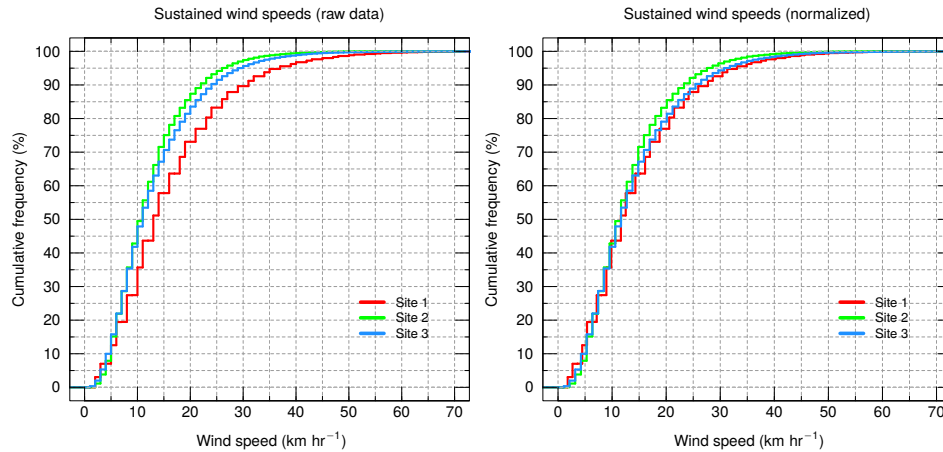


Fig. 17. We present the cumulative distributions of the sustained wind speeds for the three sites before (left panel) and after (right panel) applying the normalization from Bohigas & Núñez (2010). These graphs include data for the period 2007–2019, based upon the 5 minute average values. The color figure can be viewed online.

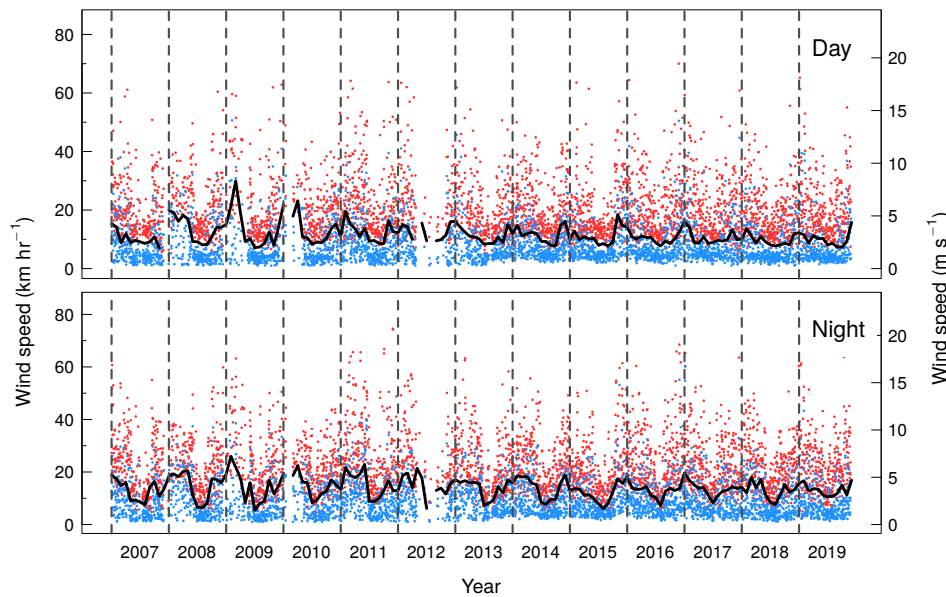


Fig. 18. We present the daily maximum (red) and minimum (blue) sustained wind speeds for daytime and nighttime data for the thirteen year time span of our data (2007–2019). In each panel the black line represents the median monthly wind speed and the vertical dashed lines indicate the first day of each year. These graphs include data from sites 1, 2 and 3. The color figure can be viewed online.

speed above this limit is 1.2% during nighttime or 51.1 hours per year (see Table 16).

In Figure 19b and Table 16, we present the cumulative distribution of sustained wind speed by season. From Figure 19b, it can be seen that the season with the strongest winds is winter, with a median value of  $14.3 \text{ km hr}^{-1}$  ( $4.0 \text{ m s}^{-1}$ ), while for the summer season this value is  $8.9 \text{ km hr}^{-1}$  ( $2.5 \text{ m s}^{-1}$ ). Spring

and autumn have median values of  $11.7 \text{ km hr}^{-1}$  ( $3.3 \text{ m s}^{-1}$ ) and  $12.7 \text{ km hr}^{-1}$  ( $\approx 3.5 \text{ m s}^{-1}$ ), respectively.

In Figure 20, we show the cumulative distribution of the difference between the wind gusts and sustained wind speeds. When compared to the sustained wind and wind gust speeds, we find that for

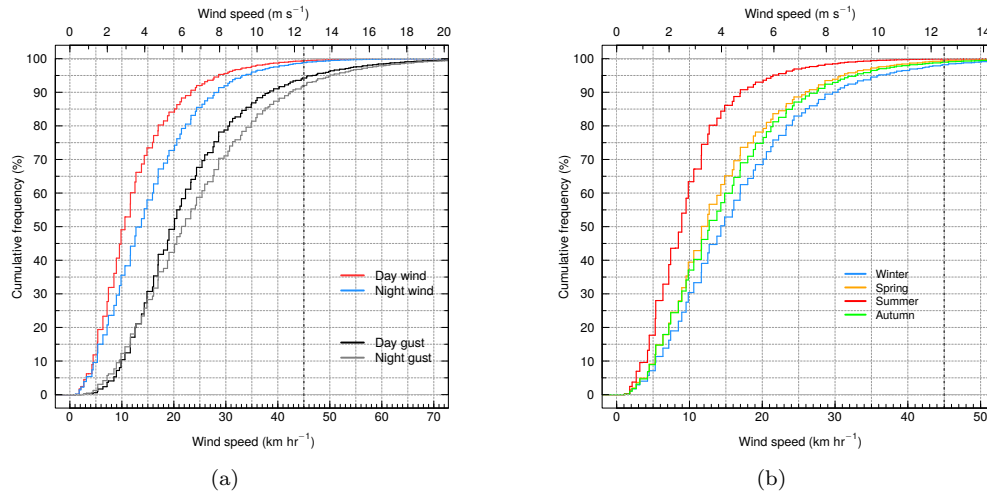


Fig. 19. We present (a) the cumulative distribution of the daytime and nighttime sustained wind speed and wind gusts for the period 2007–2019, based upon the 5 minute average and maximum values, respectively. The blue line stands for nighttime and the red line for daytime sustained wind data. The gray line stands for nighttime and the black line for daytime gusts wind data. In (b) we present the cumulative distribution of the sustained wind speed by season in the same period. The blue line stands for winter, the orange line for spring, the red line for summer and the green line for autumn. In both graphs, the dashed vertical line indicates the sustained wind speed limit of  $45 \text{ km hr}^{-1}$  at which the domes of the OAN-SPM telescopes are closed. These graphs include data from sites 1, 2 and 3. The color figure can be viewed online.

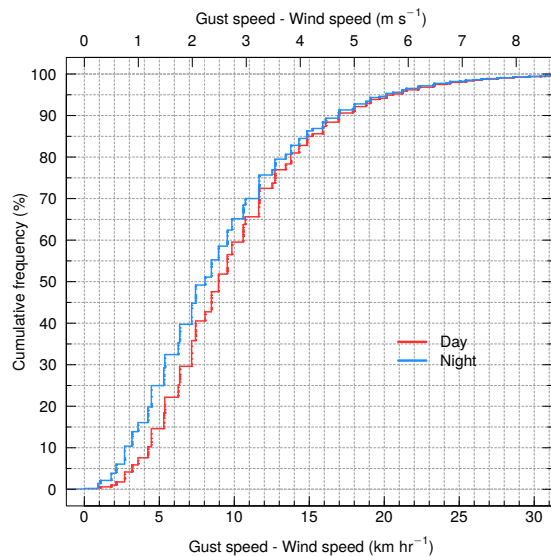


Fig. 20. We present the cumulative distribution of the daytime and nighttime difference between wind gust and sustained wind speeds for the period 2007–2019, based upon the 5 minute average and maximum values, respectively. The blue line stands for nighttime and the red line for daytime data. Values of the x-axis higher than  $30 \text{ km hr}^{-1}$  represent less than 1% of the cases. This graph includes data from sites 1, 2 and 3. The color figure can be viewed online.

50% of the time wind gusts are stronger than sustained winds by  $8.1 \text{ (nighttime)}$  and  $8.9 \text{ km hr}^{-1}$  (daytime) ( $2.3$  and  $2.5 \text{ m s}^{-1}$ ). The difference between the wind gust and the sustained wind speeds rarely exceeds  $20 \text{ km hr}^{-1}$  ( $5.6 \text{ m s}^{-1}$ ), which occurs for less than 6% of the time.

In Figure 21 we present hexagonal bin plots to show the distribution of values of the difference between wind gust and sustained wind speeds as a function of sustained wind speed for daytime and nighttime data. The color bar in the right part of each graph indicates the number of counts in each hexagonal bin. From Figure 21, it can be seen that given the limit of  $45 \text{ km hr}^{-1}$  ( $12.5 \text{ m s}^{-1}$ ) in sustained wind speed, the corresponding wind gust speed will most probably be inside the range of  $55\text{--}85 \text{ km hr}^{-1}$  ( $15.3\text{--}23.6 \text{ m s}^{-1}$ ).

Table 17 and Figure 24 present the monthly means of the sustained wind speed, where it can be seen that the strongest winds occur in December, January, February and March. Table 18 presents the dates with very strong sustained winds, defined as speeds  $\geq 65 \text{ km hr}^{-1}$  ( $\geq 18 \text{ m s}^{-1}$ ) for more than 15 min. Most of the time, these very strong winds occur during November to February and come from SSW direction. Surprisingly, most of these events oc-

TABLE 16  
DISTRIBUTION OF SUSTAINED WIND AND WIND GUST SPEEDS

Speed (km hr <sup>-1</sup> )	Wind		Gusts		Wind			
	Day	Night	Day	Night	Winter	Spring	Summer	Autumn
5	0.1183	0.0958	0.0058	0.0126	0.0711	0.0909	0.1768	0.0893
10	0.4909	0.3555	0.1041	0.1229	0.3039	0.3943	0.6338	0.3707
15	0.7345	0.5795	0.3071	0.2830	0.5287	0.6514	0.8611	0.5994
20	0.8409	0.7268	0.4920	0.4234	0.6848	0.7816	0.9301	0.7480
25	0.9202	0.8551	0.6765	0.5873	0.8293	0.8861	0.9693	0.8709
30	0.9559	0.9194	0.7876	0.7106	0.9001	0.9388	0.9848	0.9294
35	0.9777	0.9603	0.8685	0.8139	0.9453	0.9723	0.9942	0.9650
40	0.9870	0.9754	0.9104	0.8734	0.9647	0.9841	0.9972	0.9792
45	0.9939	0.9883	0.9425	0.9202	0.9819	0.9938	0.9991	0.9897
50	0.9969	0.9939	0.9621	0.9488	0.9900	0.9974	0.9998	0.9944
55	0.9986	0.9972	0.9754	0.9671	0.9949	0.9992	1	0.9974
60	0.9993	0.9985	0.9843	0.9789	0.9974	0.9996	...	0.9986
65	0.9998	0.9995	0.9909	0.9872	0.9992	0.9999	...	0.9994
70	0.9999	0.9998	0.9946	0.9924	0.9997	1	...	0.9998
75	1	0.9999	0.9965	0.9951	0.9998	...	...	0.9999
80	...	1	0.9980	0.9971	0.9999	...	...	1
85	...	...	0.9990	0.9984	1	...	...	...
90	...	...	0.9994	0.9990	...	...	...	...
95	...	...	0.9997	0.9995	...	...	...	...
100	...	...	0.9998	0.9997	...	...	...	...
105	...	...	0.9999	0.9999	...	...	...	...
110	...	...	0.9999	0.9999	...	...	...	...
115	...	...	1	1	...	...	...	...

curred during daytime. For these events, wind gust speeds usually are 20–30 km hr<sup>-1</sup> stronger than the sustained wind speed. The strongest wind gust speed registered is 129 km hr<sup>-1</sup> and it has been recorded four times since 2015, coming from SSW direction at night.

Wind direction statistics are evaluated by calculating the percentage of the time in which the wind comes from each direction. The wind roses have been divided into sixteen mean directions. We have restricted sustained wind speed to values larger than or equal to 1 km hr<sup>-1</sup> (0.3 m s<sup>-1</sup>), in order to obtain a set of wind direction values that is reliable. We tabulate lower wind speeds separately, without regard for their direction.

The wind roses of the sustained wind direction for daytime and nighttime are shown in Figures 22a and 22b, respectively. From this figure, there is little difference between daytime and nighttime in terms of wind direction. Taken as a whole, the predominant wind directions are SSW (202°±11°) and N

(0°±11°). The wind rarely comes from the West or East. The strongest winds, those ≥45 km hr<sup>-1</sup>, only come from South and SSW directions, while low speed winds mostly come from the North. Also, from Figures 22a and b it can be seen that high speed winds (≥20 km hr<sup>-1</sup>) are more common at night, while low speed winds (5–20 km hr<sup>-1</sup>) come during daytime.

Since the wind direction is similar for daytime and night data, in the following we present only the nighttime wind roses. In Figure 23, we present the wind roses for each season. From this figure, it can be seen that during winter and spring the dominant wind direction is SSW direction (202°), and that the strongest winds (> 45 km hr<sup>-1</sup>) also come from this direction. During the summer, there is a bipolar distribution of the winds, with North and South dominant directions, but no strong winds. Finally, in the autumn, most of the winds come from the North and some strong winds from the South and SSW direction.

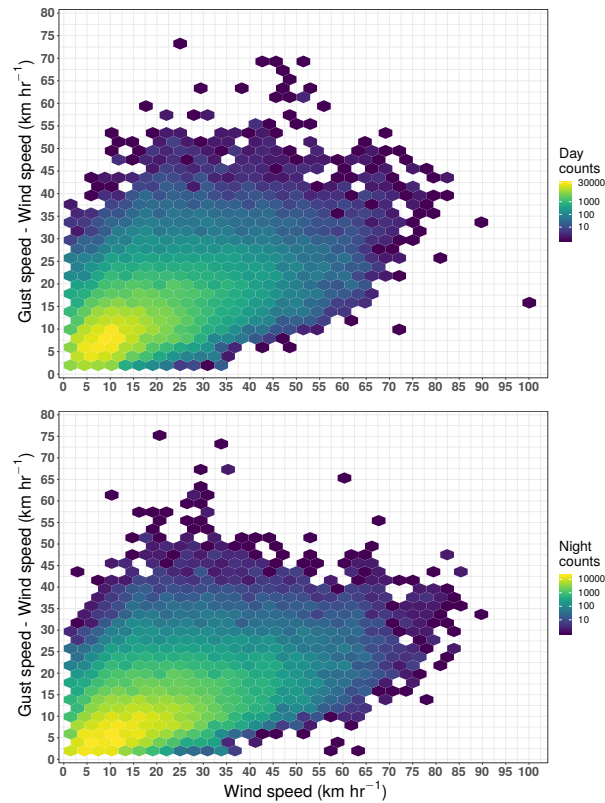


Fig. 21. We present hexagonal bin plots of the daytime (upper panel) and nighttime (bottom panel) difference between wind gust and sustained wind speeds as a function of sustained wind speed based upon the 5 minute average (sustained wind) and maximum (wind gust) values for the period 2007–2019. These graphs include data from sites 1, 2 and 3. The color figure can be viewed online.

#### 4. CONCLUSIONS

We analyze thirteen years of weather conditions at the Observatorio Astronómico Nacional in the Sierra San Pedro Mártir. The weather parameters we consider are: air temperature, relative humidity, atmospheric pressure, precipitation, sustained and wind gust speeds and direction. The data have been split in two sets, one for daytime and the other for nighttime. Figure 24 summarizes many of our results. Our main conclusions are:

- Most of the time, the air temperature is below  $15^{\circ}\text{C}$ . The median temperature is  $10.3^{\circ}\text{C}$  and  $7.0^{\circ}\text{C}$  for daytime and nighttime, respectively, with a median diurnal variation of  $\Delta T = 5.4^{\circ}\text{C}$ . At night, the temperature is quite constant with a mean value of the rate of change of  $-0.06 \pm 0.22^{\circ}\text{C}$  per hour around midnight.

TABLE 17

MONTHLY MEAN SUSTAINED WIND AND WIND GUST SPEEDS

Month	Wind		Gusts	
	Day	Night	Day	Night
	(km hr <sup>-1</sup> )			
January	15 ± 10	17 ± 9	26 ± 14	27 ± 14
February	17 ± 10	19 ± 11	29 ± 15	30 ± 15
March	14 ± 10	18 ± 10	26 ± 14	28 ± 14
April	14 ± 8	17 ± 10	25 ± 12	27 ± 14
May	13 ± 8	16 ± 10	23 ± 11	25 ± 13
June	12 ± 7	15 ± 9	21 ± 10	23 ± 13
July	9 ± 5	9 ± 6	17 ± 7	16 ± 8
August	9 ± 5	10 ± 6	17 ± 7	17 ± 9
September	10 ± 6	12 ± 8	19 ± 10	20 ± 12
October	12 ± 8	15 ± 9	22 ± 12	24 ± 12
November	13 ± 9	16 ± 10	23 ± 13	25 ± 14
December	16 ± 10	17 ± 10	28 ± 15	28 ± 15

TABLE 18

HIGH WIND SPEEDS<sup>a</sup>

Date	Wind Gust speed		Wind direction	Time lapse <sup>b</sup>
	(km hr <sup>-1</sup> )			
Dec 22, 2009	66	83	W	at 9:25–9:50 hrs
Nov 4, 2011	68	102	SSW	at 16:25–16:55 hrs
Jan 23, 2012	68	94	SSW	at 14:30–15:05 hrs
Dec 16, 2016	70	101	S	at 6:10–7:30 hrs
Feb 2, 2019	67	96	SSW	at 16:00–17:25 hrs
Feb 14, 2019	73	109	SSW	at 12:10–17:25 hrs

<sup>a</sup>Sustained wind speed  $\geq 65 \text{ km hr}^{-1}$  for more than 15 minutes.

The coldest month is January with a mean temperature of  $2.1^{\circ}\text{C}$  and the warmest month is July with a mean temperature of  $15.1^{\circ}\text{C}$ . We searched for an increase in temperature over the last thirteen years and over the last 50 years (using data from Álvarez et al. 2007), but have not found any significant variation, at least at the 95% confidence level. Also, we have not found any increase in the number of warm days nor a decrease in the number of cold days over the thirteen years spanned by our data.

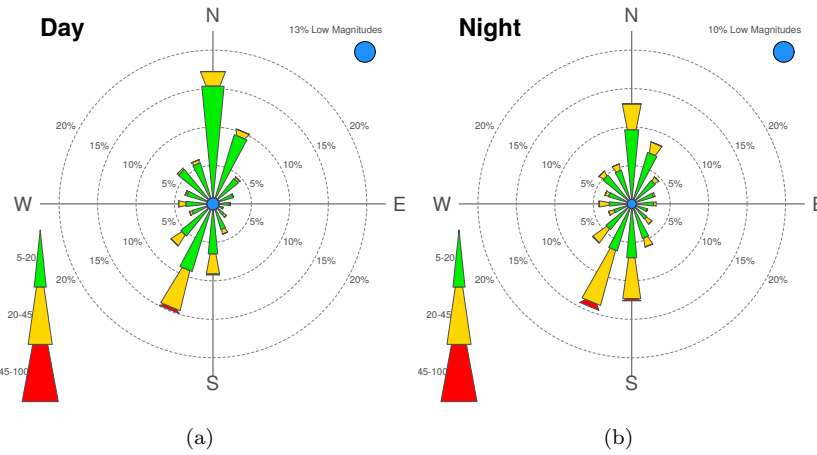


Fig. 22. We present wind roses (a) for daytime and (b) nighttime. The different colors within the roses indicate different velocity ranges. In the center of the wind roses, “low magnitudes” represent velocities in the range (1 km hr<sup>-1</sup> – 5 km hr<sup>-1</sup>). The highest velocities, 45–100 km hr<sup>-1</sup> are represented in red color. The data used here are from sites 1 and 3. The color figure can be viewed online.

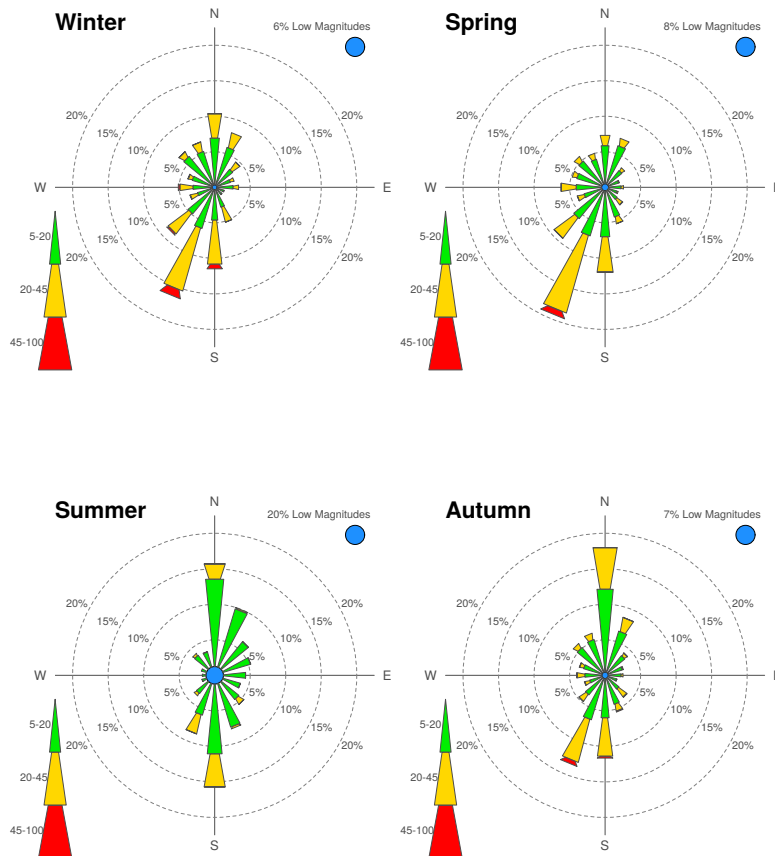


Fig. 23. We present nighttime wind roses for each season. The different colors within the roses indicate different velocity ranges. In the center of the wind roses, “low magnitudes” represent velocities in the range (1 km hr<sup>-1</sup> – 5 km hr<sup>-1</sup>). The highest velocities, 45–100 km hr<sup>-1</sup> are represented in red color. The data used here are from sites 1 and 3. The color figure can be viewed online.

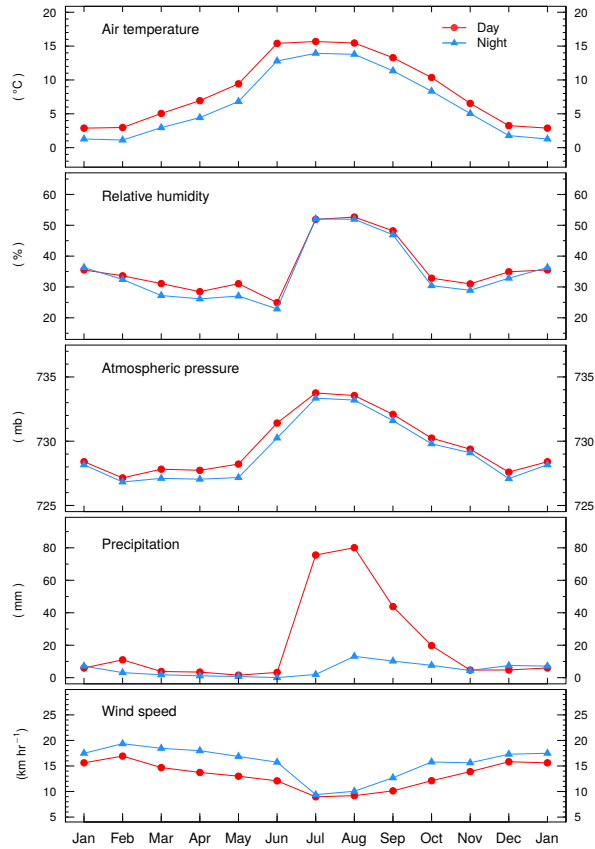


Fig. 24. We present the seasonal trends for (top to bottom) the mean air temperature, relative humidity, atmospheric pressure, precipitation, and sustained wind speed for daytime (circles/red) and nighttime (triangles/blue) for the period 2007-2019. The color figure can be viewed online.

- The relative humidity is statistically different for daytime and nighttime with median values of 30 % and 27 %, respectively. The diurnal variation of this parameter shows that the relative humidity is quite constant from midnight to sunrise, but that it varies during the rest of the day. The largest variations are found in spring and summer. The driest season is spring, with a median relative humidity of 23 % while the most humid season is summer, with median relative humidity of 51 %. We find no evidence for a long term evolution in the relative humidity over the time span of our data.
- The median value of the atmospheric pressure is  $\approx 730$  mb. During daytime, the atmospheric pressure is slightly higher than at night, by 0.5 mb. This parameter varies seasonally, with

the highest atmospheric pressure during summer. The diurnal variation of the atmospheric pressure is  $\approx 2$  mb, due to the phenomenon known as atmospheric tides. On average, the atmospheric pressure has increased by 1 mb in the last decade (95 % confidence level).

- The annual mean accumulated precipitation is  $\approx 313$  mm, 70 % of which occurs during summer time. Also, on average it rains four times more during the day than at night. However, our precipitation data for winter is an under-estimate of the true precipitation due to insensitivity of our sensors to frozen precipitation. Correcting for this, we estimate that the total annual precipitation at the OAN-SPM is 400-450 mm. The annual accumulated precipitation has increased over the time span of our data, with 30 mm more precipitation every year since 2009 (99 % confidence level).
- The median value of the sustained wind speed is  $11 \text{ km hr}^{-1}$  during the day and  $13 \text{ km hr}^{-1}$  at night. The predominant wind directions are SSW ( $202^\circ$ ) and North ( $0^\circ$ ). The sustained wind is stronger at night, during the winter, and comes mainly from SSW direction. The median values of the wind gust speed are  $20 \text{ km hr}^{-1}$  and  $22 \text{ km hr}^{-1}$  for daytime and nighttime, respectively. Wind gust speeds are  $9 \text{ km hr}^{-1}$  stronger than sustained wind speeds 50% of the time. Only 5% of the time does the difference between wind gust and sustained wind speeds exceed  $20 \text{ km hr}^{-1}$ .

We thank the anonymous referee for the careful reading and time spent to analyze this manuscript and the constructive comments and suggestions. This work is based upon observations carried out at the Observatorio Astronómico Nacional on the Sierra San Pedro Mártir (OAN-SPM), Baja California, México. We thank the daytime and night support staff at the OAN-SPM for facilitating and helping obtain these data: E. Cadena, T. Calvario, U. Ceseña, A. Córdova, A. Franco, B. García, F. Guillén, G. Guisa, J. Hernández, J. Herrera, D. Hiriart, E. López, B. Martínez, G. Melgoza, F. Montalvo, S. Monroy, F. Murillo, C. Narváez, M. Núñez, J. L. Ochoa, F. Quiros, M. Reyes, H. Serrano, E. Valdés, J. Valdez, F. Valenzuela, I. Zavala and S. Zazueta. This paper is dedicated to the memory of our friends Gabriel Leyva Arias y Roberto Higuera Escalante.

Finally I. P-F. wants to acknowledge the use of the R package, which is a free software environment for statistical computing and graphics<sup>6</sup>.

## REFERENCES

- Álvarez, M. & Maisterrena, Y. 1977, RMxAA, 2, 43
- Álvarez, M., Michel, R., Reyes-Coca, S., & Troncoso-Gaytán, R. 2007, RMxAA, 31, 113
- Ávila, R., Valdés-Hernández, O., Sánchez, L. J., et al. 2019, MNRAS, 490, 1397
- Bohigas, J. & Núñez, J. M. 2010, RMxAA, 46, 89
- Bohigas, J., Núñez, J. M., Guillén, P. F., et al. 2008, RMxAA, 44, 231
- Chapman, S. & Lindzen, R. S. 1970, Atmospheric tides. Thermal and gravitational (Dordrecht, Holland: Reidel)
- Colorado, E. & Hiriart, D. 2007, Comunicaciones Internas del Instituto de Astronomía - UNAM, CI-2007-04
- Douglas, M. W., Maddox, R. A., Howard, K., & Reyes, S. 1993, JCLI, 6, 1665
- Duane, W. J., Pepin, N. C., Losleben M. L., & Hardy, D. R. 2008, AAAR, 40, 323
- Echevarría, J., Tapia, M., Costero, R., et al. 1998, RMxAA, 34, 47
- Echevarría, J. 2003, RMxAA, 19, 41
- Haurwitz, B. & Cowley, A. D. 1973, PApGe, 102, 193
- Higgins, R. W., Yao, Y., & Wang, X. L. 1997, JCLI, 10, 2600
- Hiriart, D. 2003, RMxAA, 19, 90
- IPCC, 2018: Summary for Policymakers. In *Global Warming of 1.5° C. An IPCC Special Report on the impacts of global warming of 1.5° C above pre-industrial levels and related global greenhouse gas emission pathways, in the context of strengthening the global response to the threat of climate change, sustainable development, and efforts to eradicate poverty* [Masson-Delmotte, V., P. Zhai, H.-O. Pörtner, D. Roberts, J. Skea, P. R. Shukla, A. Pirani, W. Moufouma-Okia, C. Péan, R. Pidcock, S. Connors, J. B. R. Matthews, Y. Chen, X. Zhou, M.I. Gomis, E. Lonnoy, T. Maycock, M. Tignor, and T. Waterfield (eds.)]. In Press
- Le Blancq, F. 2011, Royal Meteorological Society, Vol. 66, N. 11, 306
- Mendoza, E. E. 1971, BOTT, 6, 95
- \_\_\_\_\_. 1973, Mercu, 2, 9
- Mendoza, E. E., Luna, J., & Gómez, T. 1972, BOTT, 6, 215
- Michel, R., Bohigas, J., Arroyo, E., & Zazueta, S. 2001, RMxAA, 37, 165
- Michel, R., Hiriart, D., & Chapela, A. 2003, RMxAA, 19, 99
- Otárola, A., Hiriart, D., & Pérez-León, J. E. 2009, RMxAA, 45, 151
- Otárola, A., Travouillon, T., Schöck, et al. 2010, PASP, 122, 470
- Plauchu-Frayn, I., Richer, M. G., Colorado, E., et al. 2017, PASP, 129, 5003
- Pugh, D. T. 1987, Tides, Surges and Mean Sea-Level (Swindon, UK: John Wiley & Sons) 472
- Sánchez, L. J., Cruz-González, I., Echevarría, J., et al. 2012, MNRAS, 426, 635
- Schöck, M., Els, S., Riddle, R., et al. 2009, PASP, 121, 384
- Schuster, W. J. & Parrao, L. 2001, RMxAA, 37, 187
- Siebert, M. 1961, AdGeo, 7, 105
- Skidmore, W., Els, S., Travouillon, T., et al. 2009, PASP, 121, 1151
- Stull, R. B. 1988, An Introduction to boundary layer meteorology (Dordrecht: Kluwer)
- Tapia, M. 1992, RMxAA, 24, 179
- \_\_\_\_\_. 2003, RMxAC, 19, 75
- Tapia, M., Hiriart, D., Richer, M., & Cruz-González, I. 2007, RMxAC, 31, 47
- Tovmassian, G., Hernandez, M. S., Ochoa, J. L., et al. 2016, PASP, 128, 5004
- Walker, M. F. 1971, PASP, 83, 401

- E. Colorado, I. Plauchu-Frayn, and M. G. Richer: Instituto de Astronomía, Universidad Nacional Autónoma de México, Apartado Postal 106, 22800 Ensenada, B. C., México. (colorado, ilse, richer@astro.unam.mx).
- C. Herrera-Vázquez: Centro de Investigación Científica y Educación Superior de Ensenada, Carr. Ensenada-Tijuana No. 3918, Zona Playitas, C. P. 22860, Ensenada, B. C., México (cherrera@cicese.edu.mx).

<sup>6</sup><http://www.r-project.org/>.

## FOUR NEW $\gamma$ DORADUS VARIABLES IN ECLIPSING BINARIES: REVISED PULSATION PERIOD RELATIONS

O. Özdarcan and Ö. Çakirli

Ege University, Science Faculty, Astronomy and Space Science Dept., 35100 Bornova, İzmir, Turkey.

Received May 18 2020; accepted August 15 2020

### ABSTRACT

We present photometric light curve modelling of four Kepler eclipsing binaries KIC 2720354, KIC 10063044, KIC 11724091 and KIC 8565912. The modelling results show that KIC 10063044 is a semi-detached eclipsing binary, while the other systems are detached eclipsing binaries. Estimated physical parameters of these systems and residuals from the best-fitting light curve models strongly indicate  $\gamma$  Dor type pulsations on the primary components of the target systems. Evaluating the relations between pulsation period ( $P_{puls}$ ) and orbital period ( $P_{orb}$ ), the force exerted to per gram on the surface of the pulsating star ( $F/M_{puls}$ ) and the fractional radius of the pulsating star ( $r$ ), we find that linear relations on a logarithmic scale still exist, but with a smaller slope than reported in previous studies.

### RESUMEN

Presentamos modelos de la curva de luz de cuatro binarias eclipsantes de la misión Kepler, KIC 2720354, KIC 10063044, KIC 11724091 y KIC 8565912. Los modelos muestran que KIC 10063044 es una binaria eclipsante semi-separada, mientras que las otras son binarias separadas. Los parámetros físicos de estos sistemas y los resultados de los mejores modelos para las curvas de luz indican que las primarias presentan pulsaciones tipo  $\gamma$  Dor. Evaluamos las relaciones entre los períodos de pulsación ( $P_{puls}$ ) y los períodos orbitales ( $P_{orb}$ ), así como entre la fuerza ejercida por gramo en la superficie de la estrella pulsante ( $F/M_{puls}$ ) y el radio fraccional de la misma ( $r$ ). Encontramos que existen relaciones lineales en escala logarítmica, pero con pendientes menores que las reportadas en estudios previos.

*Key Words:* binaries: eclipsing — stars: individual: KIC 2720354, KIC 8565912, KIC 10063044, KIC 11724091 — stars: oscillations

### 1. INTRODUCTION

Very high precision space-born photometry provided by space telescopes such as *CoRoT* (Baglin et al. 2006), *Kepler* (Koch et al. 2010; Borucki et al. 2010) and *TESS* (Ricker et al. 2015) not only allows us to discover exoplanets via transit light curves but also enables us to detect further light variations with sub-millimag amplitude. Detecting very low amplitude light variations in stars expands our understanding of stellar variability and evolution, and suggests new questions. In the case of pulsating stars, very precise photometry enables us to detect numerous pulsation frequencies possessing different modes, which is very useful for extracting information on the inner rotation profile of the star (see, e.g., Van Reeth et al. 2016), and provides constraints on basic stel-

lar parameters, such as mass, radius and effective temperature (see, e.g., Van Reeth et al. 2015; Guo & Li 2019). In addition, relations between pulsational and orbital properties of binary stars with a pulsating component are also interesting to study pulsational characteristics in binary systems. Such relations were found for binary Delta Scuti ( $\delta$  Sct) variables (Soydugan et al. 2006). Later, Zhang et al. (2013) confirmed the relation between pulsational and orbital period via extending the stellar sample. They also provided a theoretical derivation of the relation and concluded that the relation was a function of the pulsation constant  $Q$ .

Regarding Gamma Doradus ( $\gamma$  Dor) variables, which are low amplitude pulsators ( $\lesssim 0^m 1$ ) with pulsation periods between 0.4 and 3 days (Kaye et al.

1999), ground-based observations are insufficient to study their pulsational properties since these observations have gaps due to day-night cycles and suffer from low precision compared to space-based observations. Furthermore, a very high resolution frequency amplitude spectrum is needed to extract precise information on the inner rotation and structure of the star, which could be achieved by analysing continuous photometric data covering a time base of at least one year. These requirements make the *Kepler* space telescope an excellent instrument to study the pulsational properties of the  $\gamma$  Dor variables, with its very high precision and continuous data spanning over 4 years. Using *Kepler* data, more than 100 eclipsing binaries with a  $\gamma$  Dor component were discovered so far (Gaulme & Guzik 2019). Ibanoglu et al. (2018) compiled a comprehensive catalogue of  $\gamma$  Dor variables and showed that the pulsation periods of binary  $\gamma$  Dor variables are proportional to their orbital periods and pulsation constants ( $Q$ ), but inversely proportional to the fractional radii of the pulsating components. They also noted that the linear correlation is not high due to the limited sample and the scattered pattern of the data. The theoretical basis of the observed relations had already been established for p-modes previously (Çakirli & Ibanoglu 2016). However, there seems to be a weaker relation for the near-center g-modes (Hoyman et al. 2020) compared to the relations found for binary  $\delta$  Sct variables (Soydugan et al. 2006), which pulsate with non-radial p-modes.

In this study, we present photometric light curve modelling of four Kepler eclipsing binaries KIC 2720354, KIC 10063044, KIC 11724091, and KIC 8565912. In addition, we carry out a frequency analysis of the residuals from the best-fitting light curve model and re-evaluate the pulsation period relations with the four new eclipsing binaries presented in this study. We briefly summarize the *Kepler* data in the next section. We give all details on light curve modelling in Section 3 and estimate the absolute parameters of the systems in Section 4. An analysis of the residuals from the best-fitting light curve model is given in Section 5. We present revised pulsation period relations in Section 6 and summarize our findings in the last section.

## 2. DATA

We use very high precision photometric data with 29.4 minutes of exposure time (long cadence), provided by the *Kepler* space telescope. The CCD camera of the telescope is capable of collecting photons between 4100 Å and 9100 Å, which greatly in-

creases the precision. Prša et al. (2011) and Slawson et al. (2011) investigated the *Kepler* data and compiled the *Kepler* eclipsing binary catalogue<sup>1</sup>. This catalogue contains de-trended and normalized fluxes for each eclipsing binary. De-trending and normalization procedures are described in Slawson et al. (2011). We adopt detrended and normalized fluxes of the target stars from this catalogue. All-stars have four years of continuous photometry without any missing quarter, except KIC 8565912, which was observed only in quarter 16 and 17. In total, 65072, 62697, 63112 and 4635 data points were obtained for KIC 2720354, KIC 10063044, KIC 11724091 and KIC 8565912, respectively. The Mikulski Archive for Space Telescopes (MAST) database reports fairly weak (2–3%) contamination from the possible background light sources. No short cadence data (58.9 second exposure time) are available for any of the targets.

## 3. LIGHT CURVE MODELLING

Light curve modelling is based on pure Kepler photometry. First, we aim to find geometric, radiative and physical parameters via averaged light curves over the whole long cadence *Kepler* photometry. For each target, we prepare a representative phase-binned light curve with a phase step of 0.002. The phase-binned light curve makes the modelling process much less time consuming, since only 500 data points are used in the modelling, instead of thousands of them. After we find the best-fitting light curve model for each target, we obtain residuals from the model and investigate the light variation in the residuals.

We use the PyWD2015 software (Güzel & Özdarcan 2020) for light curve modelling, which has a very useful GUI and covers almost all features of the 2015 version of the Wilson-Devinney (WD) eclipsing binary modelling code (Wilson & Devinney 1971; Wilson & Van Hamme 2014). The modelling basically relies on accurate determination of two critical parameters, i.e., the effective temperature of the primary component ( $T_1$ ) and the mass ratio of the system ( $q = M_2/M_1$ ). For a given eclipsing binary, modelling the optical spectrum of the binary and spectroscopic orbit is the most reliable way to obtain the effective temperatures of the components and the mass ratio of the binary.

LAMOST spectroscopic observations of KIC 2720354, KIC 10063044 and KIC 11724091 had already been done, and effective temperatures

<sup>1</sup><http://keplerebs.villanova.edu/>.

are provided by Qian et al. (2018). Since there is no LAMOST spectrum for KIC 8565912, we adopt the effective temperature given in Berger et al. (2018) for this target. Thus, adopted effective temperatures for the primary components of KIC 2720354, KIC 10063044, KIC 11724091 and KIC 8565912 are 6600 K, 7100 K, 6800 K, and 7000 K, respectively. We estimate that average uncertainty of the effective temperatures is around  $\approx 200$  K.

Unfortunately, no published spectroscopic orbit solution is available for our targets. In this case, we only rely on pure photometric modelling. In order to determine the other critical parameter, i.e. the mass ratio, we apply a mass ratio search procedure. In this procedure, we choose different trial mass ratio values and find the best-fitting model. Then we adopt the mass ratio with the smallest rms residuals as the final mass ratio value. We choose trial mass ratios between 0 and 1 with steps of 0.025, where the step size is also adopted as the uncertainty of the mass ratio. In light-curve-only methods, estimating the uncertainty of the mass ratio can be done by setting it as adjustable parameter together with the other adjustable parameters. In this case, formal errors are reported by a differential correction routine, which is mostly optimistic and considerably underestimates the errors due to the correlation between adjustable parameters. More reliable estimates can be done by combining radial velocity measurements of both components and a light curve data with proper weighting. Since we do not have radial velocity measurements, we make an implicit assumption on the uncertainty of the mass ratio.

We apply this procedure by assuming detached and semi-detached configurations (MODE 2 and 5 in the WD code, respectively) for each target separately. Light curve modelling results indicate that KIC 10063044 is a semi-detached system, while the remaining targets are detached systems. We show the results of the mass ratio search in Figure 1.

During the whole light curve modelling process, we assume that all target stars possess convective outer envelopes; thus, we fix the values of the radiative parameters (gravity darkening  $g$ , albedo  $A$ ) to their typical values. Here, we note that the estimated effective temperatures of the primary components are in range between 6600 K and 7200 K. This temperature range corresponds to the boundary region between convective and radiative outer envelopes, so it is not easy to distinguish whether the primary components possess convective or radiative envelopes. For each system, trial light curve solutions assuming a convective outer envelope re-

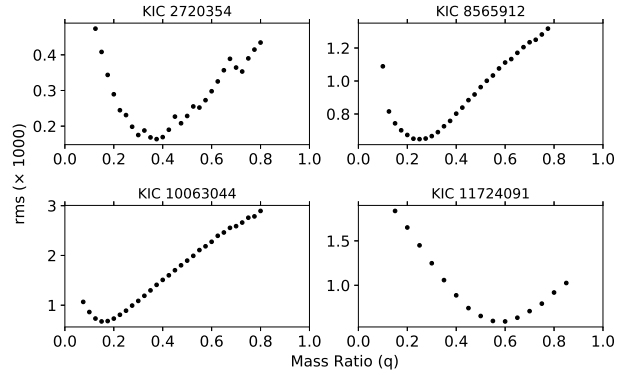


Fig. 1. Mass ratio search results for target stars.

sult in rms residuals very similar to the solutions with radiative outer envelopes. Thus we implicitly assume that the primary components of the target systems possess convective outer envelopes. We use the limb darkening coefficients of van Hamme (1993) by adopting a logarithmic law (Klinglesmith & Sobieski 1970). Inspecting the phase-folded light curve of each target, we find that all primary and secondary eclipses are located precisely at 0.0 and 0.5 orbital phases, respectively, which indicates circular orbits. Thus we assume synchronized rotation for the components and fix the rotation parameter of each component ( $F$ ) to unity. For detached systems, we adopt the phase shift, the orbital inclination ( $i$ ), the effective temperature of the secondary component ( $T_2$ ), the dimensionless potentials of the components ( $\Omega_1$  and  $\Omega_2$ ) and the luminosity of the primary ( $L_1$ ) as adjustable parameters. In the case of the semi-detached system KIC 10063044, the secondary component completely fills its Roche lobe. Hence we fix  $\Omega_2$  to the inner critical potential value as a result of the constraint defined in MODE 5 of the Wilson-Devinney code. Due to lobe filling, the secondary component has a distorted shape. Therefore, we further adopt gravity darkening and albedo values of the secondary component as additional adjustable parameters. Moreover, we adopt the linear limb darkening law for that component and set its limb darkening coefficient as an adjustable parameter. Trial light curve models indicate that the secondary component of KIC 10063044 is  $\approx 2700$  K cooler than the primary. Considering the distorted shape of the secondary and the large temperature difference, we adopt detailed reflection ( $MREF = 2$ ,  $NREF = 2$ ). Furthermore, phase-folded residuals from trial light curve models of KIC 10063044 exhibit a stable wave pattern. A semi-detached configuration suggests the possibility of ongoing mass transfer

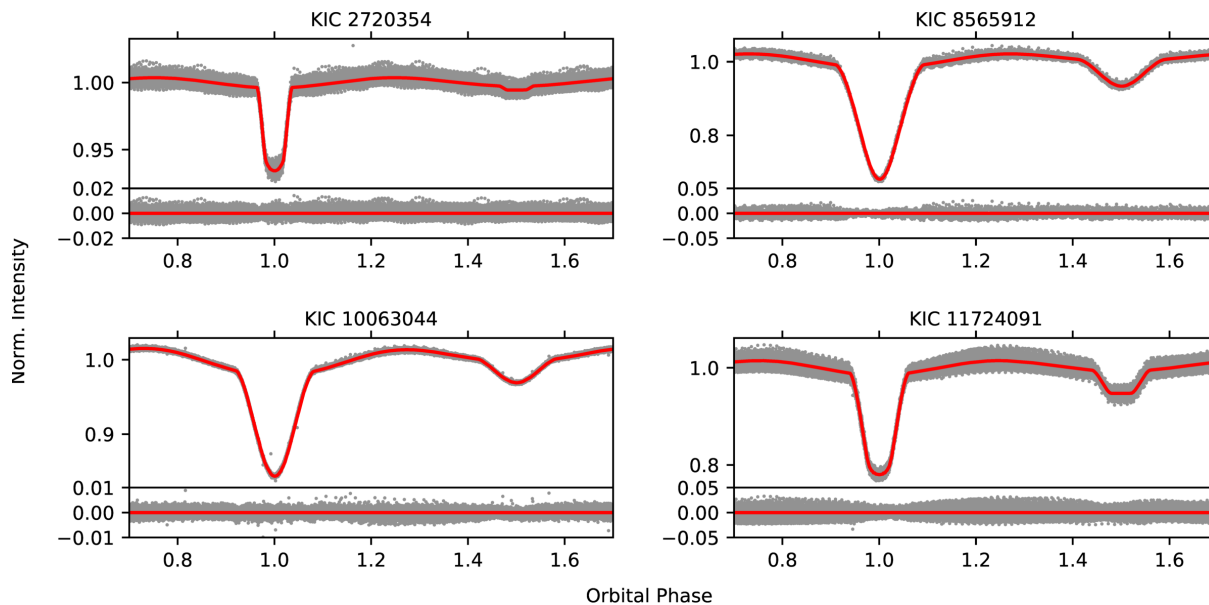


Fig. 2. Phase-folded *Kepler* light curves (gray filled circles) and best-fitting light curve models (red continuous lines) for each target. Residuals from the best-fitting model are shown under each light curve. The color figure can be viewed online.

from the secondary to the primary component, which may lead to a hot spot on the surface of the primary component. Therefore, we assume a hot spot with a temperature factor ( $TF$ ) of 1.02 on the surface of the primary component of KIC 10063044 and adjust its co-latitude ( $\theta$ ), longitude ( $\varphi$ ) and angular radius ( $r_{spot}$ ). We show phase-folded light curves and the best-fitting models in Figure 2 and tabulate light curve analysis results in Table 1. Our analyses reveal that the detached binaries KIC 2720354 and KIC 11724091 exhibit total eclipses at secondary minima.

#### 4. ABSOLUTE PARAMETERS

Although we do not have spectroscopic mass functions, we make a fair estimation for the masses of the primary components via the temperature-mass data given by Gray (2005) for main-sequence stars. For a given system, after we find the mass of the primary component, we calculate the mass of the secondary by using the adopted mass ratio. Then, the calculation of the semi-major axis of the system can be done via Kepler's third law by using the masses of the components and the orbital period. Once the semi-major axis is obtained, absolute radii of the components can be found by multiplying the fractional radius of each component by the semi-major axis, separately. The luminosity of each component is calculated via Stefan-Boltzmann's law by using values of

the effective temperature and radius. Here, we adopt the solar effective temperature as 5780 K. The logarithm of surface gravity of each component can be calculated with the mass and radius values of the corresponding component and Newton's gravitational constant. Regarding uncertainties, we first consider the assumed uncertainty of the effective temperature and determine lower and upper temperature limits. Then we find corresponding upper and lower limits for the mass of the primary component from Gray (2005). In the same way, we find upper and lower limits for the mass ratio. By using these limits, we calculate upper and lower limits for the mass of the secondary component. Applying a similar process for the remaining parameters we obtain the estimated uncertainties of the calculated parameters. We tabulate the estimated absolute parameters and their uncertainties in Table 2.

We plot the positions of the primary components on the  $\log T_{eff} - \log L/L_{\odot}$  plane in Figure 3, together with the confirmed  $\gamma$  Doradus variables. In the figure, the large filled circles show eclipsing binaries possessing a  $\gamma$  Doradus pulsator, i.e., VZ CVn (Ibanoğlu et al. 2007), CoRot 102918586 (Maceroni et al. 2013), KIC 11285625 (Debosscher et al. 2013), KIC 9851142 (Çakirli 2015), KIC 9851944 (Guo et al. 2016), V2653 Oph (Çakirli & Ibanoglu 2016), CoRot 100866999 (Chapellier & Mathias 2013), KIC 7385478 (Özdarcan & Dal 2017)

TABLE 1  
LIGHT CURVE MODELLING RESULTS OF TARGET STARS\*

Parameter	KIC 2720354	KIC 8565912	KIC 10063044	KIC 11724091
MODE	2	2	5	2
$T_0$	54956.21538	55000.33427	54965.59559	54953.85811
$P$	2.8213281	1.0121736	1.0096716	1.5590905
$q$	0.375(25)	0.250(25)	0.150(25)	0.600(25)
$T_1(K)$	6600(200)	7000(200)	7100(200)	6800(200)
$g_1, g_2$	0.32, 0.32	0.32, 0.32	0.32, 0.457(8)	0.32, 0.32
$A_1, A_2$	0.5, 0.5	0.5, 0.5	0.5, 0.385(2)	0.5, 0.5
$F_1 = F_2$	1	1	1	1
limb darkening law	log, log	log, log	log, linear	log, log
$x_1, x_2$	0.668, 0.752	0.654, 0.758	0.652, 0.184	0.661, 0.754
$y_1, y_2$	0.277, 0.322	0.289, 0.100	0.292, —	0.283, 0.113
$x_1bol, x_2bol$	—	—	0.639, 0.535	—
$y_1bol, y_2bol$	—	—	0.256, —	—
phase shift	0.00030(3)	0.00112(3)	0.00082(2)	0.00012(4)
$i$ (°)	84.36(2)	76.16(5)	68.873(8)	85.65(7)
$T_2(K)$	3639(200)	4742(200)	4476(200)	4850(200)
$\Omega_1$	5.423(5)	3.282(5)	3.077(1)	4.405(5)
$\Omega_2$	9.327(9)	2.438(2)	2.103	6.386(8)
$L_1/(L_1+L_2)$	0.99788(9)	0.91710(96)	0.93919(24)	0.96019(28)
$\langle r_1 \rangle$	0.1991(2)	0.3371(7)	0.3487(2)	0.2668(4)
$\langle r_2 \rangle$	0.0469(1)	0.2488(6)	0.2299	0.1160(2)
$\theta$ (°)	—	—	113(6)	—
$\varphi$ (°)	—	—	73(1)	—
$r_{spot}$ (°)	—	—	11(1)	—
$TF$	—	—	1.02	—
Model rms	0.00016	0.00065	0.00007	0.0006

\* $T_0$  and  $P$  denote reference ephemeris of the mid-primary eclipse in barycentric Julian days and orbital period in days, respectively. These values are from the *Kepler* eclipsing binary catalogue. Mean fractional radii of the components are shown by  $\langle r_{1,2} \rangle$ . Formal uncertainties are shown (in parentheses) for the last digits.

TABLE 2  
ESTIMATED ABSOLUTE PARAMETERS OF THE COMPONENTS\*

Target	Mass ( $M_{1,2}$ )	Radius ( $R_{1,2}$ )	$\log L_{1,2}/L_\odot$	$\log g_{1,2}$ (cgs)
KIC 2720354	1.43(8), 0.54(7)	2.10(5), 0.49(1)	0.87(7), -1.40(10)	3.951(3), 4.779(32)
KIC 8565912	1.59(8), 0.40(6)	1.80(4), 1.33(3)	0.84(6), -0.09(8)	4.130(1), 3.789(45)
KIC 10063044	1.63(8), 0.25(5)	1.82(4), 1.20(3)	0.88(6), -0.28(9)	4.130(1), 3.661(74)
KIC 11724091	1.51(8), 0.91(9)	2.03(5), 0.88(2)	0.90(6), -0.41(8)	4.004(3), 4.505(21)

\*Together with uncertainties (in parentheses) for the last digits.

and KIC 2557430 (Hoyman et al. 2020). The positions of the primary components suggest that all these stars are possible  $\gamma$  Doradus variable candidates. We test this possibility in the next section, by analysing time-based residuals from the best-fitting light curve model of each target.

## 5. VARIATIONS IN LIGHT CURVE RESIDUALS

For each target, we adopt the following method in order to obtain precise residuals from the best-fitting light curve model. First, we divide long cadence data into subsets, where each subset covers only one

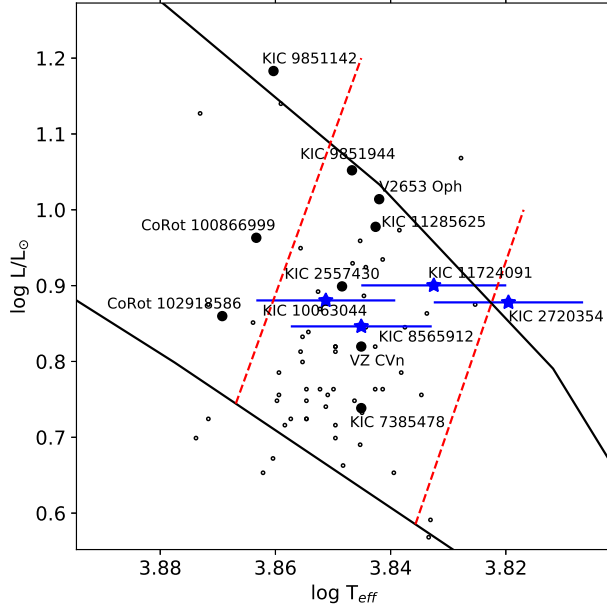


Fig. 3. Positions of the primary components on the  $\log T_{eff} - \log L/L_{\odot}$  plane (blue star symbols), together with confirmed  $\gamma$  Doradus variables. Small black open circles are  $\gamma$  Doradus stars taken from Henry et al. (2005), while large black filled circles are  $\gamma$  Doradus pulsators in eclipsing binaries from various studies (see the text), which are labelled in the plot. Note that the estimated luminosity uncertainties for the primary components are smaller than the star symbols, thus cannot be noticed in the current figure resolution. Red dashed lines show the cool and hot boundaries of the  $\gamma$  Doradus instability strip taken from Warner et al. (2003). The color figure can be viewed online.

orbital cycle. Then we adopt the best-fitting light curve model parameters and run the differential correction routine of the WD code with time option. In this step, we only adjust the ephemeris time. After adjusting the ephemeris time, we obtain residuals with respect to the Julian Day. Repeating this procedure for all subsets, we obtain the residuals from the whole long cadence data. In Figure 4, we plot all residuals and a sample of residuals covering a time span of 20 days for each target, separately.

We observe clear light variations in the residuals. In order to extract frequency signals from the residuals, we apply a multi-frequency analysis by using SIGSPEC software (Reegen 2007). SIGSPEC calculates the significance spectrum for a given non-equally spaced time series data and evaluates the probability density function of discrete Fourier transform (DFT) peaks. Multi-frequency signals can be extracted iteratively from non-equally spaced time series data via a prewhitening procedure. In each

step of the iterative prewhitening, SIGSPEC calculates the frequency, amplitude, phase and significance level of the highest peak (signal) in DFT. Then, removing the signal from the time-series data (prewhitening), the process is repeated for the prewhitened time series data. This iterative process runs until the significance level is below a defined limit. In our case, we adopt the significance level limit of 5, approximately corresponding to a signal-to-noise ratio of 4 given by Breger et al. (1993). For each star, we scan the frequency region between 0 and the Nyquist frequency of 24.46 cycle-per-day (c/d). We show the resulting amplitude spectra in Figure 5.

Inspecting Figure 5, one can easily notice a dominant group of frequency peaks below 5 c/d. In the case of KIC 8565912 and KIC 10063044, relatively low amplitude frequency peaks above 5 c/d also exist. The iterative prewhitening procedure results in 2406, 221, 1089 and 2535 frequencies above a significance level limit of 5 for KIC 2720354, KIC 8565912, KIC 10063044 and KIC 11724091, respectively. We use the Rayleigh criterion to check whether these frequencies are genuine or combination frequencies. We find the resulting number of genuine frequencies as 5, 4, 4 and 3 for our targets, in the same order as above. Following the method proposed by Kallinger et al. (2008), we calculate uncertainties of frequency, amplitude and phase of each extracted frequency. We tabulate genuine frequencies in Table 3 and plot multi-frequency analysis fits in Figure 4.

We observe that, for each star, the most dominant frequency in the amplitude spectrum is different from the corresponding orbital frequency and its harmonics. Considering the positions of these stars in Figure 3 and the defined period range for  $\gamma$  Doradus variables (between 0.4 and 3 day; Kaye et al. 1999), we conclude that the primary components of our target systems are  $\gamma$  Doradus type pulsating stars.

## 6. PULSATION PERIOD RELATIONS

Using the orbital and pulsation periods of the target stars in this study, together with previously reported  $\gamma$  Dor variables in binary systems, we evaluate the relation between pulsation period ( $P_{puls}$ ) and orbital period ( $P_{orb}$ ), the force per gram exerted on the surface of the pulsating star ( $F/M_{puls}$ ) and the fractional radius of the pulsating star ( $r$ ).  $F/M_{puls}$ , which is given by

$$\frac{F}{M_{puls}} = \frac{GM_s}{(a - R_{puls})^2}, \quad (1)$$

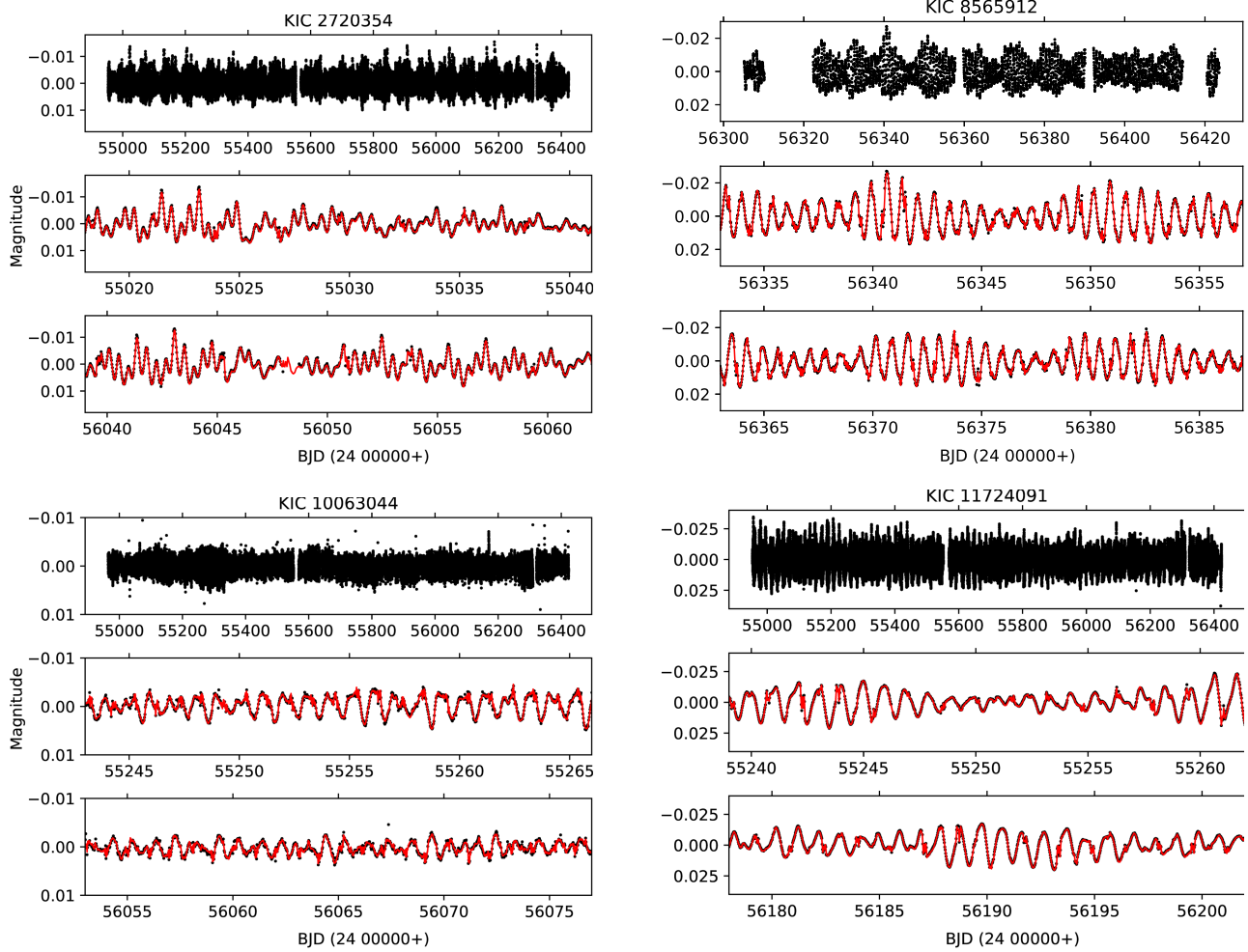


Fig. 4. All long cadence residuals from the best-fitting light curve models for each target (uppermost panels for each star) and different portions of residuals (lower panels). In the lower panels, the red continuous lines show the multi-frequency analysis fit of each star. The color figure can be viewed online.

where  $G$  is the Newton's gravitational constant,  $M_s$  is the mass of the secondary component,  $a$  is the semi-major axis of the system,  $M_{puls}$  and  $R_{puls}$  are the mass and the radius of the pulsating component, respectively (Çakirli & Ibanoglu 2016). In Figure 6, we show the pulsation period relations.

Comparing with the study of Ibanoglu et al. (2018), we see that the slope of the relations decreases as we add the  $\gamma$  Doradus variables found in this study. However, linear relations on the logarithmic scale still exist. The pulsation period increases with increasing orbital period, while an increase in the fractional radius or in the force per gram exerted the surface of the pulsating star decreases the pulsation period.

## 7. CONCLUSION

We analysed Kepler photometry of four eclipsing binaries, KIC 2720354, KIC 8565912, KIC 10063044 and KIC 11724091. Light curve modelling results, based on pure space photometry, show that KIC 2720354, KIC 8565912 and KIC 11724091 are detached eclipsing binaries, while KIC 10063044 is a semi-detached eclipsing binary. The semi-detached configuration suggests the possibility of mass transfer from the secondary (low mass) component to the primary (high mass). Phase-folded light curve residuals from the best-fitting light curve model for KIC 10063044 exhibit a stable wave pattern. This pattern indicates the existence of a cool or a hot spot on one of the components. Considering the mass transfer possibility, the primary component very likely possesses a warmer local region on its surface (compared to the surrounding photosphere),

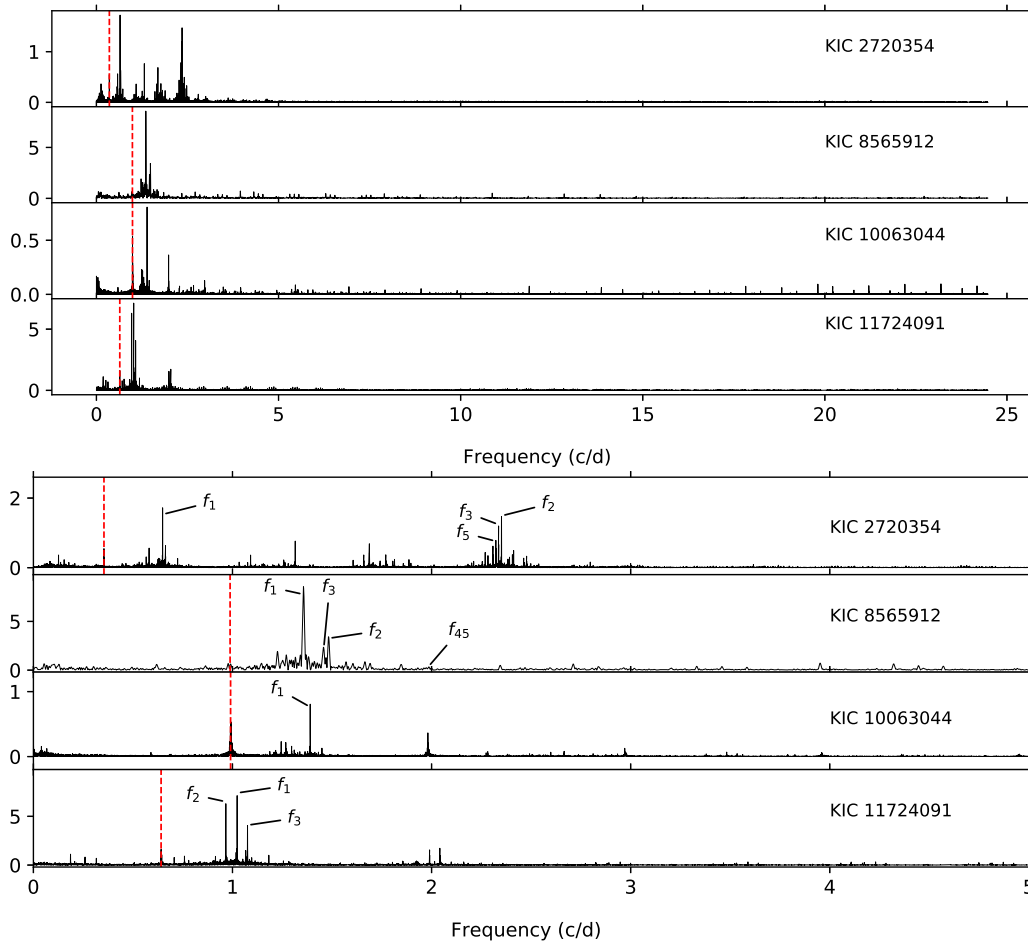


Fig. 5. *Upper panel:* Amplitude spectrum of all long cadence residuals in Figure 4. *Lower panel:* Zoomed view of amplitude spectrum between 0 and 5 c/d. The vertical red dashed line in each panel shows the orbital frequency of the corresponding system. The most dominant genuine frequencies of each star (except the orbital frequency) are marked in the plot. Note that the orbital frequencies of KIC 8565912 and KIC 10063044 are very close to each other. The color figure can be viewed online.

which could be modelled by a hot spot. This hot spot might probably be the result of a direct hit of the transferred mass on the surface of the primary component, without forming a circumstellar disk. Considering the mass ratio ( $q = 0.15$ ) of the system and the fractional radius of the primary component ( $r_1 = 0.3487$ ), we do not expect any disc formation around the primary component (Lubow & Shu 1975).

Analysing the residuals from the best-fitting light curve models, we find that multi-frequency signals exist in them. The application of multi-frequency analysis reveals a group of frequency peaks, mostly in the region between 0 and 5 c/d. For each binary, we also observe that the most dominant frequency found in the residuals is independent of the orbital frequency. The position of the primary com-

ponent of each binary in the HR diagram and the frequency value of the most dominant peak extracted in the frequency analysis clearly indicate that the primary components are  $\gamma$  Doradus-type pulsating variables. Multifrequency analysis of residuals results in thousands of frequencies above the significance limit of 5 for KIC 2720354, KIC 10063044 and KIC 11724091, while 221 frequencies were found for KIC 8565912. Here, we note that long cadence photometry of KIC 8565912 is only available for quarters 16 and 17 in the Kepler photometry, which corresponds to a time base of  $\approx 180$  days. Photometry of other targets is available for all 17 quarters ( $\approx 1400$  days). Thus, we believe that the restricted time base of the KIC 8565912 photometry is responsible for the lower number of extracted frequencies over the adopted significance level.

TABLE 3  
GENUINE FREQUENCIES FOUND BY  
FREQUENCY ANALYSIS OF TARGET STARS\*

KIC 2720354				
Frequency number	Frequency (c/d)	Amplitude (mmag)	Phase (radian)	rms (mmag)
$f_1$	0.648922(13)	1.53(3)	1.314(9)	2.753
$f_2$	2.351234(14)	1.49(3)	5.877(9)	2.470
$f_3$	2.336638(15)	1.24(3)	0.424(10)	2.240
.	.	.	.	.
$f_5$	2.322871(21)	0.76(2)	0.859(14)	1.987
.	.	.	.	.
$f_{10} = f_{orb}$	0.354463(25)	0.57(2)	4.536(17)	1.683
.	.	.	.	.
.	.	.	.	.
KIC 8565912				
$f_1$	1.35525(33)	7.78(30)	2.312(18)	7.458
$f_2$	1.48308(50)	3.27(20)	3.712(29)	4.367
$f_3$	1.45844(71)	1.96(17)	2.173(40)	3.702
.	.	.	.	.
.	.	.	.	.
$f_{45}$	1.98298(196)	0.34(8)	3.977(107)	1.693
.	.	.	.	.
.	.	.	.	.
.	.	.	.	.
KIC 10063044				
$f_1$	1.390445(14)	0.76(2)	0.141(9)	1.338
$f_2 \approx f_{orb}$	0.991355(19)	1.02(3)	0.673(13)	1.210
$f_3 \approx f_{orb}$	0.992617(18)	0.52(1)	4.429(12)	1.149
.	.	.	.	.
.	.	.	.	.
$f_{10}$	1.244700(34)	0.22(1)	5.655(23)	0.922
.	.	.	.	.
.	.	.	.	.
KIC 11724091				
$f_1$	1.023430(10)	8.60(12)	4.770(7)	8.561
$f_2$	0.966617(9)	7.98(11)	2.164(6)	6.918
$f_3$	1.075495(11)	4.09(6)	1.157(7)	5.296
.	.	.	.	.
.	.	.	.	.

\*Uncertainty of each parameter is given in parenthesis for the last digits.

The existence of pulsation period relations for  $\gamma$  Doradus variables in eclipsing binaries was reported before, along with a theoretical basis (Çakirli & Ibanoglu 2016; Ibanoglu et al. 2018). We revised the relations given by Ibanoglu et al. (2018) by adding four new  $\gamma$  Doradus variables found in our study.

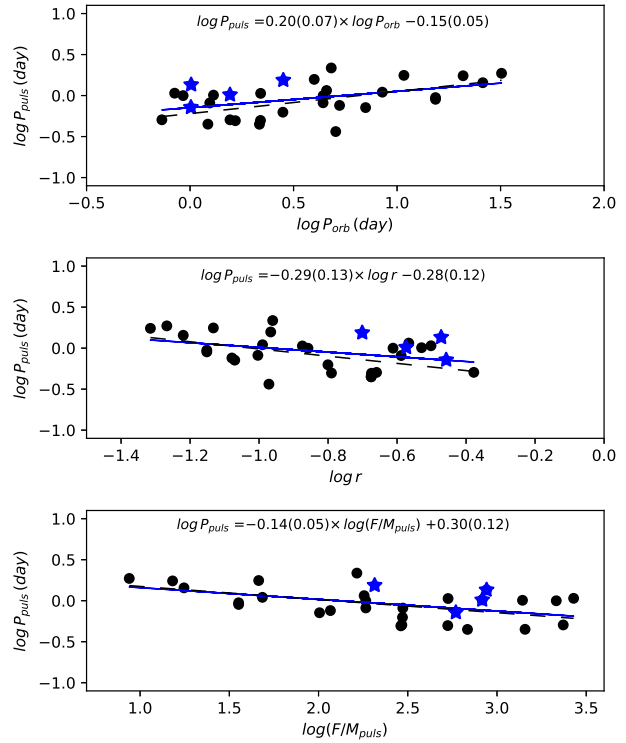


Fig. 6. Relations between pulsation period  $P_{puls}$  and  $P_{orb}$ ,  $r$ ,  $F/M_{puls}$  on logarithmic scale. Blue star symbols have the same meaning as in Figure 3. Filled black circles are taken from Hoyman et al. (2020), Ibanoglu et al. (2018) and references therein. Dashed lines show relations found by Ibanoglu et al. (2018) while continuous lines are relations updated in this study. Linear fit parameters are given in each window with uncertainties (in parentheses) for the last digits. The color figure can be viewed online.

Updated relations show weaker, but still considerable, correlations between pulsation period and orbital period, fractional radius of the pulsating component and the force per gram exerted on the surface of the pulsating star.

Further detailed spectroscopic studies of these systems are critical to obtain accurate stellar parameters of each member of these binaries, especially for the  $\gamma$  Dor primary components. This would enable the accurate study of pulsation period relations, as well as the modelling of the inner structure of the  $\gamma$  Dor primary components via asteroseismology (Li et al. 2020), which is strongly based on accurate stellar parameters.

We thank Dr. Can Akan for a careful reading of the manuscript and language improvements of the text. We also thank an anonymous referee for a dis-

cussion of the period relations, which improved the quality of the paper. This paper includes data collected by the Kepler mission. Funding for the Kepler mission is provided by the NASA Science Mission Directorate. This research has made use of NASA's Astrophysics Data System and the SIMBAD database, operated at CDS, Strasbourg, France.

## REFERENCES

- Baglin, A., Auvergne, M., Boisnard, L., et al. in 36th COSPAR Scientific Assembly, 36, 3749
- Berger, T. A., Huber, D., Gaidos, E., & van Saders, J. L. 2018, *ApJ*, 866, 99
- Borucki, W. J., Koch, D., Basri, G., et al. 2010, *Sci*, 327, 977
- Breger, M., Stich, J., Garrido, R., et al. 1993, *A&A*, 271, 482
- Çakirli, Ö. 2015, *NewA*, 38, 55
- Çakirli, Ö. & İbanoglu, C. 2016, *NewA*, 45, 36
- Chapellier, E. & Mathias, P. 2013, *A&A*, 556, 87
- Debosscher, J., Aerts, C., Tkachenko, A., et al. 2013, *A&A*, 556, 56
- Gaulme, P. & Guzik, J. A. 2019, *A&A*, 630, 106
- Gray, D. F. 2005, *The Observation and Analysis of Stellar Photospheres* (Cambridge, UK: CUP)
- Guo, Z., Gies, D. R., Matson, R. A., & García Hernández, A. 2016, *ApJ*, 826, 69
- Guo, Z. & Li, G. 2019, *ApJ*, 882, 5
- Güzel, O. & Özdarcan, O. 2020, *CoSka*, 50, 535
- Henry, G. W., Fekel, F. C., & Henry, S. M. 2005, *AJ*, 129, 2815
- Hoyman, B., Çakirli, Ö., & Özdarcan, O. 2020, *MNRAS*, 491, 5980
- İbanoglu, C., Çakirli, Ö., & Sipahi, E. 2018, *NewA*, 62, 701
- İbanoglu, C., Taş, G., Sipahi, E., & Evren, S. 2007, *MNRAS*, 376, 573
- Kallinger, T., Reegen, P., & Weiss, W. W. 2008, *A&A*, 481, 571
- Kaye, A. B., Handler, G., Krisciunas, K., Poretti, E., & Zerbi, F. M. 1999, *PASP*, 111, 840
- Klinglesmith, D. A. & Sobieski, S. 1970, *AJ*, 75, 175
- Koch, D. G., Borucki, W. J., Basri, G., et al. 2010, *ApJ*, 713, 79
- Li, G., Van Reeth, T., Bedding, T. R., et al. 2020, *MNRAS*, 491, 3586
- Lubow, S. H. & Shu, F. H. 1975, *ApJ*, 198, 383
- Maceroni, C., Montalbán, J., Gandolfi, D., Pavlovski, K., & Rainer, M. 2013, *A&A*, 552, 60
- Özdarcan, O. & Dal, H. A. 2017, *PASA*, 34, 17
- Prša, A., Batalha, N., Slawson, R. W., et al. 2011, *AJ*, 141, 83
- Qian, S. B., Zhang, J., He, J. J., et al. 2018, *ApJS*, 235, 5
- Reegen, P. 2007, *A&A*, 467, 1353
- Ricker, G. R., Winn, J. N., Vanderspek, R., et al. 2015, *JATIS*, 1, 014003
- Slawson, R. W., Prša, A., Welsh, W. F., et al. 2011, *AJ*, 142, 160
- Soydugan, E., İbanoglu, C., Soydugan, F., Akan, M. C., & Demircan, O. 2006, *MNRAS*, 366, 1289
- van Hamme, W. 1993, *AJ*, 106, 2096
- Van Reeth, T., Tkachenko, A., & Aerts, C. 2016, *A&A*, 593, 120
- Van Reeth, T., Tkachenko, A., Aerts, C., et al. 2015, *A&A*, 574, 17
- Warner, P. B., Kaye, A. B., & Guzik, J. A. 2003, *ApJ*, 593, 1049
- Wilson, R. E. & Devinney, E. J. 1971, *ApJ*, 166, 605
- Wilson, R. E. & Van Hamme, W. 2014, *ApJ*, 780, 151
- Zhang, X. B., Luo, C. Q., & Fu, J. N. 2013, *ApJ*, 777, 77

Ö. Çakirli and O. Özdarcan: Ege University, Science Faculty, Department of Astronomy and Space Sciences, 35100 Bornova, İzmir, Turkey (omur.cakirli, orkun.ozdarcan@ege.edu.tr).

## AUTHOR INDEX

- Abdel-Sabour, M. A.** Spectral Behavior of the Symbiotic Nova HM Sge in the Ultraviolet. *M. R. Sanad & M. A. Abdel-Sabour*, 63
- Abdel-Sabour, Mohamed** Analysis of a Short Periodic Pulsator: SX Phoenicis Star XX Cyg. *Mohamed Abdel-Sabour, Ahmed Shokry, & Ahmed Ibrahim*, 287
- Abdelaziz, A. E.** An Astrometric and Photometric Study of the Intermediate-Age Open Cluster NGC 2158 and its Eclipsing Binary [NBN2015]78. *A. E. Abdelaziz, Y. H. M. Hendy, A. Shokry, S. M. Saad, F. Y. Kamal, & K. A. Edris*, 245
- Acerbi, F.** First Photometric Investigation of Two Eclipsing Binary Systems CRTS J213033.6+213159 and 1SWASP J212454.61+203030.8. *M. Martignoni, C. Barani, F. Acerbi, & R. Michel*, 225
- Aceves, H.** A New Non-Eclipsing CV SDSSJ 122405.58+184102.7 – A Probable Member to the SW Sextantis Type Stars. *A. Avilés, I. Arias, C. E. Chávez, J. E. Pérez, F. J. Tamayo, E. G. Pérez-Tijerina, & H. Aceves*, 11
- Aceves, H.** Revisiting FS Aurigae and its Triple Cataclysmic Variable System Hypothesis. *C. E. Chavez, A. Aviles, N. Georgakarakos, C. Ramos, H. Aceves, G. Tovmassian, & S. Zharikov*, 19
- Aljbaae, S.** Dynamics Around an Asteroid Modeled as a Mass Tripole. *L. B. T. dos Santos, L. Marchi, P. A. Sousa-Silva, D. M. Sanchez, S. Aljbaae, & A. F. B. A. Prado*, 269
- Alton, K. B.** CCD Photometry and Evolutionary Status of the Pulsating Variable CSS J051053.0+071722. *K. B. Alton*, 129
- Arellano Ferro, Armando** Obituary – Eugenio E. Mendoza Villareal. *Armando Arellano Ferro*, 175
- Arias, I.** A New Non-Eclipsing CV SDSSJ 122405.58+184102.7 – A Probable Member to the SW Sextantis Type Stars. *A. Avilés, I. Arias, C. E. Chávez, J. E. Pérez, F. J. Tamayo, E. G. Pérez-Tijerina, & H. Aceves*, 11
- Avilés, A.** A New Non-Eclipsing CV SDSSJ 122405.58+184102.7 – A Probable Member to the SW Sextantis Type Stars. *A. Avilés, I. Arias, C. E. Chávez, J. E. Pérez, F. J. Tamayo, E. G. Pérez-Tijerina, & H. Aceves*, 11
- Aviles, A.** Revisiting FS Aurigae and its Triple Cataclysmic Variable System Hypothesis. *C. E. Chavez, A. Aviles, N. Georgakarakos, C. Ramos, H. Aceves, G. Tovmassian, & S. Zharikov*, 19
- Barani, C.** First Photometric Investigation of Two Eclipsing Binary Systems CRTS J213033.6+213159 and 1SWASP J212454.61+203030.8. *M. Martignoni, C. Barani, F. Acerbi, & R. Michel*, 225
- Biernacka, M.** The Influence of the Mass Distribution of Stellar Objects on Their Gravitational Fields. *V. A. Stephanovich, W. Godłowski, M. Biernacka, & B. Mrzygłód*, 201
- Bohigas, J.** On the Evolution of Angular Momentum, Magnetic Activity and Mass Loss Rate of Late Type Main Sequence Stars. *J. Bohigas*, 139
- Çakirli, Ö.** Four New  $\gamma$  Doradus Variables in Eclipsing Binaries: Revised Pulsation Period Relations. *O. Özdarcan & Ö. Çakirli*, 321
- Carigi, L.** The ADF and the  $t^2$  formalism in H II regions based on the upper mass limit of the IMF for the MW. *Carigi, L., Peimbert, A., Peimbert, M. & Delgado-Inglada, G.*, 235
- Castañeda, H. O.** Star Formation Rate in Late-Type Galaxies: I- The  $H_\alpha$  and FUV Integrated Values. *M. A. Magaña-Serrano, A. M. Hidalgo-Gómez, I. Vega-Acevedo, & H. O. Castañeda*, 39
- Chan, R. S.** The Properties and Stability of Self-Gravitating, Polytropic Spheres with  $\gamma = 1$  to 1.4 Specific Heat Ratios. *A. C. Raga, J. A. Osorio-Caballero, R. S. Chan, A. Esquivel, A. Rodríguez-González, V. Lora, & J. C. Rodríguez Ramírez*, 55
- Chávez, C. E.** A New Non-Eclipsing CV SDSSJ 122405.58+184102.7 – A Probable Member to the SW Sextantis Type Stars. *A. Avilés, I. Arias, C. E. Chávez, J. E. Pérez, F. J. Tamayo, E. G. Pérez-Tijerina, & H. Aceves*, 11
- Chavez, C. E.** Revisiting FS Aurigae and its Triple Cataclysmic Variable System Hypothesis. *C. E. Chavez, A. Aviles, N. Georgakarakos, C. Ramos, H. Aceves, G. Tovmassian, & S. Zharikov*, 19
- Colorado, Enrique** Thirteen Years of Weather Statistics at San Pedro Martir Observatory. *I. Plauchu-Frayn, E. Colorado, M. G. Richer, & C. Herrera-Vázquez*, 295
- Dal, H. A.**  $\gamma$  Dor: A Pulsating Component of KIC 8043961 in a Stellar Triple System. *C. Kamil, H. A. Dal, O. Özdarcan, & E. Yoldaş*, 179
- Delgado-Inglada, G.** The ADF and the  $t^2$  formalism in H II regions based on the upper mass limit of the IMF for the MW. *Carigi, L., Peimbert, A., Peimbert, M. & Delgado-Inglada, G.*, 235

- Deng, X. F.** The Environmental Dependence of the Age of Active Galaxies and the Dependence of the Clustering Properties of Active Galaxies on Age. *X.-F. Deng & X.-Q. Wen*, 87
- dos Santos, L. B. T.** Dynamics Around an Asteroid Modeled as a Mass Tripole. *L. B. T. dos Santos, L. Marchi, P. A. Sousa-Silva, D. M. Sanchez, S. Aljbaae, & A. F. B. A. Prado*, 269
- Drózdź, M.** A Search for Pulsation in Twenty-One White Dwarfs. *E. Paunzen, G. Handler, J. Janík, Z. Zemanová, M. Rode-Paunzen, M. S. O'Brien, T. K. Watson, & M. Drózdź*, 193
- Edris, K. A.** An Astrometric and Photometric Study of the Intermediate-Age Open Cluster NGC 2158 and its Eclipsing Binary [NBN2015]78. *A. E. Abdelaziz, Y. H. M. Hendy, A. Shokry, S. M. Saad, F. Y. Kamal, & K. A. Edris*, 245
- Esquivel, A.** The Properties and Stability of Self-Gravitating, Polytopic Spheres with  $\gamma = 1$  to 1.4 Specific Heat Ratios. *A. C. Raga, J. A. Osorio-Caballero, R. S. Chan, A. Esquivel, A. Rodríguez-González, V. Lora, & J. C. Rodríguez Ramírez*, 55
- García, L. A.** Can UVB Variations Reconcile Simulated Quasar Absorption Lines at High Redshift?. *L. A. García & E. V. Ryan-Weber*, 97
- García-Varela, A.** Infrared Transitions of Diatomic Molecules and the Telluric Lines. *D. Lozano-Gómez, A. García-Varela, & B. Sabogal*, 217
- Georgakarakos, N.** Revisiting FS Aurigae and its Triple Cataclysmic Variable System Hypothesis. *C. E. Chavez, A. Aviles, N. Georgakarakos, C. Ramos, H. Aceves, G. Toomassian, & S. Zharikov*, 19
- Godłowski, W.** The Influence of the Mass Distribution of Stellar Objects on Their Gravitational Fields. *V. A. Stephanovich, W. Godłowski, M. Biernacka, & B. Mrzygłód*, 201
- Handler, G.** A Search for Pulsation in Twenty-One White Dwarfs. *E. Paunzen, G. Handler, J. Janík, Z. Zemanová, M. Rode-Paunzen, M. S. O'Brien, T. K. Watson, & M. Drózdź*, 193
- Hendy, Y. H. M.** An Astrometric and Photometric Study of the Intermediate-Age Open Cluster NGC 2158 and its Eclipsing Binary [NBN2015]78. *A. E. Abdelaziz, Y. H. M. Hendy, A. Shokry, S. M. Saad, F. Y. Kamal, & K. A. Edris*, 245
- Herrera-Vázquez, Carlos** Thirteen Years of Weather Statistics at San Pedro Martir Observatory. *I. Plauchu-Frayn, E. Colorado, M. G. Richer, & C. Herrera-Vázquez*, 295
- Hidalgo-Gómez, A. M.** Star Formation Rate in Late-Type Galaxies: I- The  $H_\alpha$  and FUV Integrated Values. *M. A. Magaña-Serrano, A. M. Hidalgo-Gómez, I. Vega-Acevedo, & H. O. Castañeda*, 39
- Huepa, H.** Photometric Study of Three Short Period Variable Stars. *J. H. Peña, S. B. Juárez, A. A. Soni, H. Huepa, A. Rentería, & A. L. Zuñiga*, 259
- Ibrahim, Ahmed** Analysis of a Short Periodic Pulsator: SX Phoenicis Star XX Cyg. *Mohamed Abdel-Sabour, Ahmed Shokry, & Ahmed Ibrahim*, 287
- Ignace, R.** Erratum: Asymmetric Shapes of Radio Recombination Lines from Ionized Stellar Winds. (RMxAA, 2019, 55, 31). *R. Ignace*, 173
- Janík, J.** A Search for Pulsation in Twenty-One White Dwarfs. *E. Paunzen, G. Handler, J. Janík, Z. Zemanová, M. Rode-Paunzen, M. S. O'Brien, T. K. Watson, & M. Drózdź*, 193
- Juárez, S. B.** Photometric Study of Three Short Period Variable Stars. *J. H. Peña, S. B. Juárez, A. A. Soni, H. Huepa, A. Rentería, & A. L. Zuñiga*, 259
- Kamal, F. Y.** An Astrometric and Photometric Study of the Intermediate-Age Open Cluster NGC 2158 and its Eclipsing Binary [NBN2015]78. *A. E. Abdelaziz, Y. H. M. Hendy, A. Shokry, S. M. Saad, F. Y. Kamal, & K. A. Edris*, 245
- Kamil, C.**  $\gamma$  Dor: A Pulsating Component of KIC 8043961 in a Stellar Triple System. *C. Kamil, H. A. Dal, O. Özdarcan, & E. Yoldaş*, 179
- Lora, V.** The Jet/Counterjet Symmetry of the HH 212 Outflow. *A. Noriega-Crespo, A. C. Raga, V. Lora, & J. C. Rodríguez-Ramírez*, 29
- Lora, V.** The Properties and Stability of Self-Gravitating, Polytopic Spheres with  $\gamma = 1$  to 1.4 Specific Heat Ratios. *A. C. Raga, J. A. Osorio-Caballero, R. S. Chan, A. Esquivel, A. Rodríguez-González, V. Lora, & J. C. Rodríguez Ramírez*, 55
- Lozano-Gómez, D.** Infrared Transitions of Diatomic Molecules and the Telluric Lines. *D. Lozano-Gómez, A. García-Varela, & B. Sabogal*, 217
- Magaña-Serrano, M. A.** Star Formation Rate in Late-Type Galaxies: I- The  $H_\alpha$  and FUV Integrated Values. *M. A. Magaña-Serrano, A. M. Hidalgo-Gómez, I. Vega-Acevedo, & H. O. Castañeda*, 39
- Marchi, L.** Dynamics Around an Asteroid Modeled as a Mass Tripole. *L. B. T. dos Santos, L. Marchi, P. A. Sousa-Silva, D. M. Sanchez, S. Aljbaae, & A. F. B. A. Prado*, 269
- Martignoni, M.** First Photometric Investigation of Two Eclipsing Binary Systems CRTS J213033.6+213159 and 1SWASP J212454.61+203030.8. *M. Martignoni, C. Barani, F. Acerbi, & R. Michel*, 225
- Michel, R.** First Photometric Investigation of Two Eclipsing Binary Systems CRTS J213033.6+213159 and 1SWASP J212454.61+203030.8. *M. Martignoni, C. Barani, F. Acerbi, & R. Michel*, 225

- Mrzygłód, B.** The Influence of the Mass Distribution of Stellar Objects on Their Gravitational Fields. *V. A. Stephanovich, W. Godłowski, M. Biernacka, & B. Mrzygłód*, 201
- Noriega-Crespo, A.** The Jet/Counterjet Symmetry of the HH 212 Outflow. *A. Noriega-Crespo, A. C. Raga, V. Lora, & J. C. Rodríguez-Ramírez*, 29
- O'Brien, M. S.** A Search for Pulsation in Twenty-One White Dwarfs. *E. Paunzen, G. Handler, J. Janík, Z. Zemanová, M. Rode-Paunzen, M. S. O'Brien, T. K. Watson, & M. Drózdź*, 193
- Oliveira, T. C.** Search for Stable Orbits around the Binary Asteroid Systems 1999 KW4 and Didymos. *T. C. Oliveira & A. F. B. A. Prado*, 113
- Osorio-Caballero, J. A.** The Properties and Stability of Self-Gravitating, Polytropic Spheres with  $\gamma = 1$  to 1.4 Specific Heat Ratios. *A. C. Raga, J. A. Osorio-Caballero, R. S. Chan, A. Esquivel, A. Rodríguez-González, V. Lora, & J. C. Rodríguez Ramírez*, 55
- Özdarcan, O.** Four New  $\gamma$  Doradus Variables in Eclipsing Binaries: Revised Pulsation Period Relations. *O. Özdarcan & Ö. Çakırlı*, 321
- Özdarcan, O.**  $\gamma$  Dor: A Pulsating Component of KIC 8043961 in a Stellar Triple System. *C. Kamil, H. A. Dal, O. Özdarcan, & E. Yoldaş*, 179
- Pasquato, M.** Analytical Solutions for the Dynamical Clock A+ Indicator in a Toy Model of Pure Dynamical Friction. *M. Pasquato*, 3
- Pasquato, M.** Further Properties of the Dynamical Clock A+ Indicator in a Toy Model of Pure Dynamical Friction. *M. Pasquato*, 7
- Paunzen, E.** A Search for Pulsation in Twenty-One White Dwarfs. *E. Paunzen, G. Handler, J. Janík, Z. Zemanová, M. Rode-Paunzen, M. S. O'Brien, T. K. Watson, & M. Drózdź*, 193
- Peimbert, A.** The ADF and the  $t^2$  formalism in H II regions based on the upper mass limit of the IMF for the MW. *Carigi, L., Peimbert, A., Peimbert, M. & Delgado-Inglada, G.*, 235
- Peimbert, M.** The ADF and the  $t^2$  formalism in H II regions based on the upper mass limit of the IMF for the MW. *Carigi, L., Peimbert, A., Peimbert, M. & Delgado-Inglada, G.*, 235
- Peña, J. H.** Photometric Study of Three Short Period Variable Stars. *J. H. Peña, S. B. Juárez, A. A. Soni, H. Huepa, A. Rentería, & A. L. Zuñiga*, 259
- Pérez, J. E.** A New Non-Eclipsing CV SDSSJ 122405.58+184102.7 – A Probable Member to the SW Sextantis Type Stars. *A. Avilés, I. Arias, C. E. Chávez, J. E. Pérez, F. J. Tamayo, E. G. Pérez-Tijerina, & H. Aceves*, 11
- Pérez-Tijerina, E. G.** A New Non-Eclipsing CV SDSSJ 122405.58+184102.7 – A Probable Member to the SW Sextantis Type Stars. *A. Avilés, I. Arias, C. E. Chávez, J. E. Pérez, F. J. Tamayo, E. G. Pérez-Tijerina, & H. Aceves*, 11
- Plauchu-Frayn, Ilse** Thirteen Years of Weather Statistics at San Pedro Martir Observatory. *I. Plauchu-Frayn, E. Colorado, M. G. Richer, & C. Herrera-Vázquez*, 295
- Prado, A. F. B. A.** Search for Stable Orbits around the Binary Asteroid Systems 1999 KW4 and Didymos. *T. C. Oliveira & A. F. B. A. Prado*, 113
- Prado, A. F. B. A.** Dynamics Around an Asteroid Modeled as a Mass Tripole. *L. B. T. dos Santos, L. Marchi, P. A. Sousa-Silva, D. M. Sanchez, S. Aljbaae, & A. F. B. A. Prado*, 269
- Raga, A. C.** The Jet/Counterjet Symmetry of the HH 212 Outflow. *A. Noriega-Crespo, A. C. Raga, V. Lora, & J. C. Rodríguez-Ramírez*, 29
- Raga, A. C.** The Properties and Stability of Self-Gravitating, Polytropic Spheres with  $\gamma = 1$  to 1.4 Specific Heat Ratios. *A. C. Raga, J. A. Osorio-Caballero, R. S. Chan, A. Esquivel, A. Rodríguez-González, V. Lora, & J. C. Rodríguez Ramírez*, 55
- Ramos, C.** Revisiting FS Aurigae and its Triple Cataclysmic Variable System Hypothesis. *C. E. Chavez, A. Aviles, N. Georgakarakos, C. Ramos, H. Aceves, G. Tovmassian, & S. Zharikov*, 19
- Rentería, A.** Photometric Study of Three Short Period Variable Stars. *J. H. Peña, S. B. Juárez, A. A. Soni, H. Huepa, A. Rentería, & A. L. Zuñiga*, 259
- Richer, Michael G.** Thirteen Years of Weather Statistics at San Pedro Martir Observatory. *I. Plauchu-Frayn, E. Colorado, M. G. Richer, & C. Herrera-Vázquez*, 295
- Rode-Paunzen, M.** A Search for Pulsation in Twenty-One White Dwarfs. *E. Paunzen, G. Handler, J. Janík, Z. Zemanová, M. Rode-Paunzen, M. S. O'Brien, T. K. Watson, & M. Drózdź*, 193
- Rodríguez-González, A.** The Properties and Stability of Self-Gravitating, Polytropic Spheres with  $\gamma = 1$  to 1.4 Specific Heat Ratios. *A. C. Raga, J. A. Osorio-Caballero, R. S. Chan, A. Esquivel, A. Rodríguez-González, V. Lora, & J. C. Rodríguez Ramírez*, 55
- Rodríguez-Ramírez, J. C.** The Jet/Counterjet Symmetry of the HH 212 Outflow. *A. Noriega-Crespo, A. C. Raga, V. Lora, & J. C. Rodríguez-Ramírez*, 29
- Rodríguez Ramírez, J. C.** The Properties and Stability of Self-Gravitating, Polytropic Spheres with  $\gamma = 1$  to 1.4 Specific Heat Ratios. *A. C. Raga, J. A. Osorio-Caballero, R. S. Chan, A. Esquivel, A. Rodríguez-González, V. Lora, & J. C. Rodríguez Ramírez*, 55

- Rosado, M.**  $H\alpha$  Kinematics of the Isolated Interacting Galaxy Pair KPG 486 (NGC 6090). *M. M. Sardaneta, M. Rosado, & M. Sánchez-Cruces*, 71
- Ryan-Weber, E. V.** Can UVB Variations Reconcile Simulated Quasar Absorption Lines at High Redshift?. *L. A. García & E. V. Ryan-Weber*, 97
- Saad, S. M.** An Astrometric and Photometric Study of the Intermediate-Age Open Cluster NGC 2158 and its Eclipsing Binary [NBN2015]78. *A. E. Abdelaziz, Y. H. M. Hendy, A. Shokry, S. M. Saad, F. Y. Kamal, & K. A. Edris*, 245
- Sabogal, B.** Infrared Transitions of Diatomic Molecules and the Telluric Lines. *D. Lozano-Gómez, A. García-Varela, & B. Sabogal*, 217
- Sanad, M. R.** Spectral Behavior of the Symbiotic Nova HM Sge in the Ultraviolet. *M. R. Sanad & M. A. Abdel-Sabour*, 63
- Sanchez, D. M.** Dynamics Around an Asteroid Modeled as a Mass Tripole. *L. B. T. dos Santos, L. Marchi, P. A. Sousa-Silva, D. M. Sanchez, S. Aljbae, & A. F. B. A. Prado*, 269
- Sánchez-Cruces, M.**  $H\alpha$  Kinematics of the Isolated Interacting Galaxy Pair KPG 486 (NGC 6090). *M. M. Sardaneta, M. Rosado, & M. Sánchez-Cruces*, 71
- Sardaneta, M. M.**  $H\alpha$  Kinematics of the Isolated Interacting Galaxy Pair KPG 486 (NGC 6090). *M. M. Sardaneta, M. Rosado, & M. Sánchez-Cruces*, 71
- Shokry, A.** An Astrometric and Photometric Study of the Intermediate-Age Open Cluster NGC 2158 and its Eclipsing Binary [NBN2015]78. *A. E. Abdelaziz, Y. H. M. Hendy, A. Shokry, S. M. Saad, F. Y. Kamal, & K. A. Edris*, 245
- Shokry, Ahmed** Analysis of a Short Periodic Pulsator: SX Phoenicis Star XX Cyg. *Mohamed Abdel-Sabour, Ahmed Shokry, & Ahmed Ibrahim*, 287
- Soni, A. A.** Photometric Study of Three Short Period Variable Stars. *J. H. Peña, S. B. Juárez, A. A. Soni, H. Huepa, A. Rentería, & A. L. Zuñiga*, 259
- Sousa-Silva, P. A.** Dynamics Around an Asteroid Modeled as a Mass Tripole. *L. B. T. dos Santos, L. Marchi, P. A. Sousa-Silva, D. M. Sanchez, S. Aljbae, & A. F. B. A. Prado*, 269
- Stephanovich, V. A.** The Influence of the Mass Distribution of Stellar Objects on Their Gravitational Fields. *V. A. Stephanovich, W. Godtowski, M. Biernacka, & B. Mrzygłód*, 201
- Tamayo, F. J.** A New Non-Eclipsing CV SDSSJ 122405.58+184102.7 – A Probable Member to the SW Sextantis Type Stars. *A. Avilés, I. Arias, C. E. Chávez, J. E. Pérez, F. J. Tamayo, E. G. Pérez-Tijerina, & H. Aceves*, 11
- Tovmassian, G.** Revisiting FS Aurigae and its Triple Cataclysmic Variable System Hypothesis. *C. E. Chavez, A. Aviles, N. Georgakarakos, C. Ramos, H. Aceves, G. Tovmassian, & S. Zharikov*, 19
- Vega-Acevedo, I.** Star Formation Rate in Late-Type Galaxies: I- The  $H\alpha$  and FUV Integrated Values. *M. A. Magaña-Serrano, A. M. Hidalgo-Gómez, I. Vega-Acevedo, & H. O. Castañeda*, 39
- Watson, T. K.** A Search for Pulsation in Twenty-One White Dwarfs. *E. Paunzen, G. Handler, J. Janík, Z. Zemanová, M. Rode-Paunzen, M. S. O'Brien, T. K. Watson, & M. Drózdź*, 193
- Wen, X. Q.** The Environmental Dependence of the Age of Active Galaxies and the Dependence of the Clustering Properties of Active Galaxies on Age. *X.-F. Deng & X.-Q. Wen*, 87
- Yoldaş, E.**  $\gamma$  Dor: A Pulsating Component of KIC 8043961 in a Stellar Triple System. *C. Kamil, H. A. Dal, O. Özdarcan, & E. Yoldaş*, 179
- Zemanová, Z.** A Search for Pulsation in Twenty-One White Dwarfs. *E. Paunzen, G. Handler, J. Janík, Z. Zemanová, M. Rode-Paunzen, M. S. O'Brien, T. K. Watson, & M. Drózdź*, 193
- Zharikov, S.** Revisiting FS Aurigae and its Triple Cataclysmic Variable System Hypothesis. *C. E. Chavez, A. Aviles, N. Georgakarakos, C. Ramos, H. Aceves, G. Tovmassian, & S. Zharikov*, 19
- Zuñiga, A. L.** Photometric Study of Three Short Period Variable Stars. *J. H. Peña, S. B. Juárez, A. A. Soni, H. Huepa, A. Rentería, & A. L. Zuñiga*, 259

La *Revista Mexicana de Astronomía y Astrofísica*, fundada en 1974, publica trabajos originales de investigación en todas las ramas de la astronomía, astrofísica y temas vinculados a éstas. Se editan dos números por año y su distribución es gratuita a todas las instituciones relacionadas con los campos cubiertos por esta revista.

La política editorial de la *RMxAA* consiste en enviar a arbitrar los artículos recibidos a especialistas en el campo. Los interesados en publicar en nuestra revista deberán enviar por correo electrónico, a la dirección [rmaa@astro.unam.mx](mailto:rmaa@astro.unam.mx), la versión completa de su artículo en formato PostScript o PDF y el archivo LaTeX. Estos archivos deberán ir acompañados de una carta de presentación. Todos los trabajos deben ser preparados en inglés usando la versión más reciente del macro en LaTeX de la *RMxAA* “*rmaa.cls*” (disponible en <https://www.itya.unam.mx/rmaa/>). Se requiere un “Abstract” no mayor que 12 líneas, y un “Resumen” en español (este último podrá ser provisto por los editores de ser necesario); también se incluirán de 1 a 6 palabras clave (“Keywords”) de la lista de las revistas astronómicas internacionales. Se requiere que cada tabla incluida en el texto esté numerada y con título; las figuras deberán estar en formato PostScript (.ps) o PostScript encapsulado (.eps), estar numeradas y con leyenda explicativa. Se requiere que cada tabla y figura estén mencionadas en el texto. El estilo de las referencias sigue las normas astronómicas internacionales recientes. Para mayor información sobre el estilo de la *RMxAA* se puede consultar el archivo de ejemplo que viene incluido en los macros. La publicación es gratuita para los autores.

En 1995 se inició la Serie de Conferencias de la *Revista Mexicana de Astronomía y Astrofísica*, dedicada a la publicación de las memorias de reuniones astronómicas efectuadas en México y en otros países del continente. Hasta 1994 las memorias de reuniones astronómicas de la región se publicaron como volúmenes especiales de la *RMxAA*.

Las condiciones de publicación de cada volumen de las memorias de conferencias serán el resultado de un convenio establecido entre la *RMxAC* y los organizadores de cada evento. Los detalles de la publicación, que incluyen fechas y extensión de los textos, serán anunciados por los editores de cada conferencia. Las contribuciones extensas estarán en inglés con un resumen en español (o portugués en caso de las Reuniones regionales). Los resúmenes de las reuniones que no son temáticas tendrán una extensión máxima de 300 palabras incluyendo título, autores y afiliación; serán exclusivamente en inglés. Los macros LaTeX para las memorias se encuentran en <http://www.astroscu.unam.mx/~rmaa>. Todas las contribuciones y resúmenes deberán estar en estos formatos.

Se concede permiso a los autores de artículos y libros científicos para citar trabajos publicados en la *RMxAA* y en la *RMxAC* siempre y cuando se dé la referencia completa. También se permite la reproducción de figuras y tablas bajo las mismas condiciones.

La *RMxAA* aparece indexada en Current Contents, Science Citation Index, Astronomy and Astrophysics Abstracts, Physics Briefs, Publicaciones Científicas en América Latina, Astronomy and Astrophysics Monthly Index, PERIODICA, RedALyC, Latindex y SciELO.

The *Revista Mexicana de Astronomía y Astrofísica*, founded in 1974, publishes original research papers in all branches of astronomy, astrophysics and closely related fields. Two numbers per year are issued and are distributed free of charge to all institutions engaged in the fields covered by the *RMxAA*.

All papers received by the *RMxAA* are sent to a specialist in the field for refereeing. Authors interested in publishing in the *RMxAA* should send their papers to the e-mail address [rmaa@astro.unam.mx](mailto:rmaa@astro.unam.mx), in PostScript or PDF format, along with the LaTeX file. A submission letter should also be sent. Papers should be prepared in English, using the most recent version of the *RMxAA* LaTeX document class “*rmaa.cls*” (available from <https://www.itya.unam.mx/rmaa/>). An “Abstract” of at most 12 lines is required, as well as a “Resumen” in Spanish. The latter can be provided by the Editors, if necessary. A total of six or fewer “Keywords”, taken from the lists of international astronomical journals should be included. Tables should be numbered and include a title. Figures should be submitted in PostScript (.ps) or Encapsulated PostScript (.eps) format, should be numbered, and should include a caption. Both tables and figures should be mentioned in the text. The style of the references follows recent international astronomical usage. For more information about the style norms of *RMxAA* please consult the example included in the LaTeX package. Publication in *RMxAA* is free of charge to authors.

The Conference Series of *Revista Mexicana de Astronomía y Astrofísica* was founded in 1995 to publish the proceedings of astronomical meetings held in Mexico and other countries throughout the continent. Until 1994 such proceedings had been published as special issues of *Revista Mexicana de Astronomía y Astrofísica*.

Conditions of publication of proceedings of each conference will be the result of a mutual agreement between the *RMxAC* and the organizing committee. Details of publication, including length of papers, will be announced by the editors of each event. The extensive contributions should be in English, and should include an abstract in Spanish (or Portuguese for regional meetings). The abstracts of non-thematic meetings should not exceed 300 words including title, authors, and affiliation; they should be exclusively in English. The LaTeX templates specially prepared for proceedings can be obtained at <http://www.astroscu.unam.mx/~rmaa>; all papers should be submitted in this format.

Authors of scientific papers and books may quote articles published both in *RMxAA* and *RMxAC* provided that a complete reference to the source is given. Reproduction of figures and tables is also permitted on the same basis.

The *RMxAA* is indexed in Current Contents, Science Citation Index, Astronomy and Astrophysics Abstracts, Physics Briefs, Publicaciones Científicas en América Latina, Astronomy and Astrophysics Monthly Index, PERIODICA, RedALyC, Latindex, and SciELO.